UNIVERSITY OF HERTFORDSHIRE

Optical Measurement of Airborne Particles on Unmanned Aircraft

by

J. Girdwood

A thesis submitted to the University of Hertfordshire
in partial fulfillment for the degree of Doctor of Philosophy

in the
School of Physics, Astronomy, and Mathematics
Centre for Atmospheric and Climate Physics

October 2022

UNIVERSITY OF HERTFORDSHIRE

Abstract

School of Physics, Astronomy, and Mathematics
Centre for Atmospheric and Climate Physics

Doctor of Philosophy

by J. Girdwood

Aerosols and clouds are persistent causes of uncertainty in climate and weather models, which is due to their heterogeneous suspension and occurrence within the atmosphere, and complex interactions which are chaotic and exist on small scales. Unmanned aerial vehicles (UAVs) have grown in popularity, and are becoming more commonly used for general atmospheric measurement, particularly measurement of aerosols and clouds. This thesis presents and evaluates a synergy between two UAVs, a multi-rotor: the UH-AeroSAM octocopter and a fixed-wing: the FMI-Talon, and an optical particle instrument: the Universal Cloud and Aerosol Sounding System. Computational fluid dynamics with Lagrangian particle tracking (CFD-LPT) was used as a tool for the characterisation of the velocity fields and particle trajectories around both UAVs. In both instances CFD-LPT was used to develop an operational envelope, with particular attention to angle of attack constraints and size distribution perturbation, for the UAV – instrument synergy. UCASS was the first open path instrument to be used on a UAV, and a good case has been made for its continued use, particularly on fixed-wing UAVs, which exhibit less complex aerodynamics and superior stability in the induced sampling airflow through the instrument.

Acknowledgements

Firstly, I would like to thank my principle supervisor Warren Stanley, and former principle supervisor Helen Smith for their help and support throughout my PhD project. In addition, I am thankful for support from other supervisors I have had on a rolling basis, namely Zbigniew Ulanowski, Chris Stopford, and Charles Chemel—all of whom have always gone the extra mile to provide me with the technical help I needed to complete my PhD.

On a personal level, I would like to thank my partner Andras Sagi for always providing me with the emotional support I needed to get through both this project, and other major changes in my life.

Contents

List of Figures

List of Tables

Abbreviations

IPCC	**T**he **I**ntergovernmental **P**anel on **C**limate **C**hange
ARI	**A**erosol-**R**adiation **I**nteraction
ACI	**A**erosol-**C**loud **I**nteraction
ERF	**E**ffective **R**adiative **F**orcing
LiDaR	**Li**ght **D**etection **a**nd **R**anging
OPC	**O**ptical **P**article **C**ounter
ToF	**T**ime **o**f **F**light
TEOM	**T**apered **E**lement **O**scillating **M**icrobalance
DMA	**D**ifferential **M**obility **A**nalyser
CPC	**C**ondensation **P**article **C**ounter
SEMS	**S**canning **E**lectrical **M**obility **S**pectrometer
UFP	**U**ltra**F**ine **P**article
PMT	**P**hoto**M**ultiplier **T**ube
PD	**P**hoto**D**iode
FSSP	**F**orward **S**cattering **S**pectrometer **P**robe
FoV	**F**ield **o**f **V**iew
DoF	**D**epth **o**f **F**ield
CAPS	**C**loud, **A**erosol, and **P**recipitation **S**pectrometer
SID	**S**mall **I**ce **D**etector
CCD	**C**harge **C**oupled **D**evice

PBL	**P**lanetary **B**oundary **L**ayer
NWP	**N**umerical **W**eather **P**reditciont
CCN	**C**loud **C**ondensation **N**uclei
UAV	**U**nmanned **A**erial **V**ehicle
INP	**I**ce **N**ucleating **P**article
UCASS	**U**niversal **C**loud and **A**erosol **S**ounding **S**ystem
CLARIFY-2017	**CL**oud–**A**erosol–**R**adiation **I**nteraction and **F**orcing: **Y**ear **2017**
FAAM	**F**acility for **A**irborne **A**tmospheric **M**easurements
BBA	**B**iomass **B**urning **A**erosol
SSA	**S**ingle **S**cattering **A**lbedo
AEROCLO-SA	**AE**rosols, **R**adiati**O**n and **CLO**uds in **S**outhern **A**frica
ORACLES	**O**bse**R**vations of **A**erosols above **CL**ouds and their int**E**raction**S**
CDP	**C**loud **D**roplet **P**robe
DMT	**D**roplet **M**easurement **T**echnologies
PMS	**P**article **M**easurement **S**ystems
CSASP	**C**lassical **S**cattering **A**erosol **S**pectrometer **P**robe
ASASP	**A**ctive **S**cattering **A**erosol **S**pectrometer **P**robe
ASSP	**A**xial **S**cattering **S**pectrometer **P**robe
PPD	**P**article **P**hase **D**iscriminator
AIITS	**A**erosol **I**ce **I**nterface **T**ransmission **S**pectrometer
CAS-DPOL	**C**loud and **A**erosol **S**pectrometer with **DePOL**arisation
CAS	**C**loud and **A**erosol **S**pectrometer
CIP	**C**loud **I**maging **P**robe
SNR	**S**ignal to **N**oise **R**atio
TIA	**T**rans**I**mpedance **A**mplifier
POPS	**P**rinted **O**ptical **A**erosol **S**pectrometer
VTOL	**V**ertical **T**ake-**O**ff and **L**anding
M²AV	**M**ini **M**eteorological **A**erial **V**ehicle

MASC	**M**ultipurpose **A**irborne **S**ensor **C**arrier
SUMO	**S**mall **U**nmanned **M**eteorological **O**bserver
MAC	**M**aldives **A**utomated UAV **C**ampaign
ADC	**A**nalogue to **D**igital **C**onverter
DC	**D**irect **C**urrent
AC	**A**lternating **C**urrent
PFL	**P**rimary **F**ocal **L**ength
RTC	**R**eal **T**ime **C**lock
GPS	**G**lobal **P**ositioning **S**ystem
IMU	**I**nertial **M**easurement **U**nit
FC	**F**light **C**ontroller
MAVLink	**M**icro **A**ir **V**ehicle communication protocol
SPI	**S**erial **P**eripheral **I**nterface
CNC	**C**omputer **N**umerically **C**ontrolled
LAPSE-RATE	**L**ower **A**tmospheric **P**rofiling **S**tudies at **E**levation – a **R**emotely-piloted **A**ircraft **T**eam **E**xperiment
ATTREX	**A**irborne **T**ropical **TR**opopause **EX**periment
WISPAR	**WI**nter **S**torms and **P**acific **A**tmospheric **R**ivers

1 | Introduction

Climate change is an overwhelming geopolitical and humanitarian threat. The Intergovernmental Panel on Climate Change (IPCC) has reported increased warming rates, the extent of which meaning that the targeted maximum 1.5 °C global surface temperature increase will be unobtainable (IPCC, 2021). Here it was also stated that the influence of anthropogenic emissions on the climate system as a whole is an established fact, with high confidence of the impact of such emissions on the global water cycle and air quality. One significant contribution to total anthropogenic emission is aerosols—small liquid or solid phase species, suspended in a gaseous medium. Aerosol emissions can force climate change by directly interacting with solar radiation, and affecting the formation and evolution of clouds—known as aerosol-radiation and aerosol-cloud interactions (ARI, ACI) respectively. The total magnitude of the effective radiative forcing (ERF) resulting from aerosol emissions is highly uncertain; IPCC (2021) estimates the total aerosol ERF—from both ARI and ACI—to be between $-0.6\,\mathrm{W\,m^{-2}}$ and $-2.0\,\mathrm{W\,m^{-2}}$. While this uncertainty has decreased since 2013 (IPCC, 2013), it remains one of the largest uncertainties in the radiative forcing of climate change.

In part, the large uncertainty in total aerosol ERF results from a sparsity of atmospheric measurement of aerosols and clouds—since radiative transfer models are only as good as their input data. Both ARIs and ACIs have dependencies on aerosol concentration, morphology, size, and chemistry—all of which are parameters which need to be characterised. In addition, these aerosol parameters are highly spatially and temporally variable—particularly with

altitude—meaning measurements with high spatio-temporal resolution are required. Atmospheric aerosol measurements can be broadly divided into two categories: remote-sensing and in-situ. The former category broadly describes instrumentation which is most commonly ground-based, and used to directly measure bulk—and often abstracted—physical parameters of a large volume of air. An example of an aerosol remote-sensing technique is light detection and ranging (LiDaR). In this technique, a column of air is illuminated by a laser, and the bulk optical parameters—for example extinction and backscatter—are measured. LiDaR optical products can be used to measure vertically resolved aerosol concentration and size distribution, when combined with sun photometer data in the LIRIC and GARRLiC algorithms (Tsekeri et al., 2017). Other remote-sensing techniques can also be used to infer aerosol and cloud microphysical properties—for example cloud radar, ceilometers, and microwave radiometers—however these techniques deviate broadly from the topic of this thesis. While remote-sensing techniques are an important tool in the atmospheric physicist's toolbox, they are not an all-encompassing atmospheric measurement solution. This is because they are often limited in spatial resolution—both vertically due to detector limitations, and laterally since they can only measure in one fixed location—and have a high minimum altitude; Baars et al. (2015), Engelmann et al. (2015) define the PollyXT portable LiDaR (Althausen et al., 2009) lower limit as 100 m, with a correction factor below 600 m. In addition, these techniques directly measure variables, which are abstractions of aerosol and droplet physical properties; they also often contain convolutions of other data and artefacts, which require complex algorithms and models to extract. The aforementioned in-situ measurements, therefore, are required to validate remote-sensing.

In general, in-situ atmospheric aerosol measurements either measure ground-level aerosol, or employ a platform—for example a meteorological balloon, or an aircraft—to transport an instrument through the atmosphere, whereupon suspended aerosol is directly measured. Ground-based aerosol measurement is a broad category, ranging from networks of low-cost sensors for air quality monitoring, to cloud probes positioned on mountain-top observatories (Douglas and L'Ecuyer, 2019, Guyot et al., 2015) or towers. For the same physical quantity

output, in-situ instruments will require less assumptions when compared to a remote-sensing technique, due to the raw data being a less abstracted physical quantity. An example of this is the scattering cross-section of an individual particle being measured by an optical particle counter (OPC), compared to the backscatter coefficient measured by LiDaR, when a particle size distribution is desired as an output. The former technique requires an assumption of the aerosol particle shape and refractive index to convert scattering cross section to a radius, while—as previously mentioned—the latter requires assumptions of particle morphology (Müller et al., 2013, Wagner et al., 2013), composition, a first order Gaussian fit in the overall distribution (Tsekeri et al., 2017), and additional sun-photometer data to reach the same output.

In-situ aerosol instrumentation can manifest in various different forms; measuring a broad array of different aerosol physical parameters. The aerodynamic cross section—that is, the area of a particle which effects an airflow continuum—of a particle can be measured by an aerodynamic particle spectrometer (APS, Chien et al., 2016). An APS will accelerate or decelerate a particle via an aerodynamic force—most commonly achieved by using a nozzle to produce a continuum velocity gradient longitudinal to the particles direction of travel—and measure the particles time of flight (ToF) between two fixed points. The aerodynamic force on the particle, and therefore its aerodynamic cross section, can then be calculated. This technique has a strong advantage in air quality measurements, since the aerodynamic cross section of a particle is the unabstracted parameter that affects particle transport into the lungs. The major disadvantage of APS measurements occurs when applying the described technique to liquid droplets. Secker et al. (2001) found that the induced acceleration of a droplet in the APS nozzle causes it to deform, thus changing its aerodynamic cross section during measurement. APS instruments are therefore not suited for cloud measurements.

The mass of an aerosol particle can also be directly measured using gravimetric techniques. These often involve the deposition of particles onto a filter or impactor plate, the mass of which is recorded before and after sampling, and the difference between them is the time-integrated aerosol mass. The advantage of filter methods is the high repeatability and

accuracy, while the disadvantage is temporal resolution, since each time series data point requires a new filter or impactor plate. Another gravimetric technique is the tapered element oscillating microbalance (TEOM), where aerosol particles are deposited on a filter at the end of an oscillating glass tube, thus changing its inertia and therefore oscillating frequency. The frequency of oscillation is then measured and the total aerosol mass is reported. TEOM instruments can report data without the need for lab-based analysis, which makes this technique suited for personal air quality monitoring applications, as well as ground based aerosol measurements. TEOM instruments can also report cumulative change in aerosol mass over time—thus meaning temporally resolved data is possible—and the filter at the end of the glass tube can be analysed separately for a comparative measurement (Ruppecht et al., 1992).

Another aerosol physical property commonly measured with in-situ techniques is electrical mobility. A differential mobility analyser (DMA) employs an annular sample flow around a high voltage electrode. As a particle traverses the length of the electrode, it will be attracted towards it with a transverse velocity proportional to its electrical mobility, which is dependant on both the charge and aerodynamic cross section of the particle (Wang and Flagan, 1990). If a particle is assumed to be spherical, its electrical mobility is given by Zhang et al. (1995)

$$Z_p = \frac{v}{E} = \frac{neC_c}{3\pi\mu D_p} \tag{1.1}$$

Where Z_p is the electrical mobility, v is the transverse velocity ($\mathrm{ms^{-1}}$), E is the electrical field ($\mathrm{Vm^{-1}}$), n is the number of charges on a particle, e is the elementary charge ($\approx 1.602 \times 10^{-19}\mathrm{C}$), μ is the dynamic viscosity of the air ($\mathrm{Kgm^{-1}s^{-1}}$), and D_p is the diameter of the—assumed spherical—particle (m). Equation 1.1 includes the implicit assumption that a particle is spherical and therefore subject to stokes flow, thus resolving particle diameter from aerodynamic cross section—an abstract quantity with limited use. Commonly, a DMA output sample flow will be connected to a condensation particle counter (CPC)

to create a scanning electrical mobility spectrometer (SEMS, Wang and Flagan, 1990). A SEMS will vary the voltage applied to the centre electrode to select particles with different electrical mobilities in a scan, the CPC will then count the number of particles corresponding to the selected mobility, and each element of the scan is concatenated to form an electrical mobility distribution. DMAs in this configuration and similar are utilised commonly in air quality applications due to their accuracy, particle diameter resolution, and applicability to ultrafine particles (UFPs) due to their high nanoparticle sensitivity.

Aerosol particles can also be defined by their optical properties. As previously mentioned, an OPC will directly measure the elastic scattering cross section of a particle, which can then be used to calculate the diameter of the particle. Generally, this is accomplished by illuminating a particle with a light source—usually a laser—and collecting a range of light scattering angles with a mirror or lens. This light is then focused onto a detector—normally a photomultiplier tube (PMT) or photodiode (PD)—and the induced current is directly proportional to the scattering cross section. In order to calculate a concentration, the volume of air sampled must be known. This involves both a measurement of the sample flow velocity, and the area of the laser beam that is exposed to the sample flow. The latter requirement can be satisfied by either constraining the sample airflow in a tube, which is then directed immediately into the laser beam path, or defining a sampled area of the beam optically. OPCs are widely implemented in high resolution air quality sensor networks (Gupta et al., 2018, Santana et al., 2021) due to their cost effectiveness and applicability to PM2.5.

Historically, OPCs have also been used as cloud probes. The Forward Scattering Spectrometer Probe (FSSP) was one of the first examples of an OPC cloud probe (Baumgardner and Spowart, 1990, Baumgardner et al., 1985, Dye and Baumgardner, 1984, Knollenberg, 1976). The FSSP collects the forward scattered light from a particle, which is then focused onto a PD detector via a lens system, and directly reports a particle diameter through a calibration. The sampled area of the laser beam is defined optically by the laser beam width—which defines the field of view (FoV)—and a light-splitting detector, which has a

mask-aperture on one channel—this defines the depth of field (DoF, see Dye and Baumgardner, 1984, for more details). This mechanism is commonly utilised in OPC cloud probes; Baumgardner et al. (2001) utilises the exact same system in the Cloud and Aerosol Spectrometer (CAS) component of the Cloud, Aerosol, and Precipitation Spectrometer (CAPS).

Elastic light scattering can also be used to infer more detailed information about a particle. Ulanowski et al. (2014), Vochezer et al. (2016) use the Small Ice Detector (SID, assessed by Cotton et al., 2010) cloud probe to observe the microphysical properties of small atmospheric ice crystals in cirrus and mixed phase clouds, and derive crystal habit information. Unlike a conventional OPC, the SID instrument does not integrate the scattered light. Instead the light from a range of angles is collimated by a lens system, and focused on a spatially resolved detector, in this case a charge coupled device (CCD). The CCD produces an image of the forward scattering pattern produced by the ice crystal. This pattern can then be combined with simulated data to infer habit and size data from the ice crystal. This technique is discussed further in Chapter 2.

All the aforementioned techniques and instruments have specific use-cases, which are required in tandem to tackle the atmospheric aerosol and cloud measurement void consistently reported by the IPCC. However, the largest gap in the atmospheric scientist's measurement arsenal is within the planetary boundary layer (PBL). The PBL is the layer of the troposphere adjacent to the earths surface, with a height that is highly variable and has multiple definitions (Seidel et al., 2010)—although it is normally below 2 km to 3 km (Garratt, 1994). It contains many processes which are responsible for regulating transport of aerosols into the free troposphere, and its characterisation is important for many applications of atmospheric science—including air quality, numerical weather prediction (NWP), and aeronautical safety (Garratt, 1994). Since a large proportion of the total aerosol is held within the PBL (Liu et al., 2009) aerosol measurements within this region are essential yet—as previously mentioned—lacking in quantity. In addition, as observed in Ding et al. (2013), PBL ARIs cause local extinction of radiation, thus reducing the surface solar radiative flux, and causing large surface temperature drops. The reduction of PBL solar flux also decreases turbulence,

which leads to less entertainment of dry air from the free troposphere, which increases relative humidity. This causes the hygroscopic growth of PBL aerosol, which further enhances PBL ARIs in a positive feedback loop (Li et al., 2017).

While ground based aerosol measurement is commonly conducted with a wide range of methodology (see Li et al., 2017, for review), aerosol vertical distribution is often assumed to be constant from the surface to the boundary layer top in radiative transfer models. As previously established, there is a large uncertainty in aerosol ERF. In addition, vertical aerosol structure strongly affects the total aerosol ERF (Liao and Seinfeld, 1998); it is critical, therefore, that vertically resolved measurements of aerosol be conducted, particularly in the PBL, where aerosol concentrations are high. Liao and Seinfeld (1998) conducted a sensitivity study of different aerosol parameters to the overall aerosol ERF; the study is regarding mineral dust aerosol, however it is adaptable to different aerosol types. Here it was found that the size of the aerosol particle was an important factor in determining shortwave and longwave radiation interactions. Therefore aerosol size spectra in particular must be resolved, in addition to altitude.

ACIs in the PBL are also important. Aerosol injection into a cloud can significantly accelerate its precipitation, and change its radiative properties, in addition to acting as cloud condensation nuclei (CCN, Fan et al., 2016). The high concentration of PBL aerosols will not only affect PBL clouds, but also affect the free troposphere due to aerosol transport from the PBL. In addition, cloud presence will alter the aerosol ERF (Liao and Seinfeld, 1998), the PBL depth (Garratt, 1994), and therefore aerosol transport processes between the PBL and free troposphere—further increasing the entanglement between clouds and aerosol.

With these points in mind, it is clear that the PBL aerosol and cloud measurement void must be addressed. Fan et al. (2016) states that action must be taken to accumulate more data for the characterisation of ARIs and ACIs. The current platforms suited for vertically resolved PBL observations are: aircraft (for example Liu et al., 2009), satellite-based LiDaR (Winker et al., 2007), meteorological towers (Sun et al., 2015), tethered balloons (Osborne et al., 2014), and meteorological soundings.

Aircraft measurements are often the most stable and versatile platform, bolstered by many studies into the accuracy and repeatability of the measurements produced by the mounted instrumentation (Bennett et al., 2019). However, aircraft are by far the most expensive option, which limits the quantity of measurements that can be performed using them. Additionally, aircraft are limited in their minimum operating altitude—500 ft in the UK—which limits their usefulness for measuring PBL aerosol. Satellite-based LiDaR can cover a wide area of the earth, and will operate perpetually, which allows for readily accessible data to be recorded over a long time period, and makes them particularly useful in climatology studies. However they suffer from the same flaws as conventional LiDaR—that is, only measuring abstracted quantities, which rely on assumption for the calculation of tangible physical parameters, and requiring validation using in-situ data. Meteorological towers can be used for consistent data at one lateral position, with—normally—ground-based aerosol instruments positioned at vertical intervals. While this extends the applicability of reliable, tested, and diverse ground based instrumentation in one spatial dimension, they are expensive to set up and maintain, and re-positioning them is non-trivial. Tethered balloons can be used for much the same reasons as a meteorological tower, with the advantage of being more easily re-positioned, and being more cost effective. However, due to the increasing price of helium, combined with the general hesitancy to use hydrogen for safety concerns, tethered balloons are becoming less of a viable platform for PBL measurement. Additionally, tethered balloons are limited by the buoyant force they can generate—which implicitly governs both instrumentation payload mass and maximum altitude, since the mass of the carried tether will increase with balloon altitude. This links into the first problem, since more helium is required to increase the buoyant force. Meteorological balloons are untethered, and sample a Lagrangian column of atmosphere from launch to burst altitude—a function of the balloons surface tension, maximum volume, and amount of helium. They are a proven platform for atmospheric parameter measurement, and commonly used. However, their applicability to aerosol measurement is limited, because aerosol instrumentation is generally expensive, and the balloon payload often cannot be retrieved.

None of the listed platforms are ideal for PBL aerosol measurement. The ideal platform has the stability and versatility of the aircraft—without the minimum altitude limit; the spatio-temporal observational capability of satellite LiDaR—incorporating an in-situ instrument; and have the ease of deployment and maintenance of the tethered balloon—without the need for costly helium.

Unmanned aerial vehicles (UAVs) have gained recent popularity as an atmospheric measurement platform. For this purpose, UAV can be broadly divided into two categories: multi-rotor, and fixed-wing. The former consists of multiple (conventionally three or more) 'rotors', oriented to provide thrust in the vertical direction to provide lift through thrust; pitch, roll, yaw, and thrust are controlled by varying the power to each rotor. The latter UAV type is much the same as a conventional manned aircraft, with lift provided by an aerofoil-section wing, and pitch, roll, and yaw actuated by aerodynamic control surfaces. Generally, UAVs have distinct advantages over both manned aircraft and meteorological balloons, since they are re-usable, lightweight, and cost-effective. The two different categories of UAV posess different benefits and caveats, and are therefore used in different scenarios. The multi-rotor category has superior spatio-temporal sampling capability, due to its ability to hover and fly vertically. These also tend to require less pilot experience to fly, and are simple to design and build. Contrarily, fixed-wing UAVs are burdened—although to a lesser extent due to their smaller size—by the same spatio-temporal sampling restrictions as manned aircraft. Mamali et al. (2018), for example, used a rectangular-spiral ascent-descent pattern, where a multi-rotor could simply fly vertically upwards. However, fixed-wing aircraft are generally—both kinetically and aerodynamically—more stable instrumentation platforms, since there is often only one constantly moving part, and propellers can be mounted aft of the instruments in order to reduce aerodynamic disturbances. Fixed-wing UAV also have better endurance than their similarly sized multi-rotor equivalents, and can therefore reach higher altitudes (demonstrated in Mamali et al., 2018). UAVs are a new atmospheric measurement platform, however they have great potential to fill a gap in PBL aerosol and cloud research.

Instrumentation-platform synergy is important for repeatable and accurate measurements. In order to function on a UAV platform for PBL research, an instrument must be lightweight, tolerant to vibration and mechanical stresses associated with UAV operation, small enough to mount on a wing or multi-rotor body, and have a characterised response to external airflows. While an APS could satisfy all of these requirements with some design modification, they are not suited for cloud droplet measurements due to deformation under acceleration. Filter samplers could be modified to function on UAV platforms, and could be utilised for ice nucleating particle (INP) research (for example DeMott et al., 2016, could benefit from a UAV platform). However, a temporally—and therefore vertically—resolved instrument would be ideal for PBL research. Additionally, the total aspiration through the filter would have to be calculated in order to resolve the sampled concentration integral, therefore isokinetic flow—that is, the instrument inlet pressure being constant with the freestream dynamic pressure—is essential. Isokinetic flow requirements are discussed further in Chapter 2. Instruments based on electrical mobility are generally heavy due to their need for high-voltage power supplies and a grounded metallic chassis.

OPCs can be both small—thus making them suitable for mounting on small UAV wings—and lightweight, particularly with the advances of diode laser technology and plastic optics. They are also commonly used as larger, heavier cloud probes on conventional aircraft, and therefore can be used with strong external airflows. The following chapters, therefore, will focus on the integration of an OPC with both fixed-wing and multi-rotor UAV frames, with the aim of enhancing the field of PBL aerosol and cloud measurement.

2 | Literature Review

In order to properly establish this thesis, a review is presented here on the literature pertaining to: i) the current status of PBL aerosol and cloud measurements, to ensure a UAV OPC synergy would be suited for the task outlined in Chapter 1; ii) an insight into the range of in-situ optical particle measurement techniques available, and their suitability for UAVs—in order to provide a basis for the scope of optical measurement techniques for this use; and iii) the current applications of UAVs in atmospheric science—both regarding aerosol measurement, and otherwise.

2.1 PBL Aerosol and Cloud Measurement

As previously discussed in Chapter 1, there is a distinct gap in PBL particulate measurement. The purpose of this section is to discuss observational studies of PBL aerosol and cloud, and how a UAV – OPC platform synergy could be used to an advantage.

2.1.1 Aerosol and ARIs

Aerosols can affect radiation by scattering and absorption, which can modify the thermodynamic—and therefore meteorological—processes in the atmosphere. These are traditionally called the direct effects of aerosol. Arias et al. (2021) estimated the global aerosol direct radiative forcing to be between $-0.6\,\mathrm{W\,m^{-2}}$ and $0.0\,\mathrm{W\,m^{-2}}$—a large error margin.

Anthropogenic aerosols contribute significantly to the local atmospheric aerosol loading in urban settings. Several studies in urban China have been conducted to observe and assess the entanglement of aerosol microphysics and boundary layer meteorology (for example Ding et al., 2013, Miao and Liu, 2019, Miao et al., 2018, Quan et al., 2013, Su et al., 2020, Sun et al., 2013). Quan et al. (2013) uses a micro-pulse LiDaR to resolve aerosol backscatter coefficient against altitude, and a DMA system to resolve aerosol mass concentration on the ground level. It was concluded here that aerosol concentration *might* affect PBL height, which further increases PBL aerosol concentration—due to the tighter spacial constraint—in a positive feedback effect, which is evidenced by a negative correlation of PBL height with aerosol concentration. The proposed aerosol – PBL coupling effect—also found in Ding et al. (2013)—is driven by an ARI whereby aerosol extinction causes localised cooling, which reduces convection and therefore PBL height. The thermodynamic processes surrounding this effect were originally discussed in Atwater (1971)—building on the work of Sheppard (1958)—where it was found, through model experiments, that enhanced atmospheric stability could be caused by particulate pollutants scattering shortwave radiation, and absorbing longwave radiation. Here it was found that an enhanced elevated inversion was highly coupled with the concentration of pollutant infra-red absorbing particles. Atwater (1971) models particulate pollution as a homogeneous layer, which was an assumption based on rudimentary observational data at the time. The heterogeneity of particulate concentration in urban environments, and the extent to which this would affect ARIs, is an ongoing topic of discussion.

Sun et al. (2013) also suggests that a heterogeneous vertical distribution of aerosol, caused by changes in thermodynamic variables, is significant in urban environments. Here, PM2.5 was measured at three different altitudes with a meteorological tower, and compared with aerosol backscatter coefficient from a LiDaR. It was concluded that local changes in wind-speed, temperature, pressure, and humidity, both temporally and with altitude, caused significant unhomogenisation of the aerosol vertical distribution. This is further investigated by Sun et al. (2015), who suggests that both vertically and temporally resolved measurements

of aerosol is important to characterise intense aerosol events—which can onset rapidly—and previous 24 h filter measurements were not sufficient. In this study, the primary and secondary organic aerosol were measured separately, and it was found that their vertical and temporal variations differed significantly. Since primary organic aerosol is important for air pollution emission studies—as secondary organic aerosol is often emitted regionally—the importance of measuring both above and below the urban canopy was stressed in order to isolate the two aerosol types. Bei et al. (2021) shows that ARIs of this nature can also drive synoptic thermodynamic and meteorological systems using a model study, putting further emphasis on the importance of the observations of small perturbations in a chaotic system.

The extent of the vertical aerosol property structure in urban environments, and how it affects the PBL – aerosol feedback effect, is discussed in Su et al. (2020). Here the aerosol vertical structure is broadly separated into three types: well-mixed or homogeneous, decreasing concentration with altitude, and increasing concentration with altitude. Generally it is found that localised heating is correlated with aerosol concentration; the vertical temperature peak—and therefore aerosol radiative forcing peak—location is in the lower, middle, and upper atmosphere for the three aerosol vertical structure types defined. It was found that the aerosol – PBL coupling could form a stable or unstable atmosphere depending on which of the three categories the aerosol vertical structure was in. Therefore, measurements of the vertical aerosol structure within the urban PBL is of importance, not only for human health, but for weather prediction and climate modelling.

Several studies have been conducted into observing ARIs in the south-eastern Atlantic ocean—CLoud–Aerosol–Radiation Interaction and Forcing: Year 2017 (CLARIFY-2017 Haywood et al., 2021); AErosols, RadiatiOn and CLOuds in Southern Africa (AEROCLO-SA, Formenti et al., 2019); and ObseRvations of Aerosols above CLouds and their intEractionS (ORACLES Redemann et al., 2021). The studies investigated biomass burning aerosol (BBA) and warm stratocumulus cloud, using manned aircraft equipped with a variety of in-situ aerosol instrumentation—for example the Facility for Airborne Atmospheric Measurements (FAAM) BAe-146—as a measurement platform. Haywood et al. (2021), Wu et al.

(2020) found the BBA vertical profile to be highly spatially and temporally variable throughout the campaign—consistent with the results from a previous campaign in the region (Eck et al., 2003). The use of UAVs in a campaign similar to this would vastly improve the spatio-temporal measurement resolution. This is particularly important when measuring highly variable quantities. In addition, a UAV would be capable of performing a tighter vertical profile than the BAe-146, which would increase the lateral measurement resolution. However, the optical properties considered here are single scattering albedo (SSA), and absorption coefficient (Haywood et al., 2003, Wu et al., 2020). These would be difficult to calculate from simple OPC data, and require the assumption of sphericity and a known refractive index, the validity of the former assumption being questionable for aerosol. Taylor et al. (2020) questioned the validity of Mie calculations for the determination of the mass absorption coefficient. It is also probable that the validity of scattering calculations—similar those used by an OPC—would be questioned for highly absorbing or aspherical particles. While this finding has certain implications for the OPC – UAV combination, the successful integration of a simple OPC instrument into a UAV would lead to easier integration of more complex optical measurement techniques at a later date. This will be discussed further in Sect.2.2.

Saharan desert dust significantly contributes to overall global aerosol loading, and measurements of Saharan dust are reasonably sparse. Several studies have attempted to quantify the transport (Allen et al., 2013a), electrostatic (Daskalopoulou et al., 2021, Ulanowski et al., 2007), and optical properties of atmospheric Saharan dust (Ryder et al., 2013). During northern hemisphere summer months, a strong low pressure system develops in the central Sahara, causing the aerosolisation of desert dust particles into the lower and upper troposphere. The Fennec campaign was an extended observational campaign, conducted to increase the data-density in the Saharan region, and involved several conventional aircraft measurements. Ryder et al. (2015) described the advances in the understanding of Saharan dust made during Fennec, which include the characterisation of dust particles up to 300 µm in diameter. These ultra-coarse dust particles would contribute more significantly to the dust volume size distribution than smaller particles, and therefore have a larger impact on

SSA and absorption, thus meaning even a small quantity would significantly impact the bulk dust optical properties (Ryder et al., 2013). Ryder et al. (2019) discusses the abundance and impact of these coarse dust particles. The authors found that coarse-mode dust particles are present up to 5 km above ground level during long lasting—over 12 h—dust events. It was also found that coarse-mode particles have a larger impact on long-wave extinction than short-wave extinction, implying they enhanced radiative cooling. The coarse-mode particles are not properly represented in dust forecast models, and would therefore cause a large discrepancy in predicted mass concentrations and optical parameters. The authors also find a large concentration of coarse-mode dust particles in the transported dust, which are not represented in climate models, implying an unknown force in the opposite direction to gravitational settling. Since these dust particles have a relatively low concentration, but large impact on atmospheric radiative properties, measurements must be performed with high sensitivity, which means sampling a large amount of air. UAVs are well suited for this application because of their ability to cover large areas of the atmosphere with higher resolution, thus meaning they are more likely to encounter coarse-mode particles.

2.1.2 Clouds and ACIs

The entanglement of the aerosol impacts on cloud radiative forcing are traditionally known as the indirect effects of aerosol (Boucher et al., 2013, Fan et al., 2016). There is generally insufficient data to disentangle the aerosol affect on cloud radiative processes, and therefore a large uncertainty in the radiative forcing caused by the indirect effects of aerosol. While there has been substantial advances in reducing this uncertainty since 2013 (Arias et al., 2021, Boucher et al., 2013), it still remains the cause of one of the largest disparities in the total ERF, because ACIs contribute significantly to the aerosol ERF. Arias et al. (2021) estimates the contribution of ACIs to ERF to be between $-1.7\,\mathrm{W\,m^{-2}}$ and $-0.3\,\mathrm{W\,m^{-2}}$. Different ACIs affect different types of cloud. For the purposes of this project, only those

affecting low and mid – level clouds will be discussed, since high-level cirrus is out of the range of most small and medium sized UAVs.

Warm stratus and stratocumulus clouds are formed by cloud top radiative cooling, and have a net cooling effect on the planet, since they consist of droplets which exhibit enhanced extinction (Stephens and Slingo, 1992). The effective diameter of the droplet size distribution decreases with an increase in CCN Shrivastava et al. (2013). This has further cascading effects on the clouds radiative properties, since smaller cloud droplets reflect sunlight more efficiently (Ackerman et al., 2004). Ackerman et al. (2004) also found that the reduction in effective diameter that aerosol entrainment causes can suppress precipitation, since smaller droplets are less likely to collide and coalesce. Since stratus and stratocumulus clouds commonly form within the PBL (Fan et al., 2016), they are difficult to measure and characterise via conventional means, particularly if they form over land where strict constraints on operation of aircraft apply. Price et al. (2018) used a Cloud Droplet Probe (CDP) from Droplet Measurement Technologies (DMT) mounted to a tethered balloon to retrieve a vertical profile of PBL layered-cloud droplets. While valuable measurements were retrieved during this study, tethered balloons require a large amount of helium in order to lift heavy cloud probes, which is expensive and limited. In addition, tethered balloons cannot measure over lateral distances. UAVs could be applied to the measurement of fog and layered-cloud droplets with little technical challenges, since these phenomena form within the PBL, which is within the technical operational range of most UAVs. In addition, UAVs are able to measure laterally from a flexible range of take-off sites, so lateral heterogeneity can be characterised, which can be significant over complex terrain (Price, 2011). Fog in particular is highly heterogeneous, presenting a good application for UAVs since observations of this phenomena would benefit from the enhanced spatio-temporal resolution they [UAVs] provide.

Zeng (2008) presents and discusses the results of a modeling study, intended to explain the broadening of the ice crystal spectrum with temperature found in Heymsfield (1986). The study coined a theoretical critical relative humidity model; whereby an ice crystal would grow via vapour deposition if the relative humidity was above the critical relative humidity, and

shrink if the conditions were reversed. While the tropical mixed phase clouds are beyond the range of most small UAVs, the effect was also theorised in arctic diamond dust (Zeng, 2018b) which could be within the PBL (Gultepe et al., 2017b). Ice-phase precipitation is generally a challenging topic in meteorology (Gultepe et al., 2017a), and one of the main processes involved in cloud dissipation; more observations of precipitation mechanisms would be valuable for the validation of cloud evolution models. In addition, a similar effect was found in warm clouds through a modelling study (Zeng, 2018a). Since warm cloud exists readily within the PBL, UAVs are a good platform to conduct the model validation with. An OPC would also be a good tool for measuring warm cloud droplet size spectra; cloud droplets are spherical and non absorbing, therefore meaning Mie assumptions would be valid.

2.2 In-Situ Optical Aerosol and Cloud Measurement

As briefly discussed previously, a particle can be characterised by its optical properties, which describe how a given particle interacts with electromagnetic radiation—usually visible light. Generally the optical properties used to characterise particles are absorption cross-section, elastic scattering cross-section, inelastic scattering parameters—for example emitted fluorescence spectrum, and depolarisation ratio. This section will focus on elastic scattering and depolarisation measurements, since these are most commonly integrated into optical cloud probes.

The first quantitative measurements of colloidal suspensions of particles were performed using a primitive instrument called a Tyndallmeter by Mecklenburg (1915), which was built upon by Tolman et al. (1919). The instrument involved measuring the Tyndall effect, which is an out-of-fashion term for the reduction in intensity of a beam of light by a confined suspension of particulate matter resulting from extinction, which was generally modelled based on Rayleigh scattering. These bulk measurements were used in the fields of air quality, chemical measurement, and chemical warfare.

The first bespoke instruments designed for single-particle measurements of suspended particulates were designed during World War II. Gucker et al. (1947) presents an instrument designed to test the efficiency of gas mask filters called a Photoelectric Counter, which utilises a focused beam of non-coherent light to illuminate a confined stream of particles. The radial scattering around this beam is then focused onto a PMT. This is the first system-level design—that is, a light source, beam forming optics, light collecting optics, and a photoelectric detector and amplifier—to resemble the structure of the modern OPC. Gucker and O'Konski (1949) then present a design that uses 90° centred scattering, which improved the signal to noise ratio of the instrument. A similar 90° centred scattering design, called the Counter-Photometer, was presented and evaluated by O'Konski and Doyle (1955), which was one of the first studies to characterise an OPC. Other commercialised OPC instruments following the same basic system-level design appeared later on, for example Sinclair (1967) who used forward scattering, and a calibration curve based on Mie theory. The first non-spherical and absorbing particles were considered by Whitby and Vomela (1967) in an early instrument inter-comparison study.

The first optical scattering instruments to see common use in atmospheric science were the Knollenberg photoelectric counters, which were commercially available from Particle Measurement Systems (PMS). The simplest of these probes was the Classical Scattering Aerosol Spectrometer Probe (CSASP) which used a Helium Neon laser as a light source, and collected scattered light between 4° and 22°. The Active Scattering Aerosol Spectrometer Probe (ASASP) had a similar detecting optical configuration, the only difference being the particle illumination system. Schuster and Knollenberg (1972) describes the open-cavity laser used in the ASASP. The particle stream and light collection optics are located within the laser cavity itself in order to increase the intensity of the light at the sample area by utilising the transmitted and reflected plane waves, thus changing the scattering cross section

from

$$R = \frac{\pi}{k^2} \int_{\Omega} \left(|S_1|^2 + |S_2|^2 \right) \sin(\theta) \, \mathrm{d}\theta \tag{2.1}$$

to

$$R = \frac{\pi}{k^2} \int_{\Omega} \left(|S_1(\theta) + S_1(\pi - \theta)|^2 + |S_2(\theta) + S_2(\pi - \theta)|^2 \right) \sin(\theta) \, \mathrm{d}\theta \tag{2.2}$$

where the variable definitions are consistent with Pinnick and Auvermann (1979). This also has the advantage of removing the extinction at the gain-medium – air interface. The available power density efficiency was a significant drawback of the primitive lasers available at the time. One disadvantage of this design, however, is a highly non-monotonic instrument response versus particle size, which is demonstrated by Garvey and Pinnick (1983). In addition, the optical properties of the measured particle affect the active laser, since a scattering medium is introduced into the laser cavity (Kim, 1995, Kim and Boatman, 1990), thus causing coupling of the beam properties and the particle. These conclusions are supported by Liu et al. (1992) for salt and latex aerosol, where the Passive Cavity Aerosol Spectrometer Probe (PCASP, evaluated in Strapp et al., 1992)—another Knollenberg counter created as a higher-power alternative to the CSASP—was suggested as an alternative, since it has a similar size range to the ASASP, and does not involve an active laser cavity. For these reasons, the ASASP has largely fallen out of use, and the PCASP is used commonly in atmospheric physics.

The Axial Scattering Spectrometer Probe (ASSP, inter-comparison with other instruments in Baumgardner, 1983) was another forward scattering instrument designed with a lower gain, so larger aerosol sizes could be measured. However, this did not see frequent use and was replaced with the FSSP—another Knollenberg counter mentioned previously (Knollenberg, 1976). These particle counters are evaluated and compared by Pinnick and Auvermann (1979). One configuration disparity in particle counter design emerged during

this era: open-path versus artificially aspirated. An artificially aspirated particle counter uses a mechanism—usually a fan or pump—to move the sampled medium through the optical cavity of the instrument; examples of such a design are the CSASP and the ASASP. An open-path instrument requires the movement of the instrument itself through the sampled medium, for example the FSSP and the ASSP. One major advantage of open-path designs is the lack of aerosol transport tubing, where significant particle loss mechanisms can occur (Von Der Weiden et al., 2009). Another advantage—when the instrument is mounted on a moving platform such as an aircraft—is the lack of a requirement for isokinetic flow through the sampling inlet—that is, the stagnation pressure within the inlet needing to be the same as that in the freestream airflow. If the pressure within the inlet is higher than the freestream stagnation pressure, normally caused by a pump or fan running too slowly, the particle concentration will be under predicted by the instrument, and vice versa. In an artificially aspirated instrument on a moving platform, the aspiration mechanism must be regulated in a closed-loop system to ensure that the velocity of the air within the sampling tube matches the velocity of the air outside of the sampling tube. The effect is illustrated in Fig. 2.1 where the left panel shows a case of isokinetic flow, the middle panel shows a case of over predicting particle concentration due to anisokinetic flow, and the right panel shows a case of under predicting particle concentration due to anisokinetic flow.

The FSSP has seen extensive use in the field of cloud physics (some early studies include Heymsfield et al., 1979, Stephens et al., 1978), because it provides an ideal particle size range for cloud droplet measurements, and is straightforward to attach to aircraft since PMS determined the standard size for an aircraft wing mounting canister. Pinnick et al. (1981) discussed the effect of refractive index on the Mie curve response of the FSSP. The electrical and optical characteristics of the FSSP were evaluated by Dye and Baumgardner (1984). Some basic principles of particle counter calibration were established here, including using the modal diameter of the calibration particles, and using multiple reference points to establish the calibration curve, since instrument gains can differ. The authors also discussed the effect of increased sampling airspeed on observed droplet diameter, which is discussed

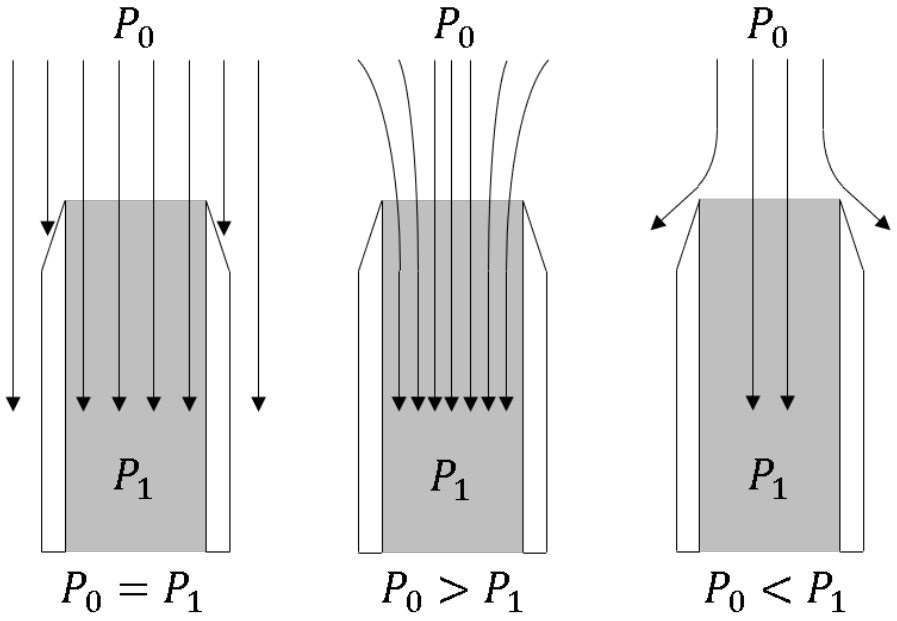

FIGURE 2.1: An illustration of isokinetic flow considerations. The left panel shows a case of isokinetic flow, the middle panel shows a case of over predicting particle concentration due to anisokinetic flow, and the right panel shows a case of under predicting particle concentration due to anisokinetic flow

further in Chapter 5. The coincidence—that is, the response of the instrument to multiple particles being in the beam at once—and dead-time—that is, the time the instrument takes after measuring a particle before it can measure a new one—characteristics of the FSSP are discussed by Baumgardner et al. (1985), Brenguier (1989), Cooper (1988); FSSP data correction factors for these two particle loss mechanisms were derived here. Baumgardner and Spowart (1990) discussed the effect of laser beam heterogeneity on the FSSP, and found that the difference in optical power across the beam width caused a broadening of the size distribution. Brenguier et al. (1993) discussed the failure modes of the FSSP, including fogging and water accretion on the optics—a problem still encountered by modern cloud probes. A review of the correction algorithms for the FSSP is presented in Brenguier et al. (1994).

Brenguier et al. (1998) evaluates an improvement to the FSSP: the Fast-FSSP, which utilises an improved sample area optical definition, and high resolution single particle data as

opposed to the fifteen histogram bins of the original FSSP. The single particle data addition allows the elimination of coincidence corrections with inter-arrival time—that is, the time between particle pulses. The Fast-FSSP has been used in several studies of warm cloud, for example Pinsky and Khain (2003, 2001) where the inter-arrival time was used to resolve droplet concentration on millimetre length scales. In addition Field et al. (2003) used inter-arrival time from the Fast-FSSP to measure the spatial distribution of ice crystals on small length scales. However, Gardiner and Hallett (1985) found the FSSP over-counted ice crystals, and suggests an inherent flaw in the instrument. Gayet et al. (1996) supports these findings for large ice crystals in cirrus clouds, but finds good agreement with other cloud probes for small ice crystals in contrails. The authors suggest that the shape of the irregular ice crystals is responsible for this discrepancy, since this would cause the actual size of the ice particle to diverge from Mie theory significantly. Field et al. (2003) suggests that the overestimation in ice crystal concentration could be caused by ice crystal shattering, which was supported by the short inter-arrival times the authors encountered. A larger ice crystal would have a larger chance of shattering than a smaller one, which explains the conclusions of Gayet et al. (1996). The significance of ice crystal shattering as an artefact was discussed by Korolev et al. (2013b), where it was found that the FSSP was completely dominated by ice shattering artefacts. Korolev et al. (2013a) presents a series of modified instrument housings—presented as Korolev tips—designed to mitigate the effects of ice crystal shattering, along with design recommendations for new instruments. However, Jackson et al. (2014) found that artefacts from ice crystal shattering were still present with the modified tips, albeit with reduced significance.

Several methods have been employed to determine the shape of an ice crystal, or simply resolve the difference between an ice crystal and a water droplet. Since different ice crystal morphologies exhibit different spatially resolved scattering patterns, this can be used to determine the size and shape of an ice crystal. This was the mechanism employed by the SID series of open-path cloud probes (currently one through three), and their artificially aspirated equivalent: the Particle Phase Discriminator (PPD). Cotton et al. (2010) demonstrated

that spatially resolved forward scattering in the SID-2 instrument could be utilised for the discrimination between water phases; Ulanowski et al. (2014) utilised SID-3 data for determining surface roughness of an ice crystal; Schmitt et al. (2016) calculates phase functions for ice crystals for forward—0° to 25°—elastic scattering using SID data; and Vochezer et al. (2016) used the SID-3 and PPD to determine the liquid water content of mixed-phase clouds, however the authors concluded that the SID-3 instrument was unsuited for this purpose due to its small sample volume. Spatially resolved extinction has also been used to determine the shape or phase of a particle. Knollenberg (1970), for example, used an optical array to create a shadowgraph, where a particle crossed a beam of light—thus creating a shadow—and an array of photo-sensors captured a series of one dimensional intensity profiles; the instrument then concatenated them to form an image. Several Knollenberg shadowgraph probes are evaluated in Korolev et al. (1998). These probes are particularly suited for the measurement of larger particles, which made them applicable to precipitation research. The CAPS instrument (Baumgardner et al., 2001) contained a Cloud Imaging Probe (CIP), a development of the Knollenberg design, for this purpose.

Another mechanism that has been employed for phase discrimination, is linear depolarisation, since spherical water droplets will not depolarise light, but an ice crystal will. The Aerosol Ice Interface Transmission Spectrometer (AIITS, Hirst et al., 2013) combined a depolarisation ratio measurement with spatial scattering detection, similar to the SID probes, with the aim of understanding and quantifying fundamental ice crystal nucleation processes, and transitions between ice crystal regimes (Harris et al., 2017). Another instrument that used depolarisation ratio to infer particle asphericity, is the Cloud and Aerosol Spectrometer with Depolarisation (CAS-DPOL, described in the CAPS paper Baumgardner et al., 2001). The CAS-DPOL is a modification to the Cloud and Aerosol Spectrometer (CAS), which features a polarised filter positioned orthogonally to the laser polarisation state (Baumgardner et al., 2011). Similarly to the AIITS, the linear depolarisation ratio is obtained from the intensity of light on the dexter side of the polarised filter. However, the AIITS also featured an additional parallel polarised filter, so the exact polarisation state can be obtained.

The CAS-DPOL also gave single-particle data, and both forward scattering and backward scattering, which has been used to classify different dust types (Glen and Brooks, 2013).

For the purposes of atmospheric particulate measurement on UAVs, the aforementioned instruments are too large and heavy to mount on most airframes. Lightweight OPCs, for example the Printed Optical Particle Spectrometer (POPS, Gao et al., 2013, 2016), have gained recent popularity for air quality due to their low cost, therefore meaning a large quantity can measure simultaneously in a network, giving a high resolution measurement. The application of such devices to UAVs is discussed in Sect. 2.3. The Universal Cloud and Aerosol Sounding System (UCASS), which is described technically in Smith et al. (2019), was chosen was the OPC for this work. This is a naturally-aspirated OPC which was originally developed as a radiosonde device, and was deployed as such for the measurement of Saharan dust in Kezoudi et al. (2021b), where results were compared against LiDaR data. The UCASS was also deployed on a fixed-wing UAV by the Cyprus institute, described in a section in Kezoudi et al. (2021a), which was performed in collaboration with the author of this thesis. This study describes the deployment of the UCASS on a "skywalker" UAV, which was used to obtain vertical profiles of Saharan dust mass concentration. In addition to the Cyprus institute, other groups are currently deploying UCASS on UAVs as a result of the work conducted in this thesis. However, it has not been published at the time of writing. A detailed overview and description of this device and its use in this thesis is discussed further in Chapter 3.

2.3 UAVs in Atmospheric Science

The first UAV based measurement of the atmosphere was performed in Konrad et al. (1970). UAV technology has vastly improved in recent years, which has paved the way for approaches to atmospheric measurement. UAVs can be configured to carry an instrumentation payload, and have been used to measure several different atmospheric parameters. The purpose of this section is to review the current methods and technology used with or on UAVs

respectively. As mentioned in Chapter 1, UAV airframes can be split into two categories which provide different benefits and challenges; these categories are multi-rotor and fixed-wing. These airframe categories are discussed separately in Sect. 2.3.1 and 2.3.2 respectively. In addition, it is important to describe the field work already conducted using UAVs, and establish a background of current UAV research and operations. This is discussed in Sect. 2.3.3

2.3.1 Multi-Rotor Airframes

Multi-rotor airframes involve two or more—usually over four—propellers, oriented so their thrust vectors provide lift to the vehicle. The propellers counter-rotate to balance their momentum. The rotational frequency of each propeller is adjusted individually to achieve pitch, roll, and yaw motion. Multi-rotors are highly manoeuvrable, have the inherent ability to hover—thus providing constant measurement in one location—are also able to accomplish vertical take-off and landing (VTOL), and are simple to pilot. However, the propeller wash from multi-rotors cause complex aerodynamic forces and turbulence to occur around the vehicle, which causes challenges for accurate sampling of many atmospheric phenomena. Multi-rotors also require a high current capacity and large batteries, which leads to a short endurance and range.

One application of multi-rotor UAVs in atmospheric science is wind vector measurement. Comprehensive reviews of the basic techniques can be found in Abichandani et al. (2020), Meier et al. (2022). One technique for measuring wind on a multi-rotor is using the integral vehicle dynamics to estimate aerodynamic forces resulting from wind using its inertial measurement unit—a system of inertia sensors which is used by the UAV itself, primarily for stability and control purposes. As the wind exerts a force on the airframe, the propellers on half of the vehicle will increase in thrust compared to the other half, which causes a tilt in the overall thrust vector—which can be obtained from the UAV inertial measurement unit.

The horizontal component of this vector is then equal in magnitude and opposite in direction to the wind vector. This technique is described in Neumann and Bartholmai (2015), where the vehicle dynamics of a multi-rotor UAV were modelled, and a calibration function between wind speed and tilt angle was obtained in a wind tunnel—a technique also used by Brosy et al. (2017). The UAV was then field tested—hovering in one position—next to an anemometer mounted on the ground, and the results were compared; the UAV inertial measurement of wind angle was within 30° of the anemometer measurement, which was a large deviation. González-Rocha et al. (2020) also developed and evaluated a wind measurement based on the vehicle dynamics of a multi-rotor, but found that the accuracy of the measured wind vector was highly dependant on the vehicle dynamics simulation used in computing the calibration function. Wetz et al. (2021) improved on the accuracy of this method, and achieved a wind speed root-mean-square difference of $0.3\,\mathrm{m\,s^{-1}}$ and a wind direction difference of 8°, when compared with ground based measurements.

Sonic anemometers, like those used in Fuertes et al. (2019), Shimura et al. (2018), Thielicke et al. (2021), can also be used for measuring the wind vector. While these methods have the potential to produce more accurate measurements, since the instrument is decoupled from vehicle dynamics modelling, they are subject to bias from the complex aerodynamic force fields that exist around multi-rotor airframes. To solve this problem, most studies utilise large booms, at the end of which the anemometer is mounted, which can cause unexpected alterations to the vehicle dynamics, and may be unsafe without appropriate precautions. Palomaki et al. (2017) found the two techniques had comparable error when compared to ground based anemometer measurement. However, since anemometer mounting, the anemometer design itself, and the specific airframe used, can produce significantly different results, the conclusions of Palomaki et al. (2017) may not be applicable to the field.

Multi-rotor UAVs have also been applied to measure thermodynamic and meteorological properties—that is: temperature, pressure, and humidity—specifically in the PBL, but also in the free troposphere. Meteorological measurements are commonly performed on UAVs in addition to observations of other phenomena, for example Brosy et al. (2017), Neumann

and Bartholmai (2015), who performed temperature, pressure, and humidity measurements in addition to the wind vector. Brosy et al. (2017) suggests that multi-rotors could be used in situations where meteorological towers may be prohibited, particularly where information regarding potential temperature is important for determining atmospheric stability. Greatwood et al. (2017) collected meteorological data up to 2 km in altitude, in addition to sampling methane. This study also compared the temperature data collected on the ascent and descent, which is important for assessing whether sensor lag artefacts are present. Sensor lag happens when the response time of the sensor of a given variable is slower than the rate at which that variable is changing with time. In order to maximise range, multi-rotor UAVs must fly as fast as possible. Assuming a vertical profile of meteorological parameters is desired, temperature and humidity often change faster than the response times of the lightweight sensors used on UAVs. Greene et al. (2018) discusses the various sources of error in temperature measurement on multi-rotors, and finds that placing the temperature sensor under one of the propellers causes forced convection on the probe, which improved the response time. Greene et al. (2018) also finds that a radiation shield is essential to prevent solar radiation from directly affecting the probe, and proposes a vertically oriented tube design. This is contrary to the later findings of Xu et al. (2022), where it was suggested that the temperature sensor should be placed in the centre. However, the multi-rotor used in this study collected data while hovering in one location, which is a less useful measurement than a vertical profile for atmospheric science purposes.

Atmospheric particulates have been measured on multi-rotor UAVs previously. A review of UAV air quality measurements—of which particulate measurement is a sub-category—was conducted by Villa et al. (2016). An early feasibility study investigating atmospheric particulates on a multi-rotor was performed by Mölders et al. (2015), where UAV data were compared to modelled data. It was found that particulate concentrations were highly sensitive to flight patterns and conditions. Brady et al. (2016) is another early study, where a multi-rotor UAV was used to vertically profile particulate concentration, with a small commercial UAV and particle counter. This study demonstrated the feasibility of using lightweight

commercial particle counters on UAVs—a method replicated in studies such as Hu et al. (2019)—although more thorough analysis of repeatability and accuracy was required. One of the first studies to use the Alphasense OPC (Kaye and Hirst, 2011), Now commonplace in the UAV community, was Alvarado et al. (2017). This study used an anemometer positioned at different points around the UAV to measure the aerodynamic force vector field in order to locate the optimum position for mounting the OPC inlet on the airframe. The authors mounted the OPC in the centre of the UAV chassis, and extended the inlet tube vertically above the centre. However, this paper reported low accuracy and repeatability, which was likely due to particle and pressure losses in the large inlet tube. Bezantakos et al. (2018) evaluated the Alphasense OPC for use on multi-rotor designs. The results were promising when compared to another commercial OPC, however this study did not involve the use of UAVs directly, and instead focused on the validation of the instrument package separately, which included a pump and a drying column. The Alphasense OPC is a promising instrument for UAV use. However, the aspiration mechanism, a fan capable of a maximum pressure drop of $50\,\mathrm{N\,m^{-2}}$, is not strong enough to ensure isokinetic flow in real conditions. The two main advantages of the Alphasense design are a quasi-monotonic Mie curve which results from the scattering angles it uses, and the robust sample area characterisation. The Universal Cloud and Aerosol Sounding System (UCASS) uses the same optical design as the Alphasense OPC, and therefore inherits its two major advantages, but with a naturally aspirated airflow mechanism—described in Smith et al. (2019)—which makes it ideal for use on UAVs. Another instrument which shows promise for use on UAVs is the POPS. However, it was discovered by Liu et al. (2021) that interference from the propellers might have caused a significant loss of particles.

2.3.2 Fixed-Wing Airframes

Fixed-wing UAV airframes are more similar to conventional aircraft than multi-rotors. Fixed-wing designs utilise a wing for lift, and a number of control surfaces for pitch, roll, and

yaw motion. These control surfaces can be the conventional wing-based aileron, horizontal tail elevator, and vertical tail rudder—each providing roll, pitch, and yaw respectively—configuration; a less conventional 'V-tail' configuration which combines the vertical and horizontal tails for combined yaw and pitch moments; or a 'flying-wing' configuration which uses two ailerons to control all of pitch, roll, and yaw with different motions. For atmospheric sampling, fixed-wing aircraft offer greater dynamic stability, less complex aerodynamics, and greater range than multi-rotors. However, they often have to measure at higher velocities—which may be an advantage if larger area coverage is desired, or a disadvantage if a large spatial resolution is desired—are more complex to pilot, and require a runway to operate.

Fixed-wing UAVs can be applied to atmospheric wind vector measurement, and have been used more extensively than multi-rotors for this purpose. This is due to the superior stability and lower complexity of aerodynamic forces on the airframe (Palomaki et al., 2017). The Aerosonde aircraft (Holland et al., 2001) was one of the first UAVs to measure the wind vector (Soddell et al., 2004). In order to calculate the wind vector at a given altitude, the Aerosonde was flown in a circle, and the airspeed from a pitot tube was compared to the ground speed to compute the wind speed. Soddell et al. (2004) found the wind speed to be within $1.3\,\mathrm{m\,s^{-1}}$ and the wind direction to be within 5° of radiosonde estimations, which is an improvement over the more modern multi-rotor estimations of the wind vector. Egger et al. (2002, 2005) used a similar method for wind measurements to measure the wind vector, with high vertical resolution in areas with complex topography, which would be inaccessible by conventional aircraft. The Mini Meteorological Aerial Vehicle (M^2AV), first used for meteorological measurement in Spiess et al. (2007), was the first UAV to use a multi-hole pitot tube to measure the wind vector. Multi-hole pitot tubes measure the airspeed vector in multiple directions, and can therefore calculate the wind vector without performing special manoeuvres, like those used in Soddell et al. (2004). This vastly increases the spatial resolution of wind measurements, and allows turbulence measurements to be performed. Martin et al. (2011), van den Kroonenberg et al. (2008), Wildmann et al. (2014c) described the characterisation and use of a multi-hole pitot tube for this purpose. The

Multipurpose Airborne Sensor Carrier (MASC), a UAV developed for measurements of wind turbine aerodynamics, uses a similar sensor package to the M^2AV, and has been utilised for the same purposes (Wildmann et al., 2014a).

As mentioned previously, the first meteorological measurements on fixed-wing UAVs were conducted by Konrad et al. (1970), where two thermistors—one with a wick to measure the wet bulb temperature—were used for temperature, and a carbon film on glass capacitive sensor was used to measure humidity—strikingly similar to many modern meteorological sensor packages. The Aerosondes described in Holland et al. (2001) were also equipped with temperature, pressure, and humidity measurements; the meteorological measurements by the Aerosonde were compared to radiosonde measurements in Soddell et al. (2004), where it was proposed that aerodynamic and kinetic heating—via friction—effects were the largest sources of error. The Small Unmanned Meteorological Observer (SUMO, Reuder et al., 2009) was designed as a cost efficient meteorological UAV for vertical profile measurements. This was one of the first fixed-wing UAVs with a foam airframe to be used in atmospheric physics—a common airframe material due to its low cost and versatility. Reuder et al. (2009) concluded that the SUMO had comparable accuracy to established measurement systems. SUMO has been used in several research campaigns, including Lothon et al. (2014), where data were compared to other fixed-wing UAVs—including the M^2AV and the MASC—multi-rotors, and radiosondes. As mentioned previously one of the largest sources of error in measuring meteorological parameters, particularly temperature and humidity, on a UAV is sensor lag. Wildmann et al. (2013) describes the design and testing of two temperature sensors designed specifically to minimise response time so they can be used on UAVs. The sensors are intended for fixed-wing UAVs but could also be used for multi-rotors. These were the first sensors designed specifically for atmospheric research on UAVs.

Compared to multi-rotors, fixed-wing atmospheric particulate research is more mature. The first significant observational study of particulates using fixed-wing UAVs was the Maldives Automated UAV Campaign (MAC). The observational structure is described by Corrigan et al. (2008), Roberts et al. (2008), where radiation measurements were performed

on three UAVs, which flew above, within, and beneath a cloud, in order to measure the albedo. Ramanathan et al. (2007) discovered during the MAC that anthropogenic aerosols can amplify the absorption of clouds, therefore increasing warming trends in Asia. This campaign used large, expensive UAVs with unmodified commercial aerosol instrumentation. Measurements of absorbing aerosol were also performed in the Arctic by Bates et al. (2013), which was fitted with an absorption photometer, and a CPC. Here data were gathered by a UAV for the purpose of validating models and LiDaR retrieval algorithms. The Application of Light-weight Aircraft for Detecting IN situ Aerosol (ALADINA) UAV, described by Altstädter et al. (2015), was a large UAV equipped with two CPCs for the measurement of ultrafine particles. ALADINA data were compared with LiDaR and reference instrumentation and concentration agreement within 20 % was shown. Ultrafine particles are less subject to aerosol transportation losses than larger particles, meaning they are comparatively straightforward to measure on a UAV. Bärfuss et al. (2018) described an improved instrumentation setup for ALADINA, which includes a multi hole probe for wind measurements. Marinou et al. (2019) compared UAV INP data with the aim of validating INP parameterisations—a task which requires significant measurement resolution, thus playing to a significant advantage of the UAV platform. Saharan dust has also been measured with UAVs. Mamali et al. (2018) shows measurements of dust with a fixed-wing UAV, which flew to an altitude of 2 km. The Saharan dust data measured by an OPC mounted on the UAV was correlated against LiDaR data, where it showed strong correlation. Saharan dust has been found to be unexpectedly coarse (Ryder et al., 2019), meaning losses in aerosol transportation tubing could have a large overall effect on the observed mass or volume size distribution, and therefore the extinction coefficient and aerosol optical depth. Therefore an open path instrument, similar to the UCASS design, where there is no necessity for aerosol transport tubing, would be ideally suited for Saharan dust measurements.

2.3.3 Field Campaigns

Several previous field campaigns have involved UAVs, both as the sole data collection mechanism, and in combination with other techniques. The Pallas Cloud Experiment (PaCE) campaigns, which had the primary goal of UAV intercomparison and validation, are discussed further in chapters 4 and 5; however, it is important to contextualise them here. These campaigns took place at the Pallas atmosphere-ecosystem super-site in Finland (Lohila et al., 2015)—a site with a unique advantage for UAV operations due to the airspace, which allows for flights up to 2 km above sea level. The first UAV measurements at this site are presented in Kezoudi et al. (2021a), which is a summary of several UAV field campaigns, including PaCE 2017. Here, UAV profiles of the boundary layer were conducted in combination with ground-based remote sensing, with the aim of studying aerosol cloud interactions. UAV in-situ and ground-based remote sensing instrumentation have implicit synergy, since the high maneuverability of a UAV is beneficial for performing validation measurements, and the remote sensing data can be used to influence UAV flight planning and operation by highlighting areas of interest in the atmosphere, in addition detecting where the cloud base is (if present). Girdwood et al. (2020, 2022) present results from PaCE 2019 and 2020, where UAVs were compared with ground-based in-situ instrumentation, which was used for both intercomparison—where the ground-based instrumentation is treated as a reference—and data quality assurance.

Synergy between different types of measurements is extremely important for the design of field campaigns generally. Different platforms and techniques can be used in different ways to exploit their respective benefits. Fennec, for example utilised a combination of ground based in-situ (Rocha-Lima et al., 2018), ground based remote sensing (Allen et al., 2013b), and aircraft based observations as mentioned previously (Ryder et al., 2013). Marsham et al. (2013) found, through analysis of remote sensing data, evidence of complex boundary layer processes. They go on to state that future analysis of Fennec data should focus on the detailed aircraft observations taken in the PBL, which is presented in Ryder et al.

(2015). This research would not have been possible without the synergy of instruments and platforms in a well planned research campaign. UAVs could also fit into modern research campaigns in a similar way, bridging a gap between ground based remote sensing and aircraft measurements. UAVs could be used to validate LiDaR retrievals during the campaign. Also, since UAV flight plans are highly adaptable when compared to conventional aircraft, remote sensing data could be used to highlight areas of interest within a highly changeable and complex boundary layer—for example during a "haboob" event observed during Fennec—then obtain high resolution in-situ measurements within the area of interest. Conventional aircraft data could then be useful for validating the data from UAVs, and UAV data could be used to influence the flight plans of conventional aircraft.

The Lower Atmospheric Profiling Studies at Elevation – a Remotely-piloted Aircraft Team Experiment (LAPSE-RATE) campaign, data and overview presented in de Boer et al. (2020), was a campaign in the San Luis Valley, Colorado, with the principle aim of studying the PBL. Barbieri et al. (2019) presents a large scale intercomparison study which resulted from this campaign. As mentioned previously, intercomparisons are particularly valuable for UAV measurements, since techniques involving UAVs are in their infancy. In addition to building a technical understanding of UAV platforms and measurement discrepancies, this study also discusses the importance of appropriately designed flight plans in UAV operations. Ground based pressure measurements are used to validate barometric readings from the UAVs, which was found to be essential to avoid altitude discrepancy between different measurements. One valuable finding from this campaign was the observation of new particle formation in the valley, which is presented in Brus et al. (2021). This is also an example of a campaign in which remote sensing data was combined radiosonde profiles, in addition to the UAV data (Bell et al., 2021). Here, the more established measurement techniques were used as benchmarks to compare with the UAVs. The remote sensing instrumentation here could have been used to influence UAV flight profile design, and multi-rotor loitering altitudes, however the principle purpose in this case was intercomparison so it was not necessary to do so.

One notable fixed-wing UAV which is commonly used in atmospheric science is the Global Hawk, which was first described by Loegering (2002). This UAV differs strongly from others described in this thesis because of its operational envelope; the Global Hawk was designed for high-altitude, long-range missions. While this UAV is fundamentally different, it is important to describe it in relation to other UAVs, including what makes it unique and why having a UAV with this capability is important. The operational envelope of the Global Hawk resembles that of a conventional aircraft with an increased ceiling—around 18.9 km (Jensen et al., 2013)—making it well suited for field campaigns in the stratosphere and tropopause. The Global Hawk is able to reach this altitude with a strong sensor payload, because it does not need to carry a crew or any life support systems which would be needed at that altitude. One example of a field campaign which takes advantage of this is the Airborne Tropical TRopopause EXperiment (ATTREX), which is described in Singh et al. (2014). Here, the high ceiling of the UAV is exploited for measurements of water vapor—in addition to multiple trace gasses—in the tropopause and stratosphere. Microphysical measurements of Cirrus clouds were also performed during this campaign (Thornberry et al., 2017); Cirrus cloud properties are very important since radiative transfer models are sensitive to them, and they are difficult to measure due to common platform limitations—thus presenting a perfect use case for the Global Hawk.

This UAV is also capable of launching dropsondes—small sensor probes which are dropped from an aircraft, usually equipped with a parachute system to slow their descent rate. This capability was demonstrated for the first time during the Winter Storms and Pacific Atmospheric Rivers (WISPAR) campaign (Intrieri et al., 2014). Since this UAV is capable of flying at extremely high altitudes, a total tropospheric profile of atmospheric variables can be retrieved using the dropsonde system, which is described by Wick et al. (2018). The UAV – dropsonde combination is also ideal for acquiring data from storms, cyclones, and extreme weather events, since there is no crew to put at risk, and the dropsondes can be dropped from far above the storm to minimise risk to the airframe. An example of this activity is described by Christophersen et al. (2018), where observations from the Global

Hawk dropsonde system are compared with satellite data. This study finds that the combination of the two measurements are far more valuable than each individually, which further demonstrates the benefit of combined observations. One implication of this study is that Global Hawk data could also be used to provide validation measurements of satellite remote sensing in the tropopause region, where sharp vertical gradients in various parameters exceed remote sensing vertical resolution (Jensen et al., 2013). This, and many other of the defining operational characteristics of the Global Hawk, would be much more difficult if it was not a UAV.

The Global Hawk presents the need for an important distinction between UAV classes in this thesis, since this aircraft and the smaller airframes exhibit entirely different operational characteristics. This distinction is emphasised again in Chapter 4, but hereafter I will refer to UAVs as per the UK Civil Aviation Authority definition of small unmanned aircraft, which are lighter than 25 kg.

3 | UCASS

Since much of the following research relies on the UCASS instrument, and developments thereof, it is proper to first establish its working principles in the mind of the reader. This section, therefore, will focus on describing the design, calibration, and use of the UCASS and associated developments within the context of UAV applications. Part of the original design (presented by Smith et al., 2019) was developed as part of the foundation of this thesis; however the original paper includes a legacy of work starting in 2010 (Kaye and Hirst, 2011), therefore rendering it improper to include the full publication here. Section 3.1 contains relevant background information regarding the UCASS working principles, and Sect. 3.2 is a detailed overview of the UCASS development conducted for this project.

3.1 UCASS Working Principles

3.1.1 Mechanical and Optical Design

Figure 3.1 shows the optical layout of the UCASS. A particle is illuminated by a 650 nm Gaussian diode laser, which is shaped by a 2 mm aperture, and focused by a 50 mm focal length lens—labeled in Fig. 3.1 as components 'b', 'c', and 'e' respectively. The purpose of the aperture is to ensure a quasi-constant laser intensity across the breadth of the sample area, by removing the light either side of the Gaussian laser intensity peak. The purpose of the lens is to maximise the light intensity at the sample volume—and therefore scattered

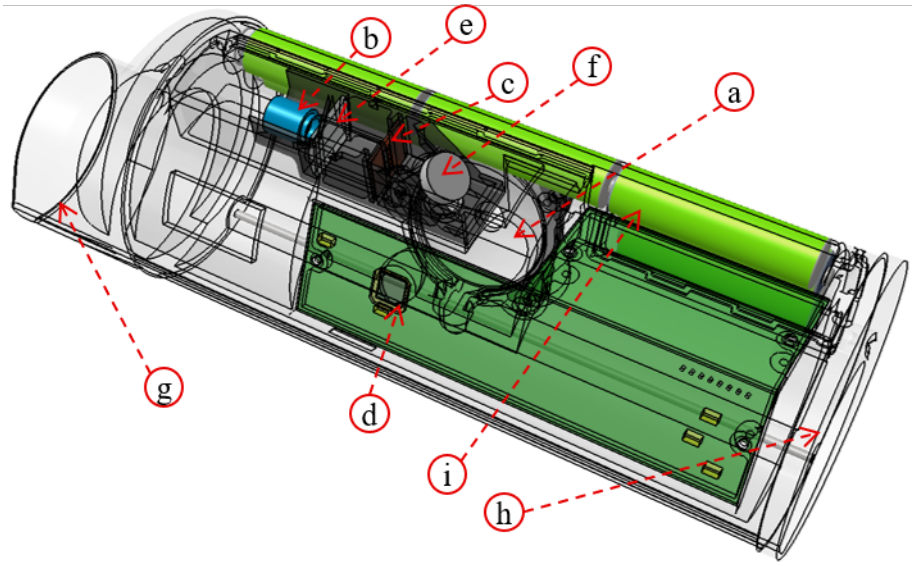

FIGURE 3.1: A view of the UCASS detailing the optical and mechanical components specifically. The elliptical mirror is labeled as component 'a', the laser as 'b', the aperture as 'c', the photodiode detector as 'd', the lens as 'e', and the laser-folding plane mirror as 'f'. The inlet is labeled as 'g', the outlet is labeled as 'h', and the—optional—batteries as 'i'.

intensity to the detecting optics—while minimising the total input laser power, and thus current draw.

The detecting optics are a combination of two optical components: an ellipsoidal mirror, 'a', and a photodoide detector, 'd'. The ellipsoidal mirror has a half angle of 43.8°, and is offset azimuthally from the laser beam axis by 60° from the forward direction. The ellipsoidal mirror also has a hole in its centre with a half angle of 10.7°. This allows scattered light to be collected between azimuth angles 'θ' of 16.2°$\leq \theta \leq$49.3° and 70.7°$\leq \theta \leq$103.8°. The choice of angle was based on a compromise of forward to side scattering. Forward scattered light is subject to higher intensity Mie oscillations when compared with side scattered light, which causes less monotonicity in the instrument size response curve. Forward scattered light also contains more dependency on particle shape, which is undesirable here since Mie scattering assumptions are made. Side scattered light has a larger dependency on refractive index, which is not desirable since many environments contain more than one aerosol chemistry,

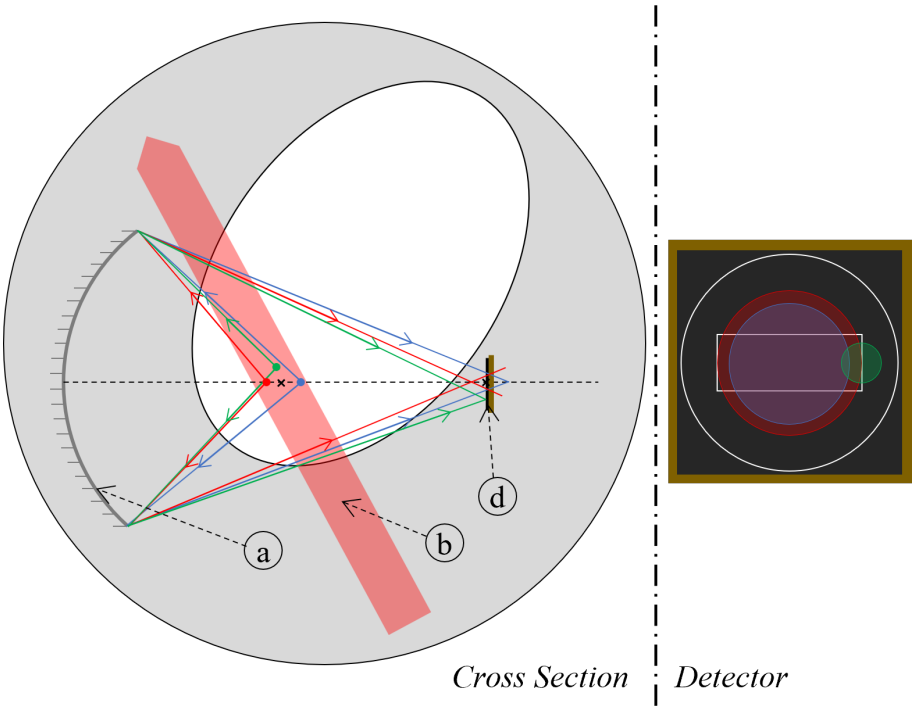

FIGURE 3.2: A cross-section view of the UCASS detecting optics and particle rejection criteria. The axis system and component labeling are consistent with Fig. 3.1.

which will differ in refractive index. Side scattered light also has a lower intensity, which leads to a lower signal to noise ratio (SNR), where the noise originates from stray light.

The ellipsoidal mirror reflects scattered light originating from its primary focal point, positioned at the centroid of the sample area, onto its secondary focal point, which is positioned at the centroid of the photodoide detector. This layout is shown for clarity in Fig. 3.2. The photodoide detector is split into two galvanically isolated parts: a rectangular inner region, surrounded by a circular outer region. Together these define a FoV, DoF, and therefore sample area—which is illustrated in Fig. 3.2. When more than 50% of the total intensity lies within the inner detector, a particle is accepted. As a particle moves across the laser beam within a plane parallel with the detector plane, the illuminated area of the detector moves proportionally, and also grows larger the further it deviates from the primary focal point of the ellipsoidal mirror, which is where the centroid of the detector area is. This defines the detector FoV. As a particle moves closer to or further away from the detector,

the illuminated area grows larger, until 50% of the total intensity lies on the outer detector. At this point the particle is rejected. This defines the detector DoF, and the sample area is $0.5\,\mathrm{mm}^2$.

Once it has been determined if a particle is within the sample volume, it is sized. The size of a particle is obtained by summing the intensity on both detector elements—since an accepted particle may have up to 50% of its total scattered intensity on the outer detector—then converting this to a digital value. The digital value is then compared with a size look-up table which is obtained through calibration, and the particle is sorted into one of 16 bins. The size range of the UCASS is 0.4 µm to 20 µm, or 1 µm to 40 µm depending on how the amplifier gain circuit is configured.

As previously established, the UCASS is a naturally-aspirated OPC; originally designed as a single use sounding device (Kaye and Hirst, 2010, Smith et al., 2019), and has been successfully deployed as such (Kezoudi et al., 2021b). This means the sample airflow is generated by the movement of the platform that UCASS is affixed to. The primary advantage to this is the elimination of the need for isokinetic flow, in addition to the lower instrument mass due to no requirement for an aspiration system. However, the speed at which the UCASS is moving must be known in order to know the sample volume, and therefore compute a particle concentration. This can be accomplished via the measurement of the platform ascent rate (Girdwood et al., 2020, Kezoudi et al., 2021b), a pitot tube or anemometer, or the ToF of the particle through a laser beam of known width (Girdwood et al., 2022).

3.1.2 Electronic and Firmware Design

The photodiode detector on the UCASS is composed of two galvanically isolated elements, these will be referred to as channels within the context of electronics and firmware. The signal from each detector channel is subjected to three analogue processing stages: transimpedance amplification, direct current (DC) restoration, and peak processing—these are shown for clarity in Fig. 3.3. The transimpedance amplifier (TIA) turns the photocurrent

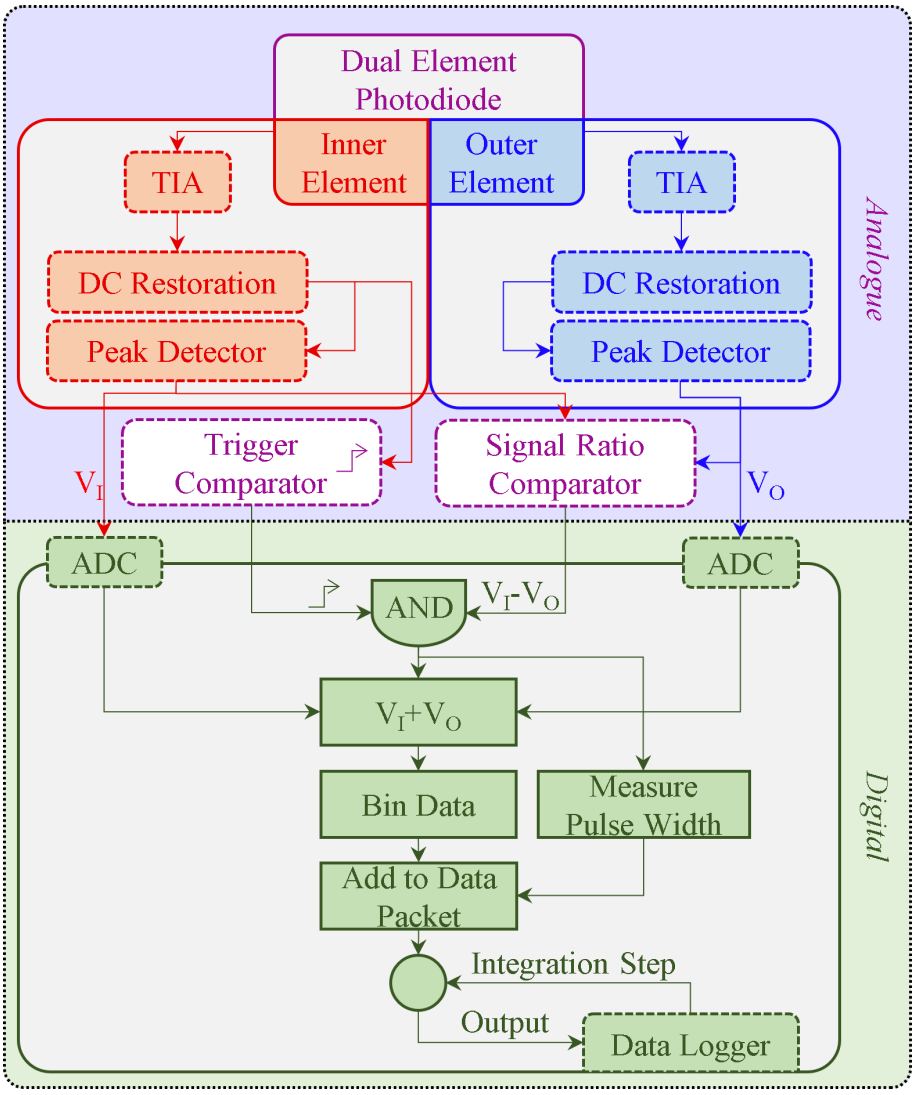

FIGURE 3.3: A flowchart detailing the firmware and electronics for the UCASS. The digital stages, which are processed on the microcontroller, are shown within the dotted line.

from the photodiode into a proportional voltage. The TIA in the UCASS has two separate gain modes. The higher gain allows for measurement of smaller particles which induce lower photocurrents; the lower gain allows measurements of larger particles with higher photocurrents, which will saturate the higher gain. The high gain was designed for measurements of aerosol, and the low gain was designed for measurements of cloud droplets.

The signal from the TIA can be decomposed into an alternating current (AC) component, and a DC component. The AC component is the signal from the particle, and the DC component is the signal from any stray light in the system—which can be caused by the laser reflecting off the internal cavity, or external light. Since the DC component is always present in the signal to an extent, it needs to be subtracted from the main signal before digitisation in order to avoid over-sizing of a particle. This is the function of the DC restoration circuit, which is the second stage after the TIA.

The third and final stage in the analogue electronics is the peak processor. This circuit first detects when a particle is present within the signal by testing if the signal magnitude has been raised above a threshold—this is known as the peak comparator—which causes the microcontroller to record the output of the peak detector. The peak detector is a circuit which holds the largest voltage the signal reaches, until it is reset. The peak detector is reset at the start of a particle signal, when the peak comparator is first triggered, and at the end of a particle signal, just after the microcontroller records the value of the peak. This voltage is converted into a 12-bit analogue to digital converter (ADC) value, which is proportional to the size of the particle. The time between resets of the peak detector circuit is the ToF value.

3.2 Development

3.2.1 Total Opto-Mechanical Redesign

As discussed further in Chapter 4, preliminary tests showed that the UCASS could not withstand the mechanical forces associated with a multi-rotor airframe. The simple test consisted of repeated multi-rotor sampling flights—with the airframe described in Chapter 4—and a comparison of the sampling efficiency over time. It was shown that after the first flight, the UCASS stopped recording all particles, despite the laser still functioning. This was due to the detecting optics—parts ‘a’ and ‘d’ in Fig. 3.1—being pushed out of alignment, so

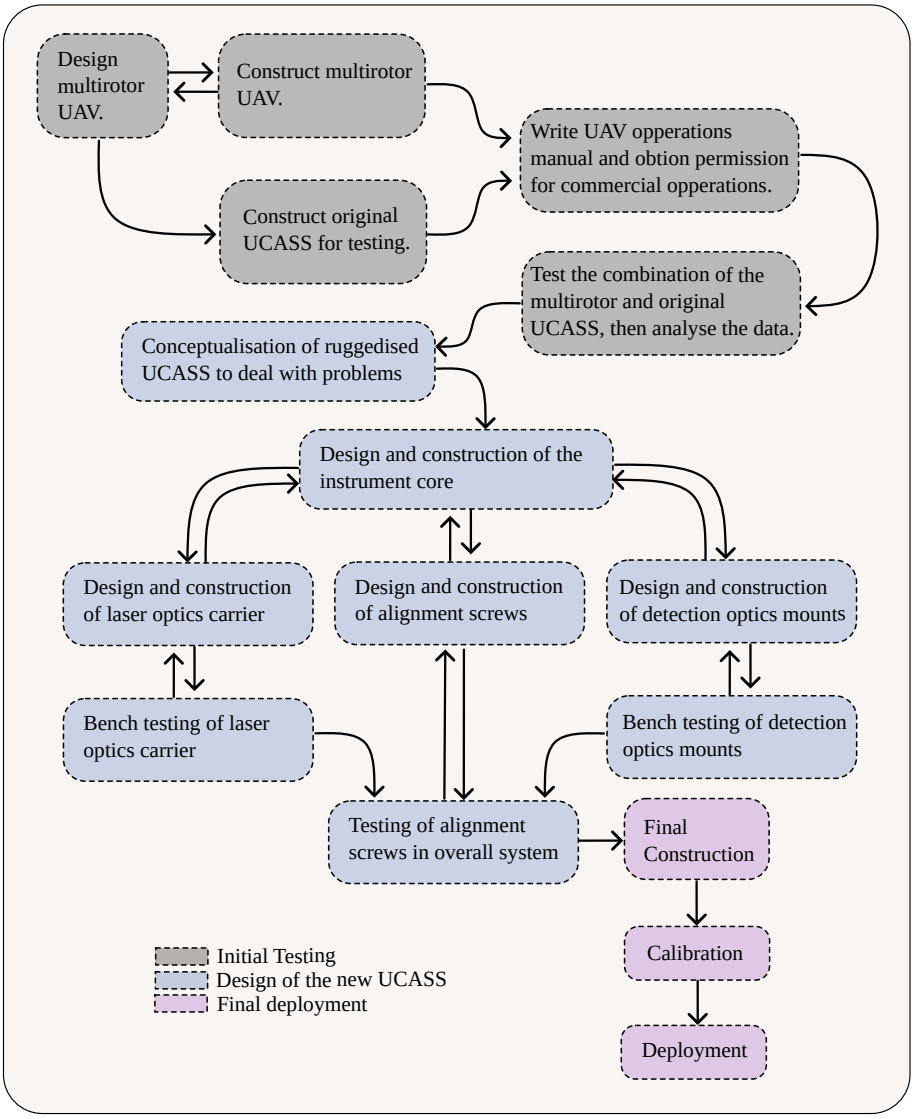

FIGURE 3.4: A flowchart detailing the design process for the optical and mechanical re-design.

the majority of the light flux scattered from the particle did not reach the PD. In order to rectify this alignment change, I decided that both the mounting of the UCASS on the UAV, and the mechanical design of UCASS itself had to be completely overhauled. The general design process for this section is summarised in Fig. 3.4.

Sensible opto-mechanical design involves a single point of reference for all aligned optical parts, to minimise tolerance stacking. In the original design, all UCASS optical components

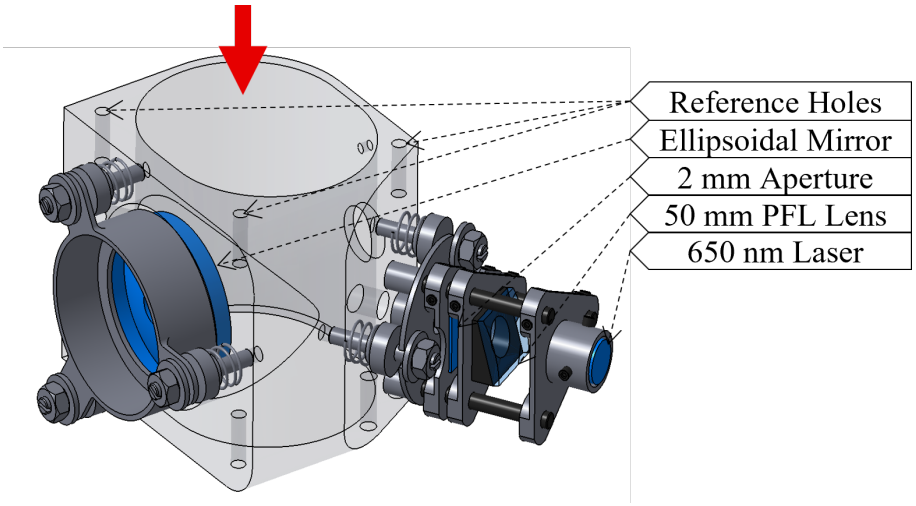

FIGURE 3.5: A labeled illustration of the optical core of the multi-rotor adaptation of UCASS. Blue parts indicate optical surfaces, the red arrow indicates the airflow direction.

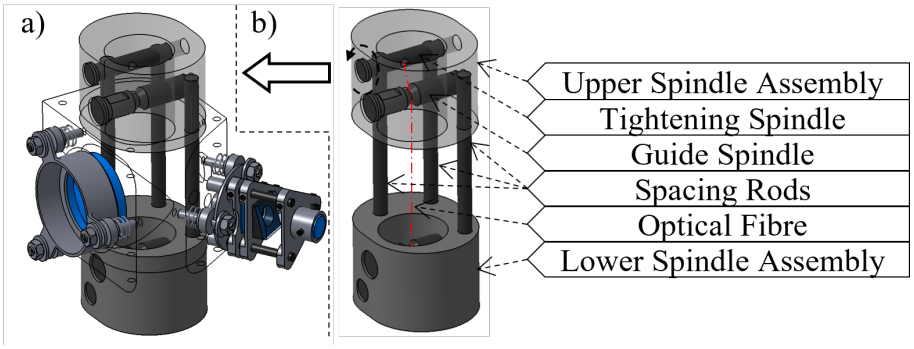

FIGURE 3.6: A labeled illustration of the fibre holder of the multi-rotor adaptation of UCASS, shown both mounted within UCASS (a) and on its own (b). The optical fibre path is indicated with the red dashed line. The circular arrow indicates the turning direction of the upper tightening spindle.

were aligned to a single optical reference point—a long, statically mounted glass fibre—aligned axially to the flow direction, and crossing the sample area centre. This was a reliable and tested method for defining an optical reference point; however the fibre mounting system used in the original design was improperly rooted, since the fibre mount relied on the interior UCASS tube to locate it. This was ineffective for two reasons: generally surfaces are more dimensionally variable than reference points, and the UCASS interior tube was not a regular shape—thus making it harder to manufacture, and amplifying the first problem.

It was convenient for this fibre to be attached to the UCASS centre chassis for the purposes of alignment, therefore I chose the three mounting holes positioned radially around the central flow tube—shown in Fig. 3.5—as the single point of reference for this design, and the mounting points for the glass alignment fibre. The position tolerance of holes can be 50 µm if drilled on a milling machine. Furthermore, the three holes are in a parallel tolerance stack, which lessens the contribution of the position of each hole individually to the overall positioning of the fibre in the centre. In order to hold the optical fibre in place, I adopted a system of two guide spindles—where the fibre was stretched across them, through grooves in the spindles. I chose this design because: the spindles could be turned on a lathe, meaning the manufacturing tolerance could be 50 µm; the fibre could be kept taut between the two spindles by the use of a secondary set of tightening spindles; since both ends of the fibre were mounted, the guide spindles are in a parallel tolerance stack, thus lessening the contribution of each one to the overall position of the sample area. The fibre holder assembly is shown in Fig. 3.6.

Due to the large manufacturing tolerances in the optical components themselves, any tolerance in UCASS static opto-mechanical part—for example lens or mirror mounts—manufacture was largely irrelevant, once the fibre position was well established. I used optical alignment mechanisms here to remove the reliance on the tolerance of the optical part manufacture. For UCASS, the necessary points of alignment are i) the laser angle to account for pointing accuracy—which has a notoriously wide angular range with many diode laser designs; ii) the laser aperture to mask the tails of the Gaussian intensity profile—this will be referred to as a top-hat beam profile; iii) the 50 mm focal length laser focusing lens to ensure the sample area is within the Raleigh length; and iv) a four-axis movement in the elliptical mirror—three axes of rotation, and one of translation normal to the focal plane—to focus the scattered light onto the detector.

In the original UCASS design a planar mirror positioned 45° to the laser carrier was used to direct the light to the sample volume. In order to address alignment point (i), the mirror angle was adjusted by deforming a bed of epoxy putty, which the mirror was positioned on.

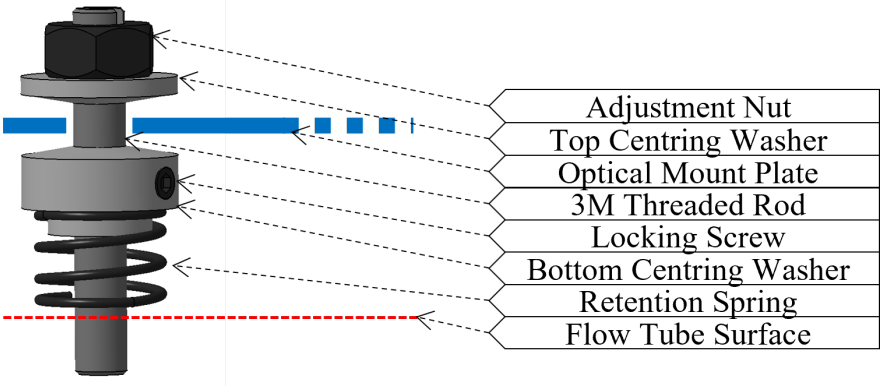

FIGURE 3.7: The alignment screw used in the UCASS multi-rotor adaptation. The same screw was used six times, with three being used to mount the ellipsoidal mirror, and three being used to mount the laser optics carrier.

The diffraction of the laser light from the optical fibre was observed, which allowed the mirror to be 'aimed' appropriately. The mirror was employed in the original design because the laser optics carrier had to be positioned parallel to UCASS, due to packaging constraints. The same design constraint was not applicable here, so I could mount the optics carrier orthogonal to the flow tube—as shown in Fig. 3.5—in order to reduce both design complexity, and the number of optical surfaces, which are generally prone to the accumulation of dirt. Therefore, to address alignment point (i), the entire laser optics carrier needed to rotate about three-axes. Since the ellipsoidal requires similar degrees of freedom to satisfy point (iv), the chosen alignment mechanism can be copied for design simplicity.

I accomplished four degrees of freedom—three rotational and one parallel translational—by mounting the optics on a plate, which was then attached to the flow tube by three posts. The distance between the plate and the flow tube could be altered by adjusting a nut on the top of each post, up to which the plate was pushed by a retention spring. The angle of the plate, and therefore the optical surface, could then be altered by adjusting one or two of the three nuts; and the distance between the plate and the flow tube—and therefore the focal point of the optical surface—could be altered by adjusting all three nuts by the same amount. This sub-assembly will be referred to as the alignment screw. The laser optical carrier mount and the ellipsoidal mirror mount were attached to the flow tube in this manor,

therefore satisfying points (i) and (iv). Each optics mount plate had three holes, each 0.1 mm larger in diameter than the alignment screw shaft, which was then centred by two tapered washers, which were positioned on the shaft either side of the mounting plate. This was necessary because, as the angle of the mounting plate with respect to the flow tube was adjusted, the edge of the mounting plate hole would foul against the alignment screw shaft. Once each alignment screw was in the correct position, the sub-assembly could be locked using a grub screw, which was attached to the lower tapered washer. The alignment screw sub assembly can be seen in Fig. 3.7, and the points at which they are positioned on the flow tube can be seen in Fig. 3.5.

The Rayleigh range of the UCASS laser beam, when focused with a 50 mm primary focal length (PFL) lens, is 12 mm. The sample volume for UCASS must lie within this range. Since this is a wide tolerance, the original UCASS design did not need to have any mechanism for focusing the beam. However, as discussed previously, the new UCASS laser optics carrier was given multiple axes of motion in order to account for the wide tolerance in laser pointing direction. This meant that, if the lens was kept statically mounted, the sample volume could conceivably be outside of the Rayleigh range after adjusting for pointing accuracy. Therefore, the lens needed to be mounted with one degree of freedom, longitudinally to the beam direction. This was accomplished by utilising a cage-type design of the laser optics carrier, to which each of the beam forming optics were mounted on sliding carriers with locking screws. This assembly can be seen in Fig. 3.5. The beam forming lens was moved along this carrier until the focal point was at the sample volume, which was observed by placing a diffusing surface at the sample volume instead of the optical fibre. This system was an effective solution to alignment problem (iii).

With the laser optics carrier constructed with this cage design, the other components were simple to position; the same sliding carrier stage design could be used for each component, and manufactured in bulk. The final optical component which needed aligning was the aperture, as per alignment point (ii). The longitudinal position of the aperture did not matter—as long as it was between the lens, and the end of the optical carrier. In the original

UCASS design, the aperture was aligned by simply observing the beam output with a camera, and adjusting its lateral position until a top-hat profile was achieved, at which point it would be bonded in place with epoxy. There were no issues with this alignment mechanism, so I repeated this in the redesign with the aperture instead being bonded to a sliding carrier stage on the optics carrier. The position of the aperture is shown in Fig. 3.5.

3.2.1.1 Practical Alignment Method

The alignment mechanism detailed in Sect. 3.2.1 is complex, and thus necessitates a short section detailing the practical method.

As mentioned previously, while compensating for the pointing accuracy of the laser, the beam direction is altered until it hits a fibre. In order to gauge the quality of alignment and gain visual feedback while adjusting the laser angle, I observed the diffraction pattern resulting from the UCASS laser beam hitting a statically mounted reference fibre which intersected the sample area. An illustration of the process is provided in Fig. 3.9. The process used to mount the fibre in its holder is shown in Fig. 3.8, some details of the fibre holder assembly can be seen in Fig. 3.6, and the technical drawings for the fibre holder components can be found in Sect. A.4. I altered the laser angle using the three alignment screws until both the diffraction pattern is visible, and the shadow of the fibre is visible in the centre lobe. Conventional approaches to alignment feedback involve targets for the laser. The advantage to the fibre method is twofold: magnification of the beam output for better visibility, and the utilisation of the same reference point as the detection system.

The alignment of the ellipsoidal mirror used the same reference fibre. In an alignment process, I considered the fibre to intersect the centre of the sample volume, since at this stage the laser pointing direction had already been altered so that it hits the fibre centrally. This means that if the scattered light from the fibre is focused onto the detector, the scattered light from a particle will follow suit. In order to view the light focused by the mirror, I utilised an endoscope. I also positioned a thin plastic film over the detector temporarily, so that the scattered light could be viewed. This was necessary because the surface of the

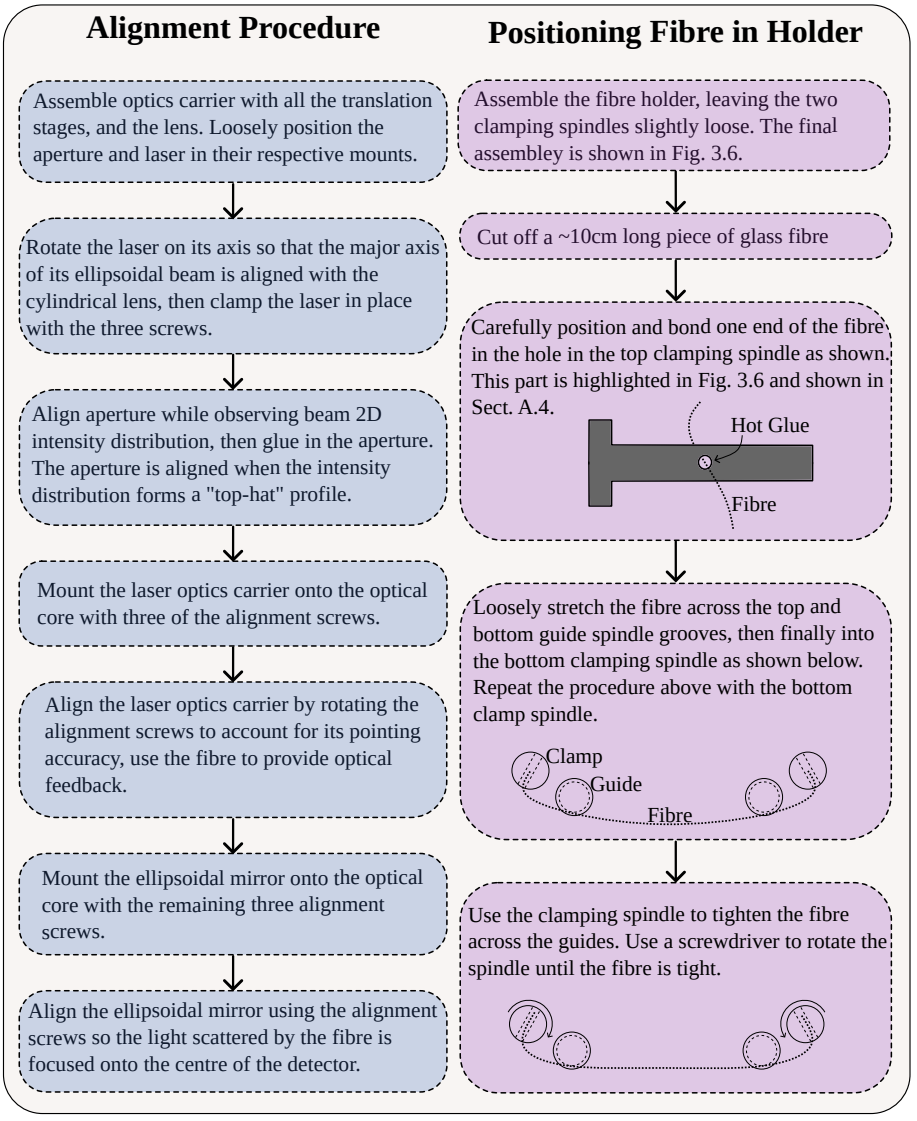

FIGURE 3.8: A flowchart detailing the alignment process for the new UCASS, in addition the process of mounting the optical alignment fibre in its holder.

detector was too absorbing to effectively view light on its surface. If all three of the alignment screws on the ellipsoidal mirror are adjusted by the same amount, the focus of the scattered light will be adjusted. If only one or two of the screws are adjusted, then the focused spot will move around the detector. Figure 3.9 shows a diagram of this process for clarification purposes. I adjusted the three screws on the ellipsoidal mirror mount until both the light was focused finely to a spot, and the spot was in the centre of the central detector element.

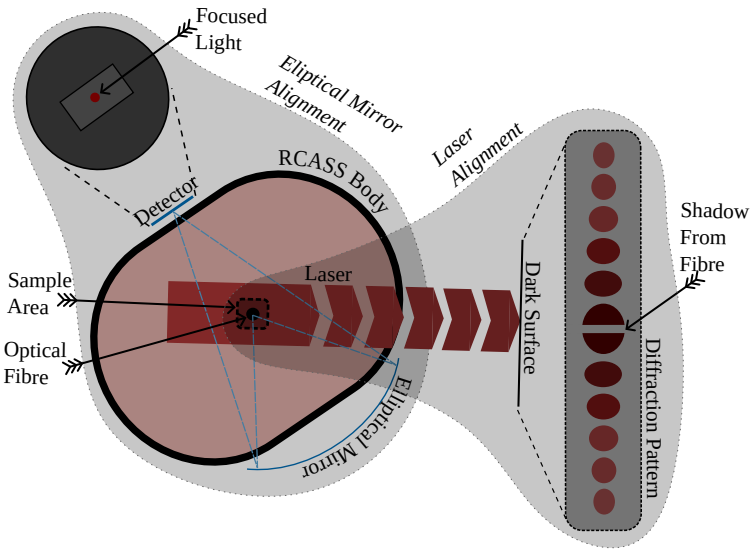

FIGURE 3.9: An illustration describing the alignment mechanism for the new UCASS, including both the laser pointing compensation and ellipsoidal mirror adjustment.

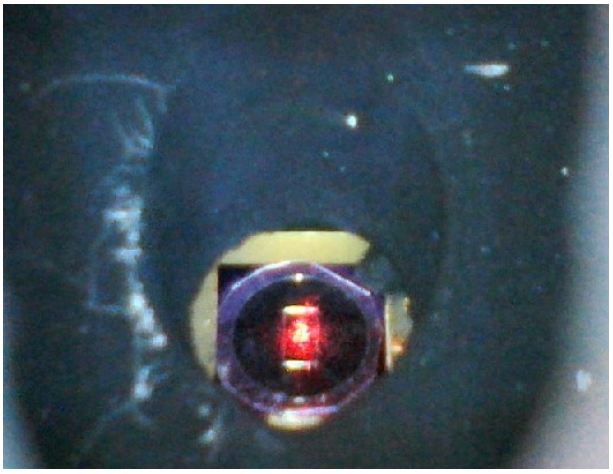

FIGURE 3.10: An endoscope image of the UCASS detector photodiode during an ellipsoidal mirror alignment.

Figure 3.10 shows the focused beam spot from the ellipsoidal mirror during an alignment.

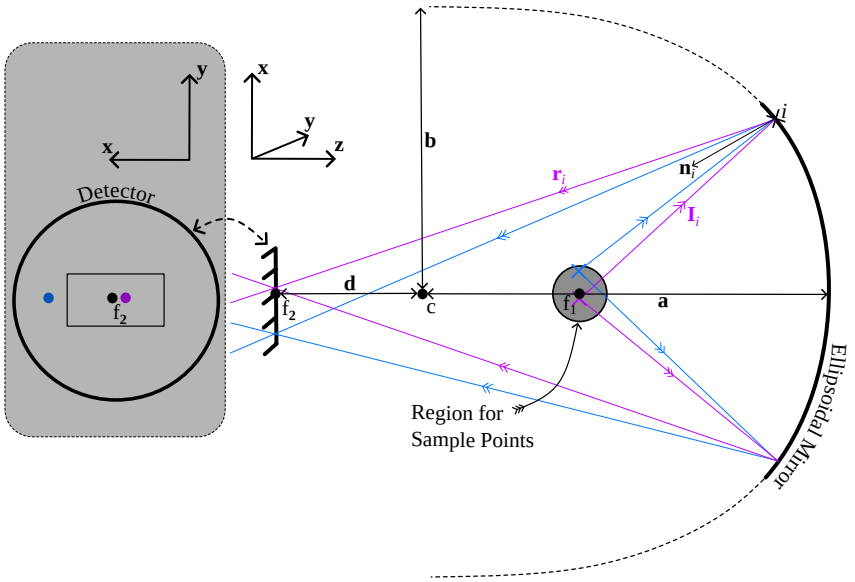

FIGURE 3.11: An illustration of the domain for the ray tracing algorithm. Rays from two example query points are illustrated, and the corresponding detector intensity distribution is shown. The rays ($\mathbf{I_i}$) from the query points near the primary reflector focal point, f_1, are reflected off point i to give vector $\mathbf{r_i}$. d is the distance between the domain centre (c, same as the ellipse centre) and the detector plane.

3.2.1.2 Sample Area Characterisation

Prior to the beginning of this project, the sample area of the UCASS was determined experimentally to be 0.5 mm^2. Briefly described, this experiment involved attaching a small microsphere to the end of an optical fibre, then moving it in the UCASS laser beam while monitoring the outputs of the two photodiodes. As previously stated, a particle is considered to be within the sample area when over 50 % of the light scattered onto the mirror is reflected onto the inner photodiode element. This criterion was used to map the perimeter of the valid sample region, which was used to calculate its area.

Since the sample area of the UCASS was likely to differ between instruments—due to manufacturing tolerances in the optics, and slightly different alignments—I decided to conduct some basic ray tracing simulations, with the initial aim of assessing the sensitivity of the sample area to changes in optical surfaces. I wrote a simple ray tracing algorithm in

MATLAB, which modeled a series of sample rays from a grid of query points. These points were distributed within a circle with a radius of 1 mm, and a centre at the primary focus of an ellipsoidal reflector. A diagram of the simulated domain is shown in Fig. 3.11.

When a ray originating from point f_1, as shown in Fig. 3.11, hits the ellipsoidal mirror, it is reflected onto f_2. The equation which governs this reflection is

$$\mathbf{r_i} = \mathbf{I_i} - 2(\mathbf{I_i} \cdot \mathbf{n_i})\mathbf{n_i} \tag{3.1}$$

where $\mathbf{n_i}$ is a (normalised) vector normal to the surface of the ellipse at the intersection point. The equation for the ellipse is

$$f(x, y, z) = \frac{z^2}{a^2} + \frac{y^2}{b^2} + \frac{x^2}{b^2} - 1 \tag{3.2}$$

and its gradient is given by

$$\nabla f(x, y, z) = \left\langle \frac{2x}{b^2}\mathbf{i}, \frac{2y}{b^2}\mathbf{j}, \frac{2z}{a^2}\mathbf{k} \right\rangle \tag{3.3}$$

where a and b are the major and minor radii of the ellipse—created by the virtual extension of the ellipsoidal mirror in the UCASSas shown in Fig. 3.11, and $\mathbf{i}$, $\mathbf{j}$, and $\mathbf{k}$ are unit vectors in the x, y, and z directions respectively. $\mathbf{n_i}$ can therefore be found by substituting the coordinates of the intersection point, i, into Eq. 3.3 then normalising. The intersection of the reflected vector and the detector plane can then be computed to give the distribution of scattered light over the detector, and the rejection criteria for the particle can be applied. Each ray had an associated stokes vector, which was calculated from Mie-Lorenz theory. The particles were assumed to be spherical water droplets with a refractive index of 1.31+0j for simplicity. It is important to distribute the scattered light this way because the intensity distribution of light will influence the rejection criteria of the particles, and therefore the size of the sample area. A particle was considered to be accepted when the total intensity on the inner detector element was greater than that on the outer element. The origin points of the

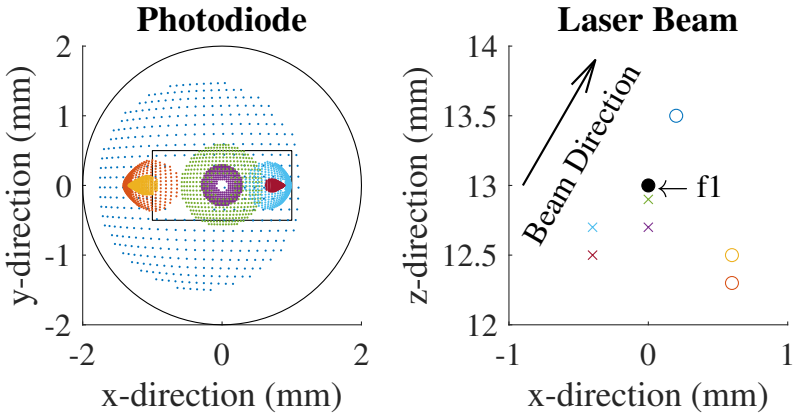

FIGURE 3.12: A plot of the simulated rays for seven example particles in different points in the laser beam. The left panel shows the patterns the rays make on the detector, and the right panel shows the origin points for the rays from each of the seven particles. In the right panel, a circle means the particle was rejected, and a cross means the particle was accepted. The colours of the points on the left and right panels are consistent and therefore indicate which particle has produced which pattern. The axis labeling is consistent with Fig. 3.11, and laser beam direction and primary focal point of the mirror, f_1, are labeled for clarity.

simulated particles were in a 9 by 9 grid with a spacing of 0.2 mm.

Figure 3.12 shows a plot of some example particles from the ray tracing simulations. The left panel shows the patterns the rays make on the detector, and the right panel shows the origin points for the rays from each of the seven particles in the laser beam; the colour of the points is consistent between panels. In the left panel, a circle point means a particle was rejected, and a cross means the particle was accepted as a valid count. These sample points were selected to show counts which was accepted and rejected for different reasons. For example, the large, dark blue pattern was rejected because it was too out of focus—i.e. it had too much z-displacement—whereas the orange and yellow particles were rejected due to lateral positioning with respect to the mirror—i.e. they had too much x-displacement.

The lime, cyan, red, and purple particles were all accepted.

The final result of the simulation showed a sample area of 1 mm, which is twice the sample area which was calculated from the measurements. The measured sample area value was already well established, and performed well in intercomparison studies (Smith et al., 2019), I determined that the discrepancy was due to an oversight in the simulation. Most likely, the issue was in the applicability to real optics, and the imperfect manufacturing in the low-cost ellipsoidal mirror. In addition, practical optical alignment is seldom perfect, and any discrepancy can result in a malformed sample volume, due to the positioning of $f1$, and $f2$ with respect to the laser and detector. Laser beams which have imperfect intensity distributions could also cause different intensity distributions across the detector, and therefore affect the rejection criteria of the particle. To include all these parameters in the simulation was deemed beyond the scope of the project at this stage. However, these results do highlight the importance of measuring the sample volume, and the magnitude by which different artefacts can affect the sample area specifically. This error would mean all concentrations measurements could be out by a factor of 2 if the sample area was not measured.

3.2.2 Calibration

For the purposes of this thesis, the calibration procedure described in Smith et al. (2019) was improved upon. The previous setup involved a flow of calibration particle standards—aerosolised from a suspension in a medical nebuliser—through a drying column, which were then passed through a UCASS unit at the base of the column. The output of the calibration was a look-up table converting instrument response into a particle diameter. The major problem with this method were: i) contamination of the measured sample in the drying column with desiccant particles; ii) a broadening of the UCASS instrument response to larger particle radii, which increased modal size ambiguity, and iii) an abstraction of the

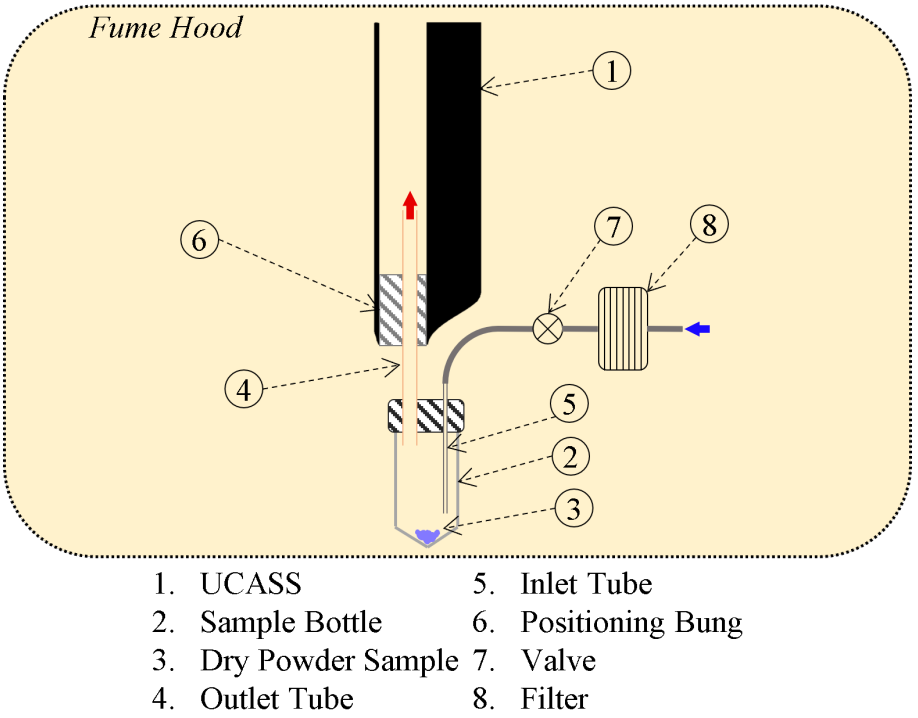

FIGURE 3.13: The new UCASS calibration apparatus, developed to solve calibration problem (i). The blue arrow indicates air from a compressor, and the red arrow indicates the direction of the particle-laden flow

calibration outputs—since the calibration is accounting for stray light and instrument gain, it was considered that these should be directly reported instead of a direct look-up table.

In order to address (i), the calibration apparatus was modified so particles would be directly injected into the UCASS sample area. This is illustrated in Fig. 3.13. This has the advantage of a reduction in particle loss due to turbulent deposition in the drier—in addition to the elimination of desiccant particulate contamination. However, the calibration procedure had to be significantly modified. The aerosolised calibration particles used had to be in dry dust form—silica or glass beads—as opposed to particles in colloidal suspension, to eliminate the need for a desiccant dryer. This therefore meant the aerosolisation method had to be altered to suit this particle type. Also illustrated in Fig. 3.13, the aerosolisation method consists of pumping clean air from a compressor into a sample tube containing the dry calibration particles. The air containing the sample is then directed into the sample area

of the UCASS via a single straight copper tube—in order to reduce particle loss through static attraction and inertial deposition. The sample airflow peak velocity must be less than $15\,\mathrm{m\,s^{-1}}$, and the minimum velocity must be above $3\,\mathrm{m\,s^{-1}}$; which was tuned experimentally via the compressor output pressure regulator, and an anemometer to measure the flow velocity at the sample area. The maximum velocity is limited by the TIA bandwidth, since smaller light pulses on the PD will have less TIA gain; discussed further in Chapter 5. The minimum velocity is determined by a firmware 'glitch trap' limit, which is set to avoid small noise pulses on the PD.

In order to address (ii), we must first explain why the instrument response is broader for larger sizes. Due to tolerances with the manufacture of particle standards, a number of calibration particles will produce a narrow Gaussian distribution of light intensity values on the PD. Since the relationship between instrument response and particle radius can be approximated by a square polynomial, the small difference in particle sizes due to manufacturing tolerances will follow the same relationship. This means that the Gaussian instrument response distribution has a larger standard deviation for larger particle sizes. While this is the case for pure instrument response, this is not the case for the calibrated output in terms of particle radius. Since the instrument response during calibration is a single value scaled between 0 and 4095, a post-binning script can be employed with larger particles to increase the reliability—at the cost of accuracy—of the modal instrument response value.

In order to address (iii), it must be understood what physical parameters the calibration is accounting for. Two UCASS units—or any other generic OPCs—can have instrument response phase spaces which differ in gradient and static offset. The gradient change is due to differences in laser power, TIA gain, and PD efficiency; the static offset is due to changes in the static stray light reflecting off instrument surfaces—which is also coupled with the gradient change. The UCASS instrument response in terms of scattering cross section is

$$V_{adc} = \frac{2^b}{V_{ref}} \left(I_l \epsilon_{pd} g_{tia} \sigma_{sca,p} + I_l \epsilon_{pd} g_{tia} \sigma_{sca,sl} \right) \tag{3.4}$$

where V_{ADC} is the 12-bit ADC output, scaled between 0 and 4095; b is the number of ADC bits—12; V_{ref} is the ADC reference voltage—3.3 V; I_l is the laser beam light flux—$1 \times 10^5\,\mathrm{W\,m^{-2}}$; ϵ_{pd} is the efficiency of the PD at the laser wavelength—$0.45\,\mathrm{A\,W^{-1}}$; g_{tia} is the static TIA gain—$1 \times 10^6\,\mathrm{V\,A^{-1}}$ for high gain, or $3.3 \times 10^5\,\mathrm{V\,A^{-1}}$ for low gain; $\sigma_{sca,sl}$ is the scattering cross section for the static stray light, resulting from reflections off instrument internal surfaces; and finally $\sigma_{sca,p}$ is the scattering cross section of the calibration particle. The instrument gain and stray light are therefore given by

$$R = \frac{2^b I_l \epsilon_{pd} g_{tia}}{V_{ref}} \tag{3.5}$$

$$V_{sl} = R\sigma_{sca,sl} \tag{3.6}$$

where R is the instrument gain, and V_{sl} is the digitised voltage contribution from stray light. Using this notation, Eq. 3.4 becomes

$$V_{adc} = V_{sca} + V_{sl} = R\left(\sigma_{sca,p} + \sigma_{sca,sl}\right) = R\sigma_{sca,p} + V_{sl} \tag{3.7}$$

where V_{sca} is the is the digitised voltage contribution from the particle scattering.

When the ADC instrument response to the aforementioned calibration procedure is plotted versus scattering cross section, a linear fit can be applied—as demonstrated in Fig. 3.14. The 0^{th} and 1^{st} fit coefficients are then R and V_{sl} in Eq. 3.7 respectively.

For a generic OPC, assuming the particle does not depolarise the laser light, the Scattering cross section in terms of particle radius is given by

$$\sigma_{sca,p} = \frac{1}{k^2} \int_0^{2\pi} \int_0^{\pi} \left(\left|S_1\left(\theta, \phi, kr_p, n\right)\right|^2 + \left|S_2\left(\theta, \phi, kr_p, n\right)\right|^2\right) \sin\left(\theta\right) \omega\left(\theta, \phi\right)\, \mathrm{d}\theta\, \mathrm{d}\phi \tag{3.8}$$

where k is the wavenumber of the incident light; $S_{1,2}$ are the first and second elements of the amplitude scattering matrix, determined form Mie-Lorenz theory; θ, ϕ are the azimuth and zenith angles respectively; and $\omega\left(\theta, \phi\right)$ is a weighting function, which describes the

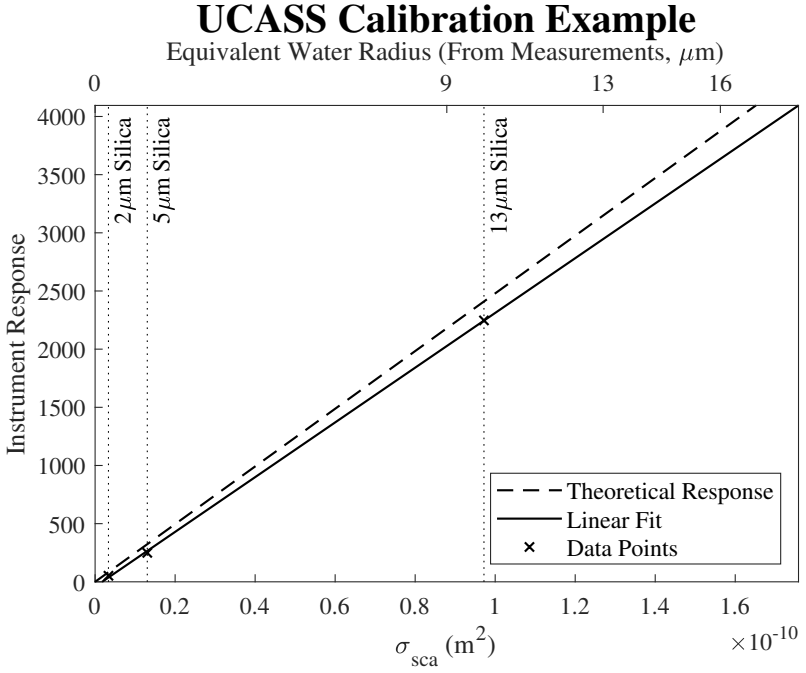

FIGURE 3.14: A plot of ADC instrument response versus scattering cross section for an example UCASS calibration, including the gain and stray light as physical calibration parameters, which were actualised to address calibration problem (iii).

collected scattering angles by the instrument optics (Rosenberg et al., 2012). The value of the weighting function in terms of both ϕ and θ will be either 1 or 0 depending on whether any given ray is collected by the detecting geometry of the instrument. Since the scattering given by Lie-Lorenz theory is rotationally symmetric around the zenith axis, the outer integral in Eq. 3.8 can be removed, thus simplifying it to

$$\sigma_{sca,p} = \frac{\pi}{k^2} \int_0^{\pi} \left(|S_1(\theta, kr_p, n)|^2 + |S_2(\theta, kr_p, n)|^2 \right) \sin(\theta) \omega(\theta) \, \mathrm{d}\theta \tag{3.9}$$

where the value of the weighting function at any given azimuth angle θ—$\omega(\theta)$—is the amount of light collected by the instrument optics around the zenith range pto 2p, and is between 0 and 1, where 0 is no light, and 1 is all light across the zenith range for a particular azimuth angle. For instruments with annular reflectors, like the FSSP, the weighting function is a

Heaviside function. For UCASS, this weighting function, from Smith et al. (2019), is

$$\omega(\theta) = \Phi_m(\theta) - \Phi_h(\theta) \tag{3.10}$$

where $\Phi_{m,h}(\theta)$ is the normalised amount of radiation captured around the zenith range for a given azimuth angle, and the subscripts m and h denote mirror and hole respectively, since the UCASS primary reflector is an ellipsoidal mirror with a hole in the centre—part 'a' in Fig. 3.1. Its lens angle is 60°, the half angle of the mirror is 43.8°, and the half angle of the hole is 10.7°. For a non-centred primary reflector, $\Phi_{m,h}$ is given by

$$\Phi_{m,h}(\theta) = \begin{cases} \frac{1}{\pi}\arccos(\alpha) & if \quad -1 < \alpha < 1 \\ 0 & if \quad \alpha \geqslant 1 \\ 1 & if \quad \alpha \leqslant -1 \end{cases} \tag{3.11}$$

$$\alpha = \frac{\cos H_{m,h} - cosLcos\theta}{sinLsin\theta} \tag{3.12}$$

where $H_{m,h}$ is the half angle of the mirror and hole respectively, L is the lens angle of the reflector, and α defines the expanse and rotation of the reflector.

One advantage to stating the calibration outputs in this manor, is ensuring the user of the UCASS is acutely aware of the assumptions that they are making in their data analysis; in addition to allowing the flexibility of post-calibration with different assumptions, since the amplitude scattering matrix—$S_{1,2}$ in Eq. 3.8—can be calculated via a number of different simulation methods, which may be appropriate for different particles. A plot of the scattering cross section of a particle (as measured by the UCASS) versus particle radius for different material refractive indices can be seen in Fig. 3.15.

3.2.3 Data Acquisition and Software

Data acquisition on UCASS was traditionally conducted using a radiosonde, which communicated with UCASS via X-Data—a simple serial protocol—and relayed data to a ground

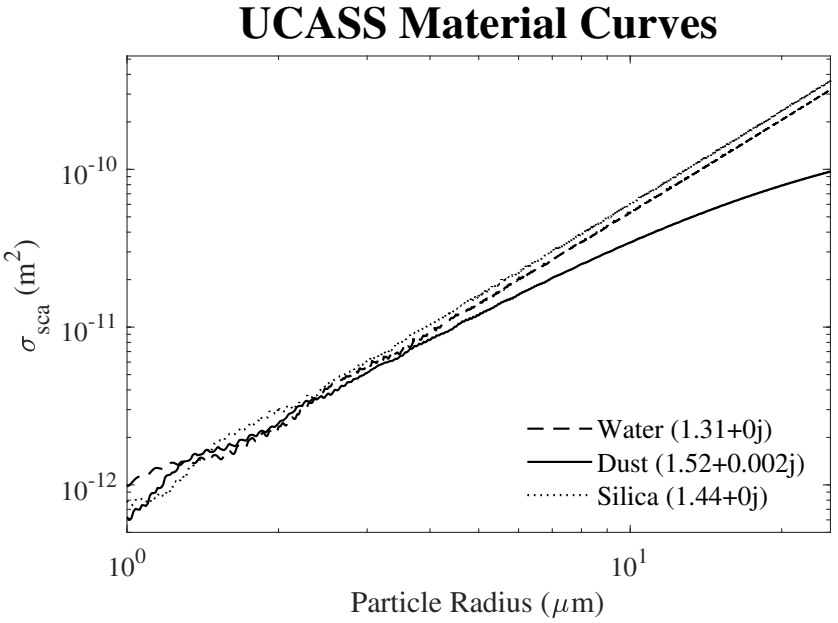

FIGURE 3.15: A plot of scattering cross section measured by the UCASS versus radius for different materials.

station, where it was stored. For the UAV version, while live data on a ground station was considered desirable, it was not strictly necessary for the work conducted in this project. In addition, the radiosonde had limited bandwidth, which meant only the first ten UCASS size bins could be transmitted—along with a timestamp and limited debug information in a binary word. The detailed UCASS debug information included: particles rejected due to long ToF, particles rejected due to short ToF, and particles rejected due to being out of the sample volume—through the system shown in Fig. 3.2. The debug information could be used to dynamically assess and reject data words. The long ToF reject count indicated times that the flow through the UCASS was too slow; the short ToF reject count was used to indicate electrical noise, or if the flow through UCASS was too fast; and the particle rejection count was used to indicate the likelihood of coincidence or dead-time artefacts. However—when data acquisition was conducted using a radiosonde—the bandwidth limitation meant only a single variable could be used, which was a boolean rejection indicator, which was set to

false by the UCASS firmware if any of the three debug variables were above certain pre-determined limits. This was a disadvantage for two reasons: the rejection limits occasionally needed to be retroactively set—for example if the UCASS was expected to travel slower than normal—and the single indicating variable could not tell the operator which one of the three debug limits had been breached. This was found to be a problem when tuning the ascent speed of balloon launches, since one could not tell if the balloon velocity was too fast or slow from the UCASS data alone. Therefore, an on-board logging system needed to be devised to obtain all sixteen UCASS bins, and detailed debug information. UCASS data are also available through a serial peripheral interface (SPI), which was chosen to be the preferred transmission protocol for data retrieval, since most single-board computers are capable of SPI communications.

In addition to UCASS particle data, auxiliary data were necessary to obtain useful particle data products. The auxiliary data required were: measurement time—since there was no real-time clock (RTC) on the UCASS, airspeed through the UCASS, position data from the UAV global positioning system (GPS), and attitude data from the UAV inertial measurement unit (IMU). All of these data could be measured and logged by a generic UAV flight controller (FC). However, data synchronisation would be necessary if it were the case that the auxiliary data were written to separate storage to the UCASS data. Since the UCASS does not contain an RTC, the time would have to be recorded when it is switched on—a large source of error, which can lead to significant data synchronisation problems, particularly if the UCASS is travelling faster than $10\,\mathrm{m\,s^{-1}}$. Therefore, it was decided that the auxiliary data must be read from the UAV FC and written to the same file as the UCASS data. Most FCs communicate via the Micro Air Vehicle communication protocol (MAVLink)—a lightweight serial protocol designed for communication between different UAV components, and between UAVs and ground-stations. MAVLink consists of a series of message packets set with pre-defined data structures; MAVLink code libraries instruct embedded systems how to send and receive those packets to/from a serial interface. The data logger firmware was therefore written to receive the MAVLink data packets which contained the UAV GPS, IMU,

airspeed, and time data, to be recorded alongside the UCASS data in the same file.

For scientific applications, it is convenient to use a single-board computer for data logging, since these are commonly available and straightforward to program. The UAV data logger was required to contain serial capability for MAVLink communications, and SPI capability for communications with the UCASS. Two readily accessible single board computers capable of such communication are the Arduino (Arduino, 2022) and the Raspberry Pi Zero (RaspberryPi-Foundation, 2015). Since both of these computers are commonly used in UAVs for data logging purposes, it was decided that libraries would be written for both of them. A Python 2.7 library for logging UCASS and auxiliary data on a Raspberry Pi Zero is available from Girdwood (2019), and C++ libraries for logging on an Arduino is available from Girdwood (2018a,b).

4 | Multi-Rotor Adaptation

4.1 Summary and Context

The following paper: 'Design and Field Campaign Validation of a Multirotor UAV and Optical Particle Counter' (published version: Girdwood et al., 2020) was submitted to the 'Atmospheric Measurement Techniques' journal in June 2020, and accepted for publication in December 2020. It was the first milestone in this project—that is, the adaptation of an OPC to a multi-rotor airframe, along with testing and validation in a realistic field campaign setting. In this work, UCASS was successfully adapted for use on a multi-rotor airframe, which was also designed and constructed as part of this project. The appropriate sampling techniques were assessed and discussed from a scientific standpoint. The manuscript presented here has been edited for typesetting in this thesis.

4.2 Design and Field Campaign Validation of a Multirotor UAV and Optical Particle Counter

J. Girdwood[1], H. Smith[1,a], W. Stanley[1], Z. Ulanowski[1,b,c], C. Stopford[1], C. Chemel[1,2], K. Doulgeris[3], D. Brus[3], D. Campbell[4], R. Mackenzie[1].

1 Centre for Atmospheric and Climate Physics, School of Physics, Astronomy and Mathematics, University of Hertfordshire, Hatfield, Hertfordshire, AL10 9AB
2 National Centre for Atmospheric Science, Centre for Atmospheric and Climate Physics, School of Physics, Astronomy and Mathematics, University of Hertfordshire, Hertfordshire, AL10 9AB
3 Finnish Meteorological Institute, PO Box 503, FI-00101, Helsinki, Finland
4 School of Physics, Astronomy and Mathematics, University of Hertfordshire, Hertfordshire, AL10 9AB
a Now at: TruLife Optics Ltd, 79 Trinity Buoy Wharf, London, UK
b Now at: Centre for Atmospheric Science, University of Manchester, Manchester, UK
c Now at: British Antarctic Survey, NERC, Cambridge, UK

4.2.1 Abstract

Small unmanned aircraft (SUA) have the potential to be used as platforms for the measurement of atmospheric particulates. The use of an SUA platform for these measurements provides benefits such as high manoeuvrability, re-usability, and low-cost when compared with traditional techniques. However, the complex aerodynamics of an SUA—particularly for multirotor airframes—poses difficulties for accurate and representative sampling of particulates. The use of a miniaturised, lightweight optical particle instrument also presents reliability problems since most optical components in a lightweight system (for example laser diodes, plastic optics, and photodiodes) are less stable than their larger, heavier, and more expensive equivalents (temperature-regulated lasers, glass optics, and photo multiplier tubes respectively). The work presented here relies on computational fluid dynamics with Lagrangian particle tracking (CFD-LPT) simulations to influence the design of a bespoke meteorological sampling system: the UH-AeroSAM. This consists of a custom built airframe, designed to reduce sampling artefacts due to the propellers, and a purpose built open-path

optical particle counter—the Ruggedised Cloud and Aerosol Sounding System (RCASS). OPC size distribution measurements from the UH-AeroSAM are compared with the Cloud and Aerosol Precipitation Spectrometer (CAPS) for measurements of Stratus cloud during the Pallas Cloud Experiment (PaCE) in 2019. Good agreement is demonstrated between the two instruments. The integrated dN/dlog(Dp) is shown to have a coefficient of determination of 0.8, and a regression slope of 0.9 when plotted 1:1.

4.2.2 Introduction

Aerosols and their interactions with clouds and radiation have been consistently highlighted by the Intergovernmental Panel on Climate Change (IPCC) as the largest uncertainty in predicting climate change today (IPCC, 2013). This is, in part, due to the difficulty of measuring such phenomena, and their high spatial heterogeneity. To reduce this uncertainty, regular measurements of aerosols and droplets (and radiation) would need to be performed with the aim of quantifying the aerosol-radiation and cloud-aerosol interactions that affect our climate. Currently, aerosol measurements are conducted using remote sensing techniques (e.g. sun photometers and LIDARs) on ground based (Baars et al., 2015, Bokoye et al., 2002, Che et al., 2009) and satellite instruments. While these methods require the least personnel and can sample a continuous vertical column, they directly measure the column-integrated optical parameters of the atmosphere, and require complex algorithms (e.g. LIRIC and GARRLiC Tsekeri et al., 2017) and various assumptions about the atmosphere to retrieve aerosol properties. Hence remote sensing requires validation from coincident, height resolved, in-situ meteorological measurement. Additionally, most remote sensing techniques have limited vertical resolution, and are unable to measure the lower parts of the planetary boundary layer (PBL). This makes in-situ measurements the only suitable sampling method for the first 100 m of the atmosphere.

In-situ aerosol and droplet data are conventionally collected using manned aircraft (Drury et al., 2010, Hara et al., 2006) and, to a lesser extent, meteorological soundings (both

on tethered and non-tethered balloons) with instruments like the LOAC (Renard et al., 2016, 2018), the UCASS (Smith et al., 2019), and the POPS (Gao et al., 2013, 2016). Manned aircraft in particular are extremely expensive to operate, maintain, and crew. Also, vertical profiling is often a valued measurement, not only for remote sensing validation, but also because important atmospheric phenomena—such as moist convection—are governed by processes occurring in the vertical direction. A direct vertical profile cannot be accomplished by a fixed-wing manned aircraft due to restrictions with mobility, often meaning "staircases" or spiral ascents with large lateral dimensions have to be employed instead. Thus, such measurements can be problematic for comparisons with remote sensing in atmospheres with high spatio-temporal variability. Furthermore, the aircraft based instruments used to measure aerosol and droplets—for example the Forward Scattering Spectrometer Probe (FSSP, evaluated by Baumgardner and Spowart, 1990, Baumgardner et al., 1985, Dye and Baumgardner, 1984); the Cloud Droplet Probe (CDP, described by Lance et al., 2010); and the Backscatter Cloud Probe (BCP, Beswick et al., 2014)—incur huge costs, and availability is often a concern. Meteorological soundings can—to an extent—negate these issues since a vertical profile can be accomplished, and some airspace restrictions—for example runway availability—do not apply. However, the payload from a non-tethered balloon is not often retrievable, making regular soundings with aerosol instruments to examine spatio-temporal variations impractical.

Unmanned aerial vehicles (UAVs), referred to here as small unmanned aircraft (SUA) according to the UK Civil Aviation Authority (CAA) definition, are becoming increasingly popular for PBL research. Fixed wing SUA designed for meteorological sampling (e.g. the designs described in Altstädter et al., 2015, Buschmann et al., 2004, Reuder et al., 2009, Wildmann et al., 2014a) have been used in numerous studies already, including, but not limited to: new particle formation (Altstädter et al., 2018); the sampling of standard metsonde parameters (Martin et al., 2011); measuring the wind vector using a 5-hole pitot probe (van den Kroonenberg et al., 2008); the sampling of black carbon aerosol (Corrigan et al., 2008, Ramanathan et al., 2007); Saharan dust aerosol (Mamali et al., 2018); Arctic

boundary layer aerosol (Bates et al., 2013); and turbulent flux measurements (Wildmann et al., 2013, 2014b,c). Rotary wing platforms (e.g. multirotors) on the other hand have been used much less extensively in atmospheric physics, likely due to problems with the validation of measurements—because of stronger aerodynamic distortions—and limitations to their endurance. However, if these issues can be overcome, multirotor platforms present many advantages over fixed-wing based platforms since they can fly directly upwards for a vertical profile; they integrate very well with auto-pilot systems allowing precise flights with minimal human interference; they require less pilot experience to operate effectively; and measurements can be repeated easily in the same location, thus providing superior spatio-temporal sampling abilities.

An SUA equipped with particle measuring instrumentation would be of particular use in the lower 120 m of the atmosphere; since beyond this limit, engineering—and often legislative—challenges have to be overcome, potentially making other platforms more suitable. SUA-based cloud droplet measurements in this part of the atmosphere, however, are of particular use to characterise fog and low-level stratus cloud. Egli et al. (2015) used a Cloud Droplet Probe (CDP) attached to a tethered balloon to characterise fog droplet vertical distribution. While the results presented here were in good agreement with theoretical calculations in fully developed fog, it was found that the platform had insufficient temporal sampling capabilities to characterise formation and dispersion.

However, the scientific validity of quantitative measurements conducted using any platform can be questioned if a proper validation process has not been implemented. This is especially true when sampling atmospheric aerosol and droplets using a multirotor SUA, due to artefacts resulting from the the aerodynamic disturbances created by the propellers. Quantifying this distortion, and its effect on particles, can be difficult due to the complexity of flow measurements (especially when considering turbulence). Alvarado et al. (2017), for example, presented an approach to validation involving anemometer-based measurements of the air velocity (in the vertical direction) in a grid pattern around a multirotor SUA at full throttle. This approach, however, will not provide enough spatio-temporal resolution

for turbulence measurements, and only involves flow measurements vertically. Also, this method does not account for any crosswind, or the motion of the SUA itself with respect to the surrounding air. Another method that is commonly applied to the validation of particle instruments, but could also be applied to SUA, is wind tunnel testing. Clarke et al. (2002) used a wind tunnel to post-evaluate a miniaturised optical particle counter (OPC), and derive a correction factor for sub-isokinetic sampling flow which can cause an under-prediction in particle concentration measurements. This technique, however, is generally only used to simulate the effects of the flow speed and angle of attack without the SUA (or manned aircraft) airframe. This is because wind tunnels are normally not large enough to accommodate the SUA, and a dimensionally similar scale model cannot be used (a technique common in the aerospace industry) since the particle instrument would have to be full size.

The purpose of this paper is to present a novel design and validation technique for sampling aerosols on a multirotor SUA. The main justification behind this approach is that the validation is simpler—and the data products more reliable—when artefacts of measurement and experimental design are considered throughout the physical engineering design process. We utilise computational fluid dynamics with Lagrangian particle tracking (CFD-LPT) as a tool to influence design decisions for the SUA—thus identifying the main sources of measurement error—which were then field tested with reference instrumentation for validation. The aircraft used in this experiment is the aerosol sampling SUA UH-AeroSAM, which is a bespoke SUA developed at the University of Hertfordshire and equipped with an open path OPC to sample atmospheric aerosol and droplets. An overview of some existing studies using SUA to measure atmospheric particulates is presented in Sect. 4.2.3, and a description of the UH-AeroSAM configuration and instrumentation is presented in Sect. 4.2.4. The CFD-LPT simulations are presented in Sect. 4.2.5, and the field validation is presented in Sect. 4.2.6. The field validation took place during the Pallas Cloud Experiment (PaCE, 2019)—a biennial experiment at the Pallas atmosphere-ecosystem super-site (Lohila et al., 2015) with the aim of characterising sub-Arctic cloud, and validating instruments.

4.2.3 Overview of Existing SUA Particle Measurements

While there exists a limited number of aerosol and droplet measurements on SUA, previous SUA studies have attempted to measure the physical properties of atmospheric particles and droplets. One such study was Bates et al. (2013), which used the MANTA SUA as a platform for a three-wavelength absorption photometer, a condensation particle counter (CPC), and a chemical filter sampler (all connected to the same artificially aspirated inlet) to measure vertical black carbon (BC) concentrations in the Arctic. This study represents an effort to obtain a greater understanding of (potentially anthropogenic) BC transport into Arctic regions, and concluded that regular SUA measurements could provide the in-situ BC (and other aerosol) data needed to validate climate models and remote sensing retrievals. However, in-situ methods (particularly using SUA) still require validation and testing before the data can be trusted for these purposes.

Another step towards the reliable, regular use of SUA data in climate models was presented in Mamali et al. (2018). This study compared vertical profiles of Saharan dust mass concentration measured using an artificially aspirated OPC mounted on a fixed wing SUA, to remote sensing retrievals (POLIPHON) over Cyprus in 2016. While the coefficient of determination between the POLIPHON-retrieved and OPC-derived aerosol mass concentration was found to be 0.8 in the first case study and 0.72 in the second, there are elements of the dust vertical structure (for example sharp changes in the spatial mass concentration profile) that were measured by the SUA but not by the remote sensing. This could be caused by such phenomena as: a highly heterogeneous dust layer causing a spatial variation in mass concentration between measurements; some measurement artefact resulting from the SUA airframe or OPC; or an underlying problem with the POLIPHON retrieval.

Multirotor airframes have better spatio-temporal sampling abilities for the validation of LIDAR, since they possess the ability to fly along a co-located profile. Additionally, proper validation of the airframe and in-situ instrumentation can minimise any artefacts in the SUA data, and a comparison of different retrievals (for instance in Tsekeri et al., 2017) can help

discover problems with remote sensing. For these reasons, more work is still to be done on the proper integration of SUA data into model datasets and remote sensing validation.

SUA enable regular measurements of atmospheric properties that cannot be accomplished by any other platform. This was fully exploited by Altstädter et al. (2018) where the fixed-wing ALADINA SUA initially proposed by Altstädter et al. (2015), using a new setup described by Bärfuss et al. (2018), was utilised for observations of new particle formation (NPF). This study was a strong example of SUA utilisation where manned aircraft measurements would be impractical. Due to the temporally variable nature of the NPF process, regular measurements would be necessary, which would incur large costs in manned aircraft. Additionally, the NPF events observed here, and during a previous study by Platis et al. (2016), occur at low altitudes where manned aircraft often cannot fly. In the UK for example, manned aircraft are often prohibited from flying below 500 ft where many of these NPF events occur. This study represents a promising step towards the regular measurements of ultra-fine atmospheric aerosol properties. However, these particles tend to be subject to higher aspiration and transportation losses, especially in turbulent flow. A series of commonly used empirical formulae initially derived from wind tunnel testing is reviewed in Von Der Weiden et al. (2009). These formulae are used to predict the losses due to the aerosol instrument transportation and aspiration mechanism, but not airframe effects which, while not as predominant on a fixed-wing SUA like ALADINA, would produce artefacts in multirotor measurements. For that reason, a CFD or experimental technique must be used to characterise airframe related artefacts.

Multirotor SUA have been used previously for atmospheric aerosol and droplet sampling. Alvarado et al. (2017), for example, aims to characterise an OPC-SUA combination using anemometer measurements, wind-tunnel tests on the instrument only, and a flight-test with an artificial particle source. A long transport tube was used to sample aerosol at a point relatively free from propeller airflow disturbance. However, significant particle loss was caused by this sampling probe, leading to a large correction factor—particularly for larger particle sizes. A naturally-aspirated instrument—for example the UCASS (Smith

FIGURE 4.1: The University of Hertfordshire aerosol sampling SUA (UH-AeroSAM). This is a bespoke SUA specifically designed to sample aerosol particles and droplets using a custom built OPC.

et al., 2019)—would completely eliminate the need for this transport tubing, and thus the correction factor.

4.2.4 Description of UH-AeroSAM

4.2.4.1 Airframe and Auxiliary Instrumentation

UH-AeroSAM is a custom built octocopter SUA, with opposing motors separated by approximately 1m. Figure 4.1 shows an image of UH-AeroSAM with its full instrumentation package installed. The open-geometry frame allows for a highly configurable payload. Consequently, the SUA can accommodate additional or different instruments in future studies. The maximum take-off mass (MTOM) is 3.2 kg, and the endurance with this MTOM is approximately 13 min depending on local wind speed and temperature. Lower take off masses will allow the SUA to achieve a longer endurance, and hence a higher altitude if a vertical profile is desired; the take off mass used for these experiments was 2 kg which provided an endurance of approximately 18 min. UH-AeroSAM is controlled using a Pixhawk flight controller (3DRobotics, 2013) with an external GPS module, which is tuned for stability in

wind gusts up to $15\,\mathrm{m\,s^{-1}}$. The positioning of the particle sensor on the airframe is discussed in Sect. 4.2.5.2.

UH-AeroSAM is equipped with an adaptation of the Universal Cloud and Aerosol Sounding System (UCASS, original design: Smith et al., 2019), the modified design—the Ruggedised Cloud and Aerosol Sounding System (RCASS)—is presented in Sect. 4.2.4.2. This OPC is a ruggedised version of the original UCASS (a single-use instrument), which withstands multiple flights, with high levels of vibration. The RCASS is a naturally aspirated—also known as 'open-path'—OPC, which relies on the movement of the platform itself to provide a flow of particles through a sensing area, as opposed to a fan or pump. The motion of the SUA platform must be taken into account during the CFD-LPT simulations.

For atmospheric research, there exist several benefits and caveats when considering building versus purchasing an airframe. In a changing world with regards to legislation on SUA, purchasing an airframe from an officially recognised distributor appears to be the most legislatively stable option. This, however, restricts the operator on payload configuration and weight—an essential consideration for atmospheric measurement in general, since the positioning of scientific instrumentation on an airframe influences the quality of meteorological data. For this application in particular, an airframe with an open geometry configuration and propellers positioned far away from the centre was not, to the authors knowledge, previously commercially available, because the centre is normally reserved for the flight controller and battery pack. The other option for positioning the OPC away from the propeller effects is to mount a boom extending outwards from the SUA, and attach the OPC on the end. This, however, would result in a disruption to the stability of any standard airframe, thus causing it to be categorised as a 'home-built' airframe which infers more strict legislation by governing bodies in some countries.

Data from the OPC is available through a serial peripheral interface (SPI). This is connected to a data-logger, which is based on a Raspberry Pi zero (RaspberryPi-Foundation, 2015). This records data from 16 configurable size bins with a frequency of 2 Hz, where each particle size distribution is integrated over this interval. This was found to be the greatest

temporal resolution the data logger could handle, although at an ascent rate of $5\,\mathrm{m\,s^{-1}}$ (a typical balloon ascent rate) it gives a better (vertical) spatial resolution than a balloon-based sonde, which often record at 1 Hz while using an x-data interface (for example the Graw DFM-09). The GPS data is corrected using an inertial measurement unit (IMU) located on-board the Pixhawk, and transferred to the data-logger using the 'MAVLINK' protocol. Pressure and time data are also transferred to the data-logger from the Pixhawk using this protocol. The time data is synchronised with a real time clock every 0.5 s.

Temperature and humidity are also measured on the SUA. A fast-tip glass bead thermistor (FP07 'Fastip' probe) and a HIH-4000 capacitive humidity sensor are mounted in a cylindrical radiation shield. The enclosure is positioned underneath the propeller for enhanced aspiration, one quarter the length of the propeller from the tip as recommended by Greene et al. (2018). It was found that the increased pressure in the enclosure due to the propellers had a negligible effect on temperature and humidity measurements. The radiation shield is constructed from P2T (recyclable carbon fibre) with a gold coating around the exterior to reflect solar radiation and avoid radiative heating of the sensor. Since the HIH-4000 sensor contains an exposed silicon element, it has a tendency to act as a photo-diode when exposed to large amounts of stray light, and give saturated humidity measurements. To avoid this, the interior of the tube was coated with a broad-band absorbing paint (Stuart Semple – Black 2.0) so stray light reflected onto the sensor element is minimised.

4.2.4.2 Aerosol Instrumentation

The OPC used on the SUA is optically and electronically similar to the UCASS. However, since a SUA platform presents entirely different design criteria to the original dropsonde design, a mechanical re-design was necessary. The first principle of design was endurance, since the original UCASS is a single-use instrument and a SUA platform is likely to subject the payload to vibrations not considered in the UCASS. The RCASS therefore features an aluminium chassis and a more robust optical alignment system to ensure the optical components do not move. A computer aided design (CAD) model of the RCASS is shown

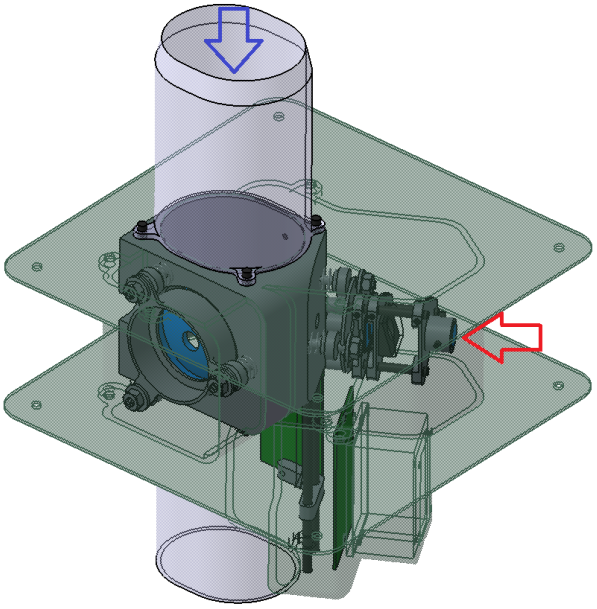

FIGURE 4.2: The RCASS—a mechanical re-design of the UCASS (Smith et al., 2019). The red and blue arrows are the laser beam and airflow directions respectively.

in Fig. 4.2. Since the original design was influenced with constraints associated with other combined systems, a mirror placed at a 45° angle directs the laser beam into the sampling tube, which is intended to reduce the package size of the instrument. The same design constraint is not present here. Therefore, in order to simplify construction, and reduce maintenance costs (e.g. optics cleaning), the optical carrier is mounted orthogonally to the sampling tube with no mirror redirecting the beam.

The mechanical re-design of the instrument also allowed an improvement of the internal aerodynamics. Smith et al. (2019) shows CFD results used to determine operational limits for the instrument based on platform-velocity derived mass concentration. However, the CFD simulations of the UCASS show an area of high stagnation pressure at the inlet on which a leading-edge vortex forms, directing particles around the sampling volume, and thus altering the mass flux through the detector region. This effect can be seen in Fig 4.3 which shows the flow profile through the UCASS for an input angle of attack of $-20°$—this effect is demonstrable for all angles of attack (and in axial flow), but $-20°$ is shown

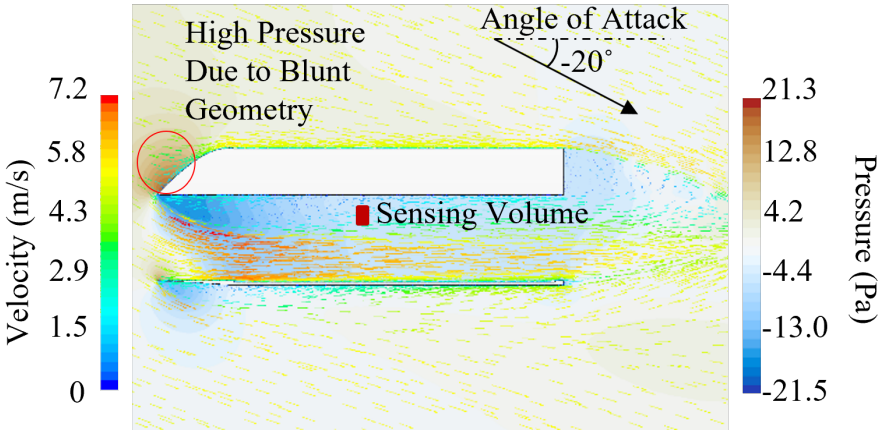

FIGURE 4.3: A vector plot of CFD simulation results for the original UCASS with an airflow angle of attack of 20°. The arrow represents angle of attack, the red circle is the high pressure region which directs particles around the sensing volume, which is labeled as a red square. The scale on the right is gauge pressure—corresponding to the colour of the background; the scale on the left is airflow velocity magnitude—corresponding to the colour of the glyphs.

for the sake of brevity. This is amplified for negative angles of attack and high airspeeds ($>10\,\mathrm{m\,s^{-1}}$), suggesting that the blunt geometry of the leading edge face is causing this high gauge pressure, and therefore the leading edge vortex. Hence the RCASS inlet features a sharp tip similar to the 'Korolev' cloud probe tips presented and simulated in Korolev et al. (2013a). Although the Korolev tips are designed to prevent shattered ice particles being sampled, the underlying process directing the ice particles into the sample volume is similar with a high pressure region forming on blunt tips forcing ice shards into the sample volume. As shown by Jackson et al. (2014), the anti-shattering tips can impact historical data—demonstrating the need to assess artefacts of measurement retroactively. Another limitation with the UCASS is the positioning of the detector region in the boundary layer of the instrument, therefore causing particles to be sampled in a region with lowered airflow velocity, and an increased likelihood of turbulent deposition. This is also shown in Fig 4.3. The new design, therefore, features a sample area positioned further away from the wall of the airflow tube. Following these results, the UCASS was also modified to include a collar around the inlet, which prevented the high pressure region from forming.

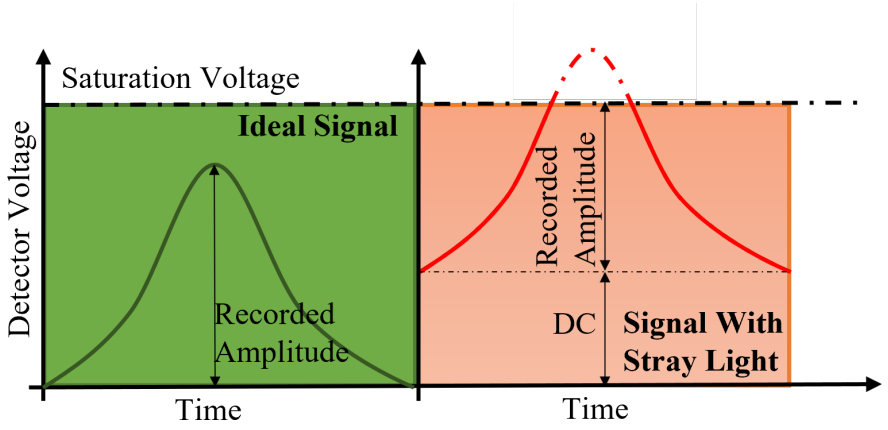

FIGURE 4.4: An illustration of the effect of stray-light on the signal output of the detector electronics (the transimpedance amplifier). Excess stray-light will cause the Gaussian pulse from a particle to stray beyond the saturation point, represented in the red area of the figure.

Since the package had been changed, the stray light issue (common among all OPCs, especially open path) needed to be re-addressed. The RCASS electronics can endure a certain amount of stray light using a direct current (DC)-restoration circuit. This is an inverted peak-detector circuit which will hold the value of the DC signal (a result of the stray light on the detector), minus any peaks from detected particles and noise. The DC signal is then subtracted from the total signal in a comparator. However, if the DC component is sufficiently large, the detector can start to saturate, exhibiting—in an ideal circuit—a Gaussian distribution with a flat top. Once the DC signal has been subtracted from this, the peaks appear smaller in amplitude, leading to the appearance of smaller particles—and eventually nothing—to be recorded. This effect is illustrated in Fig. 4.4. A stray light test was devised on a prototype RCASS design, which was improved and verified following the tests. These tests are described in detail in appendix 4.2.9.

The original UCASS is available in two different gain modes: low gain to capture larger droplets (3 µm to 40 µm); and high gain to capture smaller droplets (0.4 µm to 20 µm). On the RCASS, a mechanical switch was installed to allow the operator to change the gain mode before a flight, depending on meteorological conditions.

4.2.5 Computational Fluid Dynamics with Lagrangian Particle Tracking

4.2.5.1 CFD-LPT Methods

Simulations were performed to determine the best place on the SUA to position the RCASS. It was hypothesised that the minimal distortion of OPC measurement would be in the centre of the SUA; however a design compromise existed between the centralisation of the OPC, or the Pixhawk flight controller. A centralised flight controller makes easier dynamic stability tuning, but this may compromise OPC measurements. Previous works have used CFD as a design tool (for example Mckinney et al., 2019, Roldán et al., 2015), however the simulations used in this study are unique due to the Lagrangian particle tracking element.

Since the particle inlet is above the airframe, the aerodynamic effects of the airframe itself are negligible, and therefore have been ignored. This also allows lower computation and meshing time. The simulation domain was a virtual wind tunnel consisting of a 4 m tall cylinder with a radius of 1.5 m; the eight propellers were positioned in this cylinder on a plane 2.5 m from the base. The centre of each propeller was located on the vertices of an octagon with an 'across-flats' dimension of 0.97 m—the same geometry as the real SUA. The walls of the cylinder are assumed to generate no shear stress, and hence no boundary layer. This was to simulate a quasi-free-stream while simultaneously reducing computation time. Figure 4.5 shows a schematic of the CFD-LPT domain and propellers.

The motion of the propellers was simulated using an overset mesh (also known as a 'Chimera' mesh), which was chosen for its compatibility with the time unsteady solver (required for LPT), and its flexibility with different mesh types. The transport equations used in the simulations were the Reynolds averaged Navier Stokes (RANS) equations, with a $k - \epsilon$ turbulence model. This is a two-equation eddy viscosity model, which is commonly used for its stability and accuracy in the free stream. The $k - \epsilon$ model tends to under-predict the anisotropy of turbulence near walls and in wakes, however the points of interest

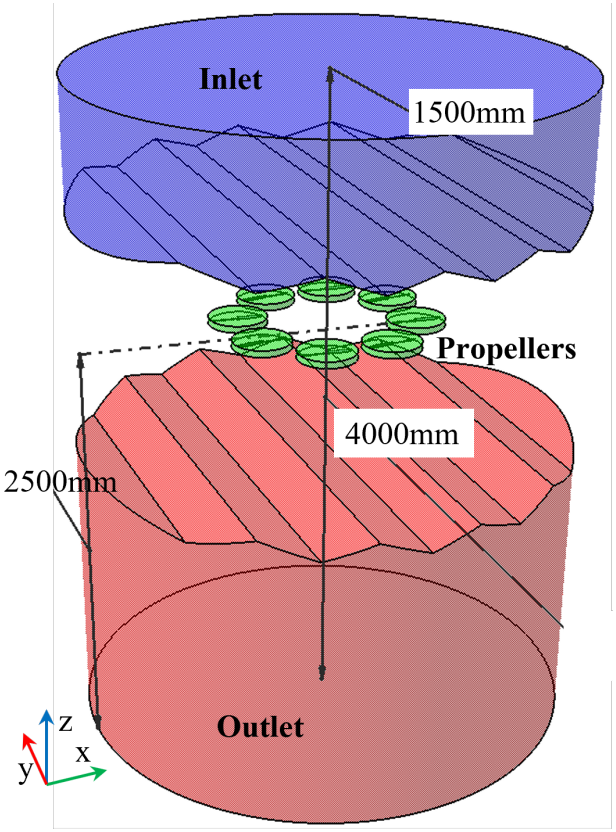

FIGURE 4.5: This figure shows the CFD-LPT domain. Air and particles enter the domain at the top of the blue section labeled "Inlet", and flow downwards past the propellers. Each of the propellers is in a small green cylinder representing the overset mesh region; a section of the cylinder is cut away here for illustration purposes. Air and particles leave the domain through the bottom face of the cylinder in the red region.

on the airframe were in the far field, away from walls. Tian and Ahmadi (2007) found that a Reynolds stress model (RSM) would more accurately predict near-wall turbulence conditions. However, in complex flows such as this, a RSM would be highly unstable and require minute time steps, which would vastly increase computation cost. While near-wall turbulence strongly influences turbulent deposition of particles, this effect was not expected to be important in this case, since all areas of interest are far away from any boundary layers. Therefore, a $k - \epsilon$ turbulence model was sufficient.

These transport equations were solved numerically by an implicit unsteady solver, which was available in the "Star CCM+" commercial code used. This solver converges a simulation

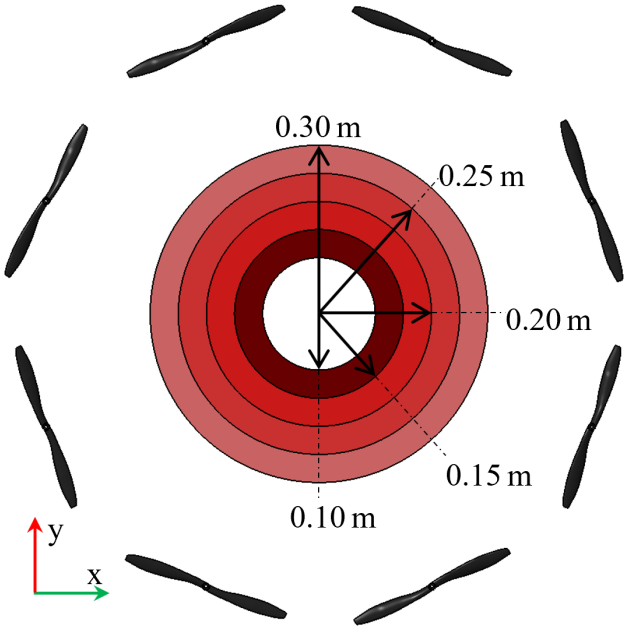

FIGURE 4.6: This figure shows the particle sampling regions and their radii, across one of the parallel sampling planes. The planes had z coordinates—relative to the propeller plane—between 0 m and 0.3 m with an equal spacing of 0.05 m, and were all identical. The propellers are shown here as a reference. The axis labeling system is consistent with Fig. 4.5.

for each time step with multiple inner iterations (sub-steps). The quasi time step for these inner iterations was calculated from a user-defined Courant number which was set to 50, other internal Courant numbers were experimented with but this was the best compromise between stability and computation time. The time-step for all simulations was 0.0005 s, which was chosen to satisfy both the Courant–Friedrichs–Lewy (CFL) condition for the mesh size chosen, and the Nyquist-Shannon sampling criterion for the motion of the propellers. Each simulation was run until it had converged, and the first particles injected into the simulation had left the domain. A sensitivity study was conducted to ensure the precision and reliability of the simulation results. This is presented in appendix 4.2.8.

The LPT component of the simulations used two models: a simple drag model to study the viscous and inertial forces exerted on the particles by the fluid, and a turbulent dispersion model to study the effects of turbulence. Models that effect the particle size distribution—for

TABLE 4.1: Details of the model setup for the CFD-LPT simulations.

Software	Star CCM+
Continuum Model	RANS
Turbulence Model	$k-\epsilon$
Solver	Implicit Unsteady
Time-step	0.0005 s
Wall Treatment	low-y+
Mesh Type	Hexahedral
Max. Mesh Aspect Ratio	1.2
Mesh Motion Treatment	Overset
Maximum Mesh Size	9 µm
particle Size Range	300 nm to 10 000 nm
Inlet Velocity	$5\,\mathrm{m\,s^{-1}}$

example droplet breakup and coagulation—are not studied in these simulations due to their complexity and lack of validation. Instead, the droplet Weber number, and fluid Reynolds number were calculated to ensure this did not happen (see Sect. 4.2.5.2). Particles in the simulation were 'sampled' when their trajectory during one time-step bisected a plane parallel with the x and y axes of the domain (parallel with the propeller plane shown in Fig. 4.5). These planes had z coordinates—relative to the propeller plane—between 0 m and 0.3 m with an equal spacing of 0.05 m, in addition to a control plane at the inlet to which the results were normalised. The planes were then split into five sampling regions, which were annular in shape with inner radii between 0 m and 0.25 m (and a maximum outer radius of 0.3 m). These regions are shown in Fig. 4.6. Using the area of these regions and the number of particles passing through them per second, mass flux was derived as a convenient parameter to relate to OPC measurements. Mass flux was chosen over mass concentration so as to separate the artefacts generated by distortions in the trajectory of the particles, from the artefacts generated by deriving mass concentration from the velocity of the SUA.

If solid atmospheric particles—for example aerosolized Saharan dust—were to be modeled, electrostatic forces from a charged airframe would need to be considered to both scavenge and deflect these particles. In principle CFD-LPT could be combined with electrostatic modelling to characterise particle trajectories. However, the electrostatic portion of the

model will be strongly dependant on the charge of an individual particle. This can significantly vary depending on aerosol type—and quantitative analysis of dust turbulent triboelectric charging, for example, is awaiting conclusions of ongoing research (Daskalopoulou et al., 2021). Also, the RCASS is mostly constructed from conductive materials, and all plastic parts were coated with RS components 514-486 conductive anti-static spray; the RCASS chassis and inlet are grounded with respect to the main flight battery. This was done in order to reduce electrostatic charging artefacts within the instrument itself.

The LPT simulations were run for a variety of particle sizes ranging from 300 nm to 10 000 nm (spaced quasi-logarithmically). This size range was chosen because it was predicted that smaller particles would be most affected by erroneous airflow, due to their lower inertia. The results of these simulations are presented in Sect. 4.2.5.2.

4.2.5.2 CFD-LPT Results and Discussion

The simulated mass flux through the annular regions on a series of planes described in Sect. 4.2.5.1 is shown in Fig. 4.8. The plot shows the variation of mass flux with the z co-ordinate of the plane the regions are coincident to (or the elevation above the propellers). The mass flux ratio is the ratio of the mass flux through a region at the top of the domain (therefore unaffected by the propellers) to the mass flux in the same region at a different elevation. The purpose of this simulation was to determine the best location on the airframe for the OPC instrument. Since the OPC directly measures mass flux, Fig. 4.8 visualizes the distortion in measurements due to the SUA propellers.

Figure 4.8 shows a consistently higher mass flux ratio for the annular region in the centre of the domain, meaning fewer particles are passing through this area. This is because the propellers create a pressure gradient in the continuous phase, and the resulting drag force on the particles pushes them out from the centre. While this drag force is lowest at the centre region (since it is furthest from the propellers), it still shows consistently lower mass flux than the outer regions because the pressure gradient is forcing particles outward towards the propellers and is essentially 'draining' the inner region. This is visualised in Fig. 4.9, which

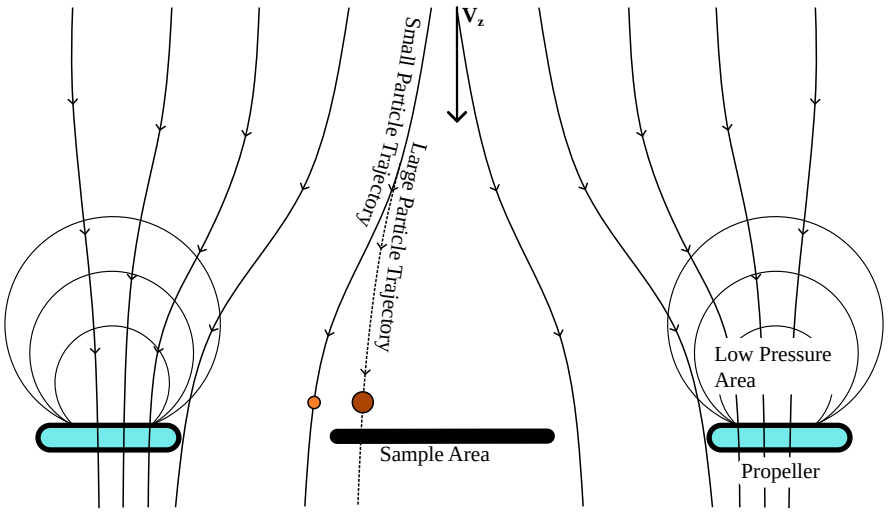

FIGURE 4.7: An illustration of the streamlines around the sample volume, the area of low pressure above the propellers, and the particle trajectories. The difference in particle trajectories between small and large particles has been exaggerated for clarity. The velocity used for the calculations of particle concentration is shown on the diagram as V_z.

shows the circumferential average of the radial velocity (implying a radial pressure gradient since the radial velocity should be zero if no other forces are acting on the continuum). An illustration of this effect is shown in Fig. 4.7, the velocity used for the calculations of particle concentration is shown on the diagram as V_z. Positive radial velocities in this figure mean airflow moving outwards from the centre towards the propellers, and positive radial velocities for all annular regions are shown with z coordinates lower than 0.3 m. Figure 4.9 also shows the angle of attack of the airflow with respect to the centre (z) axis of the domain. The purpose of this is to determine if the direction of the airflow is beyond the angle of attack limit of the UCASS sensor described in Smith et al. (2019) (10°). While the airflow angle of attack at all points on this graph was acceptable, a lower 'nominal' angle of attack will make the SUA more robust in crosswinds which will further alter this variable. Additionally, the acceleration of the airflow close to the propellers, and the high levels of turbulence in the continuous phase here mean the droplets are more likely to experience breakup effects. If a larger droplet was broken up into multiple smaller droplets—which were then sampled—the data products would show a shifted size distribution and a larger number concentration.

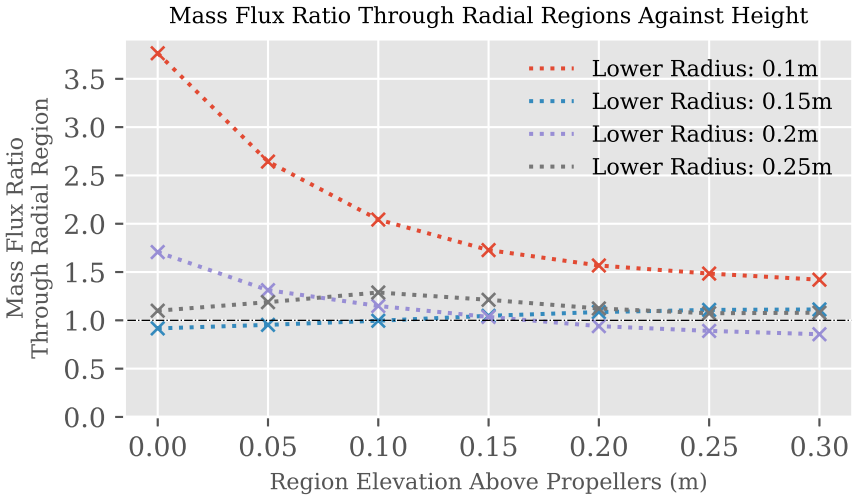

FIGURE 4.8: CFD-LPT results for the ratio of particle mass flux at the top of the domain to particle mass flux through planes with varying z coordinates. Each line represents the mass flux through an annular region with a lower radius described in the key. The size of particle for this simulation is 300 nm.

According to Reitz (1987), the breakup conditions are given by

$$We > 6 \tag{4.1}$$

and

$$We/Re^{0.5} > 0.5 \tag{4.2}$$

representing 'bag' and 'stripping' breakup respectively. The Weber number of the droplets and Reynolds number of the flow are given by

$$We = \frac{\rho_1 v_1^2 d_p}{\sigma_2} \tag{4.3}$$

and

$$Re = \frac{\rho_1 v_1 d_p}{\mu_1} \tag{4.4}$$

respectively. The subscript 1 denotes the continuous phase and 2 the discrete phase. We is

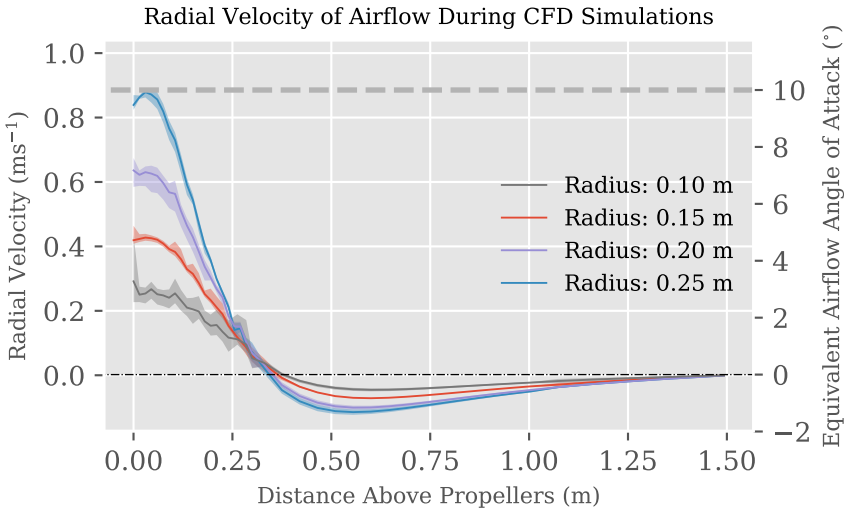

FIGURE 4.9: CFD results for the (circumferential averaged) radial velocity of the airflow as a function of distance above the propellers. The shaded regions around the lines show the variation of the air velocity around the circumference of the domain, while the bold lines show the mean. The dashed line represents the angle of attack limit specified in Smith et al. (2019).

Weber number, Re is Reynolds number, ρ is density, v is velocity, d_p is particle diameter, μ is dynamic viscosity, and σ is surface tension.

In both cases, the likelihood of the actual droplet sizes being altered is proportional to the square of the continuum velocity, which is likely to be higher closer to the propellers. Nevertheless, at all points in the analysed regions, neither the limit specified in Eq. 4.1 nor the limit in Eq. 4.2 were reached.

The induced change in continuous phase temperature changing particle size was considered during the simulation analysis. However, the maximum change in temperature throughout all points considered for sampling—including parts along the full trajectory of a droplet—was 0.012 K. Since the vertical extent of this temperature field above the propeller plane is 0.8 m, a droplet would be exposed to this temperature field for 0.16 s, which is certainly not enough of a perturbation to cause any significant change in droplet size.

Figure 4.10 is intended to demonstrate the effect the propellers have on the particle size distribution. It was hypothesised that droplets with higher sizes (and hence larger

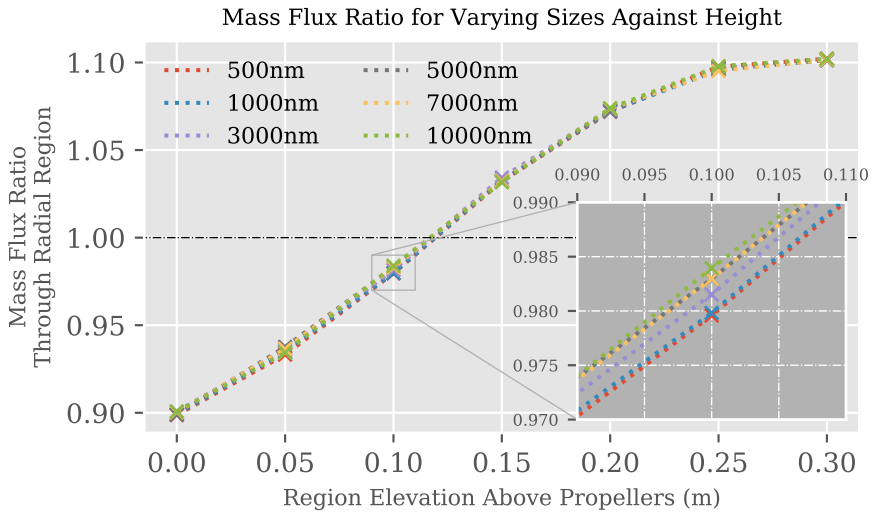

FIGURE 4.10: CFD-LPT results for the ratio of particle mass flux at the top of the domain to particle mass flux through planes with varying z coordinates. Each line represents the mass flux for a different size particle described in the key. The annular region for this plot has a lower radius of 0.15 m and an upper radius of 0.2 m

inertia) would be less effected by the propellers. While Fig. 4.10 shows this is true with the 10 000 nm size showing a mass flux ratio consistently closer to unity, the difference between the sizes is extremely small, with a mean standard deviation of 0.00097. This means that the propellers will have a small effect on the shape of the PSD when compared to its peak-height. Not only does this make it easier to apply correction factors to measurements, but atmospheric phenomena, which only require measurements of a normalized PSD (e.g. Zeng, 2018a), will be distorted by a negligible amount. Therefore, a correction factor to the particle size distribution is not required.

In contrast to most aerosol sampling methods, the smaller aerosols with less inertia are more problematic in this situation due to the airflow acting to pull particles away from the OPC. However, when a crosswind is introduced, the larger particles would become more problematic with their greater inertia causing them to impact against the walls of the RCASS. To reduce this artefact, the SUA can be allowed to drift with the wind when taking a vertical sampling profile with a crosswind. Smith et al. (2019) shows that the maximum angle of attack the UCASS can adapt to is 10°, therefore the SUA will be drifting with the wind

whenever a crosswind greater than approximately $1\,\mathrm{m\,s^{-1}}$ is expected, assuming an ascent rate of $5\,\mathrm{m\,s^{-1}}$. This, however, is not necessary for measurements of radiation fog since this phenomenon is typically associated with wind speeds less than $1\,\mathrm{m\,s^{-1}}$.

Figure 4.8 shows, for regional elevations greater than 0.15 m above the propellers, lower regional radii between 0.15 m and 0.25 m (corresponding to an annulus with a lower radius of 0.15 m and an upper radius of 0.3 m) are acceptable. However, Fig. 4.9 shows larger radial velocities closer to the propellers. While these radial velocities are within the acceptable range for the UCASS, the addition of a crosswind would add to the maximum radial velocity. Therefore, the RCASS was positioned on the SUA on an annulus with a lower radius of 0.15 m and an upper radius of 0.2 m, since this region exhibits the lowest average radial velocity.

4.2.6 Field Validation Experiment

4.2.6.1 Field Test Method

In order to evaluate the quality of the data collected by the UH-AeroSAM, a practical test was devised involving the comparison of SUA data with a calibrated in-situ cloud probe. While conventionally the validation of simulation data is achieved using a wind tunnel and measurements of a scalar quantity (for example pressure), the size of UH-AeroSAM makes it difficult to find an appropriate tunnel, accounting for a mandated blockage ratio and wall distance. Also, a spatially homogeneous particle stream with a known size distribution in the tunnel is difficult to achieve, and various environmental factors (for example turbulence) are hard to simulate in a tunnel.

Since RCASS is an OPC, and thus accurate sizing of particles relies on a known refractive index and assumes a spherical shape, the material chosen for the validation was water droplets in low level stratus (and fog). This minimised any uncertainty originating from an unknown particle refractive index; particles with unknown shape or non-homogeneous structures; or unknown artefacts resulting from surface roughness. Since both the RCASS and the reference instrumentation are OPCs, it may initially appear that these uncertainties

would apply equally to both. However, different optical designs will capture different parts of a particle's phase function (most OPC cloud probes, including the CAPS, use forward scattering), which will not vary proportionally to each-other with particle size.

The validation experiments were undertaken during the Pallas Cloud Experiment (PaCE) at the Pallas atmosphere-ecosystem super-site. This is located 170 km north of the Arctic Circle (67.973°N, 24.116°E), partly in the area of Pallas-Yllästunturi National Park (Lohila et al., 2015). A combination of a temporary restricted airspace (D527 - Pallas), a common occurrence of low level layered cloud (with a base of 300 to 500 m ASL, or 0 to 100 m above the SUA operations site), and the Sammaltunturi station made PaCE an ideal setting for the validation of UH-AeroSAM. For the duration of PaCE, a Cloud and Aerosol Precipitation Spectrometer (CAPS, Baumgardner et al. (2001)) from Droplet Measurement Technologies (DMT) was positioned at the Sammaltunturi station at the peak of a hill. The CAPS, by default, is a naturally-aspirated instrument which is unsuitable for static measurement, so a pump and inlet system was used to draw a sampling flow and turn it into an artificially-aspirated instrument. The inlet to the CAPS was oriented into the wind for the duration of all flights. Details of this, along with evaluation, can be found in Doulgeris et al. (2020).

Between the 20^{th} and 28^{th} of September 2019, 24 sampling flights where conducted. However, due to a predominantly northerly wind, the Sammaltunturi station was only in cloud on the 28^{th} when 4 flights were conducted, after which all flight batteries were depleted. The first flight was performed in 'high-gain' mode (measuring smaller sizes). However, following on-site analysis of the data, it was found that a large proportion of the data appeared in the largest size bin, indicating some particles were being undersized due to saturation of the detector. For this reason, the gain was reduced to 'low-gain' mode for the remaining three flights, increasing the lower threshold to 1 µm and the higher threshold to 40 µm. The wind speed and direction on the 28^{th} of September 2019 were 6 ms^{-1} and 240° respectively. The temperature at the station level on this date was 3.6 °C, so neither ice nor super-cooled water were expected.

In order to ensure quasi-Lagrangian measurements, the UH-AeroSAM was allowed to

drift with the wind for all flights. The profiles were, therefore, slanted towards the station due to the 240° wind. The SUA operations site was approximately 450 m away from Sammaltunturi station—meaning the SUA was approximately 350 m away when its altitude corresponded to that of the station. The RCASS data for comparison were within the altitude range of 545 to 585 m ASL, which corresponds to the station altitude ±20 m.

4.2.6.2 Field Test Results and Discussion

A comparison of normalised number concentration (dN/dlog(Dp)) can be used to assess the performance of a particle instrument, since it provides a size resolved counting efficiency, and some particle loss mechanisms tend to be size dependent. A comparative plot of normalised concentration for the SUA and CAPS is shown in Fig. 4.11. To reduce the significance of random artefacts, a 20 s arithmetic mean of the CAPS data, and a 40 m arithmetic mean of the RCASS data were taken, centred on coinciding times and altitudes. This averaging period was chosen to cover the same temporal extent. The error margin in concentration for these data is taken to be one standard deviation over the averaged range; this is represented in Fig. 4.11 by error bars.

As a general statement, Fig. 4.11 shows that the RCASS in both gain modes and CAPS agree remarkably well. As outlined in Sect. 4.2.2, one aim of this paper is to outline an operational envelope where the SUA-OPC observations can be considered reliable. Therefore the discrepancies that do exist must be, at the very least, explained. The metric used here to compare the two instruments is the re-binned dN/dlog(Dp), using the bin boundaries for the RCASS (since it has the lower resolution). This metric is indicative of both size and concentration discrepancies. Figure 4.13 shows the comparative plots for the re-binned data, the regression line, and the corresponding droplet diameter—using the geometric mean diameter of the bins—represented by the colour of the points. Reduced major axis regression (RMAR), as described in Harper (2016), was used since this technique correctly assumes that neither sampling method is perfect. Figure 4.13b is plotted on a log-log scale for clarity, leading to the appearance of a curved regression line. For Fig. 4.13b, sizes greater than 30 µm

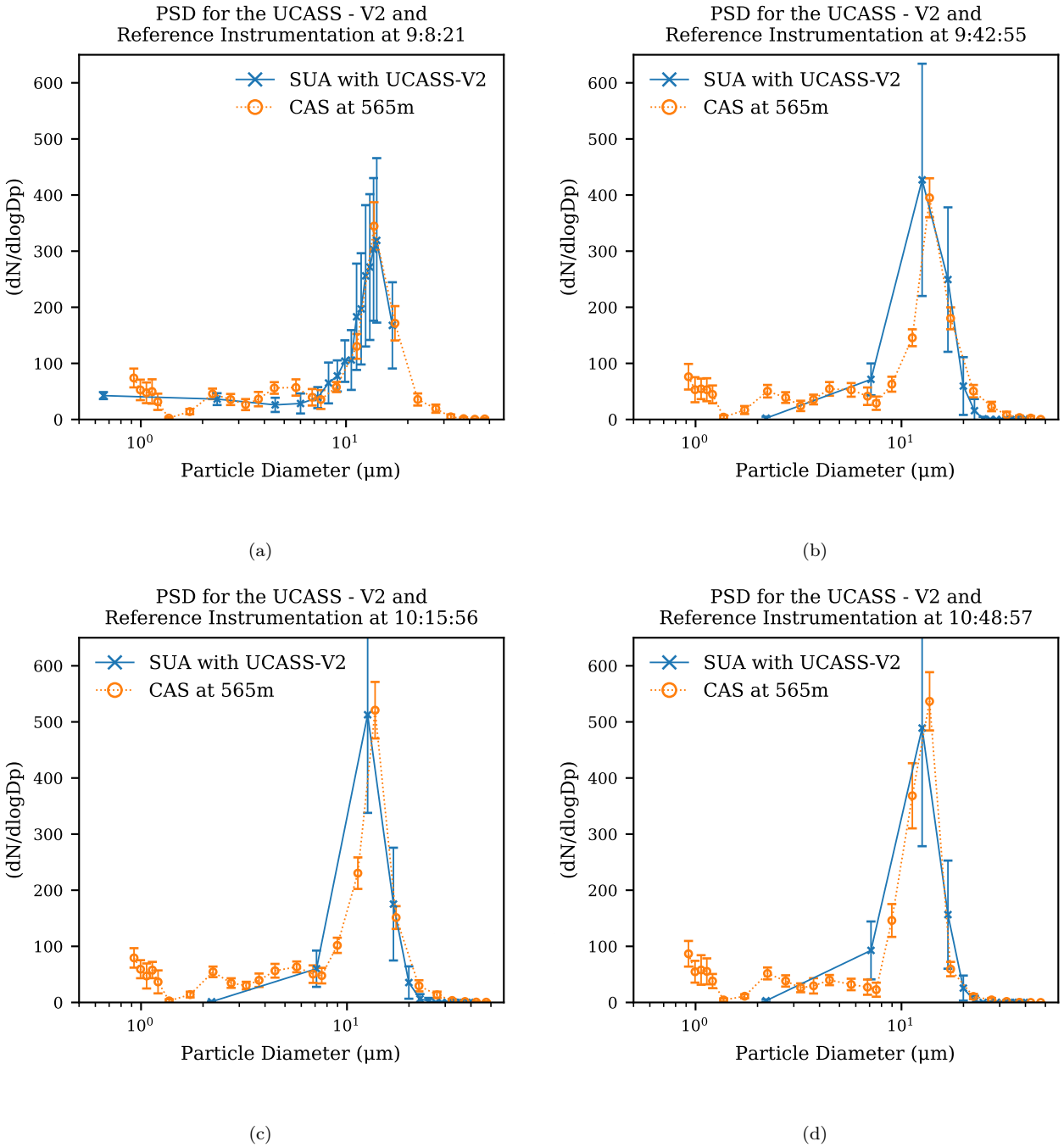

FIGURE 4.11: Number concentration plots for the SUA flights on the 28th of September 2019. The first flight in Fig. 4.11a was conducted in high gain mode where it was observed that the largest particle size was beyond the transimpedance amplifier saturation point. The remaining three flights, therefore, were conducted in low gain mode to ensure larger droplets were measured.

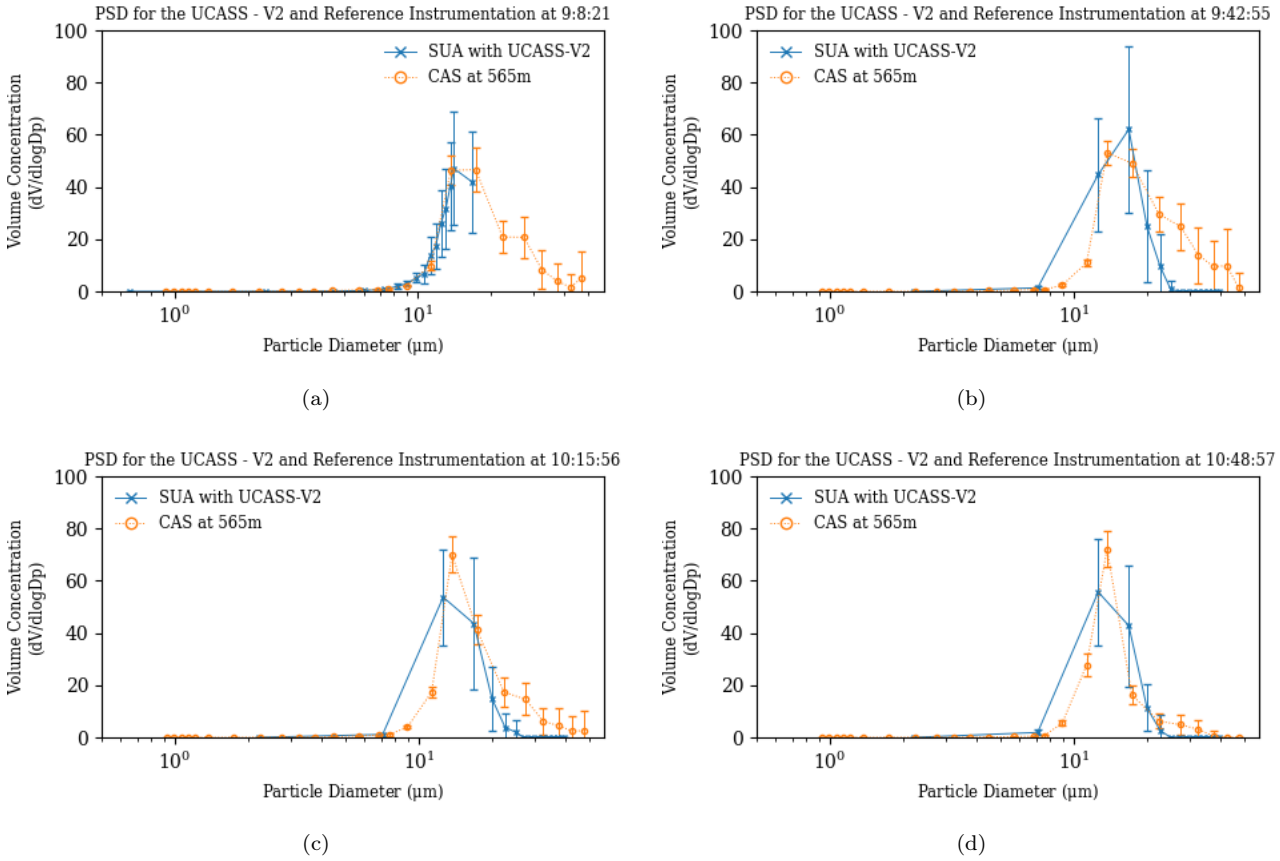

FIGURE 4.12: Volume concentration plots for the SUA flights on the 28th of September 2019. These plots were added as per the recomendations of the examiners and were therefore not included in the original paper.

were neglected because, in all cases, both the CAPS and RCASS recorded zero concentration, which would give falsely strong correlation.

Figure 4.11a shows the only data collected in high-gain mode. This mode showed the best agreement with the CAS, especially for sizes larger than 7 µm. Figure 4.13a shows a regression line gradient of 0.908 and a r^2 of 0.785 for the re-binned dN/dlog(Dp). However, these data show disagreement in two distinct places. The first is a dip in the CAPS data between 1 µm and 2 µm, which is undetected by RCASS. This is almost certainly due to the lower size-resolution in this region since it is impossible for the 2 bins (centred around 0.6 µm and 2 µm) to capture this feature. The second is a peak in the CAPS data around 5 µm; similarly the CAPS data coincident to the other three flights on this day also detected

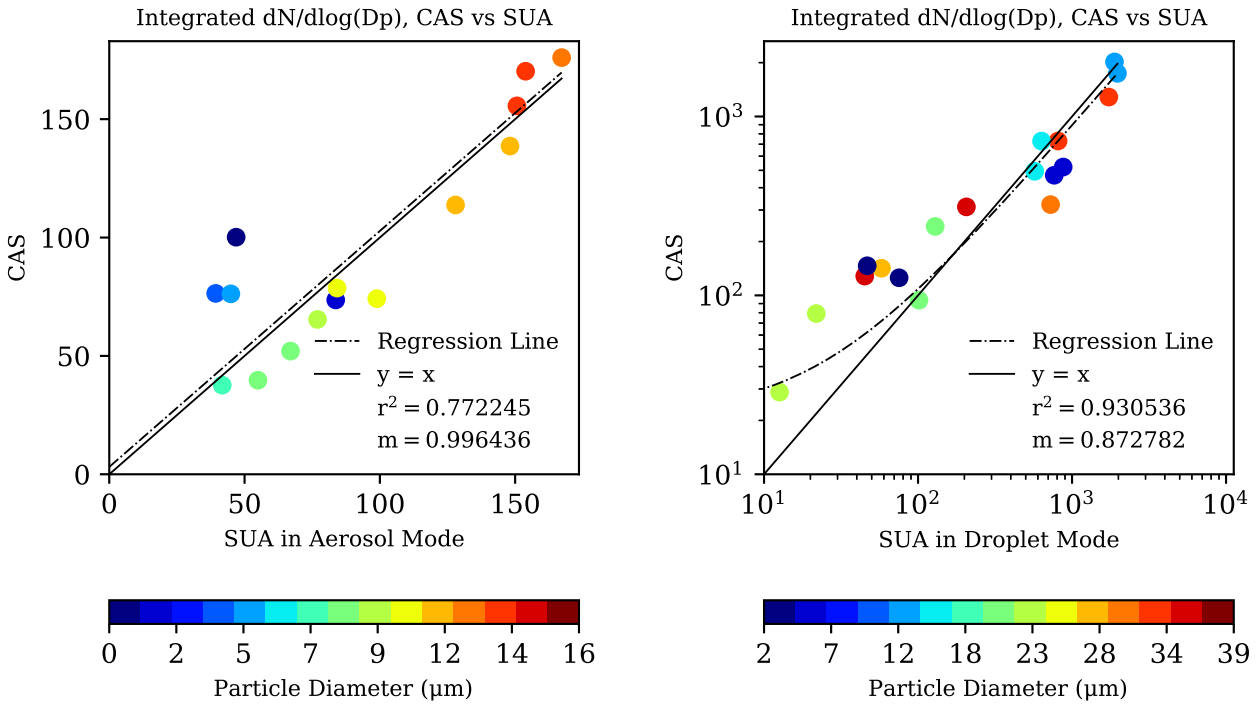

(a) (b)

FIGURE 4.13: 1:1 plots for the re-binned $dN/dlog(D_p)$. The solid line represents perfect agreement; the dotted line is the regression line using RMAR. r^2 is the coefficient of determination and m is the gradient of the regression line. In Fig. 4.13b, a log-log scale was used since most values were close to zero; the appearance of a curved regression line in Fig. 4.13b is simply due to the log-log scale. The colour of the points corresponds to the bin geometric mean diameter, which is shown on the colour-bar beneath the graph.

this peak. The RCASS has sufficient resolution to capture this peak only in high-gain mode, but the only flight in high-gain mode did not capture this peak. Within the CAPS user community, the legitimacy of this peak tends to be questioned since it is often not detected by any other instrument. Certainly this could be an artificial double peak due to the highly non-monotonic nature of the Mie curve for a forward scattering instrument; thus RCASS would not detect the peak with the more monotonic 60°-centred (with a half angle of 44°) scattering angle response curve (Smith et al., 2019). This could also be an artificial peak due to droplet shattering, although the small error margin compared to RCASS would indicate

otherwise. Since this is not the topic for this paper, and this peak does not significantly affect the plots in Fig. 4.11, this part of the graph is not discussed further here.

Figures 4.11b, 4.11c, and 4.11d show all the data collected in low-gain mode. This instrument mode has sufficient range to capture the entire major peak detected by the CAPS; and for the most part the two data sets agree well, although there are a few important points of discussion. The first is a lower resolution for smaller sizes, which causes the instrument to appear as though it disagrees. The worst case of this is presented in Fig. 4.11b. Since the high-gain mode agrees remarkably well with a higher resolution, and the only change between the two modes is a transimpedance amplifier gain, the issue can be resolved by adjusting the bin boundaries to give more resolution in this area during future measurements.

The second point is a concentration measured close to zero in the first bin. This is likely due to the instruments lower sensitivity to smaller sizes, characteristic of a typical OPC where the sample volume is defined optically. Since the useful data products that would be calculated from the RCASS low-gain mode, for example liquid water content (LWC), would mostly rely on larger sizes, this error is insignificant for the most part. Nevertheless, the authors note that one would need to consider this effect when using data from sizes approaching the spectral limits of any OPC. It was considered this effect could be due to smaller particles being pulled away from the propellers, as demonstrated in Sect. 4.2.5.2. However, this possibility was dismissed since the RCASS in high-gain mode did not suffer from this artefact, and this airflow effect would also affect all particle sizes equally.

The third, and most important, artefact is the drop off in the concentration commonly observed by RCASS for sizes greater than 25 µm, which are particularly prominent in Fig. 4.11b. This is of upmost importance for parameters which rely on particle volume (for example LWC), since larger particles contribute more significantly to the total particle volume of a distribution than smaller ones. The suspected reason for this was, while the SUA was allowed to drift with the wind, it is expected that a slip velocity exists between the airframe and the airflow. This slip velocity would get smaller in magnitude as the SUA ascends, assuming no wind shear. However, since the station is only 100 m above ground level, the slip

velocity would likely not have been smaller than the $1\,\mathrm{m\,s^{-1}}$ limit calculated in Sect. 4.2.5.2. This discrepancy is particularly visible in the volume concentraiton plots, as shown in Fig. 4.12, because larger particles contribute more to the overall volume of the suspended phase. In future measurements, to compensate for this effect, the SUA could be pre-programmed to fly to a GPS way-point, calculated so the horizontal speed of the airframe will match the wind speed. Flying upwards at faster speeds would also have the effect of increasing the aspiration efficiency of the instrument, although this might be detrimental to temperature and humidity measurements due to the slow response time of lightweight sensors introducing a lag in measurement. On the other hand, since this [size drop-off] discrepancy is mostly minute in these data, it could also easily be a co-location error. Larger droplets tend to accumulate near surface level in fog (as would be expected due to gravitational settling), which would explain the larger sizes measured by any instruments at the station. However, a more extensive data set would be needed to confirm this. Despite the minor artefacts, these data were remarkably accurate and precise, given the low instrument and platform cost.

4.2.7 Conclusions

In this paper, a novel design and validation technique for sampling aerosols on a multirotor SUA was presented. This research involved development and production of a bespoke SUA instrumeted platform (UH-AeroSAM). The developmental work using both modelling and lab results found that placement of the particle instrument had a significant influence on the particle flux travelling through its sample volume. Along with the airframe, a bespoke OPC (RCASS) was developed with a naturally aspirated inlet, specifically for use on SUA. This OPC was based on the single-use UCASS (Smith et al., 2019), and incorporated several improvements to the sample airflow, electrical design, and mechanical robustness. The SUA is intended to fly vertically with the OPC inlet pointed upwards, to achieve a vertical profile of atmospheric aerosol or droplets. RCASS can function in two gain modes: High-gain to

measure smaller sizes with high resolution; and low-gain to measure larger sizes with lower resolution.

The primary tool used in the design process was computational fluid dynamics with Lagrangian particle tracking (CFD-LPT), this revealed the physical processes affecting the flow of particles through the system. When the airflow is axial with respect to the SUA, the propellers create a lower pressure above the propellers and draw particles towards them. This was shown to effect all sizes measured by the RCASS equally. The CFD-LPT simulations revealed a significantly changing particle flux across the airframe due to the propellers, these simulations influenced the positioning of the particle counter on the airframe. An adequately compromised position was found using this method, and the SUA was constructed according to these specifications.

UH-AeroSAM was evaluated in a realistic, field-campaign setting using the cloud and aerosol precipitation spectrometer from Droplet Measurement Technologies as a reference. Across the whole measurement range, the two instruments showed excellent agreement in both RCASS gain modes.

This research delivers hitherto the next step in regular, reliable, and accurate SUA based measurements of particulate and droplet spectra. This is a quantity regularly desired in many fields of atmospheric research, but notoriously difficult to measure on SUA due to the large number of uncharacterised artefacts. However, with the measurement technique presented in this paper, the UH-AeroSAM is capable of accurately measuring the vertically-resolved droplet spectra of fog and low level clouds. This could also be extended to measure particulate matter (PM) concentration, and low level dust loading.

Future research will include adapting the RCASS for fixed wing platforms and characterising the artefacts encountered. While multirotor SUA have better spatio-temporal sampling capabilities, a fixed-wing SUA with a similar maximum take-off mass (MTOM) would have a larger payload mass and a longer endurance. Therefore, it is necessary to explore both applications for different uses.

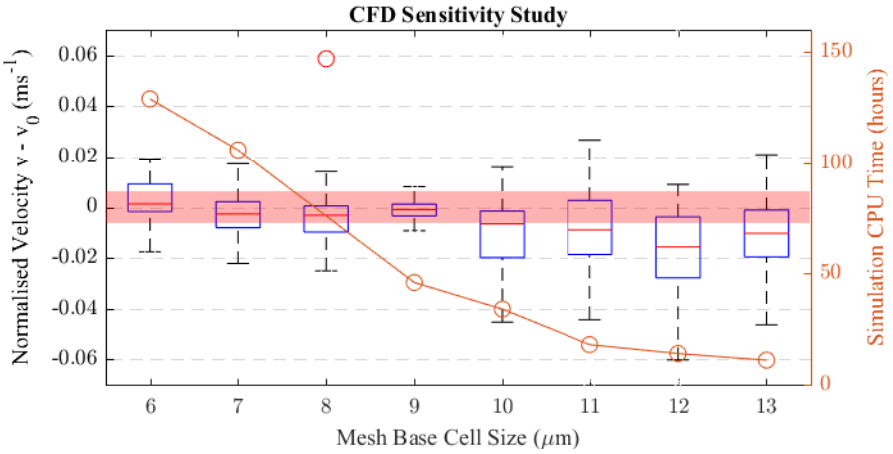

FIGURE 4.14: A box and whisker plot representation of the CFD sensitivity study results. The whiskers represent the range of the data, the boxes represent the inter-quartile range, and the lines represent the mean. On the left vertical axis is the velocity magnitude normalised to the co-located point in the simulation with the finest mesh size (5 µm). The horizontal is the base mesh size. The right vertical axis is the simulation CPU time in hours. The shaded red region represents the valid region for the mean normalised velocity magnitude.

4.2.8 Appendix A: CFD Sensitivity Study

To ensure the precision and reliability of simulation results, a mesh sensitivity study was conducted. The CFD domain described in Sect. 4.2.5.1 was used without the LPT models, since these are not affected by the mesh. The mesh size was varied between 5 µm and 13 µm, and run for the minimum convergence time, which was found during trials to be 30 time-steps. All simulations were run on the University of Hertfordshire High-Power Cluster (UHHPC) on 64 processors in parallel.

The quantity chosen here to compare the different mesh sizes was the velocity magnitude—spatially averaged across the circumference of circles (concentric with the domain cylinder) with varying radii, and distance above the propellers. The chosen radii (r) were 0.1, 0.2, and 0.3 m, on a plane parallel with the propellers. The distance (z) above the propellers was varied up to the top of the domain in intervals of 0.05 m. This positioning was chosen because it is the region of interest for the real simulations. This quantity ($\mid v \mid_{avg,i}$) was

normalized to the co-located $\mid v \mid_{avg,0}$ in the simulation with the finest mesh size—5 µm—to obtain velocity deviation ($\mid v \mid_{avg,i} - \mid v \mid_{avg,0}$). The subscript 0 denotes the simulation with the finest mesh size, and i the simulation with mesh size 'i'. The purpose of the spatial (circumferential) average was to avoid differences in velocity magnitude between time steps due to the position of the propellers, which would exist naturally and give misleading results. The spacing of the circles give 93 values of $\mid v \mid_{avg,i} - \mid v \mid_{avg,0}$ per simulation. These data, along with CPU time for each simulation, are presented in Fig. 4.14. The CPU time for the simulation with an 8 µm mesh—the red circle in Fig. 4.14—was dismissed as anomalous due to high UHHPC usage at the time this simulation was conducted

To determine which simulation to use, a limit for the mean velocity deviation had to be established. Here, this limit was defined as the velocity which produces a dynamic pressure capable of moving a particle across $\frac{1}{10}$ of a sampling region (0.01 m), when applied constantly from the inlet to the propeller plane (for 0.3 s when travelling 1.5 m at 5 m s^{-1}). This problem can be reduced to one dimension if the pressure is applied constantly as the particle travels in the vertical direction. Therefore the particle must not travel 0.01 m in 0.3 s laterally. The largest mean velocity deviation calculated for a simulation was $\pm 0.0063\,\mathrm{m\,s^{-1}}$, using Newtonian equations of motion and assuming Stokes flow. This limit is shown in Fig. 4.14 as a red shaded valid region.

The coarsest mesh that lies within this limit had a base size of 9 µm, and was therefore used for the main CFD-LPT simulations.

4.2.9 Appendix B: Stray Light Test on the RCASS

As an analog to the sun, a 12 V halogen bulb with a parabolic directional reflector was used as the stray light source due to its similar spectrum. From previous tests on both the UCASS and RCASS, it was found that stray light had a largest effect with an unobstructed path to the detector. Therefore the RCASS was rigidly mounted with a halogen bulb pointing directly at the detector, corresponding to a solar zenith angle of 25° when mounted in the

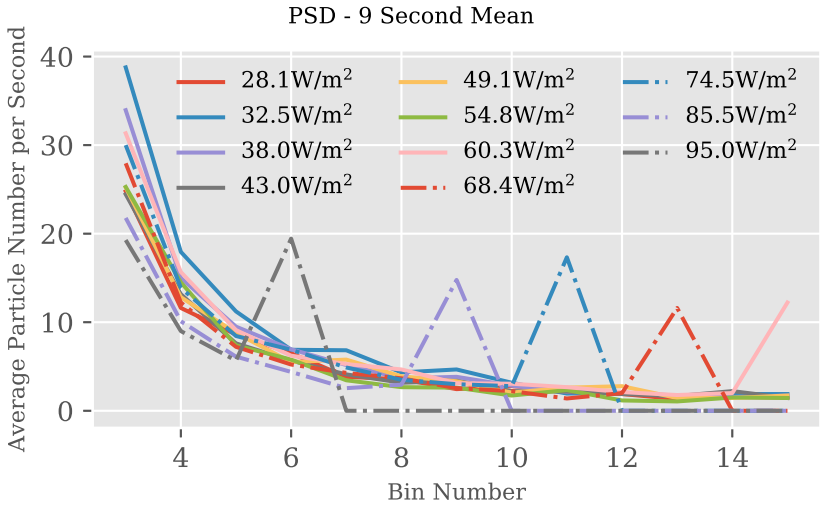

FIGURE 4.15: The results from the RCASS stray light test. Each line on this graph represents a different irradiance from the halogen bulb used as an analog to the sun. Irradiances larger than this were found to completely saturate the photodiode and cause no counts to be registered.

SUA. To measure the equivalent solar power, a laser power meter (calibrated to 500 nm, in the middle of the solar spectrum) was used to measure the radiant flux of the halogen light. This was done to make the measurements comparable to true solar irradiance, in order to define a suitable operating envelope for sampling with the SUA. From initial testing, it was found that the RCASS was unaffected by stray light resulting from a halogen bulb voltage of less then 3.1 V, and completely saturated by bulb voltages more than 4 V. The voltage was therefore varied between 3 V and 4 V in steps of 0.1 V, and the irradiance was measured at each data point.

For this experiment, polydisperse water droplets were used as the measurand because of their quasi-spherical shape—so they can be modelled using Mie theory—and ease of generation. A compressed air droplet generator was rigidly mounted for consistency between experiments. A fan was positioned behind the droplet source, causing a 1.8 $\mathrm{m\,s^{-1}}$ airflow through the RCASS. For each iteration of the experiment, the water droplets were sprayed into the instrument for 9 s. The bin boundaries for the test are spaced logarithmically between 0 and 4095 (for the 12-bit ADC).

Figure 4.15 shows the results from the stray light test. The vertical axis represents the particle counts per second averaged over the 9 s period the droplets were being sprayed, and the horizontal axis is the bin number of the OPC. The different lines on the plot represent the changing solar-equivalent irradiance. This plot clearly demonstrates the saturation of the photodiode for irradiances larger than $60\,\mathrm{W\,m^{-2}}$. For example, with the halogen bulb at $95\,\mathrm{W\,m^{-2}}$, there is a peak at bin 6, followed by no counts at all for the higher bins. This is because, for the DC signal at $95\,\mathrm{W\,m^{-2}}$, the largest peak possible is 'binned' at a 12-bit ADC value corresponding to bin 6 (578 in this case), and all other particles which would normally—with no stray light—generate larger peaks, are 'binned' here.

Although the effective zenith angular range is small, it was decided post-test that the inlet should be extended so no direct path was available for stray light to reach the detector. This test also revealed that the plastic used for some of the bodywork transmitted infra-red radiation, to which the RCASS detector is highly sensitive, so gold foil was used to surround the inlet exterior and reflect infra-red.

5 | Fixed-Wing Adaptation

5.1 Summary and Context

The following paper: 'Simulation and Field Campaign Evaluation of an Optical Particle Counter on a Fixed-Wing UAV' (published version: Girdwood et al., 2022) was submitted to the 'Atmospheric Measurement Techniques' journal in October 2021, and accepted for publication in March 2022. This publication was the second milestone in this project; on the topic of the adaptation of UCASS to a fixed-wing airframe, and the technical and scientific challenges faced. As with the paper presented in Chapter 4, CFD-LPT techniques were utilised as a tool for designing the OPC – UAV combination, and constraining the operational envelope. Novel data analysis techniques were developed and used for data quality assurance. The manuscript presented here has been edited for typesetting in this thesis.

5.2 Simulation and Field Campaign Evaluation of an Optical Particle Counter on a Fixed-Wing UAV

J. Girdwood[1], W. Stanley[1], C. Stopford[1], D. Brus[2].

1 Centre for Atmospheric and Climate Physics, School of Physics, Astronomy and Mathematics, University of Hertfordshire, Hatfield, Hertfordshire, AL10 9AB

2 Finnish Meteorological Institute, PO Box 503, FI-00101, Helsinki, Finland

5.2.1 Abstract

Unmanned aerial vehicles (UAVs) have great potential to be utilised as an airborne platform for measurement of atmospheric particulates and droplets. In particular, the spatio-temporal resolution of UAV measurements could be of use for the characterisation of aerosol, cloud, and radiation (ACR) interactions, which contribute to the largest uncertainty in the radiative forcing of climate change throughout the industrial era (Zelinka et al., 2014). UAV-instrument combinations must be extensively validated to ensure the data are repeatable and accurate. This paper presents an evaluation of a particular UAV-instrument combination: the FMI-Talon fixed-wing UAV and the UCASS open-path optical particle counter. The performance of the UCASS was previously evaluated on a multi-rotor airframe by Girdwood et al. (2020). However, fixed-wing measurements present certain advantages—namely endurance, platform stability, and maximum altitude. Airflow simulations were utilised to define limiting parameters on UAV sampling—that is, an angle of attack limit of 10° and a minimum airspeed of $20\,\mathrm{m\,s^{-1}}$—which were then applied retroactively to field campaign data as rejection criteria. The field campaign involved an inter-comparison with reference instrumentation mounted on a research station, which the UAV flew past. Cloud droplets were considered the ideal validation particle, since the underlying Mie assumptions used to compute droplet radius were more valid, future work will focus on the instrument response to aerosol particles. The effective diameter measured by the UAV largely agreed within 2 µm.

The droplet number concentration agreed within 15% on all but 5 profiles. It was concluded that UCASS would benefit from a mechanical redesign to avoid calibration drifts, and UAV attitude variations during measurement should be kept to a minimum.

5.2.2 Introduction

Paradoxically, while clouds and aerosols are some of the most studied atmospheric phenomena, their microphysical properties—and overall effect on the earth—are still not completely understood. The Intergovernmental Panel on Climate Change (IPCC)—an important avenue for scientific communication to policy-makers—has, in its fifth assessment report, cited both aerosol radiative forcing and the cloud feedback mechanism as a major uncertainties in climate prediction (IPCC, 2013). These uncertainties are magnified further when we consider that the evolution and optical properties of a cloud depend on the chemistry, morphology, and concentration of the cloud condensation nuclei (CCN)—thus coupling the aerosol and cloud feedback uncertainties. In addition, precipitation initiation involves multiple mechanisms which lack adequate explanation—particularly in warm clouds (Beard and Ochs, 1993, Laird et al., 2000, Small and Chuang, 2008), but also in mixed-phase and ice clouds.

Since cloud microphysical evolution through to precipitation depends strongly on both upwelling and downwelling radiative fluxes, aerosol, cloud, and radiation (ACR) effects are coupled. This would therefore also influence the precipitation initiation through radiation effects discussed recently by Zeng (2018a). The contributions to climate change by these ACR interactions are discussed by Zelinka et al. (2014), where it is stated that they contribute the largest uncertainty in the radiative forcing of climate change throughout the industrial era. Zelinka et al. (2014) also states that models which include aerosols in ice clouds tend to contain large radiative anomalies. Since clouds can be heterogeneous on all length scales down to 1 cm, and time scales in order of seconds (Blyth, 1993), observations with high spatio-temporal resolution need to be performed to characterise ACR interactions. Several previous studies have attempted to characterise the sign and magnitude of the ACR contribution to

the overall radiative forcing effect (for example Douglas and L'Ecuyer, 2019). However, these studies rely on remote sensing and modelled data, which results in large uncertainties. A mechanism for high-resolution, in-situ observations of cloud microphysics can reduce these uncertainties.

Conventionally, in-situ measurements of clouds are conducted using large manned aircraft. These remain the most well characterised and proven platforms for airborne atmospheric measurement, bolstered by large-scale studies into reliability and potential artefacts (Korolev et al., 2013a,b, Spanu et al., 2019). However, large maintenance and running costs for such platforms make the use of manned aircraft only feasible for a limited number of large-scale campaigns. In addition, most aviation governing bodies do not allow manned aircraft to fly below a certain altitude; the UK Civil Aviation Authority (CAA), for example, define the lower altitude limit as 500 ft (150 m)—making a large amount of atmospheric aerosol, and low level cloud, legislatively impossible to measure this way.

The problem is not only one of measurement quality, but of measurement quantity. Manned aircraft, and remote sensing techniques, are facets in a larger solution, necessitating—in addition to this—a method for the repeatable, accurate sampling of cloud droplets and aerosol in the lower portion of the atmosphere. The current lack of such a method is one of the reasons for the uncertainty in the radiative forcing of climate change, since this region in particular plays host to many clouds, and much of the total atmospheric aerosol mass.

Unmanned aerial vehicles (UAVs) have gained recent popularity as an atmospheric measurement platform. Generally, these boast distinct advantages over conventional measurement platforms, since they are low-cost, lightweight, and highly manoeuvrable—providing exceptional spatio-temporal sampling capabilities. However, largely due to the infancy of the UAV as a measurement platform, and the lack of instrumentation specifically designed for UAVs, these require extensive validation in order to ensure observations are accurate and reliable. Girdwood et al. (2020) shows the design and validation of the combination of a multi-rotor UAV and custom-built optical particle counter (OPC): an instrument class commonly used to study cloud and aerosol microphysics. This study used an adaptation

of the Universal Cloud and Aerosol Sounding System (UCASS, Smith et al., 2019). Originally designed for use on meteorological balloons as part of a sounding system, the UCASS utilises a novel naturally aspirated flow transportation mechanism which allows the negation of most aerodynamic artefacts resulting from UAV airframes, for example anisokinetic flow. The UCASS-UAV combination, therefore, is a good starting point for the characterisation of cloud evolution and ACR interactions.

Fixed-wing UAVs have several advantages over multi-rotors which render them more suitable in certain applications. For example, fixed-wings have greater flight stability, have a longer endurance and range, can reach higher altitudes, benefit from less serious consequences of icing, and induce a less complex airflow with a lower turbulent kinetic energy. These features make fixed-wings more suited for measurements where larger altitudes are desired, and in locations with access to a runway, or a suitable analogue. Therefore, this study will focus on the evaluation of UCASS on a fixed-wing platform, and assess any resulting artefacts.

5.2.3 Description of UCASS and UAV

5.2.3.1 UCASS, Data, and Limitations

Figure 5.1 is a cross-section view of UCASS, and an illustration of its working principle. As a particle travels through the UCASS unit, it has a chance of passing through the sample area. This area is optically defined by the depth of field (DoF) and field of view (FoV) of the dual-element photodiode detector, which is labeled on Fig. 5.1. When a particle or droplet passes through this region, it is illuminated by a 650 nm laser—highlighted red in Fig. 5.1—which causes light to be scattered onto an elliptical mirror. The elliptical mirror is positioned with a lens angle of 60° and has a half angle of 45°. This range of scattering angles was selected as a compromise between monotonicity of the instrument response with respect to particle optical diameter—where 90° scattering is preferable—and refractive index dependency—where forward scattering is preferable. The first focal point of the mirror is

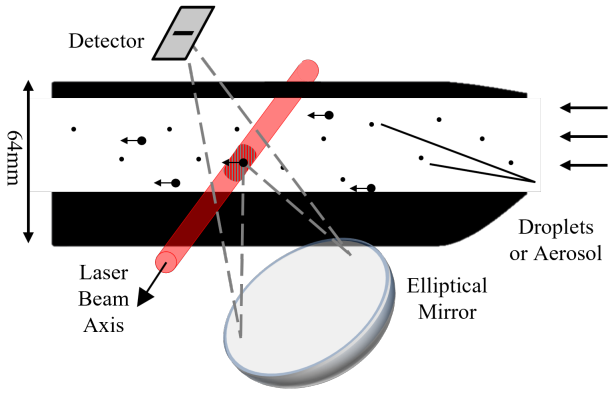

FIGURE 5.1: An illustration of the UCASS working principle: scattered light at the first focal point of the elliptical mirror is reflected onto its second. The magnitude of this light is proportional to the size of the particle causing the scattering.

located at the centre of the sample volume, while the second is located at the centre of the photodiode, thus meaning light scattered by the particle is focused on the detector. The current produced by the detector is proportional to the size of the particle or droplet. Further technical detail of the UCASS can be found in Smith et al. (2019).

A concentration can be derived from UCASS data using one of two methods: particle time of flight (ToF) through the UCASS laser beam—the width of which is fixed and known, and the velocity of the UCASS itself—normally measured using a pitot tube. The former has the advantage of being the most direct measurement of sample area velocity, while the latter has the advantage of reliability and independence from particle size. The dependence of ToF on particle size originates from the method by which the UCASS electronics calculates it—that is, the time between a pulse rising and falling above and below a threshold amplitude. Since the pulses can be assumed to be roughly Gaussian, two pulses with different maximum amplitudes through the same laser beam thickness would rise and fall above and below any threshold at different times. This difference is greater with threshold voltage height, and since the threshold must be above normal noise levels the variation is significant with increased particle size. Figure 5.2 shows an illustration of this effect. The concentration derivation methods used are discussed further in Sect. 5.2.4 and Sect. 5.2.5.

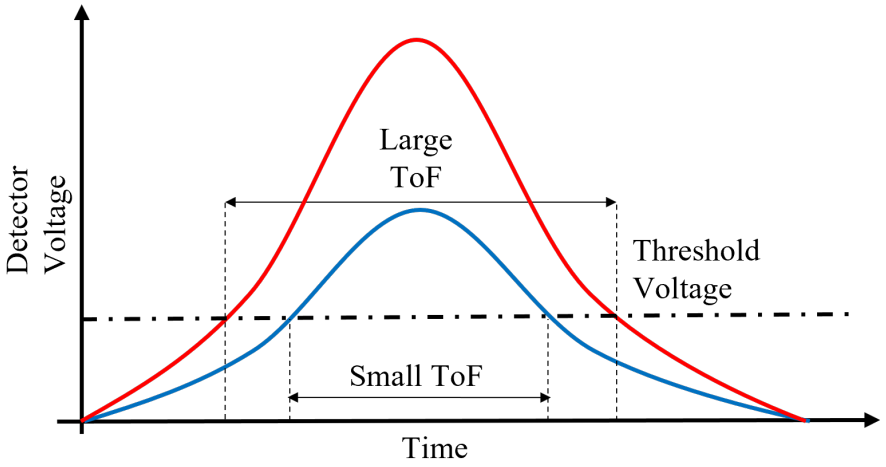

FIGURE 5.2: An illustration of the ToF dependence on particle size for UCASS measurements. The red and blue lines represent large and small particles respectively for the same laser beam thickness.

The data from UCASS are available through its serial peripheral interface (SPI). Each data-point consists of the following for a given time interval: the particle counts in each of the 16 size bins; the mean particle ToF for bins numbered 1, 3, 5, and 7; the sampling period—the amount of time UCASS records particles for a datum; and some debugging information. The debugging information includes: The amount of particles with an extremely short or long ToF, which is used to filter out noise; the cumulative sum of all the particles counted, which is used to verify the data has been logged properly; and the amount of particles which have been rejected due to being outside of the sample volume, which is used to determine if co-incidence is likely.

The three main limitations of the UCASS – fixed-wing UAV combination are airspeed, angle of attack (AoA), and endurance. Airspeed is a limitation due to the bandwidth of the transimpedance amplifier (TIA) which converts the current from the photodiode into a scaled voltage. The cut-off frequency of the TIA is approximately 417 kHz, meaning a the maximum pulse width of the signal produced by a particle scattering light onto the photodiode is 2.4 µs. Since the thickness of the laser beam at the sample area is 60 µm, a maximum airspeed of 25 $\mathrm{m\,s^{-1}}$ was allowed in these experiments. Smith et al. (2019) showed

that the particle number concentration measured by UCASS deviated from that measured by reference instrumentation when the airspeed increased above $15\,\mathrm{m\,s^{-1}}$. This was likely due to the drop off in amplification by the TIA as the frequency approached the cut-off. For this reason, the ideal airspeed for these experiments was treated as $15\,\mathrm{m\,s^{-1}}$, however this was not always possible due to environmental and engineering factors, which are discussed in later sections.

The AoA—that is, the angle between the UCASS axis and inlet airflow vector—limit for the UCASS unit was defined in Smith et al. (2019) to be $\pm 10°$. However, this assessment was only conducted for the UCASS alone, while not mounted on a platform. Therefore, this limit needed to be re-assessed for these experiments, the details of which are discussed in Sect. 5.2.4.

Water coating the light collection optics is an important factor to consider, not only with the UCASS instrument, but with all cloud probes. Both condensation and direct liquid deposition can attenuate the collected light, thus reducing the observed scattering cross section magnitude. Since the temperature change between the sampling volume and ambient air was 0.04 K—see Sect. 5.2.4 for details—the condensation risk here was negligible, although it was considered that, at faster airspeeds, hydrophobic coatings may have been required on the collecting optics. Direct liquid deposition of water droplets onto the elliptical mirror—the largest exposed optical surface, and principal scattered light collector—was a greater concern. The UCASS elliptical mirror was designed with a surrounding circular groove in the chassis, in order to prevent the droplets—which get deposited on the inner airflow surfaces near the inlet—flowing onto the optical surfaces. The UCASS was tested with this inner chassis configuration in Smith et al. (2019) where it was found that droplet deposition on the optical surfaces was limited.

Since UCASS was originally designed as a single-use instrument (commonly utilised with balloon-based sounding systems, for example Kezoudi et al., 2021b), the endurance must be questioned when operating a UCASS unit consistently throughout a research campaign. Specifically related to fixed-wing UAV operation, stresses from landings are likely to have

the largest impact. Girdwood et al. (2020) introduces a ruggedised re-design of UCASS for multi-rotor UAVs. However, the stresses exerted on the instrument by a multi-rotor design are much higher than those exerted by a fixed-wing. Also, this design could not be directly translated onto a fixed-wing due to its size, since—unlike in the original UCASS—the laser and optics carrier protruded perpendicular to the chassis. For those reasons, the original design was chosen for fixed-wing use, but the endurance throughout the campaign was assessed and is presented in Sect. 5.2.5.

5.2.3.2 UAV and Mounting

The UAV chosen for the evaluation of the nose-mounted configuration was the Talon UAV (X-UAV, Tian-Jie-Li Model Co., Ltd., China). The Talon platform was equipped for atmospheric measurements by the Finnish Meteorological Institute (FMI), with consultation from the University of Hertfordshire (UH) regarding the mounting of UCASS. This platform was chosen primarily for its flat-top and wide fuselage, which provided an adequate mounting surface for the UCASS. An image of the UCASS mounted on the FMI-Talon is shown in Fig. 5.7b. The wide fuselage also provided enough space to mount the avionics, which included: a Pixhawk 1.2 flight controller (3DRobotics, 2013) with a global positioning system (GPS) and magnetometer; a Raspberry Pi Zero (RaspberryPi-Foundation, 2015) for the logging of UCASS data; a BME280 temperature, pressure, and humidity sensor; and a pitot-static tube to record the airspeed data essential for UCASS concentration measurements. The temperature and humidity measurements are not evaluated in this paper since they do not relate to the performance of UCASS, but are mentioned for the purpose of transparency, since they are often accompanying variables in datasets. The capabilities of the FMI-Talon are summarised in Table 5.1. The UCASS unit was mounted on the nose cone, with its inlet protruding well out of the fuselage boundary layer. This was influenced by the CFD-LPT experiments presented in Sect. 5.2.4.

In order to eliminate airframe-induced aerodynamic artefacts, the UCASS unit was positioned on mounts above the nose-cone. The UAV brushless electric motor was rear-facing and positioned at the back of the aircraft behind the tail, therefore no aerodynamic artefacts resulting from the propeller wash were expected. In addition to this, the position of the motor means that no artefacts due to the charging—and subsequent deflection—of aerosols by its oscillating magnetic field are expected. The expected influence of the airframe aerodynamics on measurements, and the exact positioning of UCASS, is discussed in Sect. 5.2.4.

5.2.4 Computational Fluid Dynamics with Lagrangian Particle Tracking

5.2.4.1 CFD-LPT Method

The aim of these simulations—as with Girdwood et al. (2020)—was to define a series of UAV operating conditions, with particular focus on airspeed and AoA, in which UCASS would be able to make representative measurements, with reasonable tolerance.

The presented simulations were conducted using the Star-CCM+ commercial code. Two main mounting configurations were considered for the simulations: a configuration whereby the UCASS was positioned as far forward as the centre of gravity (CoG) tolerance of the FMI-Talon allowed, and a configuration were the UCASS was positioned further back from the end of the nose cone. Hereafter, these will be referred to as the fore and aft configurations

Table 5.1: Technical specification for the FMI-Talon UAV.

Airframe	Talon
Flight Controller	Pixhawk 2.1
Wing Area	0.6 m^2
Wingspan	1718 mm
Length	1100 mm
Maximum Take-off Mass	3 kg
Aircraft Mass Used Here	2.7 kg

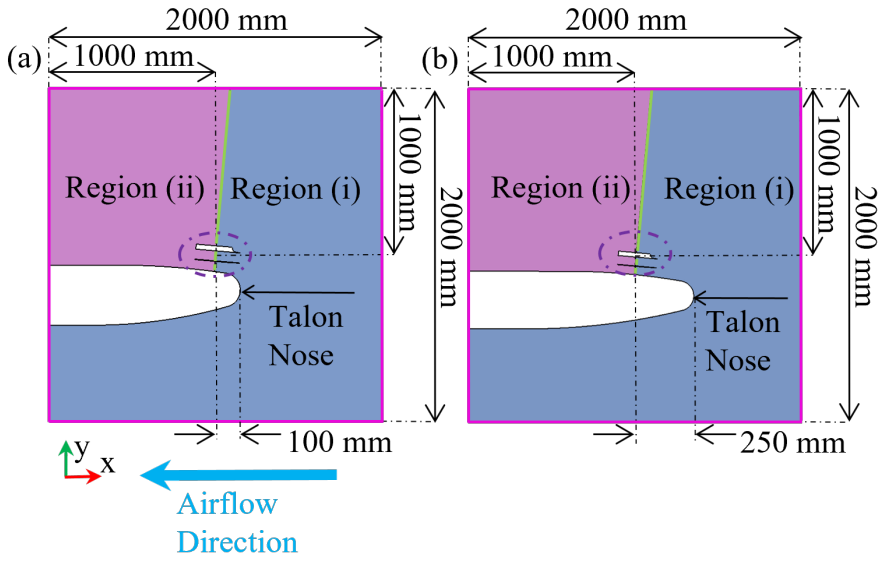

FIGURE 5.3: Illustrations of the CFD-LPT domains for the two investigated configurations. Figure 5.3a shows the fore configuration and Fig. 5.3b the aft. The airflow direction and geometrical axes shown in 5.3a are consistent throughout. The UCASS is shown in the purple dashed circle, and the FMI-Talon nose cone is indicated. The purple lines represent free-stream boundaries, and the green line represents the divide between regions (i) and (ii)—which is where the LPT droplets are sampled.

respectively. The former was expected to be advantageous only if the UCASS could be positioned far enough forwards to escape aerodynamic influence from the nose cone. The latter was expected to suffer from aerodynamic artefacts resulting from a non-zero AoA—that is, the angle between the axis of UCASS and the airflow velocity vector.

The domains for the fore and aft configurations are shown in Fig. 5.3a and Fig. 5.3b respectively. The fore configuration shows the UCASS positioned as far forward as the CoG tolerance allowed. The domain was a two-dimensional slice through the FMI-Talon, bisecting the centre of UCASS and the UAV nose—indicated with the purple dashed circle and the black arrow in Fig. 5.3 respectively. The domain was a 2 m by 2 m square, which was found by trial and improvement to suffer from no artefacts due to pressure wave reflections at the desired airspeed. The main point of interest for the simulations was the UCASS sample area, which was made the centre-point of both domains. In both domains, the air flowed

in the direction of the blue arrow shown in Fig. 5.3a, and LPT droplets were injected from the right hand wall. Since droplets are sampled when they cross a boundary, a boundary line was set up in the domain between regions (i) and (ii)—marked with the green line in Fig. 5.3—which crossed the UCASS sampled volume. The pink lines around the perimeter of both domains represent 'free-stream' regions which are treated as infinitely extending regions with constant temperature and pressure—defined here as 280 K and 980 hPa respectively.

The same mesh input parameters were used for both fore and aft configurations, since the differences in simulation convergence, simulation time, and accuracy were found to be to be small for the same mesh. A similar mesh dependency test to that presented in Girdwood et al. (2020) was conducted, but the full results are not shown here for the sake of brevity. The chosen base cell size of 10 mm, refined to 1mm in the region surrounding UCASS and by the walls, was influenced by the mesh dependency test results. A polyhedral mesh was chosen since initial tests showed better convergence when compared to tetrahedral or hexahedral.

Since no motion needed to be simulated, the simulation was time-steady—meaning it was solved for one instance and iterated until converged. The simulation was considered to be converged when the continuity residual—that is, the difference in the average imbalance in continuity between adjacent solution iterations—was less than 1×10^{-4}. Since direct numerical simulation was deemed to be too computationally expensive, a Reynolds-averaged Navier-Stokes (RANS) continuum model with a turbulence parameterisation model was used. The turbulence parameterisation model used was $k-\omega$, which was chosen due to superior estimates of near-wall turbulence when compared to $k-\epsilon$. The simulation and mesh parameters are summarised in Table 5.2.

5.2.4.2 CFD-LPT Results and Discussion

Since the aft configuration—shown in Fig. 5.3b—was only intended to be used if the UCASS could not be positioned out of the nose-cone influence due to CoG limits, the fore simulation was conducted first with an angle of attack of 0°. Figure 5.4 shows a magnification of the pressure and velocity fields around UCASS and the FMI-Talon nose cone, in both fore and

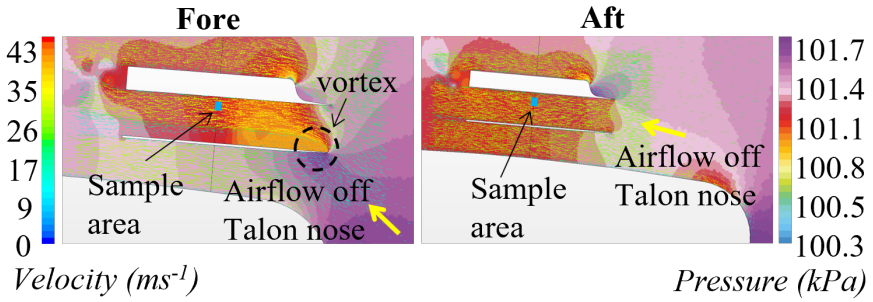

FIGURE 5.4: A plot of the pressure and velocity fields of the fore and aft simulations, with an AoA of 0°. The fore simulation results are shown in the left panel, and the aft results are shown in the right panel. The colour of the background is the absolute pressure of the continuum, and the colour and direction of the glyphs show the velocity field. The black dashed circle indicates a leading-edge vortex at the UCASS inlet in the fore simulation, the blue square indicates the UCASS sample volume, and the yellow arrow shows the airflow direction at the UCASS inlet.

aft configurations—the left and right panels respectively. The colour of the background is the absolute pressure of the continuum, and the colour and direction of the glyphs show the velocity field. In the fore configuration, the airflow deflection off the nose cone of UCASS, as indicated by the yellow arrow in Fig. 5.4, was sufficiently large to create a leading edge vortex on the lower half of the UCASS inlet, which is indicated by the black dashed line. As shown in the background pressure plot of Fig. 5.4, this leading edge vortex compressed the airflow at the sample volume—indicated by the blue square—which caused the velocity to increase to $31\,\mathrm{m\,s^{-1}}$. As previously stated in Sect. 5.2.3.1, this velocity is well beyond what UCASS is able to tolerate due to the TIA bandwidth, therefore the fore configuration was

TABLE 5.2: Parameters used for the CFD-LPT simulations.

Software	Star CCM+
Continuum Model	RANS
Turbulence Model	$k-\omega$
Solver	Time steady
Wall Treatment	low-y+
Mesh Type	Polyhedral
Max. Mesh Aspect Ratio	1.2
Maximum Mesh Size	10 µm
Droplet Material	Water

abandoned at this stage. Droplets were not simulated for this geometry due to the inability of UCASS to measure them even if their trajectory and theoretical concentration would be unaffected by the leading edge vortex. The aft configuration, the results for which are shown in the right panel of Fig. 5.4, did not encounter this problem since a laminar boundary layer was attached to the aerodynamic surface of the FMI-Talon fuselage, meaning the airflow was directed parallel to UCASS. This non-ideal positioning could have been subverted by the use of a custom built airframe—similar to Girdwood et al. (2020), Mamali et al. (2018)—which would have more flexibility around positioning and could be designed around UCASS. However, the design and construction of a custom airframe would be intensive and was beyond the scope of this research.

The remaining simulations were conducted using the aft geometry in Fig. 5.3b. Since it was predicted that the aft configuration would be more sensitive to AoA changes, the first experiment was designed to keep droplet size and continuum velocity constant, while varying the free-stream velocity angle with respect to the FMI-Talon nose. The droplet diameter used was 20 µm, which was chosen to be slightly above a typical modal value of the droplet size distribution in a mature stratus cloud. Since the AoA limit for the UCASS without a platform is 10°, the AoA range chosen was -20° to 20°—since an AoA of ±20° was deemed unlikely to be acceptable. Using Fig. 5.3 as a reference, a negative AoA was considered to be one which points downwards towards negative 'y'. An AoA step of 5° was chosen as a balance of computation time and resolution. The injected concentration of droplets was 9 m^{-2}, which was determined by experimentation to be the lowest concentration that could provide a statistically significant number of droplet streams at the UCASS sample volume. The value of 9 m^{-2} was largely abstract since the simulations were time steady and therefore conducted for one specific instance. The droplets were therefore simulated as parcel streams with inertia. The injected concentration of 9 m^{-2} corresponded to 10 parcel streams per 100 mm at the simulation inlet. The airspeed used for these simulations was 20 $m\,s^{-1}$ since this was the target maximum airspeed for the UAV.

Since not enough droplets could be simulated to for a statistically significant quantity

at the true 0.5 mm sample area of UCASS, a droplet was considered to have crossed the UCASS sample area if its trajectory crossed a plane coincident with the sample area, within 10 mm of its origin. As discussed previously in Sect. 5.2.3.1, there are two possible definitions of concentration from real UCASS data: ToF and pitot tube. Both definitions had to be assessed for differences, and therefore re-defined in the context of these CFD-LPT simulations. Droplet number concentration is defined here as

$$N_c = \frac{n_{s10}}{A \times v \times t} \tag{5.1}$$

where N_c is the simulated number concentration (m^{-2}), n_{s10} is the number of droplet parcel streams which intersect the sample plane within 10 mm of the sample area origin, A is the area around the sample area origin where a particle was considered to be sampled—10 mm in this case—v is a velocity (ms^{-1}), and t is time (s)—which is an arbitrary scaling factor in this instance since time is steady. For all simulations, t was set equal to 1 for both the input and calculated output concentrations. The velocity, v, used depended on the sample volume calculation method. For the ToF equivalent, the droplet velocity at the sample plane was used; for the pitot tube, the freestream velocity of $20\,m\,s^{-1}$ was used.

Figure 5.5 shows a plot of concentration and droplet airspeed through the sample volume versus AoA for the simulation. The red and blue lines are the concentration versus AoA calculated using the ToF and pitot tube methods respectively, and the black dotted line is the mean velocity of the droplets as they cross the sample plane. The solid black line is the injected concentration of droplets at the inlet, and the shaded region is ±25% of the inlet concentration which was considered an acceptable error margin for concentration. This was because a light-weight OPC agreeing with a reference within this margin is generally considered robust, for example in Clarke et al. (2002). It was observed in the simulations that the concentration of droplets generally increased with AoA until 10°, after which no droplet trajectories at all reached the sample area. This was because any AoA above this would cause boundary layer separation from the upper part of the fuselage, thus putting it

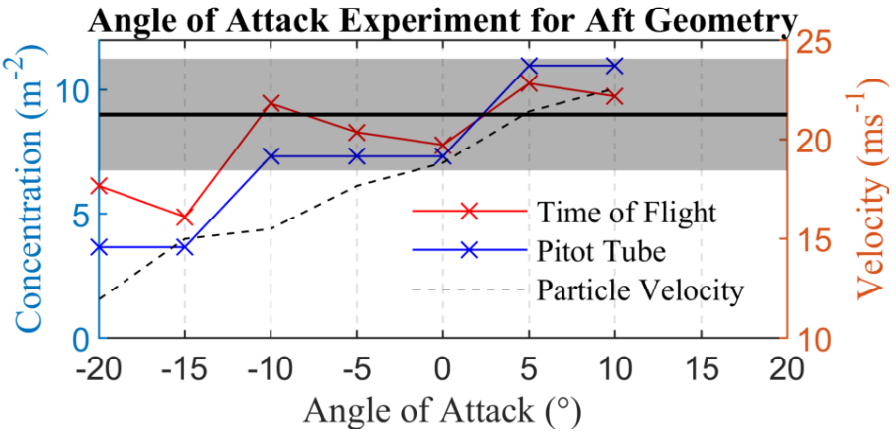

FIGURE 5.5: Calculated droplet concentration against AoA for CFD-LPT simulated data. The solid black line shows the input concentration, and the black shaded region around it represents ±25% of the input. The red and blue lines are the concentration data calculated using simulation equivalent droplet ToF and pitot tube airspeed respectively. The black dotted line is the mean velocity of a droplet as its simulated trajectory crossed the UCASS sample area.

under stall conditions and causing the majority of the droplets to be deflected around the resulting vortex.

The general increase of droplet concentration with AoA is due to the convergence of continuum streamlines towards the upper part of UCASS before the boundary layer separates. This effect both increased the convergence of droplet parcel streams—and thus the pitot tube estimated concentration—and the particle velocity at the sample plane. These effects conflict in their influence on the ToF particle concentration, since as velocity increases, the concentration calculated from Eq. 5.1 will decrease. This caused an increase in accuracy of the ToF concentration, which was within ±15% of the injected concentration for AoAs between -10° and 10°.

Both ToF and pitot tube derived concentrations are found to be within acceptable limits, within the AoA range of -10° and 10°. This is the same range as the UCASS without factoring in platform artefacts (Smith et al., 2019).

The effect of temperature and humidity fields on droplet size was considered, however—with an angle of attack of -10°—the temperature of the air at the sample volume is 280.19

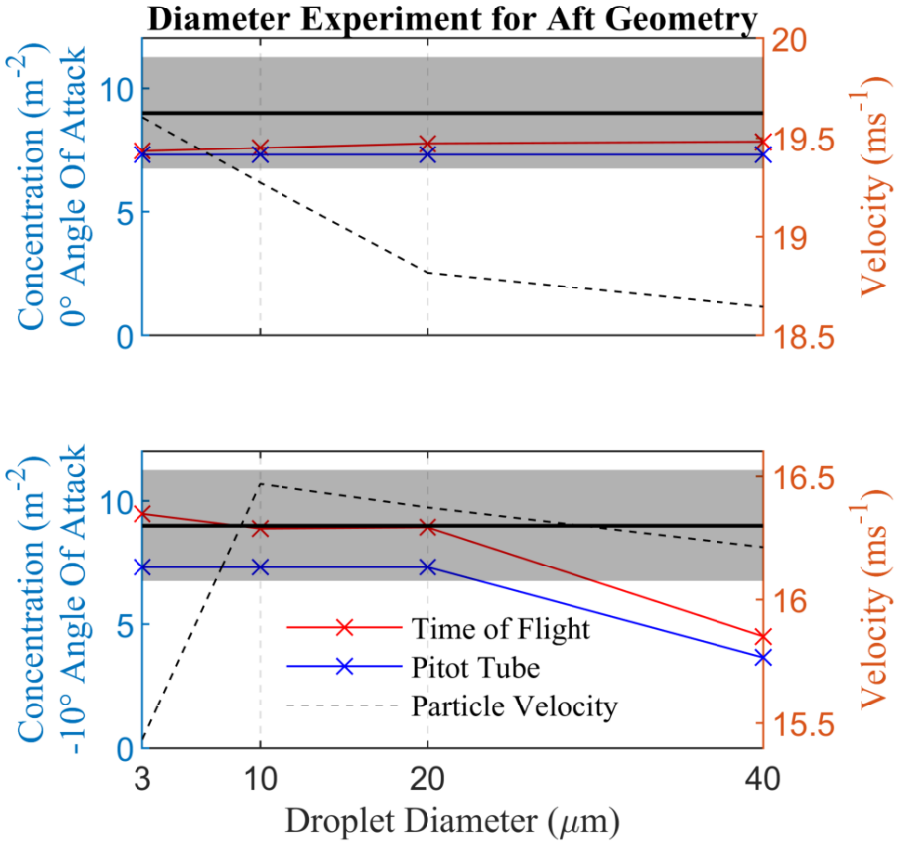

FIGURE 5.6: Calculated droplet concentration against droplet diameter for two different AoAs. The solid black line shows the input concentration, and the black shaded region around it represents ±25% of the input. The red and blue lines are the concentration data calculated using simulation equivalent droplet ToF and pitot tube airspeed respectively. The black dotted line is the mean velocity of a droplet as its simulated trajectory crossed the UCASS sample area.

K and the temperature of the air at the inlet was 280.23 K. At the time the manuscript was written, we did not consider the 0.04 K change in temperature to have a considerable effect on droplet diameter, or the relative humidity of the air.

In addition to the AoA dependency, droplet size dependency was also tested in order to ensure the shape of the size distribution was not affected. Since it was predicted that increased AoA would amplify size dependency, the simulations were run for AoAs of 0° and -10°. The latter limit was chosen since, for negative AoAs, the inertia of larger droplets was

predicted to force them away from the sample volume, which was closer to the upper edge of UCASS. The sizes used for the simulation were 3, 10, 20, and 40 µm, which were chosen since this range spanned the full size range of the UCASS in low-gain mode, and was distributed approximately logarithmically. The results of this simulation are shown in Fig. 5.6, where the top panel shows the results for 0°, and the bottom shows the results for -10°. The graph legend is consistent with Fig. 5.5. The results of this simulation show that, for an AoA of 0°, the size dependency is minimal—this can be seen in the top panel of Fig. 5.6. During these simulations—for an AoA of 0°—the particle velocity did not deviate much from $20\,\mathrm{m\,s^{-1}}$, meaning the ToF and pitot tube derived concentrations were found to be similar, with a slight deviation for a size of 40 µm due to the slower acceleration within the UCASS inlet.

The size dependency results for an AoA of -10° are shown in the bottom panel of Fig. 5.6. This experiment revealed a larger concentration discrepancy for 40 µm droplets, which resulted from their larger inertia deflecting them away from the sample area. This discrepancy was beyond the ±25% limit which was considered acceptable. Beyond a re-design of the UCASS aerodynamics, however, there was little methodology which could rectify this. A large uncertainty of ±45%—the percentage difference between the measured and input concentration of 40 µm droplets—is therefore placed on measurements of droplets above 30 µm, which is where the ToF derived concentration strays beyond limits using linear interpolation.

The CFD-LPT simulations showed that ToF was, theoretically, the superior method for determining airspeed, since concentration derived using this method was always closer to the input. However, in practice this was not always the reality. This was because of the dependence of ToF determined airspeed on a fixed beam width, which would change if the UCASS were to be subjected to large mechanical forces that could misalign the optics. In addition—as previously mentioned in Sect. 5.2.3.1—ToF measured by the UCASS was dependent on the measured droplet size, so a calibration for each bin had to be applied. Also, if enough droplet measurements were not performed in a time-step integrated histogram, a statistically significant ToF measurement of that histogram cannot be performed. Pitot tube

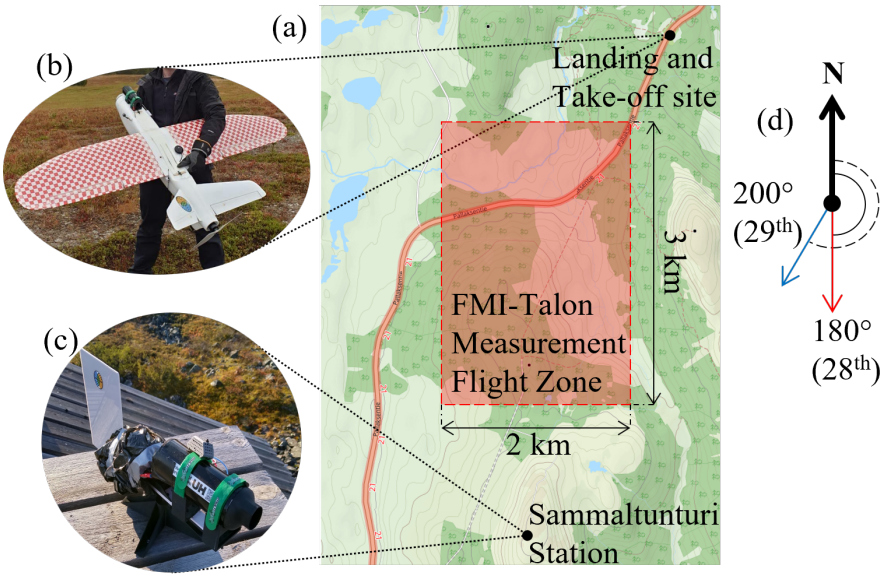

FIGURE 5.7: A series of illustrations designed to give context to the measurement campaign. Figure 5.7a shows a map of the area including Sammaltunturi station—obtained from OpenStreetMap-Contributors (2017), the UAV landing site, and the flight operations zone in the red square; b shows the UCASS mounted to the FMI-Talon; c is an image of the UCASS – wind-vane system mounted to the station; and d shows the wind directions, measured by Sammaltunturi station, on the 28th and 29th with red and blue arrows respectively.

airspeed was therefore used when there were too few particles to perform a ToF measurement.

5.2.5 Field Campaign Testing and Validation

5.2.5.1 Field Campaign Method

The validation flights were undertaken during the Pallas Cloud Experiment (PaCE) in September 2020, at the Pallas atmosphere-ecosystem super-site. The site, as shown in Fig. 5.7a, is located 170 km north of the Arctic Circle (67.973°N, 24.116°E), partly in the area of Pallas-Yllästunturi National Park (Lohila et al., 2015). Measurements were taken from the 24th to the 30th of September, however stratus cloud was only present from the 28th to the 30th. A fault in the data-logger used to gather flight data was persistent on the 30th, therefore only flights conducted on the 28th and 29th will be considered in this analysis. On each

day, 4 profiles were conducted. Each profile consisted of an ascent and a descent through the entire cloud, which was approximately 1 km thick throughout the experiments. On the 28$^{\text{th}}$ of September the mean wind speed throughout the day of flights was approximately $7\,\mathrm{m\,s^{-1}}$, the wind direction 200° from north, and the temperature 5 °C. On the 29$^{\text{th}}$ of September the mean wind speed throughout the day of flights was approximately $5\,\mathrm{m\,s^{-1}}$, the wind direction 180° from north, and the temperature 8 °C. The wind direction is illustrated in Fig. 5.7d.

The layered stratus cloud common to Pallas-Yllästunturi, combined with the airspace D527-Pallas reserved by FMI made this location perfect for the validation of UAV based optical particle instruments. Since stratus cloud is normally laterally homogeneous within the distance scales discussed in this paper (the 2 km by 3 km measurement area shown in Fig. 5.7a, Lawson et al., 2001, Tsay and Jayaweera, 1984), co-location errors between the UAV and station could be assumed to be minimal. The measured particles within the stratus cloud were all assumed to be water droplets, therefore the calibration lookup table for UCASS was made using a refractive index of 1.31+0i—the refractive index of water. Cloud droplets were considered the ideal validation particle since the UCASS calibration relies on Mie scattering, and the droplets can be assumed to be spherical. Water droplets also exhibit low absorption of 650 nm light—the wavelength of the UCASS laser. This is beneficial since absorption can cause artefacts in particle size measurements which utilise scattering like UCASS.

For comparative data, instruments were mounted on the roof of Sammaltunturi station, which was located on a hill 565 m above sea level. The instrument chosen for the comparison was an identical UCASS unit, with the same TIA gain, oriented into the wind via the means of a wind vane and turret system, an image of which is shown in Fig. 5.7c. The only differences in the data between the two UCASS units would be due to platform artefacts, since they were otherwise identical. The aspiration airflow for UCASS was provided by the wind. The minimum airflow required for UCASS operation is $3\,\mathrm{m\,s^{-1}}$, since particles which produce longer ToFs than this are rejected in a firmware noise filter. At all instances during the campaign, the wind speed was faster than $3\,\mathrm{m\,s^{-1}}$. The wind speed for each UCASS

data-point was measured using an anemometer on Sammaltunturi station. The UCASS – wind-vane set-up was secured to the roof each morning, before the daily flights started, and removed after flying was stopped for the day. This was to prevent damage to UCASS during the night, which may cause optical misalignment.

The FMI-Talon ascents and descents were conducted utilising a mixture of spiral patterns and wind-parallel patterns—both of which are commonly conducted in literature (Mamali et al., 2018, Martin et al., 2011). The conducted flight patterns are summarised in Table 5.3, and the number concentration profiles are shown for context in Fig. 5.8. The purpose of this was to compare the two patterns to determine which is superior for UCASS measurements. Beyond the limits of the stratus cloud, when insufficient particles were present, the pitot tube airspeed was used to derive a sample volume. Within the cloud ToF was used. It was also observed that within the cloud the pitot tube would become blocked, which caused the airspeed reported by the pitot tube to increase beyond physically possible limits. Not only did this render pitot tube measurements of sample volume impossible, the FMI-Talon also had to be manually piloted through the cloud since the large over-prediction in airspeed would cause the autopilot to stall the aircraft. Data from UCASS were recorded at 0.5 s intervals by a Raspberry Pi Zero (RaspberryPi-Foundation, 2015); pitot airspeed, attitude, and GPS data were recorded by the flight controller; and temperature, pressure and humidity were recorded by a separate Raspberry Pi. The flights considered for analysis were the only flights for which all three data loggers were operating.

TABLE 5.3: A table detailing the profile types of the UAV flights considered for analysis. The profile IDs are shown for the ascending and descending profiles respectively.

IDs	Date	Time	Ascent	Descent
1&2	2020/09/28	10:42	Lines	Lines
3&4	2020/09/28	11:26	Lines	Lines
5&6	2020/09/28	12:09	Spiral	Spiral
7&8	2020/09/28	12:45	Lines	Spiral
9&10	2020/09/29	07:51	Lines	Spiral
11&12	2020/09/29	08:21	Lines	Spiral
13&14	2020/09/29	08:21	Lines	Spiral
15&16	2020/09/29	12:52	Lines	Spiral

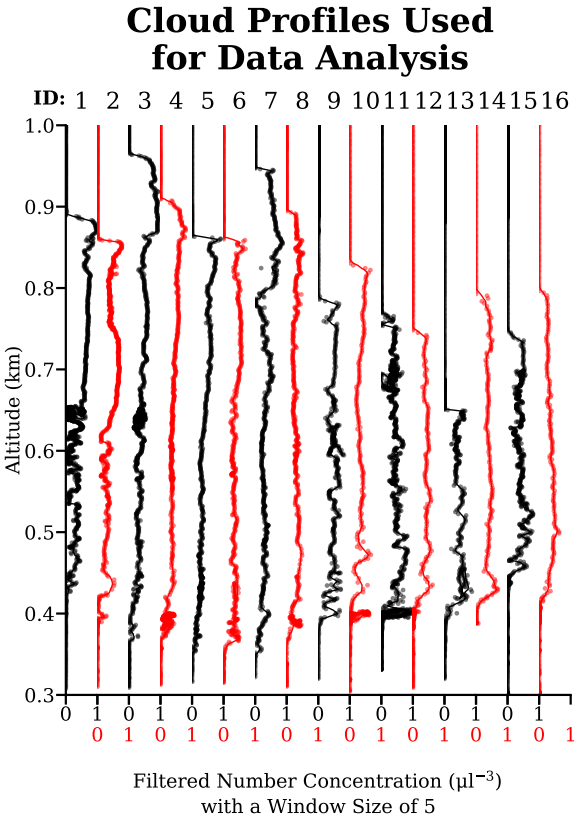

FIGURE 5.8: The number concentration profiles through the stratus cloud, shown for context of the campaign. The profile ID is shown above each panel, and is consistent with Table 5.3. The ascending profiles are shown in black, and the descending profiles are shown in red.

The data were filtered based on two criteria, the first of which was a maximum airspeed limit, which was set to $20\,\mathrm{m\,s^{-1}}$. This was set because, even though the cut-off frequency of the TIA corresponds to an airspeed of $25\,\mathrm{m\,s^{-1}}$, the CFD-LPT simulations revealed that a droplet could travel faster through the UCASS sample area than the free-stream depending on AoA. An airspeed limit of $20\,\mathrm{m\,s^{-1}}$ ensures that, for all valid AoAs, the airspeed through the sample area never exceeds $25\,\mathrm{m\,s^{-1}}$. The second was an AoA limit defined as $\pm 10°$, resulting from the CFD-LPT simulations in Sect. 5.2.4. AoA was defined here as the angle between the UAV axis, and the resultant airspeed vector. The resultant airspeed vector is equal to the sum of the wind-speed vector, the vertical velocity of the UAV, and the UAV

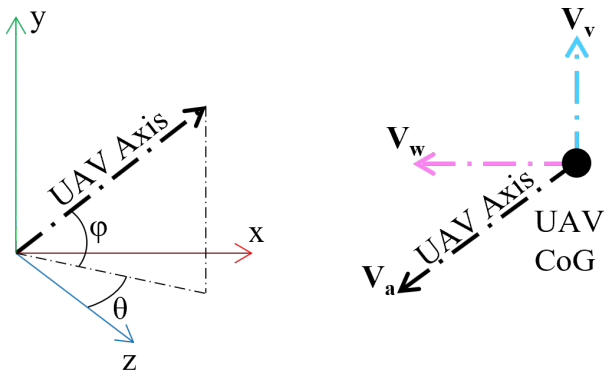

FIGURE 5.9: An illustration clarifying the angle and velocity variable definitions used for the computation of AoA.

airspeed vector. The UAV airspeed vector was defined as

$$\boldsymbol{V_a} = V_{pit} \left(\frac{\left| \sin\theta\cos\phi \quad \cos\theta\cos\phi \quad \sin\phi \right|}{\sqrt{(\sin\theta\cos\phi)^2 + (\cos\theta\cos\phi)^2 + (\sin\phi)^2}} \right) \tag{5.2}$$

where $\boldsymbol{V_a}$ is the UAV airspeed vector, V_{pit} is the pitot tube airspeed, ϕ is the UAV elevation angle, and θ is azimuth angle of the UAV with respect to north—these were calculated from the pitch, roll, and yaw angles of the UAV. The angles and velocities are illustrated in Fig. 5.9 for clarity. Equation 5.2 is a normalised vector parallel to the UAV axis multiplied by the UAV airspeed (V_{pit}). Since wind-speed was considered likely to change as the UAV ascended, the wind angle measured by Sammaltunturi station was assumed constant with altitude, and the difference between the UAV ground-speed and 'xz' component of airspeed was used to calculate the wind-speed vector. This was given by

$$\boldsymbol{V_w} = \frac{\boldsymbol{V_{xz,w}} - \boldsymbol{V_{xz,g}}}{\pi - \cos\alpha_w} \tag{5.3}$$

where

$$\boldsymbol{V_{xz,g}} = V_g \left(\frac{\left| \sin\theta \quad \cos\phi \quad 0 \right|}{\sqrt{(\sin\theta)^2 + (\cos\phi)^2}} \right) \tag{5.4}$$

$$\boldsymbol{V_{xz,w}} = \boldsymbol{V_a} \cos\phi \begin{vmatrix} 1 \\ 1 \\ 0 \end{vmatrix} \tag{5.5}$$

α_w is the wind angle clockwise from north measured by Sammaltunturi station; $\boldsymbol{V_w}$ is the wind-speed vector; $\boldsymbol{V_{xz,a}}$ is the 'xz' component of UAV airspeed; and $\boldsymbol{V_{xz,g}}$ is the UAV ground speed (V_g) expressed in vector form. The vertical velocity of the UAV was given by

$$\boldsymbol{V_v} = \left| 0 \quad 0 \quad V_v \right| \tag{5.6}$$

where V_v is the vertical speed reported by the flight controller. The resultant airspeed vector was then given by

$$\boldsymbol{V_{r,a}} = \boldsymbol{V_v} + \boldsymbol{V_w} + \boldsymbol{V_a} \tag{5.7}$$

therefore AoA was finally defined as

$$AoA = \arccos\left(\frac{\boldsymbol{V_{r,a}} \cdot \boldsymbol{V_a}}{|\boldsymbol{V_{r,a}}||\boldsymbol{V_a}|} \right) \tag{5.8}$$

The V_a used in Eq. 5.8 could be replaced with any vector parallel to UCASS, but this was used since it was already calculated in Eq. 5.2. The wind measurements produced via this method were not considered accurate nor reliable enough to be utilised in scientific datasets, simply because they were not validated here, and were likely to suffer from measurement artefacts. However, they were considered robust enough to be used as rejection criteria for the UCASS particle spectrum data.

5.2.5.2 Field Campaign Results and Discussion

Figures 5.10 and 5.11 show a comparison of $\mathrm{dN/dlog(D_p)}$ against droplet diameter, measured by the FMI-Talon and Static UCASS when coincident, for September the 28$^{\mathrm{th}}$ and 29$^{\mathrm{th}}$ respectively. The blue and orange bars represent the $\mathrm{dN/dlog(D_p)}$ measured in each bin of the FMI-Talon UCASS and the Static UCASS respectively. The effective diameters recorded by both UCASS units are also shown on the plot. Effective diameter, as in Korolev et al. (1999), was defined as the ratio of the third and second statistical moments; that is, for binned UCASS data,

$$D_{eff} = \frac{\sum_{i=1}^{16} n_i D_i^3}{\sum_{i=1}^{16} n_i D_i^2} \tag{5.9}$$

where D_{eff} is the effective diameter, and n_i is the number concentration in bin i which has the geometric mean diameter D_i. The take-off time and date of each flight is also shown in the bottom left corner. In each figure, the left hand column of sub-figures shows data gathered on the ascending profile, and the right hand column shows that gathered on the descending profile. The $\mathrm{dN/dlog(D_p)}$ was calculated from

$$dN/dlog(D_p) = \frac{c_{n,i}}{\log D_{l,i} - \log D_{l,i+1}} \tag{5.10}$$

where $c_{n,i}$ is the number concentration in bin i, $D_{l,i}$ is the lower size bin boundary of bin i, and $D_{l,i+1}$ is the lower size bin boundary of bin $i+1$. The FMI-Talon data used in Fig. 5.10 and Fig. 5.11 was averaged over a 40 m vertical distance—centred on the station altitude. The static UCASS data was averaged over 10 s—centred on the instance the Talon passed the altitude of Sammaltunturi station.

The effective diameter measured by the UAV on the 28$^{\mathrm{th}}$ of September overall was within 15% of that measured by the static UCASS. However there was an observed increase in the difference between the UAV and reference data with time, which would normally point to a calibration discrepancy caused by an offset in optical alignment. However, on the

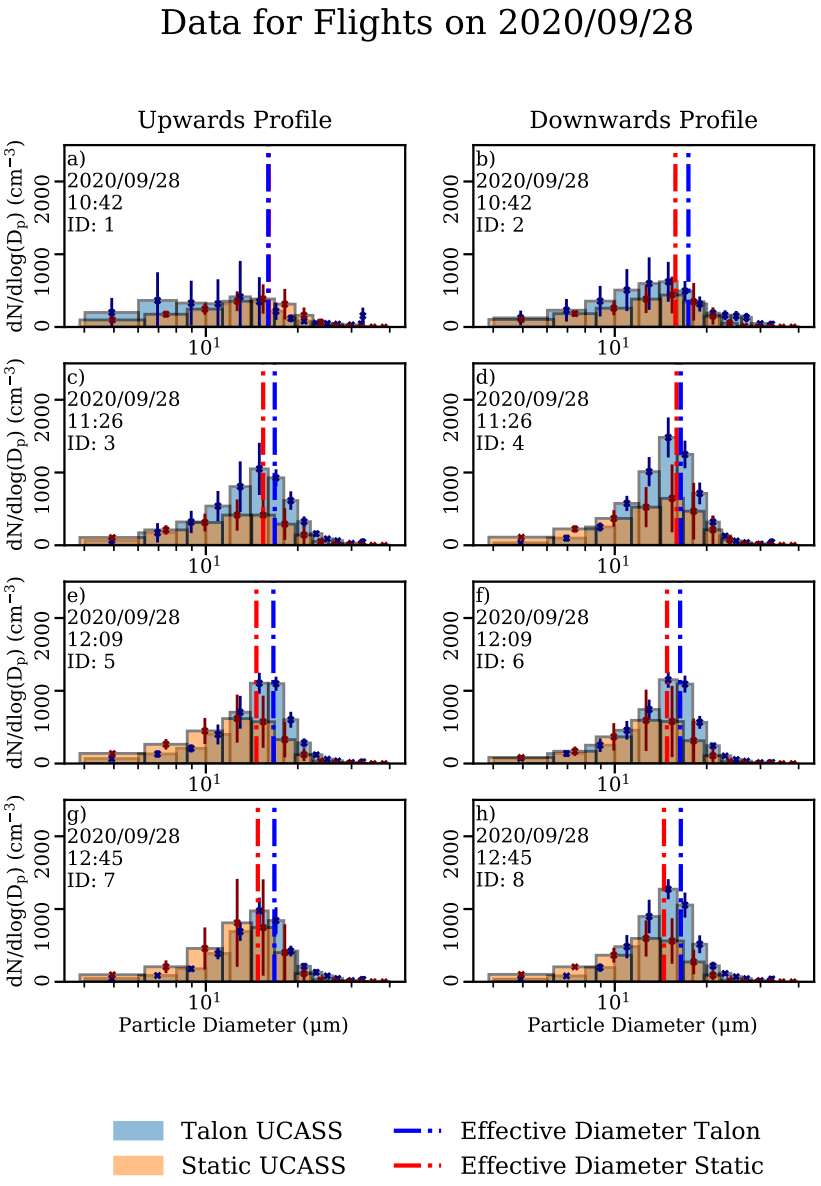

FIGURE 5.10: Plots of $dN/dlog(D_p)$ plotted against droplet diameter for the flights conducted on the 28th of September 2020. The left hand column of plots is the data taken on the ascent and the right hand column is that taken on the descent. The thickness of each bar is a UCASS bin, the orange bars are the static UCASS data, and the blue bars are the FMI-Talon – UCASS data. The red dashed line is the effective diameter for the Static UCASS data, and the blue dashed line is that of the FMI-Talon – UCASS data. The profile ID stated is consistent with Table 5.3.

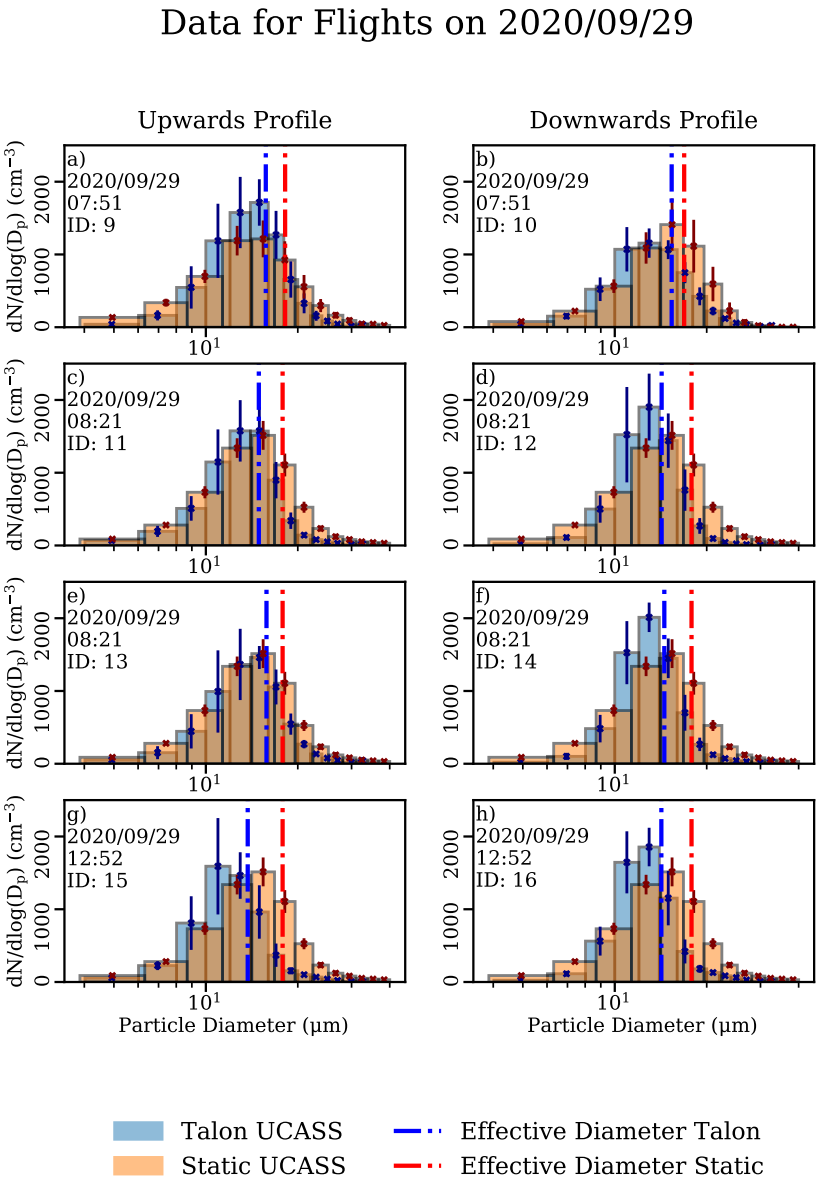

FIGURE 5.11: Plots of $dN/dlog(D_p)$ plotted against droplet diameter for the FMI-Talon – UCASS combination coincident with Sammaltunturi station, for the flights conducted on the 29th of September 2020. The legend and axes are consistent with Fig. 5.10. The profile ID stated is consistent with Table 5.3.

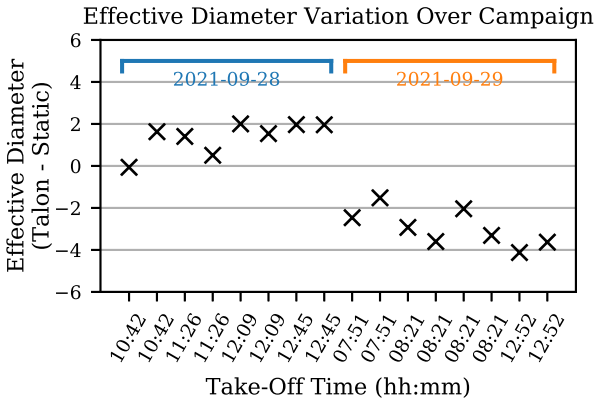

FIGURE 5.12: A plot of the difference in effective diameter between the station mounted UCASS and the UAV mounted UCASS over the progression of the campaign. The two days discussed are highlighted in blue and orange.

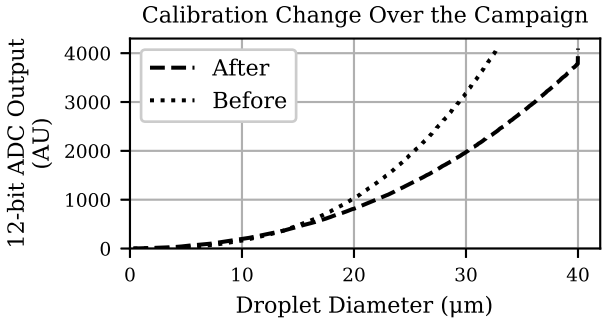

FIGURE 5.13: A plot of the two instrument response curves—that is, 12-bit ADC output versus scattering cross section diameter—from calibration data collected before and after the campaign.

28^{th}, the effective diameter measured by the static UCASS was smaller. This was unusual because the FMI-Talon UCASS had undergone much larger stresses, which would cause it to measure lower than the static UCASS if a calibration offset in alignment was the case—since it is unlikely that an offset in alignment would *increase* the intensity of light incident to the photodiode. This trend can be seen in Fig. 5.12 in the points under the blue line. Laser mode hopping resulting from a temperature change was considered as a possible cause, however the temperature only changed by 0.9 °°C throughout the day of flights, which was not enough to cause a significant perturbation in laser wavelength, and therefore the measured effective

diameter.

Since the static UCASS was left immersed in the stratus cloud for an extended period of time, it was observed that some water droplets accumulated on the elliptical mirror—which was the largest exposed optical surface. These water droplets likely caused extinction of the scattered light from the droplets before it reached the photodiode. The decreased intensity of the photodiode incident light would cause under-sizing of the droplets, which would lead to a gradual decrease in effective diameter over time. Since this trend was observed in the data in Fig. 5.12, this was treated as the most probable cause for the increase of discrepancy in effective diameter over time. When the wind-vane – UCASS rig was re-attached on the station roof on the 29$^{\text{th}}$, the UCASS was oriented in its mount with the mirror on top to reduce the number of droplets which were deposited on the mirror via gravitational settling. However, some droplets were still observed to be deposited on the mirror, which indicated that a proportion of the droplets settle via turbulent deposition or droplet shedding. This would require a re-design of the internal UCASS aerodynamics, similar to Korolev et al. (2013a).

On the 28$^{\text{th}}$ and 29$^{\text{th}}$ of September, a larger difference in effective diameter between the static UCASS and FMI-Talon UCASS was measured, which can be seen in Fig. 5.11. Contrary to measurements taken on the 28$^{\text{th}}$, the static UCASS measured a larger effective diameter than the FMI-Talon UCASS, which can be more clearly seen in Fig. 5.12 under the orange line. The most likely cause for this was an offset in alignment in the FMI-Talon UCASS causing less light to be focused on the photodiode, and thus a smaller diameter to be measured. Since there was a significant step in the measured effective diameter between the 28$^{\text{th}}$ and 29$^{\text{th}}$, the most probable cause of the alignment offset was deemed to be transportation of the UCASS unit to or from the UAV launch site.

This alignment offset can be seen in Fig. 5.13, which is a plot of the UCASS instrument response—a 12-bit analogue to digital converter (ADC) value—against scattering cross section diameter, created from calibration data collected before and after the campaign with the same unit. A large differential can be seen between the two curves, particularly for

droplets which would produce an ADC output of 1000 or higher. For example, a droplet which produces an ADC output of 3000 would be sized as 30 µm using the calibration data taken before the campaign, and 36 µm using that taken after the campaign. All the data discussed here used the calibration conducted prior to the campaign. The re-calibration data were not applied retroactively, since there would be a combination of steady shifts and discrete steps in calibration offset which would be difficult to account for and interpolate. In addition, flights which were not analysed here were also performed after the 29$^{\text{th}}$ of September, which would have caused calibration offsets that would not be applicable to these data. The degradation in UCASS alignment over the course of the campaign points to a need for a mechanical re-design of UCASS before it's regular utilisation on fixed-wing UAVs, similar to that conducted in Girdwood et al. (2020). However, one single unknown event—as opposed to a gradual offset over time—between the two days appears to be the source of the misalignment, since there is a large step in the effective diameter differential between the two days considered.

The concentration measured by the FMI-Talon and Static UCASS units agreed within 15% in all cases, apart from profiles 3, 4, 5, 6, and 8. The dN/dlog(D_p) for these profiles can be seen in Fig. 5.10c through f, and h. In each case, the concentration measured by the FMI-Talon – UCASS was larger than that measured by the wind-vane – UCASS. This was unusual since most artefacts the FMI-Talon – UCASS could suffer from—for example large AoA values—would cause its measured concentration to decrease. Indeed regression of the absolute number concentration differential and AoA yielded 'p' values much larger than 0.05, indicating low statistical significance. Additionally, the difference in effective diameter for the measurements conducted on the 28$^{\text{th}}$ was minimal, and AoA effects would cause a shift in the measured size distribution towards smaller sizes, as demonstrated in Sect. 5.2.4. A difference between profile type—that is, spiral versus wind-parallel lines—was also considered as a possible cause, however the flights departing at 11:26 utilised a wind-parallel profile, and the spiral descent profiles conducted on the 29$^{\text{th}}$ did not suffer from the same concentration differential.

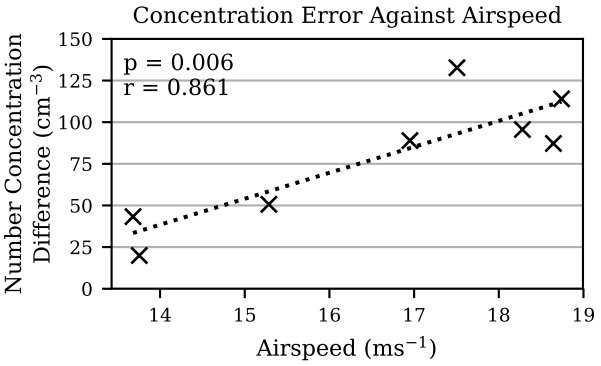

FIGURE 5.14: A correlation plot of the absolute difference in measured number concentration between the FMI-Talon and Static UCASS units, and airspeed, for the 28$^{\text{th}}$ of September. The linear regression line and 'p' value are shown.

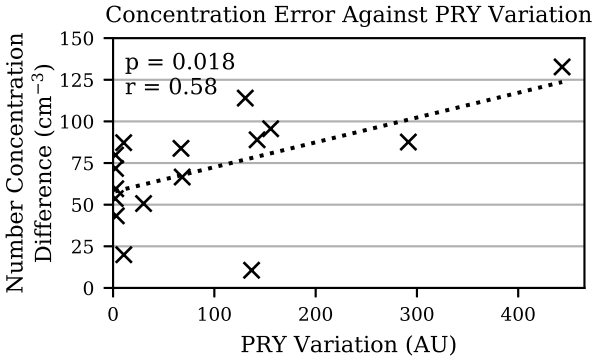

FIGURE 5.15: A correlation plot of the absolute difference in measured number concentration between the FMI-Talon and Static UCASS units, and PRY Variation, for the whole campaign. The linear regression line and 'p' value are shown.

While the regression of the absolute number concentration differential and airspeed yielded a large 'p' value over the whole campaign, when only the data for the 28$^{\text{th}}$ of September were considered, the 'p' value was 0.006—which can be seen in Fig. 5.14. The more rigid correlation on the 28$^{\text{th}}$ than the 29$^{\text{th}}$ indicated a dependence of the airspeed induced concentration differential on another variable, which changed between the two days. Initial observations revealed that the variation in pitch, roll, and yaw of the aircraft were much higher on the 28$^{\text{th}}$ than the 29$^{\text{th}}$. For a quantitative definition, the root mean square (RMS)

of the signal was used. In order to remove larger oscillations in the data which occurred naturally as a response to wind speed changes, the signal was first normalised against a filtered version of itself, obtained using a moving average filter with a window size of 10 seconds. This window size was chosen because it was observed that these large variations did no occur on smaller timescales than this. This variable, γ_{RMS}, was defined mathematically as

$$\gamma_{RMS} = \sqrt{\frac{1}{T_2 - T_1} \int_{T1}^{T2} \left(\frac{f(t)}{f(t) \circledast (H(t) - H(t-w))} \right)^2 dt} \tag{5.11}$$

where T_1 and T_2 are the time limits corresponding to when the UAV was at the altitude of Sammaltunturi station $\pm$20 m; t is time; w is the window size in seconds, which in this instance was 20 s; $f(t)$ is the pitch, roll, and yaw (PRY) of the UAV as a function of time; and $H(t)$ is the Heaviside function of time. This was then calculated for PRY, which were then multiplied together to give the total PRY variation.

Figure 5.15 shows the correlation of number concentration differential with PRY variation throughout the whole campaign. The regression yielded a 'p' value of 0.018, which indicated statistical significance. The combination of the high Reynolds number resulting from a larger airspeed, and the large PRY perturbations encountered on the 28$^{\text{th}}$, would result in an increased likelihood of turbulence. Turbulence can both cause a droplet to enter the sample area at an oblique angle, and slow down the airspeed at the sample volume. Both of these effects would cause a larger ToF and therefore concentration to be recorded. Since the pitot tube was blocked throughout the cloud there was unfortunately no other airspeed measurement to compare with, however turbulence was considered the most likely cause of the concentration differential. This result further exaggerated the need for smooth and steady sampling flight with a UAV. Since over half of the affected profiles were spiral-type, it was considered likely that the constant movement exacerbated the PRY variations. Since much of the data also had to be rejected from the spiral-type profiles, due to AoAs exceeding limitations defined in Sect. 5.2.4, the wind-parallel line profiles were considered more reliable for sampling with UCASS.

5.2.6 Conclusions

In this paper, a UCASS OPC was integrated on board a fixed-wing UAV—the FMI-Talon—and investigations were conducted into the accuracy and reliability of the combination. The UCASS, presented in Smith et al. (2019), utilised a gain configuration which allowed it to measure a size range of approximately 1 µm to 33 µm. Unlike in Girdwood et al. (2020), the UCASS was not re-designed for mechanical robustness. The FMI-Talon was capable of performing multiple sampling flights up to 1 km altitude, and functioning consistently throughout the day. It was also configured with temperature and humidity sensors which were not used in this research.

The investigations were composed of CFD-LPT simulations of the combinations, and a field campaign examination, involving an inter-comparison with reference instrumentation. The CFD-LPT simulations focused on two UCASS positions on the airframe. The first configuration involved the UCASS placed as far forward as the CoG tolerance of the FMI-Talon would allow. It was found that the UCASS could not be positioned forward enough to be beyond the influence of the deflection of the air by the nose cone, which caused a leading edge vortex to form on the UCASS inlet. Therefore the second configuration had to be considered, that is, positioning the UCASS far enough back so an attached airflow would be axial to UCASS. This configuration was tested for a range of AoAs and simulated droplet sizes. It was found that the original AoA limit of UCASS, $\pm 10^{\circ}$, was still acceptable with the FMI-Talon in this mounting configuration. However a large uncertainty value of 45% had to be placed on the concentration of droplets measured above 30 µm since their larger inertia caused a deflection around the UCASS sample area. The CFD-LPT simulations also compared two different methods for calculating droplet concentration: ToF and pitot-tube. It was found that the ToF method provided a more accurate concentration, but was unreliable when used in environments with a sparse ambient number concentration.

During the field campaign, the UAV was flown—utilising a mixture of spiral and wind-parallel profiles—through a stratus cloud up to approximately 1 km and UCASS data were

collected. A static UCASS mounted on a wind vane was positioned on the roof of a station 565 m above sea level, this provided the reference data to which the FMI-Talon – UCASS was compared. The analysed flights were conducted on the 28$^{\text{th}}$ and 29$^{\text{th}}$ of September 2020. Data were rejected according to AoA and airspeed criteria derived from the CFD-LPT simulations. For the measurements conducted on the 28$^{\text{th}}$, the difference in effective diameter of the size distributions between the Talon and Static UCASS units was under 2 µm. However, the measurements conducted on the 29$^{\text{th}}$ revealed a high difference in effective diameter. This cause of this was found to be an offset in optical alignment—which likely occurred during transportation to and from the launch site, or a hard landing—which caused less light to reach the photodiode and therefore smaller sizes to be recorded. This was proven to be the case by re-calibrating the UCASS unit after the campaign and observing the offset. This result pointed to a need for a mechanical re-design of UCASS, similar to Girdwood et al. (2020), before its consistent utilisation on UAVs can be realised. Since a similar assessment of the longevity of light-weight OPCs on UAVs has not been performed, the authors expect that this will also occur in many other instruments.

A discrepancy in number concentration between the static and UAV UCASS units was also observed on some of the profiles conducted on the 28$^{\text{th}}$, where the FMI-Talon – UCASS measured higher values than the static UCASS. The number concentration discrepancy correlated well with the UAV airspeed only for the flights conducted on the 28$^{\text{th}}$. The variation in pitch, roll, and yaw given by Eq. 5.11 was found to correlate well with number concentration discrepancy throughout the campaign, but only reached high values on the 28$^{\text{th}}$. The concentration discrepancy was therefore determined to be caused by turbulence induced by the combination of these two variables, which would cause droplets to enter the sample area at oblique angles which would increase their measured ToF, and therefore concentration. This effect points to the need for steady sample flights, under auto-pilot if possible. Auto-pilot, however, was not possible for this campaign since the pitot tube used to measure airspeed would become blocked in the cloud.

The spiral and wind-parallel profiles were both found to be acceptable. However, more

data had to be rejected from the spiral profiles than the wind-parallel profiles due to AoA constraints, and the wind-parallel profiles appeared to induce less pitch, roll, and yaw variations. Therefore, the wind-parallel profiles are recommended where possible.

Future work relating to this project will be largely focused on a design overhaul of the UCASS instrument to deal with the mechanical stresses encountered during an intensive UAV field campaign. The updated UCASS will also include an extended size range, and particle-by-particle data as opposed to bins. Future work will also be conducted into evaluating the new UCASS for aerosol measurements.

6 | Conclusions and Future Work

Aerosols and clouds are persistent causes of uncertainty in climate and weather models. This is due to their heterogeneous suspension and occurrence within the atmosphere, and complex interactions which are chaotic and very on small scales. There is a large measurement gap of these phenomena, which is in part due to reliance on conventional measurement platforms, for example: conventional aircraft. Unmanned aerial vehicles (UAVs) have grown in popularity, and are becoming more commonly used for general atmospheric measurement, and measurement of aerosols and clouds in particular. However, UAVs suffer from relative infancy as a measurement platform when compared with conventional aircraft, meaning they generally lack standardisation and characterisation. This is the main reason why unmanned aircraft aerosol and cloud data are not currently commonplace.

This thesis presents and evaluates a synergy between two UAVs, a multi-rotor: the UH-AeroSAM octocopter and a fixed-wing: The FMI-Talon, and an optical particle instrument—the Universal Cloud and Aerosol Sounding System (UCASS, Smith et al., 2019). The UCASS was chosen since it is an open path instrument, similar to the classical cloud probes used on conventional aircraft. This means the airflow through the instrument is simpler to characterise, and there is no need to ensure isokinetic flow since the sample flow through the UCASS is the freestream air. The application of an open path instrument to a UAV was found to have a unique set of challenges, which were different for multi-rotor and fixed-wing aircraft. These applications were described separately in two different published articles (Girdwood et al., 2020, 2022).

Computational fluid dynamics with Lagrangian particle tracking (CFD-LPT) proved to be a valuable tool for the characterisation of the velocity fields and particle trajectories which existed around both UAVs. In both instances CFD-LPT was used to develop an operational envelope, with particular attention to angle of attack constraints and size distribution perturbation, for the UAV – instrument synergy.

For the multi-rotor, the CFD-LPT simulations were time variant, in order to simulate the motion of the propellers, which meant they were computationally expensive. For a vertical profile, the UCASS was designed to be mounted with its inlet pointing upwards, and UAV was intended to fly vertically to induce a sample flow through the instrument. These simulations revealed the eight propellers created an area of low pressure towards the centre of the airframe, which the particles were drawn into, following the streamlines. One of the purposes of the simulations was to determine the optimum location to position the UCASS instrument on the airframe, which was found to be slightly—0.15 m—off-centre due to the negative pressure effect. Water particles were simulated with sizes 0.5 µm to 10 µm, it was found that the aerodynamic forces had a very small effect on the particle size distribution shape at the optimum instrument location. For the multi-rotor application, it was found that the mechanical design of the UCASS needed a complete overhaul, since it originally could not withstand the mechanical forces subjected to it. The re-designed UCASS was given two amplifier gain modes, which could be selected prior to flight, to achieve a larger overall size range. The design was the first open-path OPC to be specifically designed for use on a small unmanned aircraft. The multi-rotor – UCASS combination was flown during the Pallas Cloud Experiment (PaCE) in 2019, where the results from four vertical profiles were compared with reference instrumentation mounted on a hill top station. When the two instruments were correlated, the correlation coefficient was 0.772, with a gradient of 0.996 for the high-gain or 'Aerosol' mode, and 0.931 with a gradient of 0.873 for the low-gain or 'Droplet' mode. The multi-rotor – UCASS combination under-predicted the concentration of larger sizes when compared with the instruments mounted on the station. This was primarily due to a crosswind causing inertial deposition of droplets on the walls of the modified UCASS

instrument.

For the fixed-wing, the CFD-LPT simulations were time invariant since no motion needed to be simulated. The UCASS was mounted on top of the nose cone of the airframe, which was the most convenient position for the instrument to be mounted in this instance. The optimum position for the UCASS was determined from preliminary simulations. Upon reflection, the simulation of the motion of the propellers could have been simplified, and modeled as a pressure drop across a line. This is because the near-field propeller flow was revealed to have had little effect on the particle flow through the sample area. An under-wing mounting configuration was considered, but this was rejected since there was potential for the UCASS to be damaged upon landing. Water droplet sizes between 3 µm and 40 µm were simulated, and it was found that water droplets larger than 30 µm suffered from inertial deposition on the walls of the UCASS with a freestream velocity of $20\,\mathrm{m\,s^{-1}}$, and it was decided a large uncertainty would be placed on measurements of droplets larger than 30 µm. Time of flight (ToF) and pitot tube airspeed based droplet concentrations were compared. It was determined that ToF based concentration was to be used by default, and pitot tube based concentration was to be used when particle concentrations were too low to perform a reliable median ToF measurement. An airspeed limit of $20\,\mathrm{m\,s^{-1}}$ was determined based on the UCASS transimpedance amplifier bandwidth, and an angle of attack limit of 10° was determined based on the CFD-LPT simulations. The angle of attack calculations were presented, and involved an approximate calculation of the wind vector. The FMI-Talon – UCASS was flown during the PaCE campaign in 2020, where sixteen vertical profiles—eight ascending and eight descending—across two days were compared to another UCASS mounted on a wind-wane on a hill top station. The effective diameter measurements from the two units were within 2 µm of eachother for the first day, but drifted over the second day. This was confirmed to be caused by mechanical strains on the UAV mounted UCASS unit causing a drift in optical alignment, and therefore a reduction in the observed effective diameter. The number concentration measured by the two units compared well during the second flying day, but differed by over 15 % on five profiles on the first day. This correlated

with an increase in both airspeed, and a new quantity, which was called PRY variation—a quantification of the control perturbation frequency—which was proposed to induce an increase in turbulence. It was concluded that both airspeed and pilot induced perturbations should be kept to a minimum during sampling.

When considering UAVs for the future measurement of atmospheric particles and droplets, it is my recommendation that CFD-LPT is an essential design technique, and must be conducted to some degree when designing a sampling flight envelope. The aim of such simulations should be a combination of determining optimal instrument positioning and mounting, and aiding the design of airflow artefact mitigation strategies and mechanisms. However, the CFD-LPT conducted in this paper could be simplified, following on from some of the major conclusions. As previously stated, the direct modelling of the propellers, in addition to their motion, was found to be unnecessary since the flow close to the propellers had little effect on particles which were 20 cm away. This means propellers could modeled as simple pressure drops across interfaces, which would reduce simulation cost drastically, since it could be considered time invariant. In addition, the airflow around the points considered for instrument positioning was rotationally symmetric, meaning the simulations could be 2-dimensional, which would therefore further decrease computational cost.

UCASS was the first open path instrument to be used on a small UAV, and a good case has been made for its continued use, particularly on fixed-wing UAVs which exhibit less complex aerodynamics, and superior stability in the induced sampling airflow through the instrument. Future work will focus principally on three areas: i) Mechanical ruggedisation of the fixed-wing design, since the measured effective diameter drifted significantly after continued use; ii) development of the electronics to provide both a larger size range, and single particle data for analysis of cloud droplet distributions on centimetre length scales; and iii) standardisation of the instrument data outputs, including data used as rejection criteria, which would ease the integration of the data into both datasets and models, thus increasing the overall impact of UAV research. In addition, the next iteration of the UCASS will include a shadowgraph probe—similar to the Korolev design—which will provide important data on

ice crystals, precipitation research (Zeng, 2018a), and desert dust transport research (Ryder et al., 2019). In addition, the outputs of the TIAs can be directly digitised, which will allow on-line assessment of coincidence artefacts. Shape determination is also important for future instruments, and the future UCASS probe could be modified to include a scattering asymmetry parameter, which would allow some shape determination.

UAV design problems, like all engineering tasks, are multi-variable compromises, with a settling point determined by efficiency and use-case. Large UAVs, like the Globalhawk, are likely to continue operating in roughly the same envelopes as conventional aircraft, extended to reach more extreme environments. Small UAVs, on the other hand, operate in an entirely different envelope, where conventional aircraft cannot fly or manoeuvre. The principle engineering constraints in this environment are efficiency, range, and endurance. These constraints are principally dictated by battery technology. Improvements in this area directly translate into longer flight times, higher maximum altitudes, and larger payload capacity for small UAVs, the latter of which would allow more improvements to be made to the UCASS. For this reason, advances in battery technology would have a large impact on the use of UAVs in atmospheric science generally.

A | Appendix A — Ruggedised UCASS Technical Drawings

This appendix provides more detail on the construction of the Ruggedised UCASS instrument, which is presented in the published work Girdwood et al. (2020), and further described in Sect. 3.2.1. The technical drawings for the important parts are presented and described, and context is provided with figures. Please note that some of the drawings are in different page sizes; the intended size is displayed in the drawing title block.

A.1 Flow Tube and Ellipsoidal Mirror Mount

The flow tube—part number 01-FLOWT-PRT-02—of the Ruggedised UCASS was the main tolerance reference point for all Ruggedised UCASS parts. This part served as both the optical core of the instrument, and aerodynamic path for the sample flow. The important tolerances to note are the tolerances of the holes in the top of the flow tube, which were used to attach both the alignment fibre and the UAV mounts, and the shape profile of the oblong flow cutout, which was also used to position the alignment fibre. The Mirror mount for the ellipsoidal mirror—part number 01-ELMIR-PRT-02—is also included in this section because it was manufactured from the same grade of aluminium as the flow tube, utilising the same manufacturing technique—a 5-axis computer numerically controlled (CNC) mill. Once manufactured, the parts were coated in black paint to absorb stray light. The assembly can be seen highlighted on the overall design in Fig. A.1 and Fig. A.2.

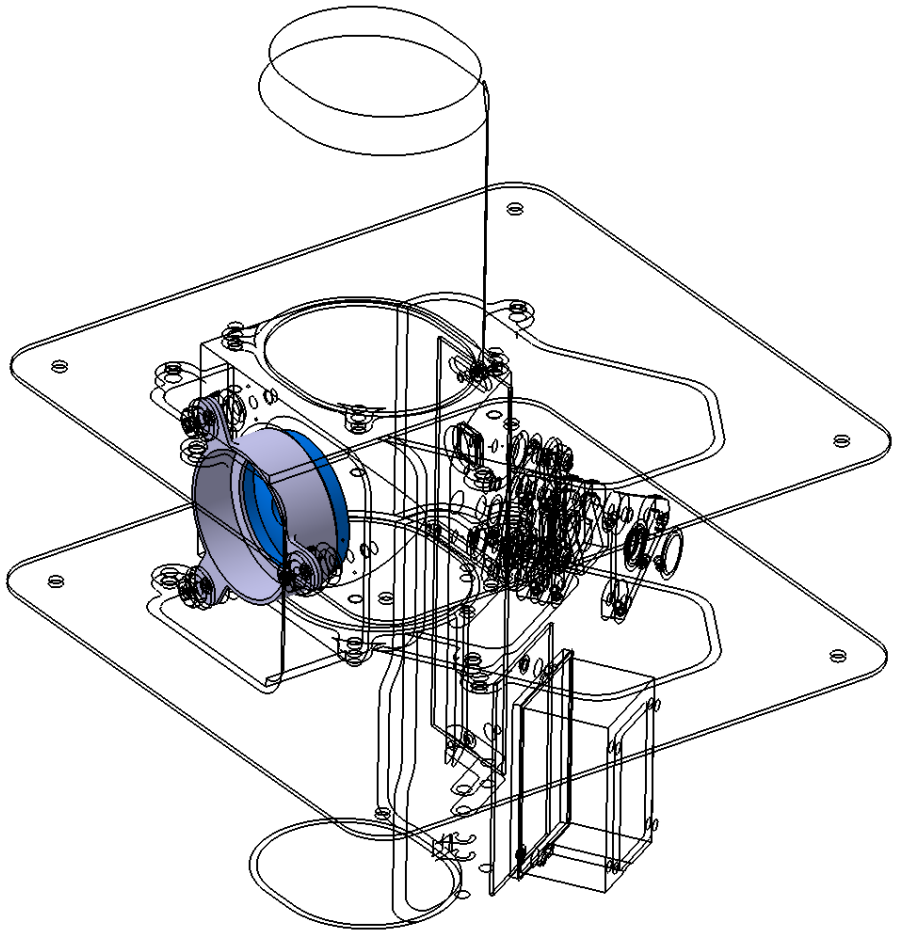

FIGURE A.1: A 3D-CAD render with the ellipsoidal mirror highlighted.

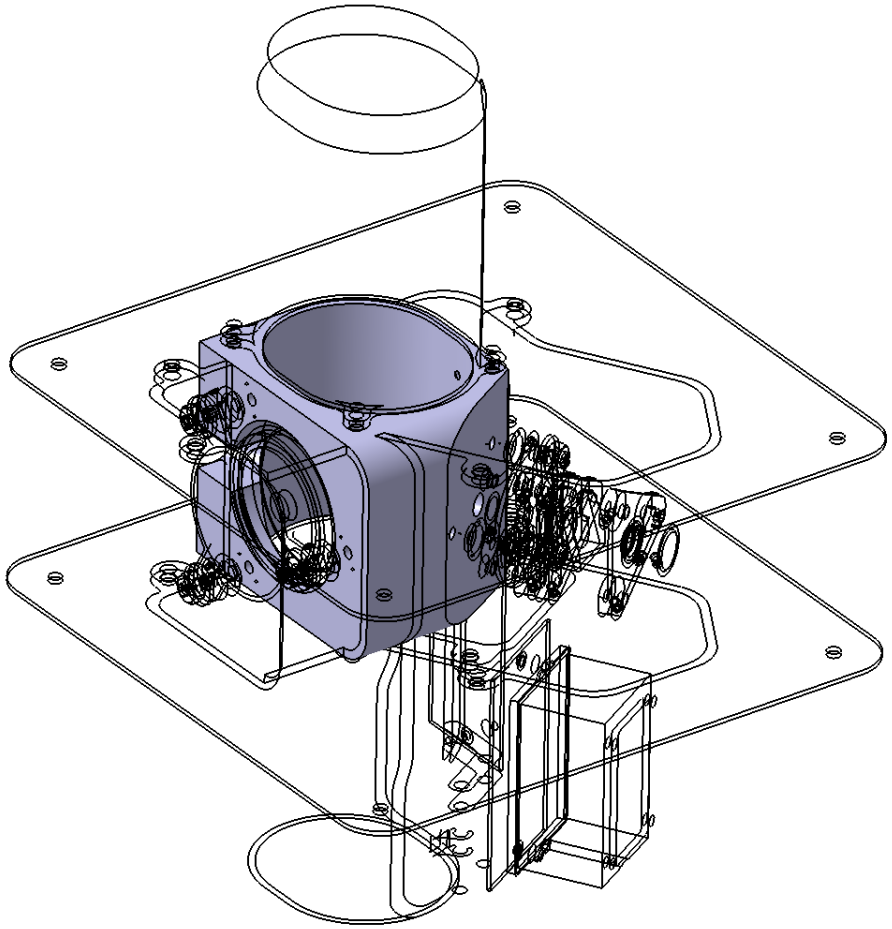

FIGURE A.2: A 3D-CAD render with the flow tube highlighted.

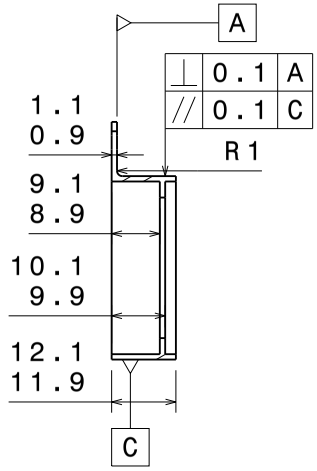

Section view A-A

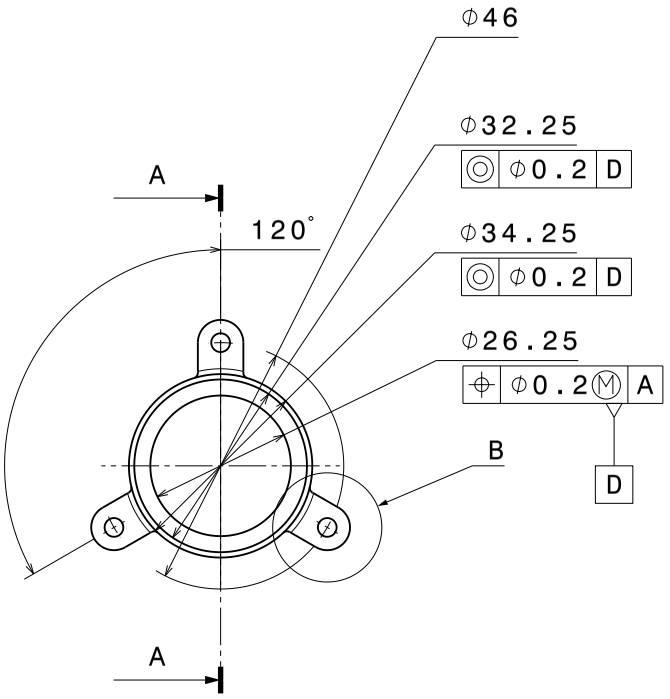

Front view

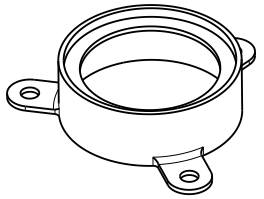

Isometric view

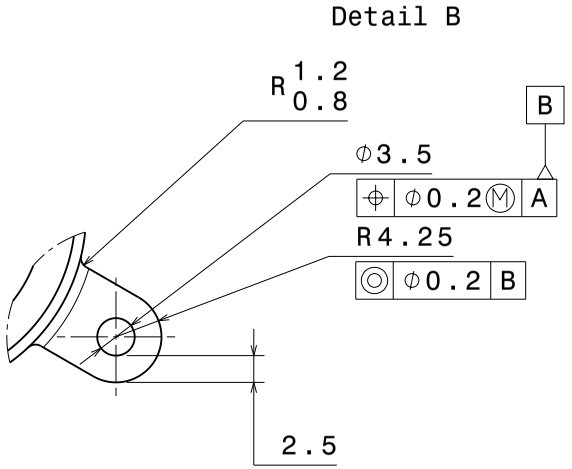

NB: EACH TAB IS IDENTICAL

NOTES:

ALL DIMENSIONS ARE IN mm
UNTOLERANCED DIMENSIONS ARE BASIC
DRAWING IN 3rd ANGLE PERSPECTIVE
TURN FROM T6061 ALUMINIUM
THREAD STANDARD DIN975

TOLERANCES:

0.2
0.08

DRAWN BY	jg17acv	DATE 10/09/2018
CHECKED BY	XXX	DATE XXX
DESIGNED BY	JGirdwood	DATE 05/09/2018

PID Research Group

DRAWING TITLE: Elliptical Mirror Mount

SIZE	DRAWING NUMBER	REV
A3	01-ELMIR-PRT-02	A

SCALE	WEIGHT(kg)		SHEET
1:1	0.00		1/1

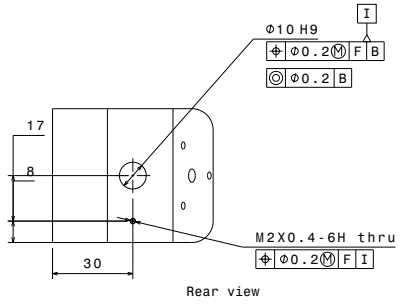

Rear view

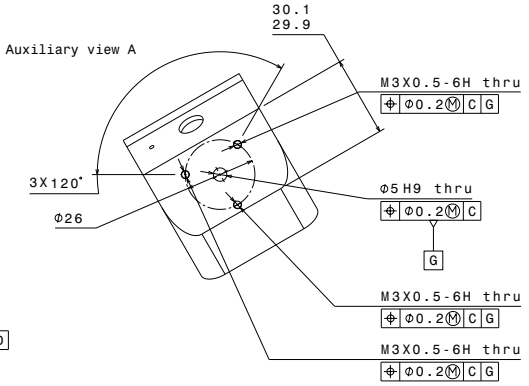

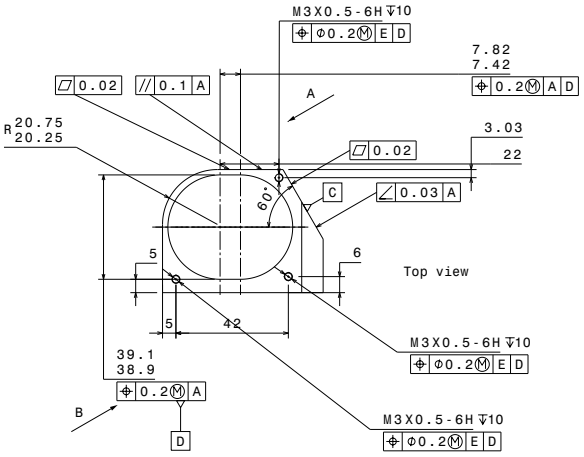

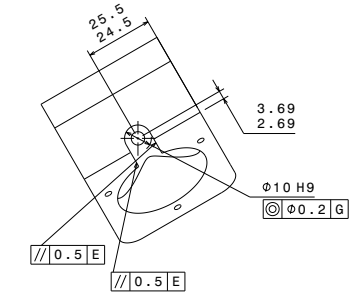

Auxiliary view B

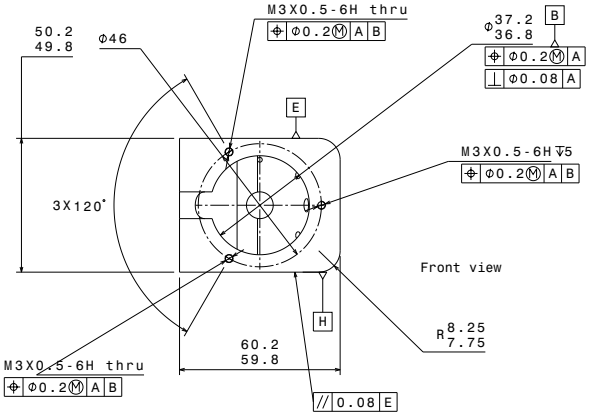

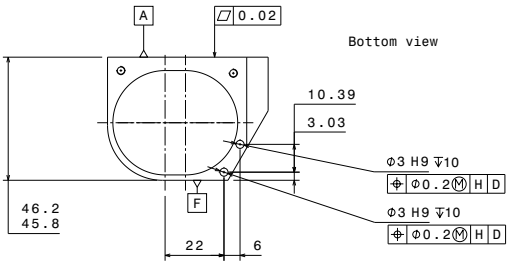

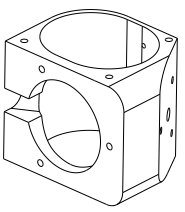

Isometric view

NOTES:

ALL DIMENSIONS ARE IN mm
UNTOLERANCED DIMENSIONS ARE BASIC
DRAWING IN 3rd ANGLE PERSPECTIVE
MILL FROM T6061 ALUMINIUM
THREAD STANDARD DIN975

TOLERANCES:

0.2
0.08

DRAWN BY	JGirdwood	DATE 05/09/2018
CHECKED BY	XXX	DATE xxx
DESIGNED BY	JGirdwood	DATE 05/09/2018

PID Research Group

DRAWING TITLE: FLOWTUBE

SIZE	DRAWING NUMBER	REV
A1	01-FLOWT-PRT-02	A

SCALE 1:1 | WEIGHT(kg) 0.11 | SHEET 1/1

A.2 Alignment Screws

The alignment screws were an important piece of the overall design, since this was the primary mechanism of retention for the optical system. The tolerances of these screws can be fairly loose, since the optical components are all aligned with a feedback system. The alignment screws are a shaft-based sub-assembly composed of a main shaft which is threaded at the top and bottom for attaching to the flow tube; two tapered washers—described in the drawings as pinchers—for centring the attached optical component; a retention spring which is only used during the alignment process; and two grub screws which lock the bottom tapered washer in place, and thus the whole assembly. The assembly can be seen highlighted on the overall design in Fig. A.3.

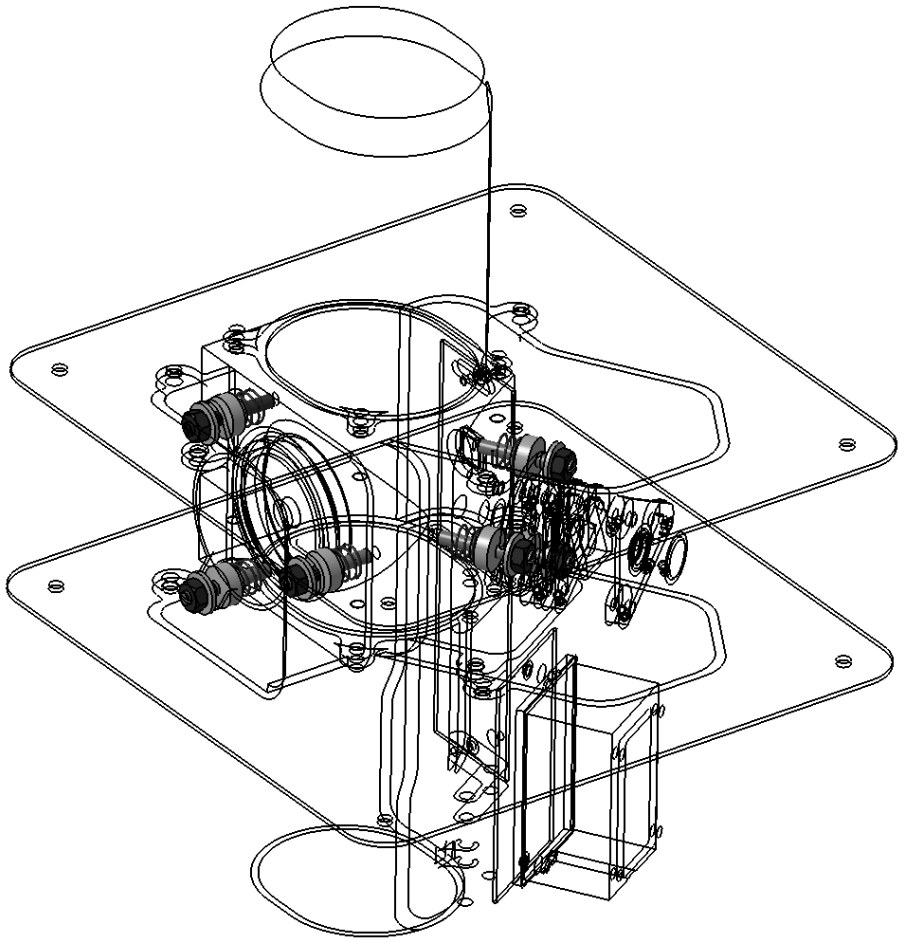

FIGURE A.3: A 3D-CAD render with the alignment screws highlighted.

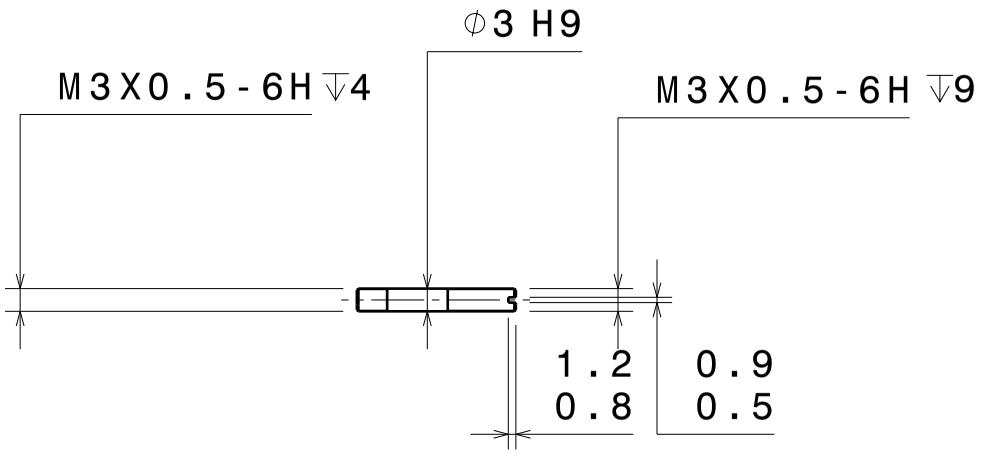

Front view

Isometric view

NOTES:

ALL DIMENSIONS ARE IN mm
UNTOLERANCED DIMENSIONS ARE BASIC
DRAWING IN 3rd ANGLE PERSPECTIVE
TURN FROM T6061 ALUMINIUM
THREAD STANDARD DIN975

TOLERANCES:

⌓ 0.2

▱ 0.08

PID Research Group

DRAWN BY: JGirdwood	DATE: 10/09/2018	DRAWING TITLE: Alignment Shaft			
CHECKED BY: XXX	DATE: XXX	SIZE: A4	DRAWING NUMBER: 02-ASHFT-PRT-01		REV: A
DESIGNED BY: JGirdwood	DATE: 05/09/2018	SCALE: 1:1	WEIGHT(kg): 0.00		SHEET: 1/1

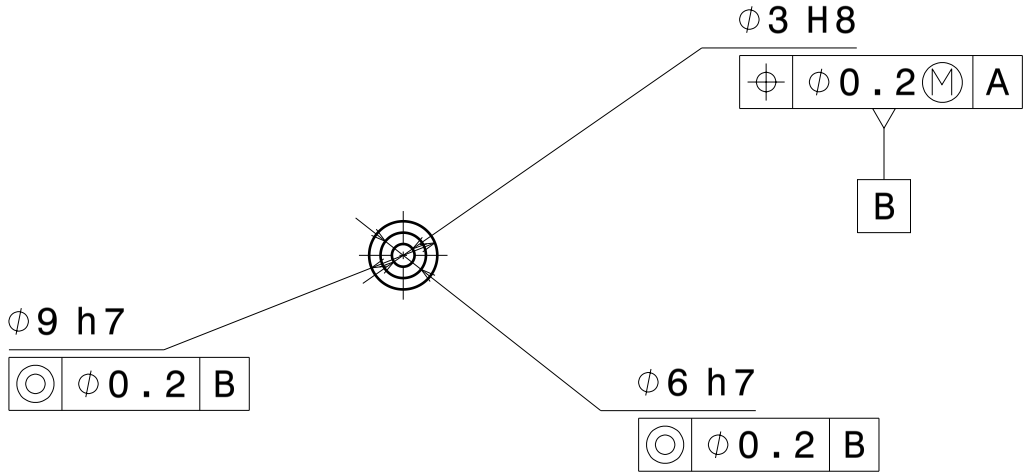

Front view

Isometric view

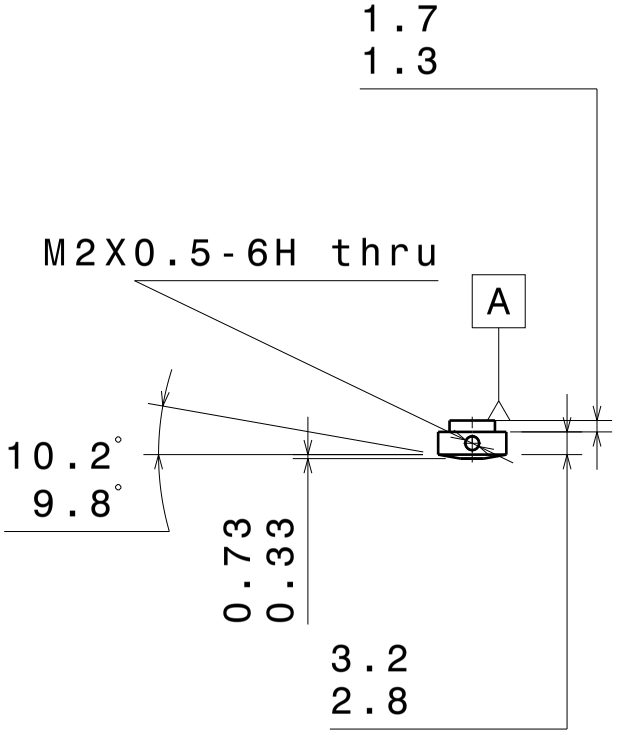

Bottom view

NOTES:

ALL DIMENSIONS ARE IN mm
UNTOLERANCED DIMENSIONS ARE BASIC
DRAWING IN 3rd ANGLE PERSPECTIVE
TURN FROM T6061 ALUMINIUM
THREAD STANDARD DIN975

TOLERANCES:

⌓	0.2
▱	0.08

PID Research Group

DRAWN BY	JGirdwood
DATE	10/09/2018
CHECKED BY	XXX
DATE	XXX
DESIGNED BY	JGirdwood
DATE	05/09/2018

DRAWING TITLE

Alignment Pincher Bottom

SIZE	DRAWING NUMBER	REV
A4	02-PBOT-PRT-01	A

SCALE	WEIGHT(kg)		SHEET
1:1	0.00		1/1

Front view

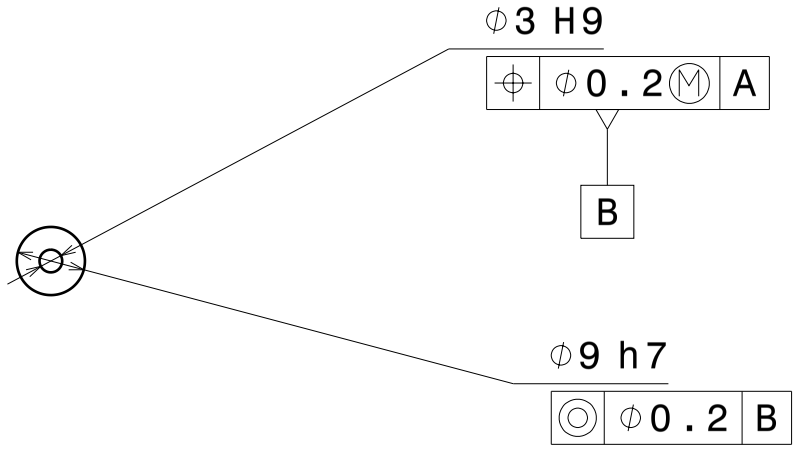

Isometric view

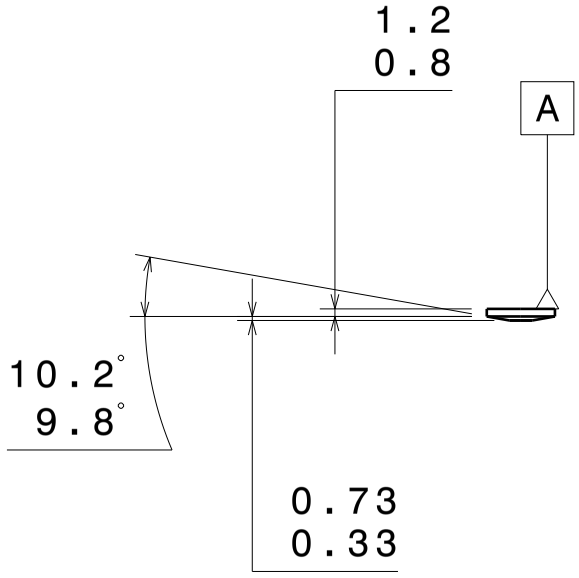

Top view

NOTES:

ALL DIMENSIONS ARE IN mm
UNTOLERANCED DIMENSIONS ARE BASIC
DRAWING IN 3rd ANGLE PERSPECTIVE
TURN FROM T6061 ALUMINIUM
THREAD STANDARD DIN975

TOLERANCES:

⌓ 0.2
▱ 0.08

PID Research Group

DRAWN BY	DATE
jg17acv	10/09/2018
CHECKED BY	DATE
XXX	XXX
DESIGNED BY	DATE
XXX	XXX

DRAWING TITLE

Alignment Pincher Top

SIZE	DRAWING NUMBER	REV
A4	02-PTOP-PRT-01	A

SCALE	WEIGHT(kg)		SHEET
1:1	0.00		1/1

A.3 Laser Carrier

The laser carrier was the generic name I gave to the opto-mechanical component which housed the aperture, beam focusing lens, and diode laser. The sub assembly is held together by three carbon fibre shafts, which each optical carrier is locked to with grub screws. The alignment screws, which were detailed in Sect. A.2, were attached to the laser carrier base (part number 04-CBASE-PRT-01); the aperture was mounted to part 04-HOLDA-PRT-01, which has cut outs for the heads of the alignment screws; the lens was mounted to part 04-HOLDG-PRT-01, which I designed as a generic optics holder to be used to hold any optical components should the need arise; and the laser was held by part 04-HOLDL-PRT-01. The assembly can be seen highlighted on the overall design in Fig. A.4.

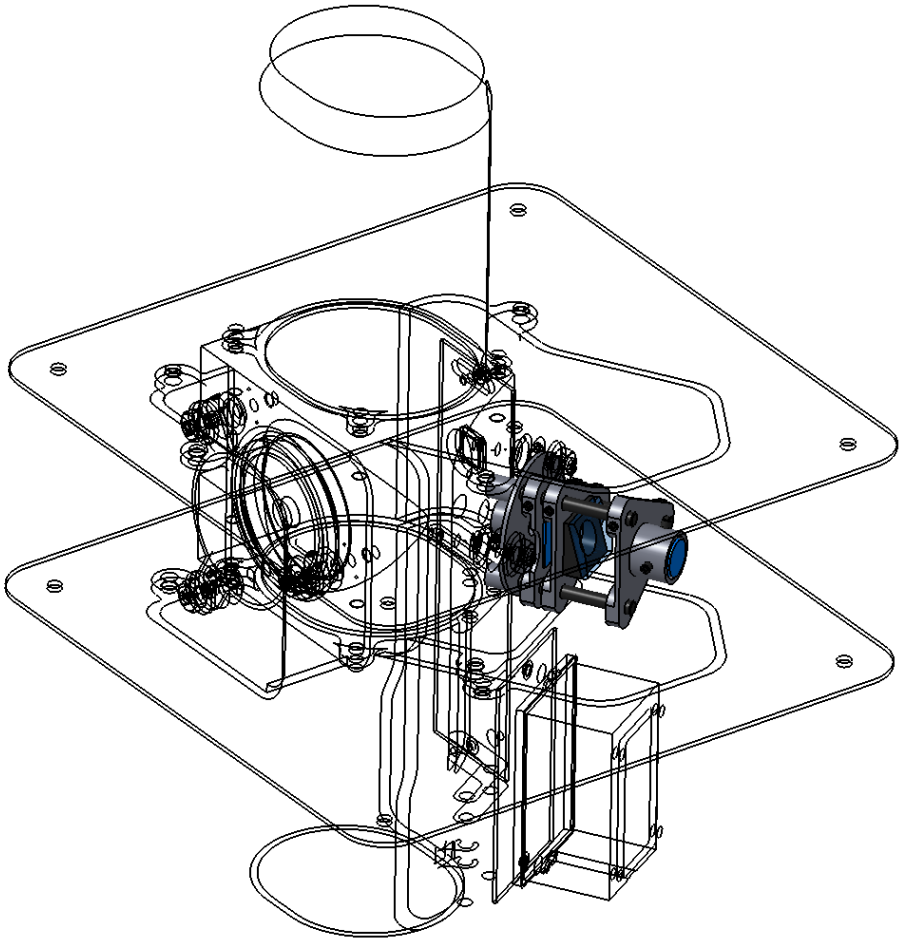

FIGURE A.4: A 3D-CAD render with the laser carrier highlighted.

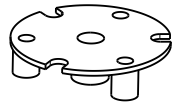

Isometric view

Front view

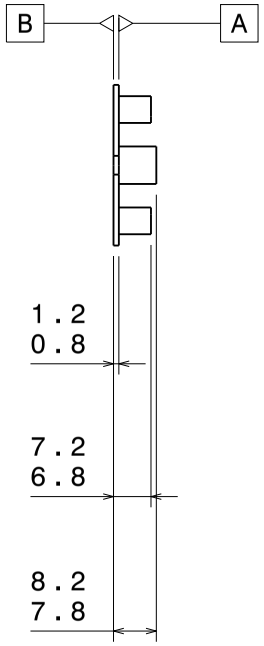

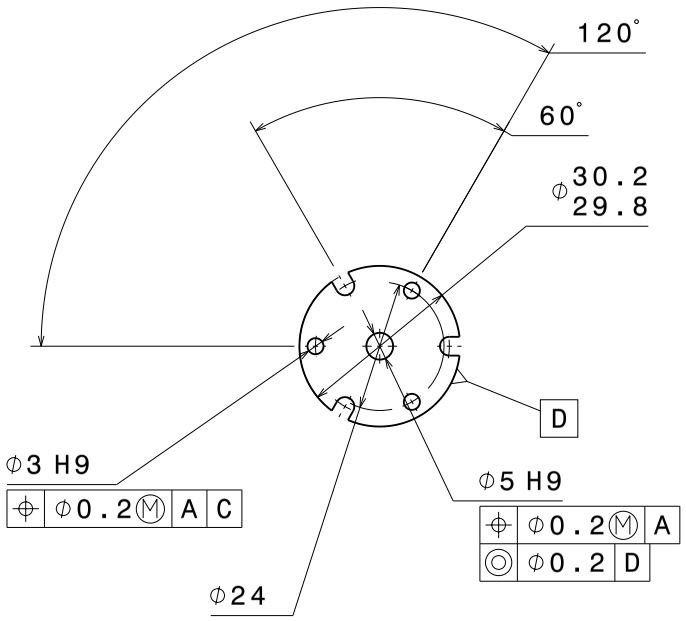

Left view

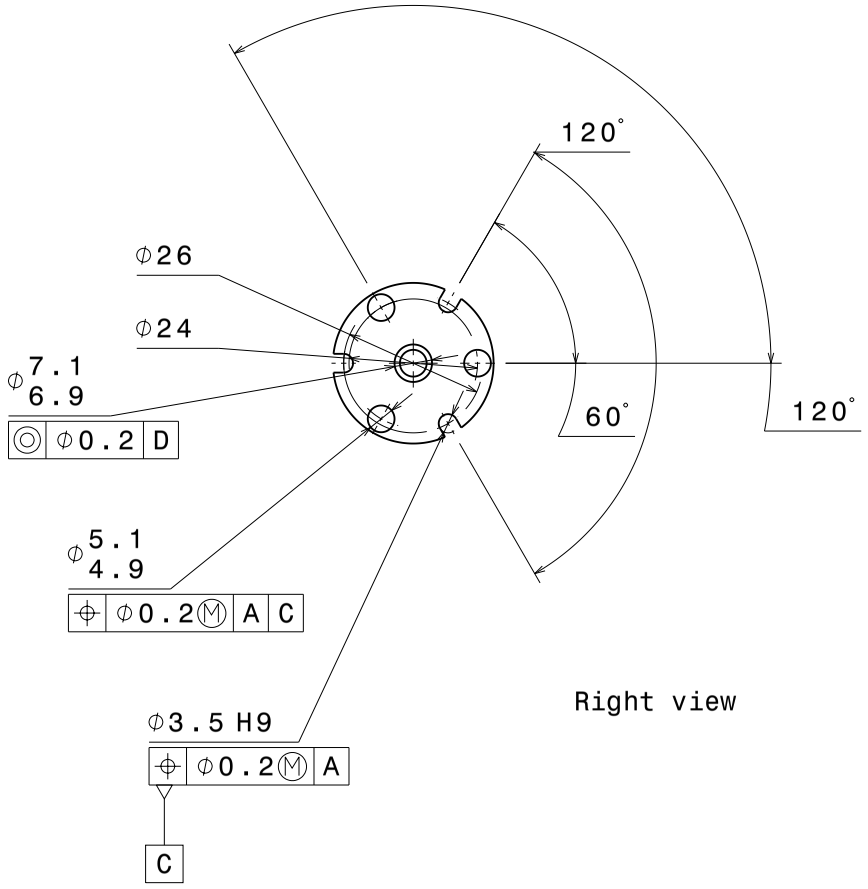

Right view

NOTES:

ALL DIMENSIONS ARE IN mm
UNTOLERANCED DIMENSIONS ARE BASIC
DRAWING IN 3rd ANGLE PERSPECTIVE
TURN FROM T6061 ALUMINIUM
THREAD STANDARD DIN975

TOLERANCES:

⌓	0.2
▱	0.08

DRAWN BY	JGirdwood	DATE 13/09/2018
CHECKED BY	XXX	DATE XXX
DESIGNED BY	JGirdwood	DATE 05/09/2018

PID Research Group

DRAWING TITLE

Laser Carrier Base

SIZE	DRAWING NUMBER	REV
A3	04-CBASE-PRT-01	A

SCALE	WEIGHT(kg)		SHEET
1:1	0.00		1/1

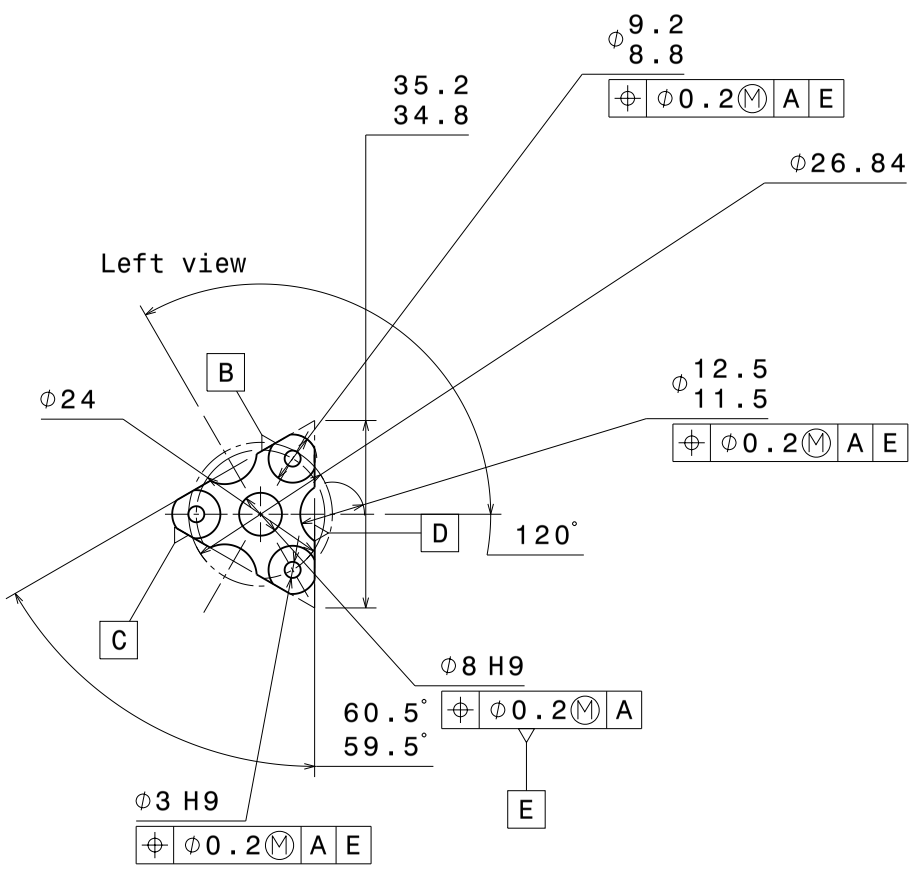

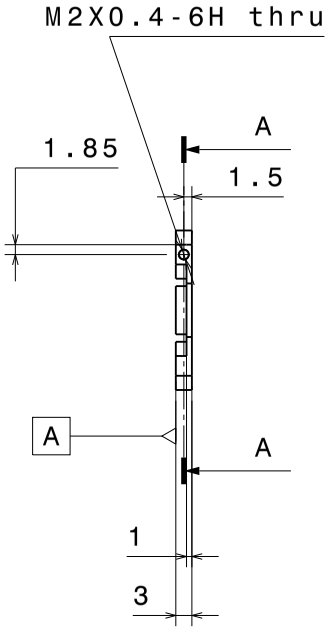

Front view

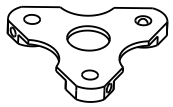

Isometric view

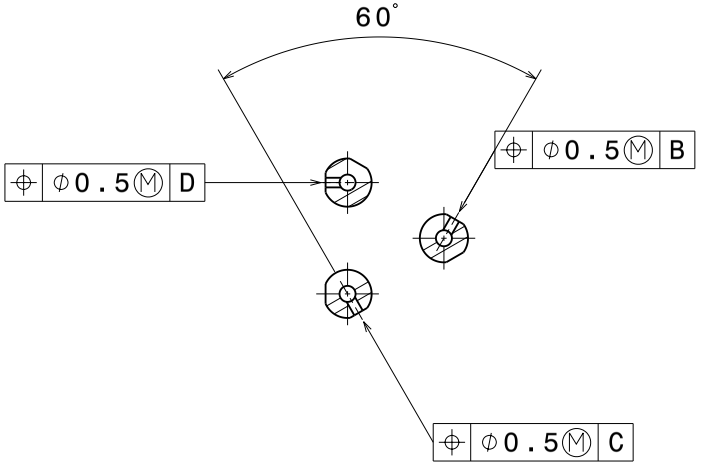

Section view A-A

NOTES:

ALL DIMENSIONS ARE IN mm
UNTOLERANCED DIMENSIONS ARE BASIC
DRAWING IN 3rd ANGLE PERSPECTIVE
TURN FROM T6061 ALUMINIUM
THREAD STANDARD DIN975

TOLERANCES:

⌓ 0.2
▱ 0.08

DRAWN BY	JGirdwood	DATE 24/09/2018
CHECKED BY	XXX	DATE XXX
DESIGNED BY	JGirdwood	DATE 05/09/2018

PID Research Group

DRAWING TITLE: Aperture Holder

SIZE	DRAWING NUMBER	REV
A3	04-HOLDA-PRT-01	A

SCALE 1:1 | WEIGHT(kg) XXX | SHEET 1/1

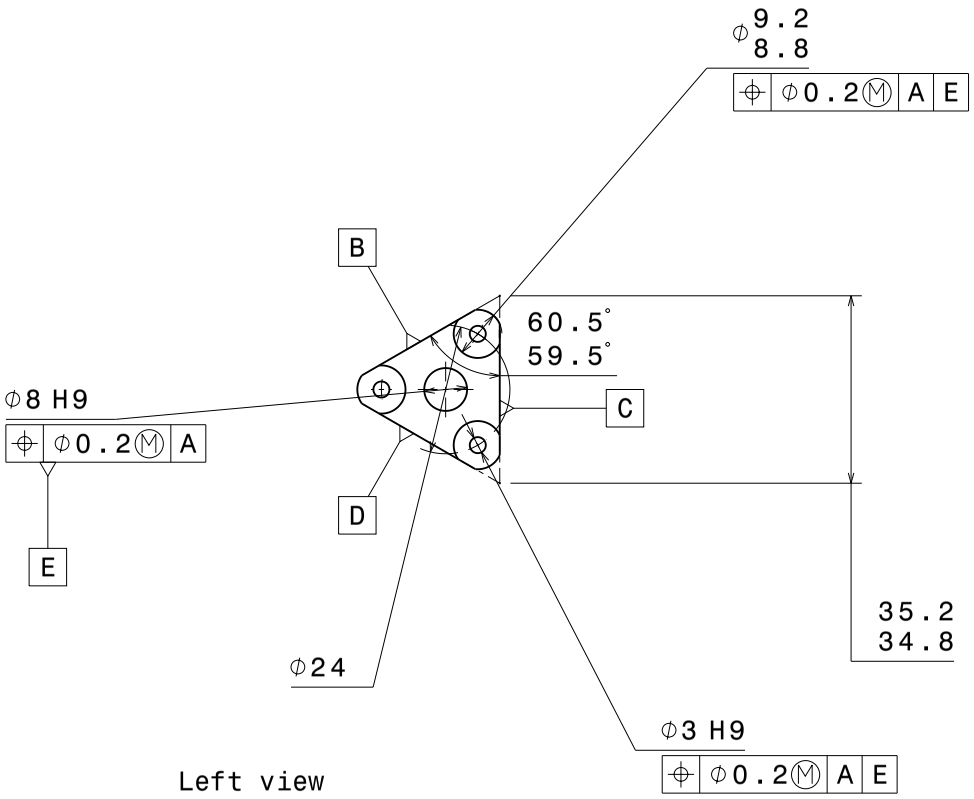

Left view

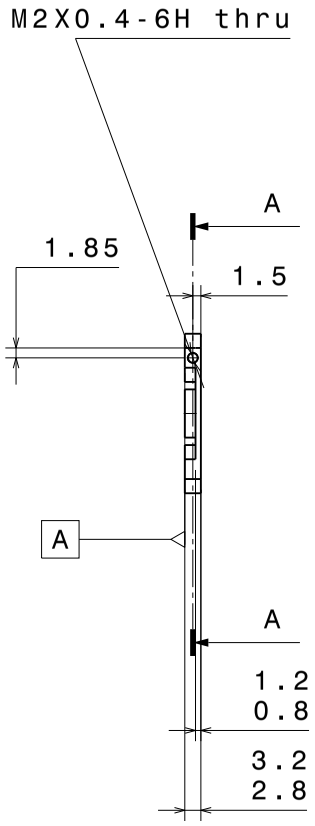

Front view

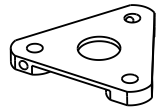

Isometric view

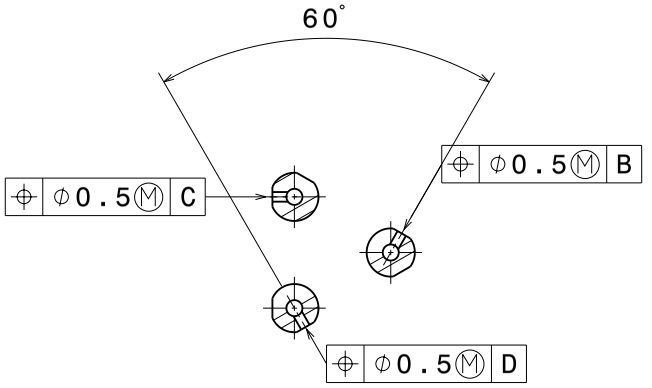

Section view A-A

NOTES:

ALL DIMENSIONS ARE IN mm
UNTOLERANCED DIMENSIONS ARE BASIC
DRAWING IN 3rd ANGLE PERSPECTIVE
TURN FROM T6061 ALUMINIUM
THREAD STANDARD DIN975

TOLERANCES:

⌓	0.2
▱	0.08

DRAWN BY	JGirdwood	DATE 18/09/2018
CHECKED BY	XXX	DATE XXX
DESIGNED BY	JGirdwood	DATE 05/09/2018

PID Research Group

DRAWING TITLE: Generic Optics Holder

SIZE	DRAWING NUMBER	REV
A3	04-HOLDG-PRT-01	A

SCALE	WEIGHT(kg)		SHEET
1:1	0.00		1/1

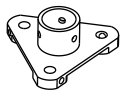

Isometric view

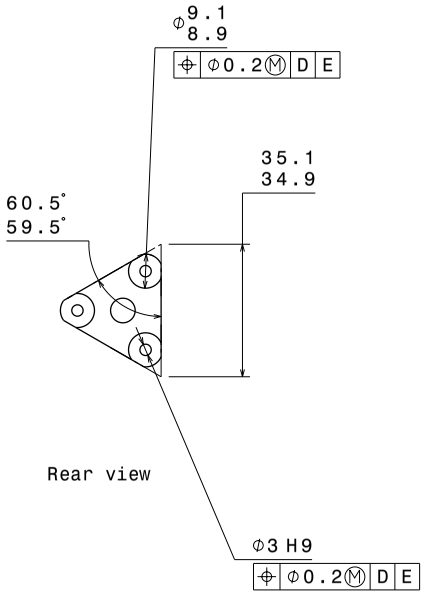

Rear view

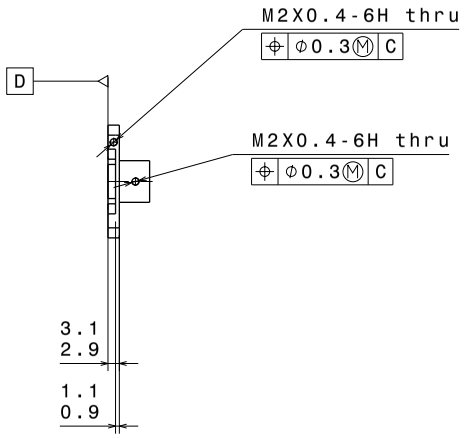

Left view

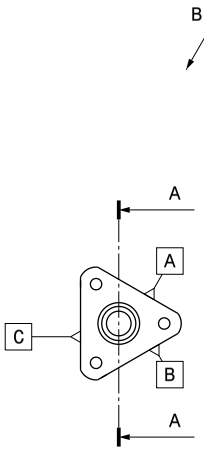

Front view

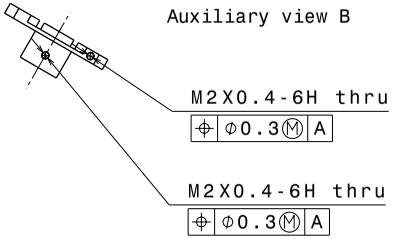

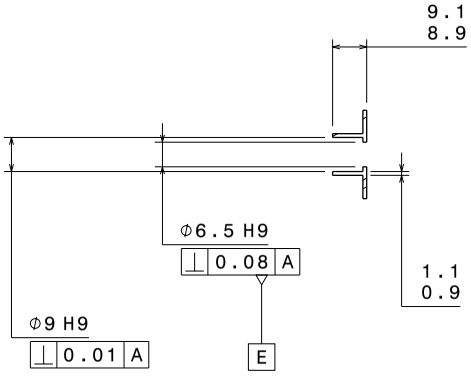

Section cut A-A

C

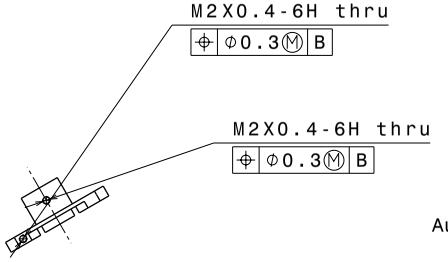

Auxiliary view C

NOTES:

ALL DIMENSIONS ARE IN mm
UNTOLERANCED DIMENSIONS ARE BASIC
DRAWING IN 3rd ANGLE PERSPECTIVE
MILL FROM T6061 ALUMINIUM
THREAD STANDARD DIN975

TOLERANCES:

0.2
0.08

DRAWN BY	JGirdwood	DATE 25/09/2018
CHECKED BY	XXX	DATE XXX
DESIGNED BY	JGirdwood	DATE 05/09/2018

PID Research Group

DRAWING TITLE: Laser Holder

SIZE	DRAWING NUMBER	REV
A2	04-HOLDL-PRT-01	A

SCALE 1:1 | WEIGHT(kg) 0.00 | SHEET 1/1

A.4 Alignment Fibre Mount

The alignment fibre mount is an important tolerance point for the overall design, since every optical part was referenced to the position of a static fibre running through the sample area. The fibre was held tight between two spindles, and rested in a groove; a secondary spindle—05-TSPIN-JIG-01—was turned to tighten the fibre over a primary spindle—05-GSPIN-JIG-01—which contained the groove to locate the fibre. I chose this configuration mainly for two reasons. The first was that spindles can be turned on a lathe, where tighter tolerances can be achieved, as opposed to a mill. The second was that the total tolerance of the fibre position at the sample area is actually half of the tolerance of the position of the groove on a single spindle, since the sample area is half way between the two. The spindles were held in two different mounting blocks—05-FHBOT-JIG-01 and 05-FHTOP-JIG-01, which were mirrors of each-other—which were held apart by three steel spacers, which had part number 05-ASPAC-JIG-01. The positioning of the fibre holder in the ruggedised UCASS during an alignment process is shown in Fig. A.5.

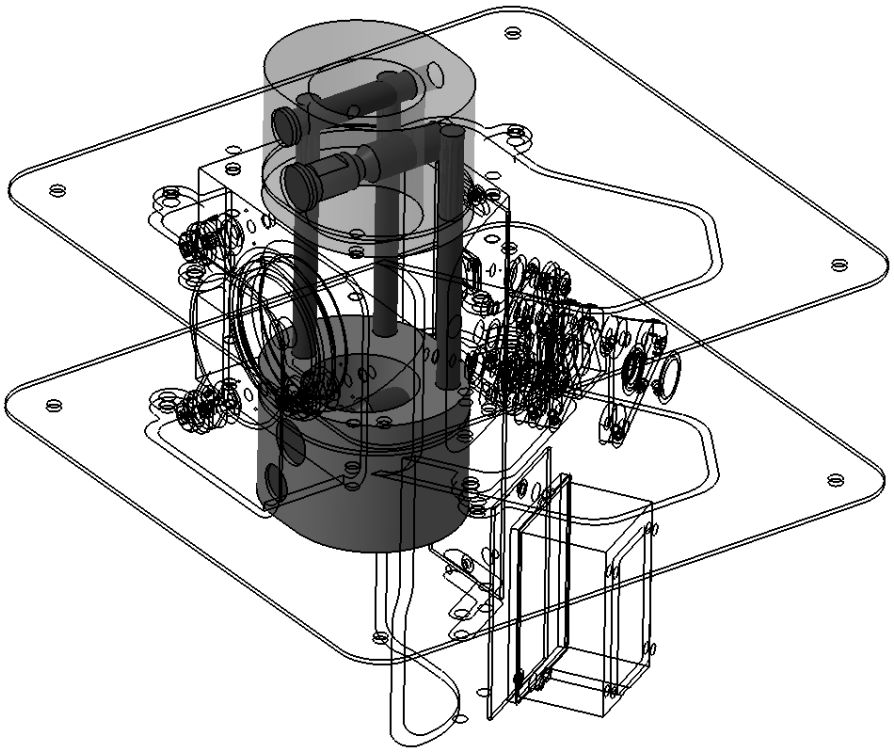

FIGURE A.5: A 3D-CAD render with the fibre holder highlighted.

Front view

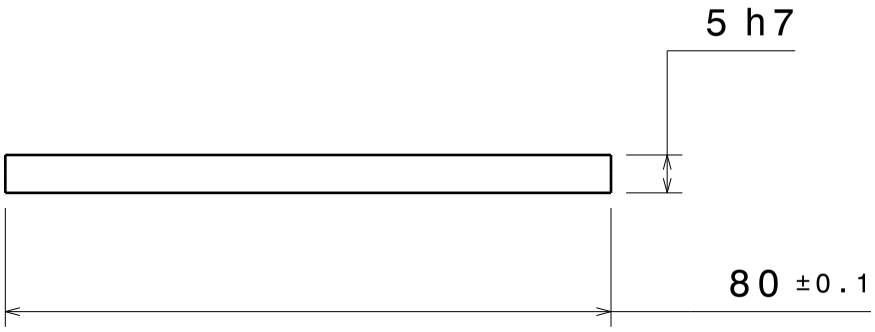

NOTES:

ALL DIMENSIONS ARE IN mm
UNTOLERANCED DIMENSIONS ARE BASIC
DRAWING IN 3rd ANGLE PERSPECTIVE
TURN FROM 304 STAINLESS STEEL
THREAD STANDARD DIN975

TOLERANCES:

⌓	0.2
▱	0.08

PID Research Group

DRAWN BY	JGirdwood	DATE	10/12/2018	DRAWING TITLE	Fibre Holder Standoff
CHECKED BY	XXX	DATE	XXX	SIZE: A4	DRAWING NUMBER: 05-ASPAC-JIG-01 — REV: A
DESIGNED BY	JGirdwood	DATE	27/11/2018	SCALE: 1:1	WEIGHT(kg): 0.01 — SHEET: 1/1

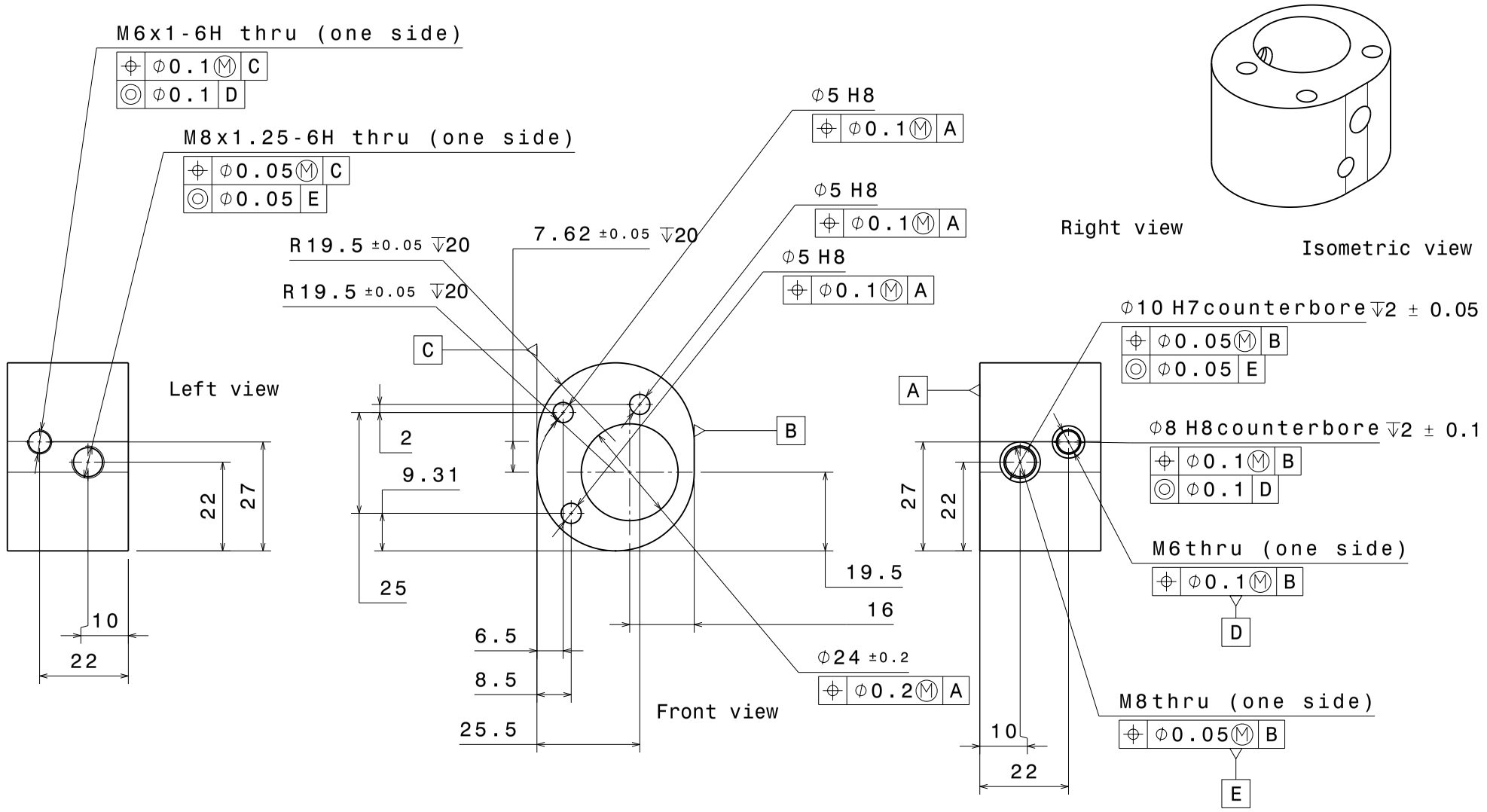

NOTES:

ALL DIMENSIONS ARE IN mm
UNTOLERANCED DIMENSIONS ARE BASIC
DRAWING IN 1st ANGLE PERSPECTIVE
TURN FROM T6061 ALUMINIUM
THREAD STANDARD DIN975

TOLERANCES:

⌓ 0.2
▱ 0.08

DRAWN BY	J Girdwood	DATE 28/11/2018
CHECKED BY	XXX	DATE XXX
DESIGNED BY	J Girdwood	DATE 27/11/2018

PID Research Group

DRAWING TITLE: Fibre Holder Bottom

SIZE	DRAWING NUMBER	REV
A3	05-FHBOT-JIG-01	A

SCALE	WEIGHT(kg)		SHEET
1:1	0.08		1/1

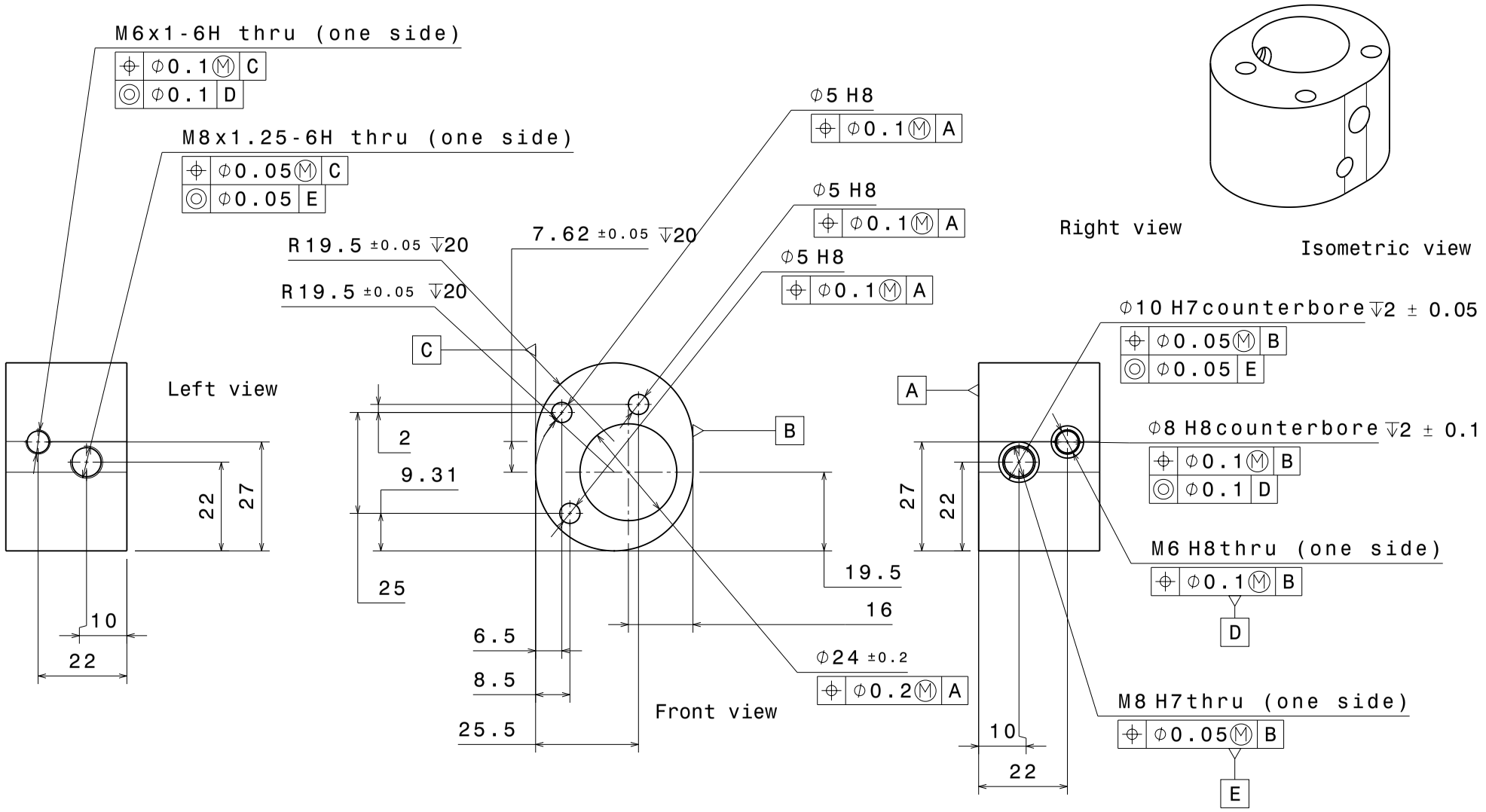

NOTES:

ALL DIMENSIONS ARE IN mm
UNTOLERANCED DIMENSIONS ARE BASIC
DRAWING IN 3rd ANGLE PERSPECTIVE
TURN FROM T6061 ALUMINIUM
THREAD STANDARD DIN975

TOLERANCES:

⌓ 0.2
▱ 0.08

DRAWN BY	J Girdwood	DATE 28/11/2018
CHECKED BY	XXX	DATE XXX
DESIGNED BY	J Girdwood	DATE 27/11/2018

PID Research Group

DRAWING TITLE: Fibre Holder Top

SIZE	DRAWING NUMBER	REV
A3	05-FHTOP-JIG-01	A

SCALE	WEIGHT(kg)		SHEET
1:1	0.08		1/1

Front view

Right view

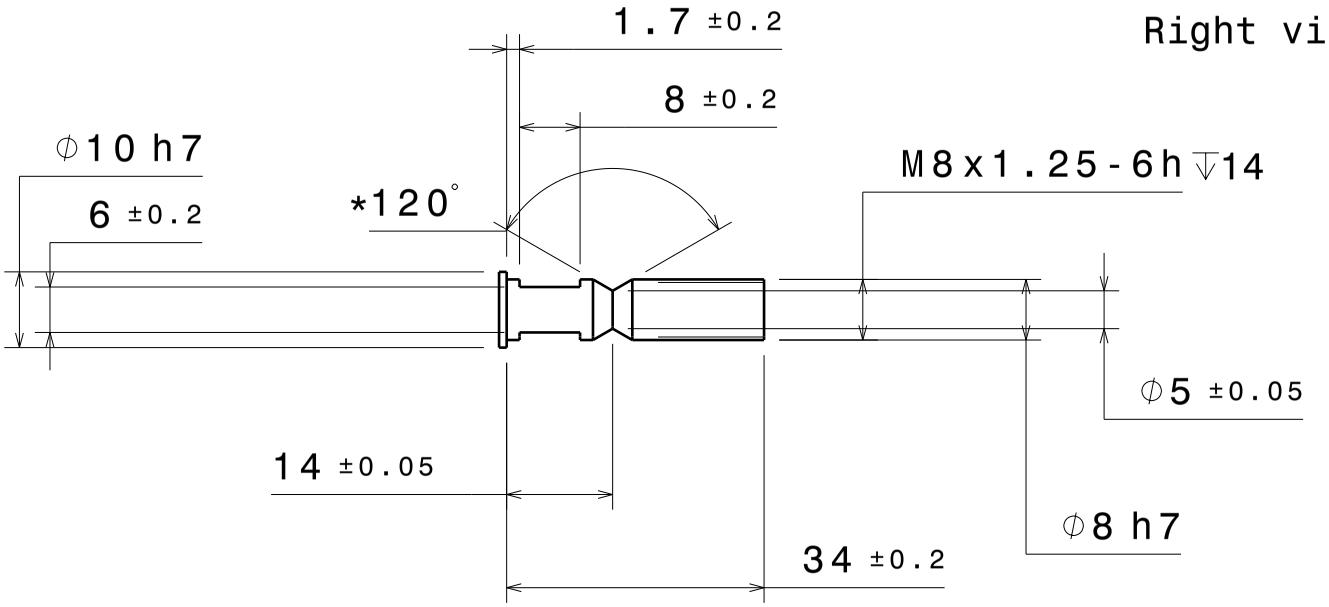

* Actual value of this angle is not important, dependant on tool used. Working tolerance: ±100°

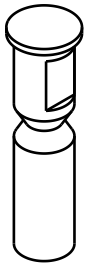

Isometric view

NOTES:

ALL DIMENSIONS ARE IN mm
UNTOLERANCED DIMENSIONS ARE BASIC
DRAWING IN 3rd ANGLE PERSPECTIVE
TURN FROM 304 STAINLESS STEEL
THREAD STANDARD DIN975

TOLERANCES:

⌓	0.2
▱	0.08

PID Research Group

DRAWN BY	JGirdwood
DATE	10/12/2018
CHECKED BY	XXX
DATE	XXX
DESIGNED BY	JGirdwood
DATE	27/11/2018

DRAWING TITLE

Fibre Guide Spindle

SIZE	DRAWING NUMBER	REV
A4	05-GSPIN-JIG-01	A

SCALE	WEIGHT(kg)		SHEET
1:1	0.01		1/1

Front view

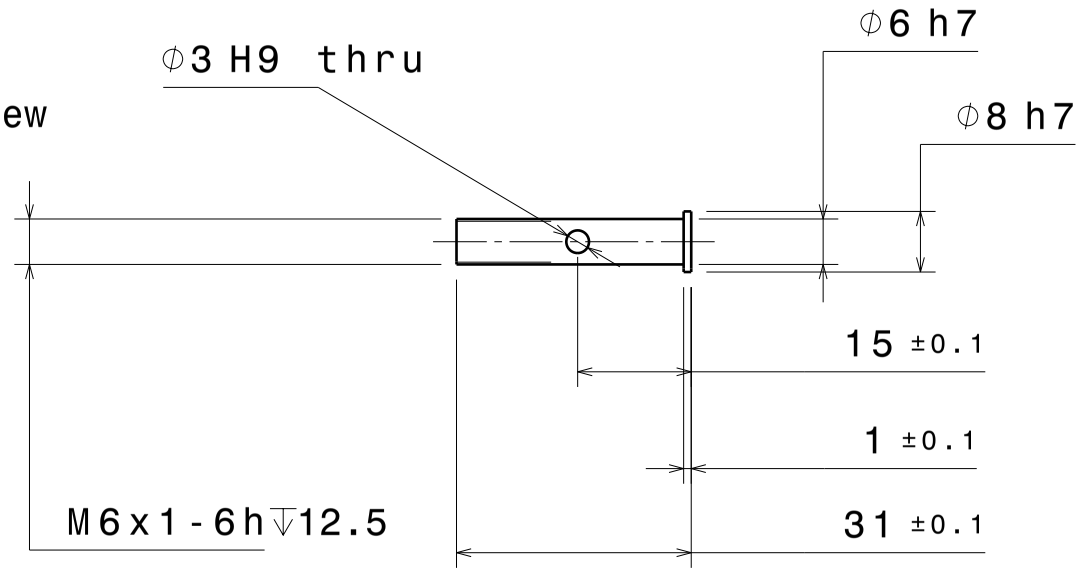

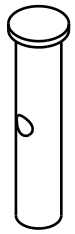

Isometric view

NOTES:

ALL DIMENSIONS ARE IN mm
UNTOLERANCED DIMENSIONS ARE BASIC
DRAWING IN 3rd ANGLE PERSPECTIVE
TURN FROM 304 STAINLESS STEEL
THREAD STANDARD DIN975

TOLERANCES:

⌓	0.2
▱	0.08

PID Research Group

DRAWING TITLE

Fibre Clamping Spindle

DRAWN BY: JGirdwood	DATE: 10/12/2018	SIZE: A4	DRAWING NUMBER: 05-TSPIN-JIG-01	REV: A
CHECKED BY: XXX	DATE: XXX			
DESIGNED BY: JGirdwood	DATE: 27/11/2018	SCALE: 1:1	WEIGHT(kg): 0.01	SHEET: 1/1

Bibliography

3DRobotics. Pixhawk 1.2, 2013. URL https://pixhawk.org/.

P. Abichandani, D. Lobo, G. Ford, D. Bucci, and M. Kam. Wind Measurement and Simulation Techniques in Multi-Rotor Small Unmanned Aerial Vehicles. *IEEE Access*, 8:54910–54927, 2020. ISSN 21693536. doi: 10.1109/ACCESS.2020.2977693.

A. S. Ackerman, M. P. Kirkpatrick, D. E. Stevens, and O. B. Toon. The impact of humidity above stratiform clouds on indirect aerosol climate forcing. *Nature*, 432(7020):1014–1017, 2004. ISSN 00280836. doi: 10.1038/nature03174.

C. J. Allen, R. Washington, and S. Engelstaedter. Dust emission and transport mechanisms in the central Sahara: Fennec ground-based observations from Bordj Badji Mokhtar, June 2011. *Journal of Geophysical Research Atmospheres*, 118(12):6212–6232, 2013a. ISSN 21698996. doi: 10.1002/jgrd.50534.

C. J. T. Allen, R. Washington, and S. Engelstaedter. Dust emission and transport mechanisms in the central sahara: Fennec ground-based observations from bordj badji mokhtar, june 2011. *Journal of Geophysical Research: Atmospheres*, 118(12):6212–6232, 2013b. doi: https://doi.org/10.1002/jgrd.50534. URL https://agupubs.onlinelibrary.wiley.com/doi/abs/10.1002/jgrd.50534.

D. Althausen, R. Engelmann, H. Baars, B. Heese, A. Ansmann, D. Müller, and M. Komppula. Portable Raman Lidar Polly XT for Automated Profiling of Aerosol Backscatter, Extinction, and Depolarization. *Journal of Atmospheric and Oceanic Technology*, 26(11):2366–2378, 11 2009. ISSN 0739-0572. doi: 10.1175/2009JTECHA1304.1. URL http://journals.ametsoc.org/doi/10.1175/2009JTECHA1304.1.

B. Altstädter, A. Platis, B. Wehner, A. Scholtz, N. Wildmann, M. Hermann, R. Käthner, H. Baars, J. Bange, and A. Lampert. ALADINA – an unmanned research aircraft for observing vertical and

horizontal distributions of ultrafine particles within the atmospheric boundary layer. *Atmospheric Measurement Techniques*, 8(4):1627–1639, 4 2015. ISSN 1867-8548. doi: 10.5194/amt-8-1627-2015. URL https://amt.copernicus.org/articles/8/1627/2015/.

B. Altstädter, A. Platis, M. Jähn, H. Baars, J. Lückerath, A. Held, A. Lampert, J. Bange, M. Hermann, and B. Wehner. Airborne observations of newly formed boundary layer aerosol particles under cloudy conditions. *Atmospheric Chemistry and Physics*, 18(11):8249–8264, 2018. ISSN 16807324. doi: 10.5194/acp-18-8249-2018.

M. Alvarado, F. Gonzalez, P. Erskine, D. Cliff, and D. Heuff. A Methodology to Monitor Airborne PM10 Dust Particles Using a Small Unmanned Aerial Vehicle. *Sensors*, 17(2):343, 2 2017. ISSN 1424-8220. doi: 10.3390/s17020343. URL http://www.mdpi.com/1424-8220/17/2/343.

Arduino. Arduino, 2022. URL https://www.arduino.cc/.

P. Arias, N. Bellouin, E. Coppola, R. Jones, G. Krinner, J. Marotzke, V. Naik, M. Palmer, G.-K. Plattner, J. Rogelj, M. Rojas, J. Sillmann, T. Storelvmo, P. Thorne, B. Trewin, K. Achuta Rao, B. Adhikary, R. Allan, K. Armour, G. Bala, R. Barimalala, S. Berger, J. Canadell, C. Cassou, A. Cherchi, W. Collins, W. Collins, S. Connors, S. Corti, F. Cruz, F. Dentener, C. Dereczynski, A. Di Luca, A. Diongue Niang, F. Doblas-Reyes, A. Dosio, H. Douville, F. Engelbrecht, V. Eyring, E. Fischer, P. Forster, B. Fox-Kemper, J. Fuglestvedt, J. Fyfe, N. Gillett, L. Goldfarb, I. Gorodetskaya, J. Gutierrez, R. Hamdi, E. Hawkins, H. Hewitt, P. Hope, A. Islam, C. Jones, D. Kaufman, R. Kopp, Y. Kosaka, J. Kossin, S. Krakovska, J.-Y. Lee, J. Li, T. Mauritsen, T. Maycock, M. Meinshausen, S.-K. Min, P. Monteiro, T. Ngo-Duc, F. Otto, I. Pinto, A. Pirani, K. Raghavan, R. Ranasinghe, A. Ruane, L. Ruiz, J.-B. Sallée, B. Samset, S. Sathyendranath, S. Seneviratne, A. Sörensson, S. Szopa, I. Takayabu, A.-M. Tréguier, B. van den Hurk, R. Vautard, K. von Schuckmann, S. Zaehle, X. Zhang, and K. Zickfeld. *Technical Summary. In Climate Change 2021: The Physical Science Basis. Contribution of Working Group I to the Sixth Assessment Report of the Intergovernmental Panel on Climate Change.* Cambridge University Press, Cambridge, 2021. URL https://www.ipcc.ch/report/ar6/wg1/downloads/report/IPCC_AR6_WGI_TS.pdf.

M. A. Atwater. The Radiation Budget for Polluted Layers of the Urban Environment. *Journal of Applied Meteorology*, 10(2):205–214, 4 1971. ISSN 0021-8952. doi: 10.1175/1520-0450(1971)010<0205:TRBFPL>2.0.CO;2. URL http://journals.ametsoc.org/doi/10.1175/1520-0450(1971)010%3C0205:TRBFPL%3E2.0.CO;2.

H. Baars, T. Kanitz, R. Engelmann, D. Althausen, B. Heese, M. Komppula, J. Preißler, M. Tesche, A. Ansmann, U. Wandinger, J.-H. Lim, J. Y. Ahn, I. S. Stachlewska, V. Amiridis, E. Marinou, P. Seifert, J. Hofer,

A. Skupin, F. Schneider, S. Bohlmann, A. Foth, S. Bley, A. Pfüller, E. Giannakaki, H. Lihavainen, Y. Viisanen, R. K. Hooda, S. Pereira, D. Bortoli, F. Wagner, I. Mattis, L. Janicka, K. M. Markowicz, P. Achtert, P. Artaxo, T. Pauliquevis, R. A. F. Souza, V. P. Sharma, P. G. van Zyl, J. P. Beukes, J. Y. Sun, E. G. Rohwer, R. Deng, R. E. Mamouri, and F. Zamorano. PollyNET: a global network of automated Raman-polarization lidars for continuous aerosol profiling. *Atmospheric Chemistry and Physics Discussions*, 15 (19):27943–28004, 10 2015. ISSN 1680-7375. doi: 10.5194/acpd-15-27943-2015.

L. Barbieri, S. T. Kral, S. C. C. Bailey, A. E. Frazier, J. D. Jacob, J. Reuder, D. Brus, P. B. Chilson, C. Crick, C. Detweiler, A. Doddi, J. Elston, H. Foroutan, J. González-Rocha, B. R. Greene, M. I. Guzman, A. L. Houston, A. Islam, O. Kemppinen, D. Lawrence, E. A. Pillar-Little, S. D. Ross, M. P. Sama, D. G. Schmale, T. J. Schuyler, A. Shankar, S. W. Smith, S. Waugh, C. Dixon, S. Borenstein, and G. de Boer. Intercomparison of Small Unmanned Aircraft System (sUAS) Measurements for Atmospheric Science during the LAPSE-RATE Campaign. *Sensors*, 19(9):2179, Jan. 2019. ISSN 1424-8220. doi: 10.3390/s19092179. URL `https://www.mdpi.com/1424-8220/19/9/2179`. Number: 9 Publisher: Multidisciplinary Digital Publishing Institute.

K. Bärfuss, F. Pätzold, B. Altstädter, E. Kathe, and S. Nowak. New Setup of the UAS ALADINA for Measuring Boundary Layer Properties, Atmospheric Particles and Solar Radiation. *Atmosphere*, 9(1):28, 1 2018. ISSN 2073-4433. doi: 10.3390/atmos9010028. URL `http://www.mdpi.com/2073-4433/9/1/28`.

T. S. Bates, P. K. Quinn, J. E. Johnson, A. Corless, F. J. Brechtel, S. E. Stalin, C. Meinig, and J. F. Burkhart. Measurements of atmospheric aerosol vertical distributions above Svalbard, Norway, using unmanned aerial systems (UAS). *Atmospheric Measurement Techniques*, 6(8):2115–2120, 2013. ISSN 18671381. doi: 10.5194/amt-6-2115-2013.

D. Baumgardner. An Analysis and Comparison of Five Water Droplet Measuring Instruments. *Journal of Climate and Applied Meteorology*, 22(5):891–910, 5 1983. ISSN 0733-3021. doi: 10.1175/1520-0450(1983)022<0891:AAACOF>2.0.CO;2. URL `http://journals.ametsoc.org/doi/abs/10.1175/1520-0450%281983%29022%3C0891%3AAAACOF%3E2.0.CO%3B2`.

D. Baumgardner and M. Spowart. Evaluation of the Forward Scattering Spectrometer Probe. Part III: Time Response and Laser Inhomogeneity Limitations. *Journal of Atmospheric and Oceanic Technology*, 7(5): 666–672, 10 1990. ISSN 0739-0572. doi: 10.1175/1520-0426(1990)007<0666:EOTFSS>2.0.CO;2. URL `http://journals.ametsoc.org/doi/10.1175/1520-0426(1990)007%3C0666:EOTFSS%3E2.0.CO;2`.

D. Baumgardner, W. Strapp, and J. E. Dye. Evaluation of the Forward Scattering Spectrometer Probe. Part II: Corrections for Coincidence and Dead-Time Losses. *Journal of Atmospheric and Oceanic Technology*, 2

(4):626–632, 12 1985. ISSN 0739-0572. doi: 10.1175/1520-0426(1985)002<0626:EOTFSS>2.0.CO;2. URL http://journals.ametsoc.org/doi/10.1175/1520-0426(1985)002%3C0626:EOTFSS%3E2.0.CO;2.

D. Baumgardner, H. Jonsson, W. Dawson, D. O'Connor, and R. Newton. The cloud, aerosol and precipitation spectrometer: a new instrument for cloud investigations. *Atmospheric Research*, 59-60:251–264, 10 2001. ISSN 01698095. doi: 10.1016/S0169-8095(01)00119-3. URL https://linkinghub.elsevier.com/retrieve/pii/S0169809501001193.

D. Baumgardner, J. L. Brenguier, A. Bucholtz, H. Coe, P. DeMott, T. J. Garrett, J. F. Gayet, M. Hermann, A. Heymsfield, A. Korolev, M. Krämer, A. Petzold, W. Strapp, P. Pilewskie, J. Taylor, C. Twohy, M. Wendisch, W. Bachalo, and P. Chuang. Airborne instruments to measure atmospheric aerosol particles, clouds and radiation: A cook's tour of mature and emerging technology. *Atmospheric Research*, 102 (1-2):10–29, 2011. ISSN 01698095. doi: 10.1016/j.atmosres.2011.06.021.

K. V. Beard and H. T. Ochs. Warm-Rain Initiation: An Overview of Microphysical Mechanisms. *Journal of Applied Meteorology*, 32(4):608–625, 4 1993. ISSN 0894-8763. doi: 10.1175/1520-0450(1993)032<0608:WRIAOO>2.0.CO;2. URL http://journals.ametsoc.org/doi/abs/10.1175/1520-0450%281993%29032%3C0608%3AWRIAOO%3E2.0.CO%3B2.

N. Bei, X. Li, Q. Wang, S. Liu, J. Wu, J. Liang, L. Liu, R. Wang, and G. Li. Impacts of Aerosol-Radiation Interactions on the Wintertime Particulate Pollution under Different Synoptic Patterns in the Guanzhong Basin, China. *Advances in Atmospheric Sciences*, 38(7):1141–1152, 2021. ISSN 18619533. doi: 10.1007/s00376-020-0329-7.

T. M. Bell, P. M. Klein, J. K. Lundquist, and S. Waugh. Remote-sensing and radiosonde datasets collected in the San Luis Valley during the LAPSE-RATE campaign. *Earth System Science Data*, 13(3):1041–1051, Mar. 2021. ISSN 1866-3508. doi: 10.5194/essd-13-1041-2021. URL https://essd.copernicus.org/articles/13/1041/2021/. Publisher: Copernicus GmbH.

C. J. Bennett, G. J. Nott, A. Wellpott, N. Lawson, M. Delise, B. Woodcock, and G. B. Gratton. Characterizing Instrumentation Canister Aerodynamics of FAAM BAe-146-301 Atmospheric Research Aircraft. *Journal of Aerospace Engineering*, 32(4):04019047, 7 2019. ISSN 0893-1321. doi: 10.1061/(ASCE)AS.1943-5525.0001044. URL http://ascelibrary.org/doi/10.1061/%28ASCE%29AS.1943-5525.0001044.

K. Beswick, D. Baumgardner, M. Gallagher, A. Volz-Thomas, P. Nedelec, K. Y. Wang, and S. Lance. The backscatter cloud probe-a compact low-profile autonomous optical spectrometer. *Atmospheric Measurement Techniques*, 7(5):1443–1457, 2014. ISSN 18678548. doi: 10.5194/amt-7-1443-2014.

S. Bezantakos, F. Schmidt-Ott, and G. Biskos. Performance evaluation of the cost-effective and lightweight Alphasense optical particle counter for use onboard unmanned aerial vehicles. *Aerosol Science and Technology*, 52(4):385–392, 2018. ISSN 15217388. doi: 10.1080/02786826.2017.1412394. URL https://doi.org/10.1080/02786826.2017.1412394.

A. M. Blyth. Entrainment in Cumulus Clouds. *Journal of Applied Meteorology*, 32(4):626–641, 4 1993. ISSN 0894-8763. doi: 10.1175/1520-0450(1993)032<0626:EICC>2.0.CO;2. URL http://journals.ametsoc.org/doi/abs/10.1175/1520-0450%281993%29032%3C0626%3AEICC%3E2.0.CO%3B2.

A. I. Bokoye, A. Royer, N. T. O'Neill, and L. J. Bruce McArthur. A North American Arctic aerosol climatology using ground-based sunphotometry. *Arctic*, 55(3):215–228, 2002. ISSN 00040843.

O. Boucher, C. Granier, C. Hoose, and J. Andy. Clouds and Aerosols. In Intergovernmental Panel on Climate Change, editor, *Climate Change 2013 - The Physical Science Basis*, volume 9781107057, pages 571–658. Cambridge University Press, Cambridge, 2013. ISBN 9781107415324. doi: 10.1017/CBO9781107415324.016. URL https://www.cambridge.org/core/product/identifier/CBO9781107415324A024/type/book_part.

J. M. Brady, M. D. Stokes, J. Bonnardel, and T. H. Bertram. Characterization of a Quadrotor Unmanned Aircraft System for Aerosol-Particle-Concentration Measurements. *Environmental Science & Technology*, 50(3):1376–1383, 2 2016. ISSN 0013-936X. doi: 10.1021/acs.est.5b05320. URL http://pubs.acs.org/doi/10.1021/acs.est.5b05320.

J. L. Brenguier. Coincidence and Dead-Time Corrections for Particles Counters. Part II: High Concentration Measurements with an FSSP. *Journal of Atmospheric and Oceanic Technology*, 6(4):585–598, 8 1989. ISSN 0739-0572. doi: 10.1175/1520-0426(1989)006<0585:CADTCF>2.0.CO;2. URL http://journals.ametsoc.org/doi/10.1175/1520-0426(1989)006%3C0585:CADTCF%3E2.0.CO;2.

J.-L. Brenguier, A. Rodi, G. Gordon, and P. Wechsler. Real-Time Detection of Performance Degradation of the Forward-scattering Spectrometer Probe. *Journal of Atmospheric and Oceanic Technology*, 10(1):27, 1993. ISSN 0739-0572. doi: 10.1175/1520-0426(1993)010<0027:RTDOPD>2.0.CO;2. URL http://journals.ametsoc.org/doi/10.1175/1520-0426(1993)010%3C0027:RTDOPD%3E2.0.CO;2.

J. L. Brenguier, D. Baumgardner, and B. Baker. A Review and Discussion of Processing Algorithms for FSSP Concentration Measurements. *Journal of Atmospheric and Oceanic Technology*, 11(5):1409–1414, 10 1994. ISSN 0739-0572. doi: 10.1175/1520-0426(1994)011<1409:ARADOP>2.0.CO;2.

J. L. Brenguier, T. Bourrianne, A. A. De Coelho, J. Isbert, R. Peytavi, D. Trevarin, and P. Weschler. Improvements of droplet size distribution measurements with the fast-FSSP (Forward Scattering Spectrometer Probe). *Journal of Atmospheric and Oceanic Technology*, 15(5):1077–1090, 1998. ISSN 07390572. doi: 10.1175/1520-0426(1998)015<1077:IODSDM>2.0.CO;2.

C. Brosy, K. Krampf, M. Zeeman, B. Wolf, W. Junkermann, K. Schäfer, S. Emeis, and H. Kunstmann. Simultaneous multicopter-based air sampling and sensing of meteorological variables. *Atmospheric Measurement Techniques*, 10(8):2773–2784, 8 2017. ISSN 1867-8548. doi: 10.5194/amt-10-2773-2017. URL `https://www.atmos-meas-tech.net/10/2773/2017/`.

D. Brus, J. Gustafsson, V. Vakkari, O. Kemppinen, G. de Boer, and A. Hirsikko. Measurement report: Properties of aerosol and gases in the vertical profile during the LAPSE-RATE campaign. *Atmospheric Chemistry and Physics*, 21(1):517–533, Jan. 2021. ISSN 1680-7316. doi: 10.5194/acp-21-517-2021. URL `https://acp.copernicus.org/articles/21/517/2021/`. Publisher: Copernicus GmbH.

M. Buschmann, J. Bange, and P. Vörsmann. MMAV-a miniature unmanned aerial vehicle (Mini-UAV) for meteorological purposes. In *Proceedings of the 16th Symposium on Boundary Layers and Turbulence*, pages 21–27, 2004.

H. Che, X. Zhang, H. Chen, B. Damiri, P. Goloub, Z. Li, X. Zhang, Y. Wei, H. Zhou, F. Dong, D. Li, and T. Zhou. Instrument calibration and aerosol optical depth validation of the China aerosol remote sensing network. *Journal of Geophysical Research Atmospheres*, 114(3):1–12, 2009. ISSN 01480227. doi: 10.1029/2008JD011030.

C. H. Chien, A. Theodore, C. Y. Wu, Y. M. Hsu, and B. Birky. Upon correlating diameters measured by optical particle counters and aerodynamic particle sizers. *Journal of Aerosol Science*, 101:77–85, 2016. ISSN 18791964. doi: 10.1016/j.jaerosci.2016.05.011. URL `http://dx.doi.org/10.1016/j.jaerosci.2016.05.011`.

H. Christophersen, R. Atlas, A. Aksoy, and J. Dunion. Combined Use of Satellite Observations and Global Hawk Unmanned Aircraft Dropwindsondes for Improved Tropical Cyclone Analyses and Forecasts. *Weather and Forecasting*, 33(4):1021–1031, Aug. 2018. ISSN 1520-0434, 0882-8156. doi: 10.1175/WAF-D-17-0167.1. URL `https://journals.ametsoc.org/view/journals/wefo/33/4/waf-d-17-0167_1.xml`. Publisher: American Meteorological Society Section: Weather and Forecasting.

A. D. Clarke, N. C. Ahlquist, S. Howell, and K. Moore. A miniature optical particle counter for in situ aircraft aerosol research. *Journal of Atmospheric and Oceanic Technology*, 19(10):1557–1566, 2002. ISSN 07390572. doi: 10.1175/1520-0426(2002)019<1557:AMOPCF>2.0.CO;2.

W. A. Cooper. Effects of Coincidence on Measurements with a Forward Scattering Spectrometer Probe. *Journal of Atmospheric and Oceanic Technology*, 5(6):823–832, 12 1988. ISSN 0739-0572. doi: 10.1175/1520-0426(1988)005<0823:EOCOMW>2.0.CO;2. URL http://journals.ametsoc.org/doi/10.1175/1520-0426(1988)005%3C0823:EOCOMW%3E2.0.CO;2.

C. E. Corrigan, G. C. Roberts, M. V. Ramana, D. Kim, and V. Ramanathan. Capturing vertical profiles of aerosols and black carbon over the Indian Ocean using autonomous unmanned aerial vehicles. *Atmospheric Chemistry and Physics*, 8(3):737–747, 2008. ISSN 16807324. doi: 10.5194/acp-8-737-2008.

R. Cotton, S. Osborne, Z. Ulanowski, E. Hirst, P. H. Kaye, and R. S. Greenaway. The Ability of the Small Ice Detector (SID-2) to Characterize Cloud Particle and Aerosol Morphologies Obtained during Flights of the FAAM BAe-146 Research Aircraft. *Journal of Atmospheric and Oceanic Technology*, 27(2):290–303, 2 2010. ISSN 1520-0426. doi: 10.1175/2009JTECHA1282.1. URL http://journals.ametsoc.org/doi/10.1175/2009JTECHA1282.1.

V. Daskalopoulou, S. A. Mallios, Z. Ulanowski, G. Hloupis, A. Gialitaki, I. Tsikoudi, K. Tassis, and V. Amiridis. The electrical activity of Saharan dust as perceived from surface electric field observations. *Atmospheric Chemistry and Physics*, 21(2):927–949, 1 2021. ISSN 1680-7324. doi: 10.5194/acp-21-927-2021. URL https://acp.copernicus.org/articles/21/927/2021/.

G. de Boer, A. Houston, J. Jacob, P. B. Chilson, S. W. Smith, B. Argrow, D. Lawrence, J. Elston, D. Brus, O. Kemppinen, P. Klein, J. K. Lundquist, S. Waugh, S. C. C. Bailey, A. Frazier, M. P. Sama, C. Crick, D. Schmale III, J. Pinto, E. A. Pillar-Little, V. Natalie, and A. Jensen. Data generated during the 2018 LAPSE-RATE campaign: an introduction and overview. *Earth System Science Data*, 12(4):3357–3366, Dec. 2020. ISSN 1866-3508. doi: 10.5194/essd-12-3357-2020. URL https://essd.copernicus.org/articles/12/3357/2020/. Publisher: Copernicus GmbH.

P. J. DeMott, T. C. Hill, C. S. McCluskey, K. A. Prather, D. B. Collins, R. C. Sullivan, M. J. Ruppel, R. H. Mason, V. E. Irish, T. Lee, C. Y. Hwang, T. S. Rhee, J. R. Snider, G. R. McMeeking, S. Dhaniyala, E. R. Lewis, J. J. Wentzell, J. Abbatt, C. Lee, C. M. Sultana, A. P. Ault, J. L. Axson, M. D. Martinez, I. Venero, G. Santos-Figueroa, M. D. Stokes, G. B. Deane, O. L. Mayol-Bracero, V. H. Grassian, T. H. Bertram, A. K. Bertram, B. F. Moffett, and G. D. Franc. Sea spray aerosol as a unique source of ice nucleating particles. *Proceedings of the National Academy of Sciences of the United States of America*, 113(21):5797–5803, 2016. ISSN 10916490. doi: 10.1073/pnas.1514034112.

A. J. Ding, C. B. Fu, X. Q. Yang, J. N. Sun, T. Petäjä, V. M. Kerminen, T. Wang, Y. Xie, E. Herrmann, L. F. Zheng, W. Nie, Q. Liu, X. L. Wei, and M. Kulmala. Intense atmospheric pollution modifies weather:

A case of mixed biomass burning with fossil fuel combustion pollution in eastern China. *Atmospheric Chemistry and Physics*, 13(20):10545–10554, 2013. ISSN 16807316. doi: 10.5194/acp-13-10545-2013.

A. Douglas and T. L'Ecuyer. Quantifying variations in shortwave aerosol-cloud-radiation interactions using local meteorology and cloud state constraints. *Atmospheric Chemistry and Physics*, 19(9):6251–6268, 2019. ISSN 16807324. doi: 10.5194/acp-19-6251-2019.

K.-m. Doulgeris, M. Komppula, S. Romakkaniemi, A.-p. Hyvärinen, V.-m. Kerminen, and D. Brus. In situ cloud ground-based measurements in the Finnish sub-Arctic: intercomparison of three cloud spectrometer setups. *Atmospheric Measurement Techniques*, 13(9):5129–5147, 9 2020. ISSN 1867-8548. doi: 10.5194/amt-13-5129-2020. URL `https://doi.org/10.5194/amt-13-5129-2020https://amt.copernicus.org/articles/13/5129/2020/`.

E. Drury, D. J. Jacob, R. J. Spurr, J. Wang, Y. Shinozuka, B. E. Anderson, A. D. Clarke, J. Dibb, C. McNaughton, and R. Weber. Synthesis of satellite (MODIS), aircraft (ICARTT), and surface (IMPROVE, EPA-AQS, AERONET) aerosol observations over eastern North America to improve MODIS aerosol retrievals and constrain surface aerosol concentrations and sources. *Journal of Geophysical Research Atmospheres*, 115(14):1–17, 2010. ISSN 01480227. doi: 10.1029/2009JD012629.

J. E. Dye and D. Baumgardner. Evaluation of the Forward Scattering Spectrometer Probe. Part I: Electronic and Optical Studies. *Journal of Atmospheric and Oceanic Technology*, 1(4):329–344, 12 1984. ISSN 0739-0572. doi: 10.1175/1520-0426(1984)001<0329:EOTFSS>2.0.CO;2. URL `http://journals.ametsoc.org/doi/10.1175/1520-0426(1984)001%3C0329:EOTFSS%3E2.0.CO;2`.

T. F. Eck, B. N. Holben, D. E. Ward, M. M. Mukelabai, O. Dubovik, A. Smirnov, J. S. Schafer, N. C. Hsu, S. J. Piketh, A. Queface, J. Le Roux, R. J. Swap, and I. Slutsker. Variability of biomass burning aerosol optical characteristics in southern Africa during the SAFARI 2000 dry season campaign and a comparison of single scattering albedo estimates from radiometric measurements. *Journal of Geophysical Research: Atmospheres*, 108(13):1–21, 2003. ISSN 01480227. doi: 10.1029/2002jd002321.

J. Egger, S. Bajrachaya, R. Heinrich, P. Kolb, S. Lämmlein, M. Mech, J. Reuder, W. Schäper, P. Shakya, J. Schween, and H. Wendt. Diurnal Winds in the Himalayan Kali Gandaki Valley. Part III: Remotely Piloted Aircraft Soundings. *Monthly Weather Review*, 130(8):2042–2058, 8 2002. ISSN 0027-0644. doi: 10.1175/1520-0493(2002)130<2042:DWITHK>2.0.CO;2. URL `http://journals.ametsoc.org/doi/10.1175/1520-0493(2002)130%3C2042:DWITHK%3E2.0.CO;2`.

J. Egger, L. Blacutt, F. Ghezzi, R. Heinrich, P. Kolb, S. Lämmlein, M. Leeb, S. Mayer, E. Palenque, J. Reuder, W. Schäper, J. Schween, R. Torrez, and F. Zaratti. Diurnal Circulation of the Bolivian Altiplano. Part I: Observations. *Monthly Weather Review*, 133(4):911–924, 4 2005. ISSN 0027-0644. doi: 10.1175/MWR2894.1. URL `http://journals.ametsoc.org/doi/10.1175/MWR3033.1https://journals.ametsoc.org/doi/10.1175/MWR2894.1`.

S. Egli, F. Maier, J. Bendix, and B. Thies. Vertical distribution of microphysical properties in radiation fogs — A case study. *Atmospheric Research*, 151:130–145, 1 2015. ISSN 01698095. doi: 10.1016/j.atmosres.2014.05.027. URL `http://dx.doi.org/10.1016/j.atmosres.2014.05.027https://linkinghub.elsevier.com/retrieve/pii/S0169809514002361`.

R. Engelmann, T. Kanitz, H. Baars, B. Heese, D. Althausen, A. Skupin, U. Wandinger, M. Komppula, I. S. Stachlewska, V. Amiridis, E. Marinou, I. Mattis, H. Linné, and A. Ansmann. EARLINET Raman Lidar PollyXT: the neXT generation. *Atmospheric Measurement Techniques Discussions*, 8(7):7737–7780, 2015. ISSN 1867-8610. doi: 10.5194/amtd-8-7737-2015. URL `http://www.atmos-meas-tech-discuss.net/8/7737/2015/`.

J. Fan, Y. Wang, D. Rosenfeld, and X. Liu. Review of aerosol-cloud interactions: Mechanisms, significance, and challenges. *Journal of the Atmospheric Sciences*, 73(11):4221–4252, 2016. ISSN 15200469. doi: 10.1175/JAS-D-16-0037.1.

P. R. Field, R. Wood, P. R. Brown, P. H. Kaye, E. Hirst, R. Greenaway, and J. A. Smith. Ice particle interarrival times measured with a fast FSSP. *Journal of Atmospheric and Oceanic Technology*, 20(2):249–261, 2003. ISSN 07390572. doi: 10.1175/1520-0426(2003)020<0249:IPITMW>2.0.CO;2.

P. Formenti, B. D'Anna, C. Flamant, M. Mallet, S. J. Piketh, K. Schepanski, F. Waquet, F. Auriol, G. Brogniez, F. Burnet, J. P. Chaboureau, A. Chauvigné, P. Chazette, C. Denjean, K. Desboeufs, J. F. Doussin, N. Elguindi, S. Feuerstein, M. Gaetani, C. Giorio, D. Klopper, M. D. Mallet, P. Nabat, A. Monod, F. Solmon, A. Namwoonde, C. Chikwililwa, R. Mushi, E. J. Welton, and B. Holben. The aerosols, radiation and clouds in southern Africa field campaign in Namibia overview, illustrative observations, and way forward. *Bulletin of the American Meteorological Society*, 100(7):1277–1298, 2019. ISSN 00030007. doi: 10.1175/BAMS-D-17-0278.1.

F. C. Fuertes, L. Wilhelm, and F. Porté-Agel. Multirotor UAV-based platform for the measurement of atmospheric turbulence: Validation and signature detection of tip vortices of wind turbine blades. *Journal of Atmospheric and Oceanic Technology*, 36(6):941–955, 2019. ISSN 15200426. doi: 10.1175/JTECH-D-17-0220.1.

R. S. Gao, A. E. Perring, T. D. Thornberry, A. W. Rollins, J. P. Schwarz, S. J. Ciciora, and D. W. Fahey. A high-sensitivity low-cost optical particle counter design. *Aerosol Science and Technology*, 47(2):137–145, 2013. ISSN 02786826. doi: 10.1080/02786826.2012.733039.

R. S. Gao, H. Telg, R. J. McLaughlin, S. J. Ciciora, L. A. Watts, M. S. Richardson, J. P. Schwarz, A. E. Perring, T. D. Thornberry, A. W. Rollins, M. Z. Markovic, T. S. Bates, J. E. Johnson, and D. W. Fahey. A light-weight, high-sensitivity particle spectrometer for PM2.5 aerosol measurements. *Aerosol Science and Technology*, 50(1):88–99, 2016. ISSN 15217388. doi: 10.1080/02786826.2015.1131809. URL `http://dx.doi.org/10.1080/02786826.2015.1131809`.

B. A. Gardiner and J. Hallett. Degradation of In-Cloud Forward Scattering Spectrometer Probe Measurements in the Presence of Ice Particles. *Journal of Atmospheric and Oceanic Technology*, 2(2): 171–180, 6 1985. ISSN 0739-0572. doi: 10.1175/1520-0426(1985)002<0171:DOICFS>2.0.CO;2. URL `http://journals.ametsoc.org/doi/10.1175/1520-0426(1985)002%3C0171:DOICFS%3E2.0.CO;2`.

J. Garratt. Review: the atmospheric boundary layer. *Earth-Science Reviews*, 37(1-2):89–134, 10 1994. ISSN 00128252. doi: 10.1016/0012-8252(94)90026-4. URL `https://linkinghub.elsevier.com/retrieve/pii/0012825294900264`.

D. M. Garvey and R. G. Pinnick. Response Characteristics of the Particle Measuring Systems Active Scattering Aerosol Spectrometer Probe (ASASP–X). *Aerosol Science and Technology*, 2(4):477–488, 6 1983. ISSN 0278-6826. doi: 10.1080/02786828308958651. URL `http://www.tandfonline.com/doi/abs/10.1080/02786828308958651`.

J.-F. Gayet, G. Febvre, and H. Larsen. The Reliability of the PMS FSSP in the Presence of Small Ice Crystals. *Journal of Atmospheric and Oceanic Technology*, 13(6):1300–1310, 12 1996. ISSN 0739-0572. doi: 10.1175/1520-0426(1996)013<1300:TROTPF>2.0.CO;2. URL `http://journals.ametsoc.org/doi/10.1175/1520-0426(1996)013%3C1300:TROTPF%3E2.0.CO;2`.

J. Girdwood. Mavlink Interface, 2018a. URL `https://github.com/JGirdwood/MAVINT`.

J. Girdwood. UCASS Library, 2018b. URL `https://github.com/JGirdwood/UCASS-Library`.

J. Girdwood. AeroSAM-logger, 2019. URL `https://github.com/JGirdwood/AeroSAM_logger`.

J. Girdwood, H. Smith, W. Stanley, Z. Ulanowski, C. Stopford, C. Chemel, K.-M. Doulgeris, D. Brus, D. Campbell, and R. Mackenzie. Design and field campaign validation of a multi-rotor unmanned aerial vehicle and optical particle counter. *Atmospheric Measurement Techniques*, 13(12):6613–6630, 12 2020.

ISSN 1867-8548. doi: 10.5194/amt-13-6613-2020. URL https://amt.copernicus.org/articles/13/6613/2020/.

J. Girdwood, W. Stanley, C. Stopford, and D. Brus. Simulation and field campaign evaluation of an optical particle counter on a fixed-wing UAV. *Atmospheric Measurement Techniques*, 15(7):2061–2076, 4 2022. ISSN 1867-8548. doi: 10.5194/amt-15-2061-2022. URL https://amt.copernicus.org/articles/15/2061/2022/.

A. Glen and S. D. Brooks. A new method for measuring optical scattering properties of atmospherically relevant dusts using the Cloud and Aerosol Spectrometer with Polarization (CASPOL). *Atmospheric Chemistry and Physics*, 13(3):1345–1356, 2 2013. ISSN 1680-7324. doi: 10.5194/acp-13-1345-2013. URL https://acp.copernicus.org/articles/13/1345/2013/.

J. González-Rocha, S. F. De Wekker, S. D. Ross, and C. A. Woolsey. Wind profiling in the lower atmosphere from wind-induced perturbations to multirotor UAS. *Sensors (Switzerland)*, 20(5):1–29, 2020. ISSN 14248220. doi: 10.3390/s20051341.

C. Greatwood, T. Richardson, J. Freer, R. Thomas, A. MacKenzie, R. Brownlow, D. Lowry, R. Fisher, and E. Nisbet. Atmospheric Sampling on Ascension Island Using Multirotor UAVs. *Sensors*, 17(6):1189, 5 2017. ISSN 1424-8220. doi: 10.3390/s17061189. URL http://www.mdpi.com/1424-8220/17/6/1189.

B. R. Greene, A. R. Segales, S. Waugh, S. Duthoit, and P. B. Chilson. Considerations for temperature sensor placement on rotary-wing unmanned aircraft systems. *Atmospheric Measurement Techniques*, 11(10):5519–5530, 10 2018. ISSN 1867-8548. doi: 10.5194/amt-11-5519-2018. URL https://www.atmos-meas-tech.net/11/5519/2018/.

F. T. Gucker and C. T. O'Konski. An improved photoelectronic counter for colloidal particles, suitable for size-distribution studies. *Journal of Colloid Science*, 4(6):541–560, 1949. ISSN 00958522. doi: 10.1016/0095-8522(49)90052-5.

F. T. Gucker, C. T. O'Konski, H. B. Pickard, and J. N. Pitts. A Photoelectronic Counter for Colloidal Particles. *Journal of the American Chemical Society*, 69(10):2422–2431, 1947. ISSN 15205126. doi: 10.1021/ja01202a053.

I. Gultepe, A. J. Heymsfield, P. R. Field, and D. Axisa. Ice-Phase Precipitation. *Meteorological Monographs*, 58:1–6, 1 2017a. ISSN 0065-9401. doi: 10.1175/AMSMONOGRAPHS-D-16-0013.1. URL http://journals.ametsoc.org/doi/10.1175/AMSMONOGRAPHS-D-16-0013.1.

I. Gultepe, A. J. Heymsfield, M. Gallagher, L. Ickes, and D. Baumgardner. Ice Fog: The Current State of Knowledge and Future Challenges. *Meteorological Monographs*, 58:1–4, 1 2017b. ISSN 0065-9401. doi: 10.1175/AMSMONOGRAPHS-D-17-0002.1. URL `http://journals.ametsoc.org/doi/10.1175/AMSMONOGRAPHS-D-17-0002.1`.

P. Gupta, P. Doraiswamy, R. Levy, O. Pikelnaya, J. Maibach, B. Feenstra, A. Polidori, F. Kiros, and K. C. Mills. Impact of California Fires on Local and Regional Air Quality: The Role of a Low-Cost Sensor Network and Satellite Observations. *GeoHealth*, 2(6):172–181, 6 2018. ISSN 2471-1403. doi: 10.1029/2018GH000136. URL `https://onlinelibrary.wiley.com/doi/abs/10.1029/2018GH000136`.

G. Guyot, C. Gourbeyre, G. Febvre, V. Shcherbakov, F. Burnet, J. C. Dupont, K. Sellegri, and O. Jourdan. Quantitative evaluation of seven optical sensors for cloud microphysical measurements at the Puy-de-Dôme Observatory, France. *Atmospheric Measurement Techniques*, 8(10):4347–4367, 2015. ISSN 18678548. doi: 10.5194/amt-8-4347-2015.

K. Hara, Y. Iwasaka, M. Wada, T. Ihara, H. Shiba, K. Osada, and T. Yamanouchi. Aerosol constituents and their spatial distribution in the free troposphere of coastal Antarctic regions. *Journal of Geophysical Research*, 111(D15):D15216, 2006. ISSN 0148-0227. doi: 10.1029/2005JD006591. URL `http://doi.wiley.com/10.1029/2005JD006591`.

W. V. Harper. Reduced Major Axis Regression. In *Wiley StatsRef: Statistics Reference Online*, volume 9, pages 1–6. John Wiley & Sons, Ltd, Chichester, UK, 11 2016. doi: 10.1002/9781118445112.stat07912. URL `http://doi.wiley.com/10.1002/9781118445112.stat07912`.

N. R. P. Harris, L. J. Carpenter, J. D. Lee, G. Vaughan, M. T. Filus, R. L. Jones, B. OuYang, J. A. Pyle, A. D. Robinson, S. J. Andrews, A. C. Lewis, J. Minaeian, A. Vaughan, J. R. Dorsey, M. W. Gallagher, M. Le Breton, R. Newton, C. J. Percival, H. M. A. Ricketts, S. J. Bauguitte, G. J. Nott, A. Wellpott, M. J. Ashfold, J. Flemming, R. Butler, P. I. Palmer, P. H. Kaye, C. Stopford, C. Chemel, H. Boesch, N. Humpage, A. Vick, A. R. MacKenzie, R. Hyde, P. Angelov, E. Meneguz, and A. J. Manning. Coordinated Airborne Studies in the Tropics (CAST). *Bulletin of the American Meteorological Society*, 98(1):145–162, 1 2017. ISSN 0003-0007. doi: 10.1175/BAMS-D-14-00290.1. URL `https://journals.ametsoc.org/doi/10.1175/BAMS-D-14-00290.1`.

J. M. Haywood, S. R. Osborne, P. N. Francis, A. Keil, P. Formenti, M. O. Andreae, and P. H. Kaye. The mean physical and optical properties of regional haze dominated by biomass burning aerosol measured from the C-130 aircraft during SAFARI 2000. *Journal of Geophysical Research: Atmospheres*, 108(D13):

n/a–n/a, 7 2003. ISSN 01480227. doi: 10.1029/2002JD002226. URL http://doi.wiley.com/10.1029/2002JD002226.

J. M. Haywood, S. J. Abel, P. A. Barrett, N. Bellouin, A. Blyth, K. N. Bower, M. Brooks, K. Carslaw, H. Che, H. Coe, M. I. Cotterell, I. Crawford, Z. Cui, N. Davies, B. Dingley, P. Field, P. Formenti, H. Gordon, M. De Graaf, R. Herbert, B. Johnson, A. C. Jones, J. M. Langridge, F. Malavelle, D. G. Partridge, F. Peers, J. Redemann, P. Stier, K. Szpek, J. W. Taylor, D. Watson-Parris, R. Wood, H. Wu, and P. Zuidema. The CLoud-Aerosol-Radiation Interaction and Forcing: Year 2017 (CLARIFY-2017) measurement campaign. *Atmospheric Chemistry and Physics*, 21(2):1049–1084, 2021. ISSN 16807324. doi: 10.5194/acp-21-1049-2021.

A. J. Heymsfield. Ice Particles Observed in a Cirriform Cloud at -83C and Implications for Polar Stratospheric Clouds. *Journal of the Atmospheric Sciences*, 43(8):851–855, 4 1986. ISSN 0022-4928. doi: 10.1175/1520-0469(1986)043<0851:IPOIAC>2.0.CO;2. URL http://journals.ametsoc.org/doi/10.1175/1520-0469(1986)043%3C0851:IPOIAC%3E2.0.CO;2.

A. J. Heymsfield, C. A. Knight, and J. E. Dye. Ice Initiation in Unmixed Updraft Cores in Northeast Colorado Cumulus Congestus Clouds. *Journal of the Atmospheric Sciences*, 36(11):2216–2229, 11 1979. doi: 10.1175/1520-0469(1979)036<2216:IIIUUC>2.0.CO;2.

E. Hirst, C. Stopford, P. Kaye, R. Greenaway, and J. Dorsey. The Aerosol Ice Interface Transition Spectrometer – A new particle phase. In *ATTREX Science Meeting , Boulder, United States. ; Conference date: 30-09-2013*, 2013.

G. J. Holland, P. J. Webster, J. A. Curry, G. Tyrell, D. Gauntlett, G. Brett, J. Becker, R. Hoag, and W. Vaglienti. The Aerosonde Robotic Aircraft: A New Paradigm for Environmental Observations. *Bulletin of the American Meteorological Society*, 82(5):889–901, 5 2001. ISSN 0003-0007. doi: 10.1175/1520-0477(2001)082<0889:TARAAN>2.3.CO;2. URL http://journals.ametsoc.org/doi/abs/10.1175/1520-0477%282001%29082%3C0889%3ATARAAN%3E2.3.CO%3B2.

D. Hu, B. Qi, R. Du, H. Yang, J. Wang, and J. Zhuge. An Atmospheric Vertical Detection System Using the Multi-rotor UAV. In *2019 International Conference on Meteorology Observations (ICMO)*, pages 1–4. IEEE, 12 2019. ISBN 978-1-7281-6254-6. doi: 10.1109/ICMO49322.2019.9025899. URL https://ieeexplore.ieee.org/document/9025899/.

J. M. Intrieri, G. de Boer, M. D. Shupe, J. R. Spackman, J. Wang, P. J. Neiman, G. A. Wick, T. F. Hock, and R. E. Hood. Global Hawk dropsonde observations of the Arctic atmosphere obtained during the

Winter Storms and Pacific Atmospheric Rivers (WISPAR) field campaign. *Atmospheric Measurement Techniques*, 7(11):3917–3926, Nov. 2014. ISSN 1867-1381. doi: 10.5194/amt-7-3917-2014. URL https://amt.copernicus.org/articles/7/3917/2014/. Publisher: Copernicus GmbH.

IPCC. Working Group I Contribution to the IPCC Fifth Assessment Report, Climate Change 2013: The Physical Science Basis. *Ipcc*, AR5(March 2013):2014, 2013. ISSN 1098-6596. doi: 10.1017/CBO9781107415324.Summary.

IPCC. Working Group I Contribution to the IPCC Sixth Assessment Report, Climate Change 2021: The Physical Science Basis. *Ipcc*, AR6(August), 2021.

R. C. Jackson, G. M. Mcfarquhar, J. Stith, M. Beals, R. A. Shaw, J. Jensen, J. Fugal, and A. Korolev. An assessment of the impact of antishattering tips and artifact removal techniques on cloud ice size distributions measured by the 2D cloud probe. *Journal of Atmospheric and Oceanic Technology*, 31(12): 2567–2590, 2014. ISSN 15200426. doi: 10.1175/JTECH-D-13-00239.1.

E. J. Jensen, L. Pister, D. E. Jordan, D. W. Fahey, P. A. Newman, and T. Thornber. The NASA Airborne Tropical. 2013.

P. Kaye and E. Hirst. An improved low cost apparatus and method for the detection of a fluid-borne particle, 2010. URL https://patents.google.com/patent/WO2012056217A1/en.

P. Kaye and E. Hirst. Second Generation Low-Cost Particle Counter, 2011.

M. Kezoudi, C. Keleshis, P. Antoniou, G. Biskos, M. Bronz, C. Constantinides, M. Desservettaz, R.-S. Gao, J. Girdwood, J. Harnetiaux, K. Kandler, A. Leonidou, Y. Liu, J. Lelieveld, F. Marenco, N. Mihalopoulos, G. Močnik, K. Neitola, J.-D. Paris, M. Pikridas, R. Sarda-Esteve, C. Stopford, F. Unga, M. Vrekoussis, and J. Sciare. The unmanned systems research laboratory (usrl): A new facility for uav-based atmospheric observations. *Atmosphere*, 12(8), 2021a. ISSN 2073-4433. doi: 10.3390/atmos12081042. URL https://www.mdpi.com/2073-4433/12/8/1042.

M. Kezoudi, M. Tesche, H. Smith, A. Tsekeri, H. Baars, M. Dollner, V. Estellés, J. Bühl, B. Weinzierl, Z. Ulanowski, D. Müller, and V. Amiridis. Measurement report: Balloon-borne in situ profiling of Saharan dust over Cyprus with the UCASS optical particle counter. *Atmospheric Chemistry and Physics*, 21(9): 6781–6797, 5 2021b. ISSN 1680-7324. doi: 10.5194/acp-21-6781-2021. URL https://acp.copernicus.org/articles/21/6781/2021/.

Y. J. Kim. Response of the active scattering aerosol spectrometer probe (ASASP-100X) to particles of different chemical composition. *Aerosol Science and Technology*, 22(1):33–42, 1995. ISSN 15217388. doi: 10.1080/02786829408959726.

Y. J. Kim and J. F. Boatman. Size Calibration Corrections for the Active Scattering Aerosol Spectrometer Probe (ASASP-100X). *Aerosol Science and Technology*, 12(3):665–672, 1 1990. ISSN 0278-6826. doi: 10.1080/02786829008959381. URL `http://www.tandfonline.com/doi/abs/10.1080/02786829008959381`.

R. G. Knollenberg. The Optical Array: An Alternative to Scattering or Extinction for Airborne Particle Size Determination. *Journal of Applied Meteorology*, 9(1):86–103, 2 1970. ISSN 0021-8952. doi: 10.1175/1520-0450(1970)009<0086:TOAAAT>2.0.CO;2. URL `http://journals.ametsoc.org/doi/10.1175/1520-0450(1970)009%3C0086:TOAAAT%3E2.0.CO;2`.

R. G. Knollenberg. *Three New Instruments for Cloud Physics Measurements: The 2-D Spectrometer, the Forward Scattering Spectrometer Probe, and the Active Scattering Aerosol Spectrometer*. American Meteorological Society, 1 edition, 1976.

T. G. Konrad, M. L. Hill, J. R. Rowland, and J. H. Meyer. A Small, Radio-Controlled Aircraft As A Platform for Meteorlogical Sensors. *APL Technical Digest*, 1(December):11–19, 1970.

A. Korolev, E. Emery, and K. Creelman. Modification and tests of particle probe tips to mitigate effects of ice shattering. *Journal of Atmospheric and Oceanic Technology*, 30(4):690–708, 2013a. ISSN 15200426. doi: 10.1175/JTECH-D-12-00063.1.

A. V. Korolev, J. W. Strapp, and G. A. Isaac. Evaluation of the accuracy of PMS optical array probes. *Journal of Atmospheric and Oceanic Technology*, 15(3):708–720, 1998. ISSN 07390572. doi: 10.1175/1520-0426(1998)015<0708:EOTAOP>2.0.CO;2.

A. V. Korolev, G. A. Isaac, J. W. Strapp, and A. N. Nevzorov. In situ measurements of effective diameter and effective droplet number concentration. *Journal of Geophysical Research: Atmospheres*, 104(D4):3993–4003, 2 1999. ISSN 01480227. doi: 10.1029/1998JD200071. URL `http://doi.wiley.com/10.1029/1998JD200071`.

A. V. Korolev, E. F. Emery, J. W. Strapp, S. G. Cober, and G. A. Isaac. Quantification of the Effects of Shattering on Airborne Ice Particle Measurements. *Journal of Atmospheric and Oceanic Technology*, 30(11):2527–2553, 11 2013b. ISSN 0739-0572. doi: 10.1175/JTECH-D-13-00115.1. URL `http://journals.ametsoc.org/doi/10.1175/JTECH-D-13-00115.1`.

N. F. Laird, H. T. Ochs, R. M. Rauber, and L. J. Miller. Initial precipitation formation warm Florida cumulus. *Journal of the Atmospheric Sciences*, 57(22):3740–3751, 2000. ISSN 00224928. doi: 10.1175/1520-0469(2000)057<3740:IPFIWF>2.0.CO;2.

S. Lance, C. A. Brock, D. Rogers, and J. A. Gordon. Water droplet calibration of the Cloud Droplet Probe (CDP) and in-flight performance in liquid, ice and mixed-phase clouds during ARCPAC. *Atmospheric Measurement Techniques*, 3(6):1683–1706, 2010. ISSN 18671381. doi: 10.5194/amt-3-1683-2010.

R. P. Lawson, B. A. Baker, C. G. Schmitt, and T. L. Jensen. An overview of microphysical properties of Arctic clouds observed in May and July 1998 during FIRE ACE. *Journal of Geophysical Research: Atmospheres*, 106(D14):14989–15014, 7 2001. ISSN 01480227. doi: 10.1029/2000JD900789. URL `http://doi.wiley.com/10.1029/2000JD900789`.

Z. Li, J. Guo, A. Ding, H. Liao, J. Liu, Y. Sun, T. Wang, H. Xue, H. Zhang, and B. Zhu. Aerosol and boundary-layer interactions and impact on air quality. *National Science Review*, 4(6):810–833, 11 2017. ISSN 2095-5138. doi: 10.1093/nsr/nwx117. URL `https://academic.oup.com/nsr/article/4/6/810/4191281`.

H. Liao and J. H. Seinfeld. Radiative forcing by mineral dust aerosols: Sensitivity to key variables. *Journal of Geophysical Research: Atmospheres*, 103(D24):31637–31645, 12 1998. ISSN 01480227. doi: 10.1029/1998JD200036. URL `http://doi.wiley.com/10.1029/1998JD200036`.

P. Liu, C. Zhao, P. Liu, Z. Deng, M. Huang, X. Ma, and X. Tie. Aircraft study of aerosol vertical distributions over Beijing and their optical properties. *Tellus B: Chemical and Physical Meteorology*, 61(5):756–767, 1 2009. ISSN 1600-0889. doi: 10.1111/j.1600-0889.2009.00440.x. URL `https://www.tandfonline.com/doi/full/10.1111/j.1600-0889.2009.00440.x`.

P. S. K. Liu, W. R. Leaitch, J. W. Strapp, and M. A. Wasey. Response of particle measuring systems airborne ASASP and PCASP to NaCl and latex particles. *Aerosol Science and Technology*, 16(2):83–95, 1992. ISSN 15217388. doi: 10.1080/02786829208959539.

Z. Liu, M. Osborne, K. Anderson, J. D. Shutler, A. Wilson, J. Langridge, S. H. L. Yim, H. Coe, S. Babu, S. K. Satheesh, P. Zuidema, T. Huang, J. C. H. Cheng, and J. Haywood. Characterizing the performance of a POPS miniaturized optical particle counter when operated on a quadcopter drone. *Atmospheric Measurement Techniques*, 14(9):6101–6118, 9 2021. ISSN 1867-8548. doi: 10.5194/amt-14-6101-2021. URL `https://amt.copernicus.org/articles/14/6101/2021/`.

G. Loegering. Global Hawk - A New Tool for Airborne Atmospheric Sensing. In *1st UAV Conference*. American Institute of Aeronautics and Astronautics, 2002. doi: 10.2514/6.2002-3458. URL `https://arc.aiaa.org/doi/abs/10.2514/6.2002-3458`. _eprint: https://arc.aiaa.org/doi/pdf/10.2514/6.2002-3458.

A. Lohila, T. Penttilä, S. Jortikka, T. Aalto, P. Anttila, E. Asmi, M. Aurela, J. Hatakka, H. Hellén, H. Henttonen, P. Hänninen, J. Kilkki, K. Kyllönen, T. Laurila, A. Lepistö, H. Lihavainen, U. Makkonen, J. Paatero, M. Rask, R. Sutinen, J. P. Tuovinen, J. Vuorenmaa, and Y. Viisanen. Preface to the special issue on integrated research of atmosphere, ecosystems and environment at Pallas. *Boreal Environment Research*, 20(4):431–454, 2015. ISSN 12396095.

M. Lothon, F. Lohou, D. Pino, F. Couvreux, E. R. Pardyjak, J. Reuder, J. Vilà-Guerau De Arellano, P. Durand, O. Hartogensis, D. Legain, P. Augustin, B. Gioli, D. H. Lenschow, I. Faloona, C. Yagüe, D. C. Alexander, W. M. Angevine, E. Bargain, J. Barrié, E. Bazile, Y. Bezombes, E. Blay-Carreras, A. Van De Boer, J. L. Boichard, A. Bourdon, A. Butet, B. Campistron, O. De Coster, J. Cuxart, A. Dabas, C. Darbieu, K. Deboudt, H. Delbarre, S. Derrien, P. Flament, M. Fourmentin, A. Garai, F. Gibert, A. Graf, J. Groebner, F. Guichard, M. A. Jiménez, M. Jonassen, A. Van Den Kroonenberg, V. Magliulo, S. Martin, D. Martinez, L. Mastrorillo, A. F. Moene, F. Molinos, E. Moulin, H. P. Pietersen, B. Piguet, E. Pique, C. Román-Cascón, C. Rufin-Soler, F. Saïd, M. Sastre-Marugán, Y. Seity, G. J. Steeneveld, P. Toscano, O. Traullé, D. Tzanos, S. Wacker, N. Wildmann, and A. Zaldei. The BLLAST field experiment: Boundary-Layer late afternoon and sunset turbulence. *Atmospheric Chemistry and Physics*, 14(20):10931–10960, 2014. ISSN 16807324. doi: 10.5194/acp-14-10931-2014.

D. Mamali, E. Marinou, J. Sciare, M. Pikridas, P. Kokkalis, M. Kottas, I. Binietoglou, A. Tsekeri, C. Keleshis, R. Engelmann, H. Baars, A. Ansmann, V. Amiridis, H. Russchenberg, and G. Biskos. Vertical profiles of aerosol mass concentration derived by unmanned airborne in situ and remote sensing instruments during dust events. *Atmospheric Measurement Techniques*, 11(5):2897–2910, 5 2018. ISSN 1867-8548. doi: 10.5194/amt-11-2897-2018. URL `https://www.atmos-meas-tech.net/11/2897/2018/`.

E. Marinou, M. Tesche, A. Nenes, A. Ansmann, J. Schrod, D. Mamali, A. Tsekeri, M. Pikridas, H. Baars, R. Engelmann, K. A. Voudouri, S. Solomos, J. Sciare, S. Groß, F. Ewald, and V. Amiridis. Retrieval of ice-nucleating particle concentrations from lidar observations and comparison with UAV in situ measurements. *Atmospheric Chemistry and Physics*, 19(17):11315–11342, 2019. ISSN 16807324. doi: 10.5194/acp-19-11315-2019.

J. H. Marsham, M. Hobby, C. J. T. Allen, J. R. Banks, M. Bart, B. J. Brooks, C. Cavazos-Guerra, S. Engelstaedter, M. Gascoyne, A. R. Lima, J. V. Martins, J. B. McQuaid, A. O'Leary, B. Ouchene, A. Ouladichir, D. J. Parker, A. Saci, M. Salah-Ferroudj, M. C. Todd, and R. Washington. Meteorology and dust in the central Sahara: Observations from Fennec supersite-1 during the June 2011 Intensive Observation Period. *Journal of Geophysical Research: Atmospheres*, 118(10):4069–4089, 2013. ISSN 2169-8996. doi: 10.1002/jgrd.50211. URL `https://onlinelibrary.wiley.com/doi/abs/10.1002/jgrd.50211`. _eprint: https://onlinelibrary.wiley.com/doi/pdf/10.1002/jgrd.50211.

S. Martin, J. Bange, and F. Beyrich. Meteorological profiling of the lower troposphere using the research UAV "m2AV Carolo". *Atmospheric Measurement Techniques*, 4(4):705–716, 2011. ISSN 18671381. doi: 10.5194/amt-4-705-2011.

K. A. Mckinney, D. Wang, J. Ye, J. B. D. Fouchier, P. C. Guimarães, C. E. Batista, R. A. Souza, E. G. Alves, D. Gu, A. B. Guenther, and S. T. Martin. A sampler for atmospheric volatile organic compounds by copter unmanned aerial vehicles. *Atmospheric Measurement Techniques*, 12(6):3123–3135, 2019. ISSN 18678548. doi: 10.5194/amt-12-3123-2019.

V. W. Mecklenburg. Zeitschrift ffir wissenschaftliche und technische Kolloidchemie. *Kolloid-Zeitschrift*, 16 (April):97, 1915.

K. Meier, R. Hann, J. Skaloud, and A. Garreau. Wind Estimation with Multirotor UAVs. *Atmosphere*, 13 (4):551, 2022. ISSN 20734433. doi: 10.3390/atmos13040551.

Y. Miao and S. Liu. Linkages between aerosol pollution and planetary boundary layer structure in China. *Science of the Total Environment*, 650:288–296, 2019. ISSN 18791026. doi: 10.1016/j.scitotenv.2018.09.032. URL `https://doi.org/10.1016/j.scitotenv.2018.09.032`.

Y. Miao, J. Guo, S. Liu, C. Zhao, X. Li, G. Zhang, W. Wei, and Y. Ma. Impacts of synoptic condition and planetary boundary layer structure on the trans-boundary aerosol transport from Beijing-Tianjin-Hebei region to northeast China. *Atmospheric Environment*, 181(January):1–11, 2018. ISSN 18732844. doi: 10.1016/j.atmosenv.2018.03.005. URL `https://doi.org/10.1016/j.atmosenv.2018.03.005`.

N. Mölders, M. K. Butwin, J. M. Madden, H. N. Q. Tran, K. Sassen, and G. Kramm. Theoretical Investigations on Mapping Mean Distributions of Particulate Matter, Inert, Reactive, and Secondary Pollutants from Wildfires by Unmanned Air Vehicles (UAVs). *Open Journal of Air Pollution*, 04(03):149–174, 2015. ISSN 2169-2653. doi: 10.4236/ojap.2015.43014.

D. Müller, I. Veselovskii, A. Kolgotin, M. Tesche, A. Ansmann, and O. Dubovik. Vertical profiles of pure dust and mixed smoke–dust plumes inferred from inversion of multiwavelength Raman/polarization lidar data and comparison to AERONET retrievals and in situ observations. *Applied Optics*, 52(14):3178, 5 2013. ISSN 1559-128X. doi: 10.1364/AO.52.003178. URL `https://www.osapublishing.org/abstract.cfm?URI=ao-52-14-3178`.

P. P. Neumann and M. Bartholmai. Real-time wind estimation on a micro unmanned aerial vehicle using its inertial measurement unit. *Sensors and Actuators, A: Physical*, 235:300–310, 2015. ISSN 09244247. doi: 10.1016/j.sna.2015.09.036. URL `http://dx.doi.org/10.1016/j.sna.2015.09.036`.

C. T. O'Konski and G. J. Doyle. Light-Scattering Studies in Aerosols with a New Counter-Photometer. *Analytical Chemistry*, 27(5):694–701, 1955. ISSN 15206882. doi: 10.1021/ac60101a002.

OpenStreetMap-Contributors. Planet dump retrieved from https://planet.osm.org, 2017. URL `https://www.openstreetmap.org`.

S. R. Osborne, S. J. Abel, I. A. Boutle, and F. Marenco. Evolution of Stratocumulus Over Land: Comparison of Ground and Aircraft Observations with Numerical Weather Prediction Simulations. *Boundary-Layer Meteorology*, 153(2):165–193, 11 2014. ISSN 0006-8314. doi: 10.1007/s10546-014-9944-0. URL `http://link.springer.com/10.1007/s10546-014-9944-0`.

R. T. Palomaki, N. T. Rose, M. van den Bossche, T. J. Sherman, and S. F. De Wekker. Wind estimation in the lower atmosphere using multirotor aircraft. *Journal of Atmospheric and Oceanic Technology*, 34(5):1183–1191, 2017. ISSN 15200426. doi: 10.1175/JTECH-D-16-0177.1.

R. Pinnick and H. Auvermann. Response characteristics of knollenberg light-scattering aerosol counters. *Journal of Aerosol Science*, 10(1):55–74, 1 1979. ISSN 00218502. doi: 10.1016/0021-8502(79)90136-8. URL `https://linkinghub.elsevier.com/retrieve/pii/0021850279901368`.

R. G. Pinnick, D. M. Garvey, and L. D. Duncan. Calibration of Knollenberg FSSP Light-Scattering Counters for Measurement of Cloud Droplets. *Journal of Applied Meteorology*, 20(9):1049–1057, 9 1981. ISSN 0021-8952. doi: 10.1175/1520-0450(1981)020<1049:COKFLS>2.0.CO;2. URL `http://journals.ametsoc.org/doi/10.1175/1520-0450(1981)020%3C1049:COKFLS%3E2.0.CO;2`.

M. Pinsky and A. Khain. Fine Structure of Cloud Droplet Concentration as Seen from the Fast-FSSP Measurements. Part II: Results of In Situ Observations. *Journal of Applied Meteorology*, 42(1):65–73, 1 2003. ISSN 0894-8763. doi: 10.1175/1520-0450(2003)042<0065:FSOCDC>2.0.CO;2. URL `http://journals.ametsoc.org/doi/10.1175/1520-0450(2003)042%3C0065:FSOCDC%3E2.0.CO;2`.

M. Pinsky and A. P. Khain. Fine Structure of Cloud Droplet Concentration as Seen from the Fast-FSSP Measurements. Part I: Method of Analysis and Preliminary Results. *Journal of Applied Meteorology*, 40(8): 1515–1537, 8 2001. ISSN 0894-8763. doi: 10.1175/1520-0450(2001)040<1515:FSOCDC>2.0.CO;2. URL http://journals.ametsoc.org/doi/10.1175/1520-0450(2001)040%3C1515:FSOCDC%3E2.0.CO;2.

A. Platis, B. Altstädter, B. Wehner, N. Wildmann, A. Lampert, M. Hermann, W. Birmili, and J. Bange. An Observational Case Study on the Influence of Atmospheric Boundary-Layer Dynamics on New Particle Formation. *Boundary-Layer Meteorology*, 158(1):67–92, 1 2016. ISSN 0006-8314. doi: 10.1007/s10546-015-0084-y. URL http://link.springer.com/10.1007/s10546-015-0084-y.

J. Price. Radiation Fog. Part I: Observations of Stability and Drop Size Distributions. *Boundary-Layer Meteorology*, 139(2):167–191, 2011. ISSN 00068314. doi: 10.1007/s10546-010-9580-2.

J. D. Price, S. Lane, I. A. Boutle, D. K. E. Smith, T. Bergot, C. Lac, L. Duconge, J. McGregor, A. Kerr-Munslow, M. Pickering, and R. Clark. LANFEX: A Field and Modeling Study to Improve Our Understanding and Forecasting of Radiation Fog. *Bulletin of the American Meteorological Society*, 99(10):2061–2077, 10 2018. ISSN 0003-0007. doi: 10.1175/BAMS-D-16-0299.1. URL http://journals.ametsoc.org/doi/10.1175/BAMS-D-16-0299.1.

J. Quan, Y. Gao, Q. Zhang, X. Tie, J. Cao, S. Han, J. Meng, P. Chen, and D. Zhao. Evolution of planetary boundary layer under different weather conditions, and its impact on aerosol concentrations. *Particuology*, 11(1):34–40, 2013. ISSN 16742001. doi: 10.1016/j.partic.2012.04.005. URL http://dx.doi.org/10.1016/j.partic.2012.04.005.

V. Ramanathan, M. V. Ramana, G. Roberts, D. Kim, C. Corrigan, C. Chung, and D. Winker. Warming trends in Asia amplified by brown cloud solar absorption. *Nature*, 448(7153):575–578, 2007. ISSN 14764687. doi: 10.1038/nature06019.

RaspberryPi-Foundation. Raspberry Pi Zero, 2015. URL https://www.raspberrypi.org/products/raspberry-pi-zero/.

J. Redemann, R. Wood, P. Zuidema, S. J. Doherty, B. Luna, S. E. LeBlanc, M. S. Diamond, Y. Shinozuka, I. Y. Chang, R. Ueyama, L. Pfister, J. M. Ryoo, A. N. Dobracki, A. M. da Silva, K. M. Longo, M. S. Kacenelenbogen, C. J. Flynn, K. Pistone, N. M. Knox, S. J. Piketh, J. M. Haywood, P. Formenti, M. Mallet, P. Stier, A. S. Ackerman, S. E. Bauer, A. M. Fridlind, G. R. Carmichael, P. E. Saide, G. A. Ferrada, S. G. Howell, S. Freitag, B. Cairns, B. N. Holben, K. D. Knobelspiesse, S. Tanelli, T. S. L'Ecuyer, A. M. Dzambo, O. O. Sy, G. M. McFarquhar, M. R. Poellot, S. Gupta, J. R. O'Brien, A. Nenes, M. Kacarab,

J. P. Wong, J. D. Small-Griswold, K. L. Thornhill, D. Noone, J. R. Podolske, K. Sebastian Schmidt, P. Pilewskie, H. Chen, S. P. Cochrane, A. J. Sedlacek, T. J. Lang, E. Stith, M. Segal-Rozenhaimer, R. A. Ferrare, S. P. Burton, C. A. Hostetler, D. J. Diner, F. C. Seidel, S. E. Platnick, J. S. Myers, K. G. Meyer, D. A. Spangenberg, H. Maring, and L. Gao. An overview of the ORACLES (ObseRvations of aerosols above CLouds and their intEractionS) project: Aerosol-cloud-radiation interactions in the south-east Atlantic basin. *Atmospheric Chemistry and Physics*, 21(3):1507–1563, 2021. ISSN 16807324. doi: 10.5194/acp-21-1507-2021.

D. Reitz. Modeling Atomization Processes in High-Pressure Vaporizing Sprays. *Atomisation and Spray Technology*, 3:309–337, 1987. ISSN 0266-3481.

J. B. Renard, F. Dulac, G. Berthet, T. Lurton, D. Vignelles, F. Jégou, T. Tonnelier, M. Jeannot, B. Couté, R. Akiki, N. Verdier, M. Mallet, F. Gensdarmes, P. Charpentier, S. Mesmin, V. Duverger, J. C. Dupont, T. Elias, V. Crenn, J. Sciare, P. Zieger, M. Salter, T. Roberts, J. Giacomoni, M. Gobbi, E. Hamonou, H. Olafsson, P. Dagsson-Waldhauserova, C. Camy-Peyret, C. Mazel, T. Décamps, M. Piringer, J. Surcin, and D. Daugeron. LOAC: A small aerosol optical counter/sizer for ground-based and balloon measurements of the size distribution and nature of atmospheric particles-Part 2: First results from balloon and unmanned aerial vehicle flights. *Atmospheric Measurement Techniques*, 9(8):3673–3686, 2016. ISSN 18678548. doi: 10.5194/amt-9-3673-2016.

J.-B. Renard, F. Dulac, P. Durand, Q. Bourgeois, C. Denjean, D. Vignelles, B. Couté, M. Jeannot, N. Verdier, and M. Mallet. In situ measurements of desert dust particles above the western Mediterranean Sea with the balloon-borne Light Optical Aerosol Counter/sizer (LOAC) during the ChArMEx campaign of summer 2013. *Atmospheric Chemistry and Physics*, 18(5):3677–3699, 3 2018. ISSN 1680-7324. doi: 10.5194/acp-18-3677-2018. URL `https://www.atmos-chem-phys.net/18/3677/2018/`.

J. Reuder, P. Brisset, M. Jonassen, M. Müller, and S. Mayer. The Small Unmanned Meteorological Observer SUMO: A new tool for atmospheric boundary layer research. *Meteorologische Zeitschrift*, 18(2):141–147, 2009. ISSN 09412948. doi: 10.1127/0941-2948/2009/0363.

G. C. Roberts, M. V. Ramana, C. Corrigan, D. Kim, and V. Ramanathan. Simultaneous observations of aerosol-cloud-albedo interactions with three stacked unmanned aerial vehicles. *Proceedings of the National Academy of Sciences*, 105(21):7370–7375, 2008. ISSN 0027-8424. doi: 10.1073/pnas.0710308105. URL `http://www.pnas.org/cgi/doi/10.1073/pnas.0710308105`.

A. Rocha-Lima, J. V. Martins, L. A. Remer, M. Todd, J. H. Marsham, S. Engelstaedter, C. L. Ryder, C. Cavazos-Guerra, P. Artaxo, P. Colarco, and R. Washington. A detailed characterization of the saharan

dust collected during the fennec campaign in 2011: in situ ground-based and laboratory measurements. *Atmospheric Chemistry and Physics*, 18(2):1023–1043, 2018. doi: 10.5194/acp-18-1023-2018. URL `https://acp.copernicus.org/articles/18/1023/2018/`.

J. J. Roldán, G. Joossen, D. Sanz, J. del Cerro, and A. Barrientos. Mini-UAV based sensory system for measuring environmental variables in greenhouses. *Sensors (Switzerland)*, 15(2):3334–3350, 2015. ISSN 14248220. doi: 10.3390/s150203334.

P. D. Rosenberg, A. R. Dean, P. I. Williams, J. R. Dorsey, A. Minikin, M. A. Pickering, and A. Petzold. Particle sizing calibration with refractive index correction for light scattering optical particle counters and impacts upon PCASP and CDP data collected during the Fennec campaign. *Atmospheric Measurement Techniques*, 5(5):1147–1163, 2012. ISSN 18671381. doi: 10.5194/amt-5-1147-2012.

E. Ruppecht, M. Meyer, and H. Patashnick. The tapered element oscillating microbalance as a tool for measuring ambient particulate concentrations in real time. *Journal of Aerosol Science*, 23:635–638, 1 1992. ISSN 00218502. doi: 10.1016/0021-8502(92)90492-E. URL `https://linkinghub.elsevier.com/retrieve/pii/002185029290492E`.

C. L. Ryder, E. J. Highwood, P. D. Rosenberg, J. Trembath, J. K. Brooke, M. Bart, A. Dean, J. Crosier, J. Dorsey, H. Brindley, J. Banks, J. H. Marsham, J. B. McQuaid, H. Sodemann, and R. Washington. Optical properties of Saharan dust aerosol and contribution from the coarse mode as measured during the Fennec 2011 aircraft campaign. *Atmospheric Chemistry and Physics*, 13(1):303–325, 2013. ISSN 16807316. doi: 10.5194/acp-13-303-2013.

C. L. Ryder, J. B. McQuaid, C. Flamant, P. D. Rosenberg, R. Washington, H. E. Brindley, E. J. Highwood, J. H. Marsham, D. J. Parker, M. C. Todd, J. R. Banks, J. K. Brooke, S. Engelstaedter, V. Estelles, P. Formenti, L. Garcia-Carreras, C. Kocha, F. Marenco, H. Sodemann, C. J. Allen, A. Bourdon, M. Bart, C. Cavazos-Guerra, S. Chevaillier, J. Crosier, E. Darbyshire, A. R. Dean, J. R. Dorsey, J. Kent, D. O'Sullivan, K. Schepanski, K. Szpek, J. Trembath, and A. Woolley. Advances in understanding mineral dust and boundary layer processes over the Sahara from Fennec aircraft observations. *Atmospheric Chemistry and Physics*, 15(14):8479–8520, 2015. ISSN 16807324. doi: 10.5194/acp-15-8479-2015.

C. L. Ryder, E. J. Highwood, A. Walser, P. Seibert, A. Philipp, and B. Weinzierl. Coarse and giant particles are ubiquitous in Saharan dust export regions and are radiatively significant over the Sahara. *Atmospheric Chemistry and Physics*, 19(24):15353–15376, 12 2019. doi: 10.5194/acp-19-15353-2019. URL `https://acp.copernicus.org/articles/19/15353/2019/`.

P. Santana, A. Almeida, P. Mariano, C. Correia, V. Martins, and S. M. Almeida. Air quality mapping and visualisation: An affordable solution based on a vehicle-mounted sensor network. *Journal of Cleaner Production*, 315(June):128194, 9 2021. ISSN 09596526. doi: 10.1016/j.jclepro.2021.128194. URL `https://linkinghub.elsevier.com/retrieve/pii/S0959652621024124`.

C. G. Schmitt, M. Schnaiter, A. J. Heymsfield, P. Yang, E. Hirst, and A. Bansemer. The Microphysical Properties of Small Ice Particles Measured by the Small Ice Detector-3 Probe during the MACPEX Field Campaign. *Journal of the Atmospheric Sciences*, 73(12):4775–4791, 12 2016. ISSN 0022-4928. doi: 10.1175/JAS-D-16-0126.1. URL `https://journals.ametsoc.org/doi/10.1175/JAS-D-16-0126.1`.

B. G. Schuster and R. Knollenberg. Detection and Sizing of Small Particles in an Open Cavity Gas Laser. *Applied Optics*, 11(7):1515, 1972. ISSN 0003-6935. doi: 10.1364/ao.11.001515.

D. R. Secker, P. H. Kaye, and E. Hirst. Real-time observation of the change in light scattering from droplets with increasing deformity. *Optics Express*, 8(6):290, 3 2001. ISSN 1094-4087. doi: 10.1364/OE.8.000290. URL `https://www.osapublishing.org/abstract.cfm?URI=oe-8-6-290`.

D. J. Seidel, C. O. Ao, and K. Li. Estimating climatological planetary boundary layer heights from radiosonde observations: Comparison of methods and uncertainty analysis. *Journal of Geophysical Research*, 115 (D16):D16113, 8 2010. ISSN 0148-0227. doi: 10.1029/2009JD013680. URL `http://doi.wiley.com/10.1029/2009JD013680`.

P. A. Sheppard. The effect of pollution on radiation in the atmosphere. *International journal of air pollution*, 1(1-2):31–43, 10 1958. URL `http://www.ncbi.nlm.nih.gov/pubmed/13610489`.

T. Shimura, M. Inoue, H. Tsujimoto, K. Sasaki, and M. Iguchi. Estimation of wind vector profile using a hexarotor unmanned aerial vehicle and its application to meteorological observation up to 1000 m above surface. *Journal of Atmospheric and Oceanic Technology*, 35(8):1621–1631, 2018. ISSN 15200426. doi: 10.1175/JTECH-D-17-0186.1.

M. Shrivastava, L. K. Berg, J. D. Fast, R. C. Easter, A. Laskin, E. G. Chapman, W. I. Gustafson, Y. Liu, and C. M. Berkowitz. Modeling aerosols and their interactions with shallow cumuli during the 2007 CHAPS field study. *Journal of Geophysical Research Atmospheres*, 118(3):1343–1360, 2013. ISSN 21698996. doi: 10.1029/2012JD018218.

D. Sinclair. A new photometer for aerosol particle size analysis. *Journal of the Air Pollution Control Association*, 17(2):105–108, 1967. ISSN 00022470. doi: 10.1080/00022470.1967.10468948.

H. B. Singh, E. J. Jensen, and L. Pfister. Overview of the Airborne Tropical TRopopause EXperiment (ATTREX). 2014:A23E–3297, Dec. 2014. URL https://ui.adsabs.harvard.edu/abs/2014AGUFM.A23E3297S. Conference Name: AGU Fall Meeting Abstracts ADS Bibcode: 2014AGUFM.A23E3297S.

J. D. Small and P. Y. Chuang. New observations of precipitation initiation in warm cumulus clouds. *Journal of the Atmospheric Sciences*, 65(9):2972–2982, 2008. ISSN 00224928. doi: 10.1175/2008JAS2600.1.

H. R. Smith, Z. Ulanowski, P. H. Kaye, E. Hirst, W. Stanley, R. Kaye, A. Wieser, C. Stopford, M. Kezoudi, J. Girdwood, R. Greenaway, and R. Mackenzie. The Universal Cloud and Aerosol Sounding System (UCASS): a low-cost miniature optical particle counter for use in dropsonde or balloon-borne sounding systems. *Atmospheric Measurement Techniques*, 12(12):6579–6599, 12 2019. ISSN 1867-8548. doi: 10.5194/amt-12-6579-2019. URL https://amt.copernicus.org/articles/12/6579/2019/.

J. R. Soddell, K. McGuffie, and G. J. Holland. Intercomparison of atmospheric soundings from the aerosonde and radiosonde. *Journal of Applied Meteorology*, 43(9):1260–1269, 2004. ISSN 08948763. doi: 10.1175/1520-0450(2004)043<1260:IOASFT>2.0.CO;2.

A. Spanu, M. Dollner, J. Gasteiger, T. P. Bui, and B. Weinzierl. Flow-induced errors in airborne in-situ measurements of aerosols and clouds. *Atmospheric Measurement Techniques Discussions*, 2019 (February):1–46, 2019. doi: 10.5194/amt-2019-27. URL https://www.atmos-meas-tech-discuss.net/amt-2019-27/.

T. Spiess, J. Bange, M. Buschmann, and P. Vörsmann. First application of the meteorological Mini-UAV 'M2AV'. *Meteorologische Zeitschrift*, 16(2):159–169, 2007. ISSN 09412948. doi: 10.1127/0941-2948/2007/0195.

G. Stephens and T. Slingo. An air-conditioned greenhouse. *Nature*, 358(6385):369–370, 7 1992. ISSN 0028-0836. doi: 10.1038/358369a0. URL https://www.infodesign.org.br/infodesign/article/view/355%0Ahttp://www.abergo.org.br/revista/index.php/ae/article/view/731%0Ahttp://www.abergo.org.br/revista/index.php/ae/article/view/269%0Ahttp://www.abergo.org.br/revista/index.php/ae/article/view/106ht.

G. L. Stephens, G. W. Paltridge, and C. M. R. Platt. Radiation Profiles in Extended Water Clouds. III: Observations. *Journal of the Atmospheric Sciences*, 35(11):2133–2141, 11 1978. ISSN 0022-4928. doi: 10.1175/1520-0469(1978)035<2133:RPIEWC>2.0.CO;2. URL http://journals.ametsoc.org/doi/10.1175/1520-0469(1978)035%3C2133:RPIEWC%3E2.0.CO;2.

J. W. Strapp, W. R. Leaitch, and P. S. K. Liu. Hydrated and Dried Aerosol-Size-Distribution Measurements from the Particle Measuring Systems FSSP-300 Probe and the Deiced PCASP-100X Probe. *Journal of Atmospheric and Oceanic Technology*, 9(5):548–555, 1992. ISSN 0739-0572. doi: 10.1175/1520-0426(1992)009<0548:HADASD>2.0.CO;2. URL http://journals.ametsoc.org/doi/abs/10.1175/1520-0426(1992)009%3C0548:HADASD%3E2.0.CO;2.

T. Su, Z. Li, C. Li, J. Li, W. Han, C. Shen, W. Tan, J. Wei, and J. Guo. The significant impact of aerosol vertical structure on lower atmosphere stability and its critical role in aerosol-planetary boundary layer (PBL) interactions. *Atmospheric Chemistry and Physics*, 20(6):3713–3724, 2020. ISSN 16807324. doi: 10.5194/acp-20-3713-2020.

Y. Sun, T. Song, G. Tang, and Y. Wang. The vertical distribution of PM2.5 and boundary-layer structure during summer haze in Beijing. *Atmospheric Environment*, 74:413–421, 2013. ISSN 13522310. doi: 10.1016/j.atmosenv.2013.03.011. URL http://dx.doi.org/10.1016/j.atmosenv.2013.03.011.

Y. Sun, W. Du, Q. Wang, Q. Zhang, C. Chen, Y. Chen, Z. Chen, P. Fu, Z. Wang, Z. Gao, and D. R. Worsnop. Real-Time Characterization of Aerosol Particle Composition above the Urban Canopy in Beijing: Insights into the Interactions between the Atmospheric Boundary Layer and Aerosol Chemistry. *Environmental Science & Technology*, 49(19):11340–11347, 10 2015. ISSN 0013-936X. doi: 10.1021/acs.est.5b02373. URL https://pubs.acs.org/doi/10.1021/acs.est.5b02373.

J. W. Taylor, H. Wu, K. Szpek, K. Bower, I. Crawford, M. J. Flynn, P. I. Williams, J. Dorsey, J. M. Langridge, M. I. Cotterell, C. Fox, N. W. Davies, J. M. Haywood, and H. Coe. Absorption closure in highly aged biomass burning smoke. *Atmospheric Chemistry and Physics*, 20(19):11201–11221, 2020. ISSN 16807324. doi: 10.5194/acp-20-11201-2020.

W. Thielicke, W. Hübert, U. Müller, M. Eggert, and P. Wilhelm. Towards accurate and practical drone-based wind measurements with an ultrasonic anemometer. *Atmospheric Measurement Techniques*, 14(2):1303–1318, 2021. ISSN 18678548. doi: 10.5194/amt-14-1303-2021.

T. D. Thornberry, A. W. Rollins, M. A. Avery, S. Woods, R. P. Lawson, T. V. Bui, and R.-S. Gao. Ice water content-extinction relationships and effective diameter for TTL cirrus derived from in situ measurements during ATTREX 2014. *Journal of Geophysical Research: Atmospheres*, 122(8):4494–4507, 2017. ISSN 2169-8996. doi: 10.1002/2016JD025948. URL https://onlinelibrary.wiley.com/doi/abs/10.1002/2016JD025948. _eprint: https://onlinelibrary.wiley.com/doi/pdf/10.1002/2016JD025948.

L. Tian and G. Ahmadi. Particle deposition in turbulent duct flows—comparisons of different model predictions. *Journal of Aerosol Science*, 38(4):377–397, 4 2007. ISSN 00218502. doi: 10.1016/j.jaerosci.2006.12.003. URL https://linkinghub.elsevier.com/retrieve/pii/S002185020700002X.

R. C. Tolman, R. H. Gerkb, A. P. Brooks, A. G. Herman, R. S. Mullikbn, and H. D. Smyth. Relation between intensity of tyndall beam and size of particles. *Journal of the American Chemical Society*, 41(4):575–587, 1919. ISSN 15205126. doi: 10.1021/ja01461a008.

S.-C. Tsay and K. Jayaweera. Physical Characteristics of Arctic Stratus Clouds. *Journal of Climate and Applied Meteorology*, 23(4):584–596, 4 1984. ISSN 0733-3021. doi: 10.1175/1520-0450(1984)023<0584:PCOASC>2.0.CO;2. URL http://journals.ametsoc.org/doi/10.1175/1520-0450(1984)023%3C0584:PCOASC%3E2.0.CO;2.

A. Tsekeri, A. Lopatin, V. Amiridis, E. Marinou, J. Igloffstein, N. Siomos, S. Solomos, P. Kokkalis, R. Engelmann, H. Baars, M. Gratsea, P. I. Raptis, I. Binietoglou, N. Mihalopoulos, N. Kalivitis, G. Kouvarakis, N. Bartsotas, G. Kallos, S. Basart, D. Schuettemeyer, U. Wandinger, A. Ansmann, A. P. Chaikovsky, and O. Dubovik. GARRLiC and LIRIC: Strengths and limitations for the characterization of dust and marine particles along with their mixtures. *Atmospheric Measurement Techniques*, 10(12):4995–5016, 2017. ISSN 18678548. doi: 10.5194/amt-10-4995-2017.

Z. Ulanowski, J. Bailey, P. W. Lucas, J. H. Hough, and E. Hirst. Alignment of atmospheric mineral dust due to electric field. *Atmospheric Chemistry and Physics*, 7(24):6161–6173, 2007. ISSN 16807324. doi: 10.5194/acp-7-6161-2007.

Z. Ulanowski, P. H. Kaye, E. Hirst, R. S. Greenaway, R. J. Cotton, E. Hesse, and C. T. Collier. Incidence of rough and irregular atmospheric ice particles from Small Ice Detector 3 measurements. *Atmospheric Chemistry and Physics*, 14(3):1649–1662, 2 2014. ISSN 1680-7324. doi: 10.5194/acp-14-1649-2014. URL https://acp.copernicus.org/articles/14/1649/2014/.

A. van den Kroonenberg, T. Martin, M. Buschmann, J. Bange, and P. Vörsmann. Measuring the wind vector using the autonomous mini aerial vehicle M2AV. *Journal of Atmospheric and Oceanic Technology*, 25(11):1969–1982, 2008. ISSN 07390572. doi: 10.1175/2008JTECHA1114.1.

T. Villa, F. Gonzalez, B. Miljievic, Z. Ristovski, and L. Morawska. An Overview of Small Unmanned Aerial Vehicles for Air Quality Measurements: Present Applications and Future Prospectives. *Sensors*, 16(7):1072, 2016. ISSN 1424-8220. doi: 10.3390/s16071072. URL http://www.mdpi.com/1424-8220/16/7/1072.

P. Vochezer, E. Jarvinen, R. Wagner, P. Kupiszewski, T. Leisner, and M. Schnaiter. In situ characterization of mixed phase clouds using the Small Ice Detector and the Particle Phase Discriminator. *Atmospheric Measurement Techniques*, 9(1):159–177, 2016. ISSN 18678548. doi: 10.5194/amt-9-159-2016.

S. L. Von Der Weiden, F. Drewnick, and S. Borrmann. Particle Loss Calculator - A new software tool for the assessment of the performance of aerosol inlet systems. *Atmospheric Measurement Techniques*, 2(2): 479–494, 2009. ISSN 18678548. doi: 10.5194/amt-2-479-2009.

J. Wagner, A. Ansmann, U. Wandinger, P. Seifert, A. Schwarz, M. Tesche, A. Chaikovsky, and O. Dubovik. Evaluation of the Lidar/Radiometer Inversion Code (LIRIC) to determine microphysical properties of volcanic and desert dust. *Atmospheric Measurement Techniques*, 6(7):1707–1724, 2013. ISSN 18671381. doi: 10.5194/amt-6-1707-2013.

S. C. Wang and R. C. Flagan. Scanning electrical mobility spectrometer. *Aerosol Science and Technology*, 13(2):230–240, 1990. ISSN 15217388. doi: 10.1080/02786829008959441.

T. Wetz, N. Wildmann, and F. Beyrich. Distributed wind measurements with multiple quadrotor unmanned aerial vehicles in the atmospheric boundary layer. *Atmospheric Measurement Techniques*, 14(5):3795–3814, 2021. ISSN 18678548. doi: 10.5194/amt-14-3795-2021.

K. T. Whitby and R. A. Vomela. Response of Single Particle Optical Counters to Nonideal Particles. *Environmental Science and Technology*, 1(10):801–814, 1967. ISSN 15205851. doi: 10.1021/es60010a002.

G. A. Wick, T. F. Hock, P. J. Neiman, H. Vömel, M. L. Black, and J. R. Spackman. The NCAR–NOAA Global Hawk Dropsonde System. *Journal of Atmospheric and Oceanic Technology*, 35(8):1585–1604, Aug. 2018. ISSN 0739-0572, 1520-0426. doi: 10.1175/JTECH-D-17-0225.1. URL `https://journals.ametsoc.org/view/journals/atot/35/8/jtech-d-17-0225.1.xml`. Publisher: American Meteorological Society Section: Journal of Atmospheric and Oceanic Technology.

N. Wildmann, M. Mauz, and J. Bange. Two fast temperature sensors for probing of the atmospheric boundary layer using small remotely piloted aircraft (RPA). *Atmospheric Measurement Techniques*, 6(8):2101–2113, 8 2013. ISSN 1867-8548. doi: 10.5194/amt-6-2101-2013. URL `https://amt.copernicus.org/articles/6/2101/2013/`.

N. Wildmann, M. Hofsäß, F. Weimer, A. Joos, and J. Bange. MASC - a small Remotely Piloted Aircraft (RPA) for wind energy research. *Advances in Science and Research*, 11(May):55–61, 2014a. ISSN 1992-0636. doi: 10.5194/asr-11-55-2014. URL `http://www.adv-sci-res.net/11/55/2014/`.

N. Wildmann, F. Kaufmann, and J. Bange. An inverse-modelling approach for frequency response correction of capacitive humidity sensors in ABL research with small remotely piloted aircraft (RPA). *Atmospheric Measurement Techniques*, 7(9):3059–3069, 2014b. ISSN 18678548. doi: 10.5194/amt-7-3059-2014.

N. Wildmann, S. Ravi, and J. Bange. Towards higher accuracy and better frequency response with standard multi-hole probes in turbulence measurement with remotely piloted aircraft (RPA). *Atmospheric Measurement Techniques*, 7(4):1027–1041, 2014c. ISSN 18678548. doi: 10.5194/amt-7-1027-2014.

D. M. Winker, W. H. Hunt, and M. J. McGill. Initial performance assessment of CALIOP. *Geophysical Research Letters*, 34(19):L19803, 10 2007. ISSN 0094-8276. doi: 10.1029/2007GL030135. URL `http://doi.wiley.com/10.1029/2007GL030135`.

H. Wu, J. W. Taylor, K. Szpek, J. M. Langridge, P. I. Williams, M. Flynn, J. D. Allan, S. J. Abel, J. Pitt, M. I. Cotterell, C. Fox, N. W. Davies, J. Haywood, and H. Coe. Vertical variability of the properties of highly aged biomass burning aerosol transported over the southeast Atlantic during CLARIFY-2017. *Atmospheric Chemistry and Physics*, 20(21):12697–12719, 11 2020. ISSN 1680-7324. doi: 10.5194/acp-20-12697-2020. URL `https://acp.copernicus.org/articles/20/12697/2020/`.

R. Xu, W. Zhang, N. H. Wong, S. Tong, and X. Wu. A novel methodology to obtain ambient temperatures using multi-rotor UAV-mounted sensors. *Urban Climate*, 41(June 2021):101068, 2022. ISSN 22120955. doi: 10.1016/j.uclim.2021.101068. URL `https://doi.org/10.1016/j.uclim.2021.101068`.

M. D. Zelinka, T. Andrews, P. M. Forster, and K. E. Taylor. Quantifying components of aerosol-cloud-radiation interactions in climate models. *Journal of Geophysical Research: Atmospheres*, 119(12):7599–7615, 6 2014. ISSN 2169897X. doi: 10.1002/2014JD021710. URL `http://doi.wiley.com/10.1002/2014JD021710`.

X. Zeng. The influence of radiation on ice crystal spectrum in the upper troposphere. *Quarterly Journal of the Royal Meteorological Society*, 134(632):609–620, 4 2008. ISSN 00359009. doi: 10.1002/qj.226. URL `http://doi.wiley.com/10.1002/qj.226`.

X. Zeng. Modeling the Effect of Radiation on Warm Rain Initiation. *Journal of Geophysical Research: Atmospheres*, 123(13):6896–6906, 2018a. ISSN 21698996. doi: 10.1029/2018JD028354.

X. Zeng. Radiatively Induced Precipitation Formation in Diamond Dust. *Journal of Advances in Modeling Earth Systems*, 10(9):2300–2317, 9 2018b. ISSN 1942-2466. doi: 10.1029/2018MS001382. URL `http://doi.wiley.com/10.1029/2018MS001382`.

S. H. Zhang, Y. Akutsu, L. M. Russell, R. C. Flagan, and J. H. Seinfeld. Radial differential mobility analyzer. *Aerosol Science and Technology*, 23(3):357–372, 1995. ISSN 15217388. doi: 10.1080/02786829508965320.